

MATER. TEHNOL.	LETNIK VOLUME	47	ŠTEV. NO.	4	STR. P.	401–540	LJUBLJANA SLOVENIJA	JULY–AUG. 2013
-------------------	------------------	----	--------------	---	------------	---------	------------------------	-------------------

VSEBINA – CONTENTS

PREGLEDNI ČLANKI – REVIEW ARTICLES

Effect of heat treatment on the microstructure and mechanical properties of martensitic stainless-steel joints welded with austenitic stainless-steel fillers

Vpliv toplotne obdelave na mikrostrukturo in mehanske lastnosti martenzitnih nerjavnih spojev, varjenih z avstenitnimi nerjavnimi elektrodami

A. Calik, M. S. Karakaş 403

IZVIRNI ZNANSTVENI ČLANKI – ORIGINAL SCIENTIFIC ARTICLES

New combined bio-scouring and bio-bleaching process of cotton fabrics

Nov, združeni postopek bioizkuhanja in biobeljenja bombažnih tkanin

N. Špička, P. Forte Tavčer 409

Effect of mechanical activation on mullite formation in an alumina-quartz ceramics system

Vpliv mehanske aktivacije na nastanek mullita v keramičnem sistemu glinica-kremen

E. Elmas, K. Yildiz, N. Toplan, H. Özkan Toplan 413

Determination of the mechanical parameters of a bonded joint between a metal and a composite by comparing experiments with a finite-element model

Določanje mehanskih parametrov spoja med kovino in kompozitom s primerjavo preizkusov in modelom končnih elementov

P. Bernardin, J. Vacík, T. Kroupa, R. Kottner 417

Determination of the metal concentrations in an anode material for solid-oxide fuel cells

Določitev vsebnosti kovin v anodnem materialu za gorivne celice s trdnim elektrolitom

T. Skalar, A. Golobčič, M. Marinšek, J. Maček 423

Producing antibacterial silver-doped hydroxyapatite powders with chemical precipitation and reshaping in a spray dryer

Izdelava s srebrom dopiranega protibakterijskega prahu hidroksiapatita s kemijskim izločanjem in preoblikovanjem v razpršilnem sušilniku

F. E. Baştan, Y. Y. Özbek 431

Tribocorrosion degradation of protective coatings on stainless steel

Tribokorozijska degradacija zaščitnih prevlek na nerjavnem jeklu

D. Kek Merl, P. Panjan, M. Čekada, P. Gselman, S. Paskvale 435

Behaviour of short cracks emanating from tiny drilled holes

Vedenje kratkih razpok, ki nastanejo iz majhnih izvrtin

V. Gliha, P. Maruschak, T. Vuherer 441

Internal-oxidation kinetics of Ag-Cd alloys

Kinetika notranje oksidacije zlitin Ag-Cd

L. Balanović, V. Čosović, N. Talijan, D. Živković 447

Effects of the ageing treatment on the superelastic behavior of a nitinol stent for an application in the esophageal duct: a finite-element analysis

Učinek staranja na superelastično vedenje nitinolne opore pri uporabi v cevi požiralnika: analiza končnih elementov

F. Nematzadeh, S. K. Sadrnezhaad 453

Investigation of the effect of skin-pass rolling on the formability of low-carbon steel sheets

Preiskava učinka dresirnega valjanja na preoblikovalnost maloogljične jeklene pločevine

D. Asefi, H. Monajatizadeh, A. Ansari-pour, A. Salimi 461

Synthesis, characterization and sensing application of a solid alum/fly ash composite electrolyte

Sinteza, karakterizacija in možnost uporabe trdnega kompozitnega elektrolita galun-leteči pepel

A. Sachdeva, R. Singh, P. K. Singh, B. Bhattacharya 467

Different source atelocollagen thin films: preparation, process optimisation and its influence on the interaction with eukaryotic cells	
Različni izviri atelokolagenskih tankih plasti: priprava, optimizacija procesa in vpliv na interakcije z evkariontičnimi celicami	
J. López García, P. Humpolíček, M. Lehocký, I. Junkar, M. Mozetič	473
Evaluation of equilibrium isotherm models for the adsorption of Cu and Ni from wastewater on bentonite clay	
Ocena modelov ravnotežnih izoterm za adsorpcijo Cu in Ni iz odpadnih vod na bentonitno glino	
S. A. Al-Jilil, M. S. Latif	481
Modelling and optimization of a laser droplet-formation process	
Modeliranje in optimizacija laserskega tvorjenja kapljice	
T. Kokalj, I. Grabec, E. Govekar	487
STROKOVNI ČLANKI – PROFESSIONAL ARTICLES	
Comparison of the temperature fields of continuously cast steel slabs with different chemical compositions	
Primerjava temperaturnega polja kontinuirno ulitih jeklenih slabov različnih kemijskih sestav	
F. Kavicka, K. Stransky, B. Sekanina, J. Stetina, M. Masarik, T. Mauder, V. Gontarev	497
Investigation of the thermomechanical properties and microstructure of special magnesium alloys	
Preiskava termomehanskih lastnosti in mikrostrukture posebnih magnezijevih zlitin	
P. Lichý, M. Cagala, J. Beňo	503
Impact of casting speed on the temperature field of continuously cast steel billets	
Vpliv livne hitrosti na temperaturno polje kontinuirno ulitih gredic iz jekla	
L. Klimes, J. Stetina, P. Bucek	507
Development of the production of ultrafine-grained titanium with the conform equipment	
Razvoj proizvodnje ultradrobnozrnatega titana z opremo conform	
M. Ducheck, T. Kubina, J. Hodek, J. Dlouhy	515
Conversion of the Ms70 alpha-brass torsion-test data into hot-forming processing maps	
Pretvorba podatkov torzijskega preizkusa alfa medi Ms70 v procesne zemljevide vroče predelave	
T. Kubina, J. Bořuta, R. Pernis	519
Recycled polymer/clay composites for heavy-metals adsorption	
Recikliran kompozit polimer-glina za adsorpcijo težkih kovin	
F. D. Alsewailam, S. A. Aljlil	525
Influential factors in the surface-hardness testing of a nitrided layer	
Vplivni faktorji pri preizkušanju trdote površine nitrirane plasti	
F. Cajner, D. Landek, I. Kumić, A. Vugrinčić	531
Mechanical and microstructural properties of the fly-ash-based geopolymer paste and mortar	
Mehanske in mikrostrukturne lastnosti geopolimernih veziv in malt iz letečega pepela	
R. Zejak, I. Nikolić, D. Blečić, V. Radmilović, V. Radmilović	535

EFFECT OF HEAT TREATMENT ON THE MICROSTRUCTURE AND MECHANICAL PROPERTIES OF MARTENSITIC STAINLESS-STEEL JOINTS WELDED WITH AUSTENITIC STAINLESS-STEEL FILLERS

VPLIV TOPLOTNE OBDELAVE NA MIKROSTRUKTURO IN MEHANSKE LASTNOSTI MARTENZITNIH NERJAVNIH SPOJEV, VARJENIH Z AVSTENITNIMI NERJAVNIMI ELEKTRODAMI

Adnan Calik, Mustafa Serdar Karakaş

Department of Manufacturing Engineering, Faculty of Technology, Suleyman Demirel University, 32260 Cunur, Isparta, Turkey
adnancalik@sdu.edu.tr

Prejem rokopisa – received: 2012-11-08; sprejem za objavo – accepted for publication: 2013-01-04

AISI 422 martensitic stainless steels were welded according to the ISO 15792-1 standard with austenitic stainless-steel filler. The effects of tempering and preheating heat treatments were also evaluated. The microstructures of the welds were characterized with optical microscopy. Mechanical properties were determined via microhardness, tensile and fatigue tests, and compared to those of the unwelded AISI 422 steel. X-ray diffraction was used to characterize the phases present in the weld. Chromium carbides were observed at the grain boundaries of the welds. The precipitation was caused mainly by the diffusion of carbon into the austenitic stainless steel during the welding. The microhardness decreased from the base metal to the weld. The tensile-strength and percent-elongation values were improved with preheating and tempering heat treatments. The highest fatigue limit was obtained with preheating.

Keywords: welding, heat treatment, stainless steel, fatigue, hardness

Martenzitno nerjavno jeklo AISI 422 je bilo varjeno skladno s standardom ISO 15792-1 z elektrodami iz avstenitnega nerjavnega jekla. Ocenjen je bil vpliv kaljenja in predogrevanja. Mikrostruktura zvarov je bila opredeljena s svetlobno mikroskopijo. Mehanske lastnosti so bile določene z mikrotvdoto, nateznimi in utrujenostnimi preizkusi in primerjane z nevarjenim jeklom AISI 422. Rentgenska difrakcija je bila uporabljena za karakterizacijo faz v zvaru. Po mejah zrn v zvaru je bilo opaziti kromove karbide. Večino izločanja je povzročila difuzija ogljika v avstenitno jeklo med varjenjem. Mikrotvdota se je zmanjševala od osnovnega materiala do zvara. Vrednosti natezne trdnosti in delež raztezka so se povečali s predgrevanjem in s toplotno obdelavo. Najvišja odpornost proti utrujanju je bila dosežena s predgrevanjem.

Ključne besede: varjenje, toplotna obdelava, nerjavno jeklo, utrujenost, trdota

1 INTRODUCTION

For metals, fatigue failures occur more often in welded joints than in unwelded structures. Weld defects and imperfections affect the fatigue and other mechanical properties of structures.^{1,2} In general, fatigue strength decreases significantly with the introduction of any stress raisers in metals. Machine parts contain stress raisers in industrial applications. Fatigue cracks in structural parts almost always initiate at geometrical irregularities.³

Weld defects and imperfections can be accepted as critical stress raisers in welded structures. Fatigue properties of welded joints are more complicated because of the nature of the weld. Slag inclusions, pores, undercuts, incomplete fusion and residual stresses all affect the crack initiation and crack-propagation stages of the fatigue life of a welded joint.⁴⁻⁶ In addition, surface roughness and section changes may also affect the existing or newly developing fatigue cracks. The fatigue behavior of a welded joint is influenced by the thickness of a plate as well as by the other geometrical parameters.⁷ However, there is conflicting evidence with regard to the effect of a welding procedure on the fatigue

strength. For the fillet-welded and butt-welded joints the fatigue strength is strongly dependent on the welding procedure.^{8,9}

In spite of a poor weldability, martensitic stainless steels may be welded in the annealed, stress-relieved and tempered conditions. As an alloying element, Cr has very significant effects on the metallurgical aspect of the martensitic stainless steels. Cr and C are specifically added to steel to ensure the formation of martensite after the hardening. Ni can be added, and it enhances both the yield strength and ductility of these steels. The hardness in this type of material is dependent on the carbon content.¹⁰ The carbon content can also affect the hardness of the heat-affected zone (HAZ). Thus, the influence of hardness of HAZ may be controlled with welding characteristics. In general, the welding of the martensitic stainless steels with a carbon content higher than 0.25 % is not recommended. In the 0.05–0.15 % C range, the hardness increases with the increasing carbon concentration. Austenitic or ferritic-austenitic electrodes are used for martensitic stainless steels. The hardness and ductility of a weld and HAZ vary in a welded structure. To avoid this harmful effect on the welded AISI 420

Table 1: Chemical composition of the AISI 422 steel in mass fractions, w/%**Tabela 1:** Kemijska sestava jekla AISI 422 v masnih deležih, w/%

Element	C	Si	S	P	Mn	Ni	Cr	Mo	V	Fe
Composition	0.220	0.220	0.023	0.02	0.403	1.268	11.15	0.086	0.017	Bal.

steel, preheating and a slow cooling rate after the welding must be considered.^{11,12}

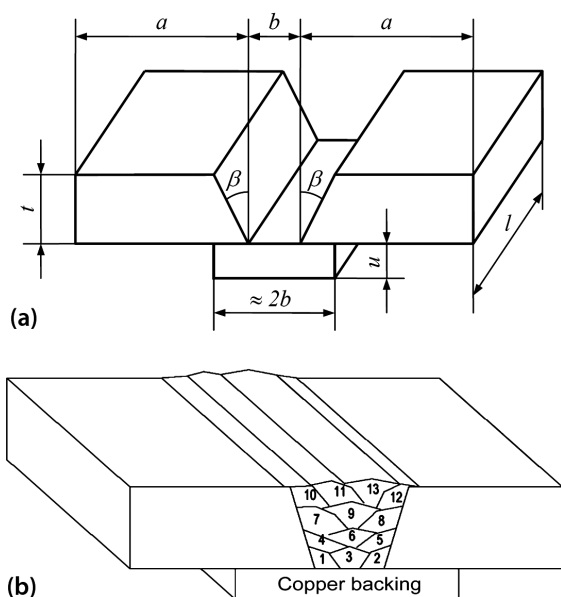
In this study, an attempt has been made to clarify the effects of pre- and post-weld treatments on the welding of the martensitic stainless steel with an austenitic stainless-steel filler. The present study highlights the effects of preheating and tempering on the microstructural, hardness and tensile properties, and on the fatigue behavior of the welded joints.

2 EXPERIMENTAL PROCEDURE

2.1 Materials

AISI 422 steel in its annealed state was used as the base metal for the welding experiments. The chemical composition of the steel is given in **Table 1**. This steel is widely used in the transmission systems of diesel locomotives. Cylindrical as-cast billets of 80 mm diameters and 1 m lengths were hot-forged at 800 °C into the plates of 25 mm thickness.

The forged plates were then machined to the weld specimen dimensions specified in the ISO 15792-1 standard. The geometry of the weld specimens is shown in **Figure 1a**. Type 1.3 specimens were used and their dimensions are given in **Table 2**. An OFHC (Oxygen Free High Conductivity) copper backing strip was used during the welding. The sequence of the welding passes is shown in **Figure 1b**.

**Figure 1:** a) Shape and dimensions of a weld specimen as indicated in the ISO 15792-1 standard; b) sequence of the welding passes**Slika 1:** a) Oblika in dimenzije varjenih vzorcev, kot je prikazano v ISO 15792-1 standardu, b) potek zaporedja prehodov v zvaru**Table 2:** Dimensions (mm) of the type 1.3 weld test specimen depicted in **Figure 1****Tabela 2:** Dimenzije (mm) preizkušanca za varjenje vrste 1.3, prikazane na sliki 1

t	a	b	u		l
20	≥ 150	16	6	10	≥ 150

The specimens were thoroughly cleaned with acetone before the welding. The austenitic stainless-steel electrodes (E310L) of a 3.25 mm diameter were used for the welding tests. The chemical composition of the welding electrodes is shown in **Table 3**. In order to prevent hydrogen-induced cracking, the electrodes were dried in a muffle furnace at 573 K for 2 h before the welding. The welding procedure was then carried out manually in a single V-butt-joint configuration using a UMS 250 DC type electric-arc welding machine with a total of 13 passes. The current was held constant at 170 A. The total of 13 runs were needed to fill the groove between the butt joints.

Table 3: Chemical composition of the E310L filler electrode in mass fractions, w/%**Tabela 3:** Kemijska sestava varilne elektrode E310L v masnih deležih, w/%

C	Mn	Si	Ni	Cr	Fe
0.10	2.0	0.4	20	25	Bal.

The effects of preheating and tempering heat treatments were investigated. The welding parameters and notations used for the as-welded, preheated and tempered specimens are summarized in **Table 4**. From here onwards, the codes AW, PH and TP shall be used to express the as-welded, preheated and tempered specimens, respectively.

Table 4: Welding parameters used for the test specimens**Tabela 4:** Parametri varjenja, uporabljeni pri preizkusnih vzorcih

Specimen	Filler metal	Preheating	PWHT
AW	E310L	N/A	N/A
PH	E310L	623 K, 2 h	N/A
TP	E310L	N/A	1023 K, 3 h

2.2 Metallography

The microstructures of the welded joints were evaluated using optical microscopy. The specimens examined were prepared using standard metallographic techniques. The original microstructure of the original AISI 422 steel (before the welding) is shown in **Figure 2**. This reveals a fine, fully martensitic microstructure.

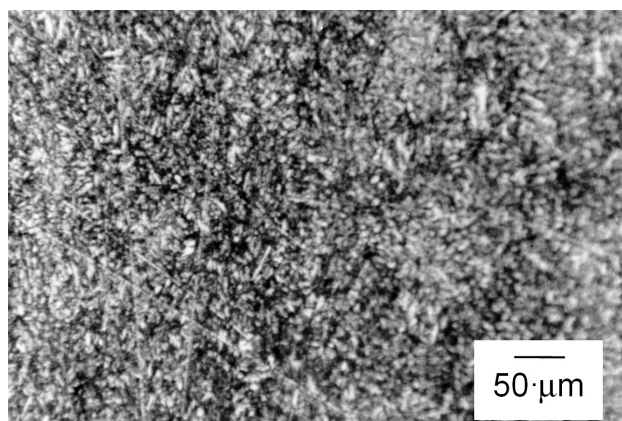


Figure 2: Microstructure of the AISI 422 base metal
Slika 2: Mikrostruktura osnovnega materiala AISI 422

2.3 Mechanical testing

Tensile, fatigue, and microhardness test specimens were extracted from the welded samples. Tensile tests were carried out at room temperature in accord with the ISO 6892-1 standard. Yield strength (YS), ultimate tensile strength (UTS) and fraction of elongation (% EL) values were determined. Fatigue tests were done using a rotating bar bending fatigue testing machine in accord

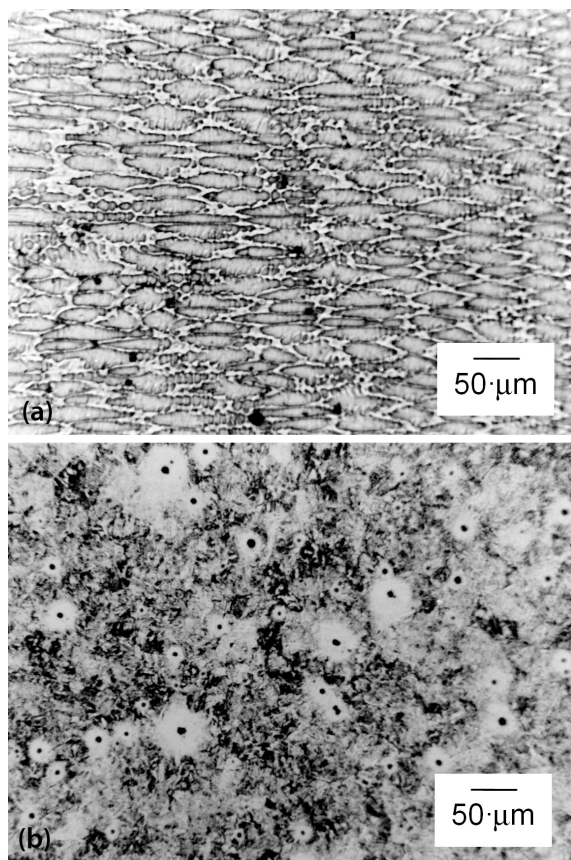


Figure 3: Microstructure of the AW specimen: a) weld metal; b) HAZ
Slika 3: Mikrostruktura AW-vzorcev: a) zvar, b) toplotno vplivana cona (HAZ)

with the ISO 1143-1 standard. Microhardness measurements were made utilizing a Vickers indenter with a load of 100 g and dwell time of 15 s. For each of the mechanical tests, a minimum of three measurements/tests were made for each experimental condition.

3 RESULTS AND DISCUSSION

After the welding, the specimens generally consisted of three distinctive regions: (i) the weld metal; (ii) the heat-affected zone (HAZ) and (iii) the base metal that was not affected by the welding process. The microstructures of the AW specimen are shown in **Figure 3**. The weld metal shows a microstructure consisting mainly of austenite (**Figure 3a**), with delta ferrite present at the grain boundaries.

The HAZ of the AW specimen revealed both martensite and austenite phases. The coexistence of the two phases in the AW specimen is shown in **Figure 3b**. The microstructure also shows the presence of precipitates (possibly inclusions) located at the centers of the austenite phases. The XRD pattern of the weld in **Figure 4** indicates the presence of chromium carbides (Cr_{23}C_6 , Cr_7C_3). High temperatures, combined with the diffusion of C from the martensitic stainless steel to the austenitic stainless steel may have caused the formation of these carbides during the welding.

The microstructures of the PH specimen are shown in **Figure 5**. The microstructure of the weld metal reveals an austenitic structure with possible delta ferrite segregated at the grain boundaries (**Figure 5a**). The heat affected zone (HAZ) between the weld and the base metal reveals the presence of martensite and austenite phases (**Figure 5b**).

The microstructures of the TP specimen are shown in **Figure 6**. The microstructure of the weld metal is austenitic, similar to the weld metal observed in the AW and PH specimens. However, the dendritic morphology of the austenitic structure is much more visible (**Figure 6a**).

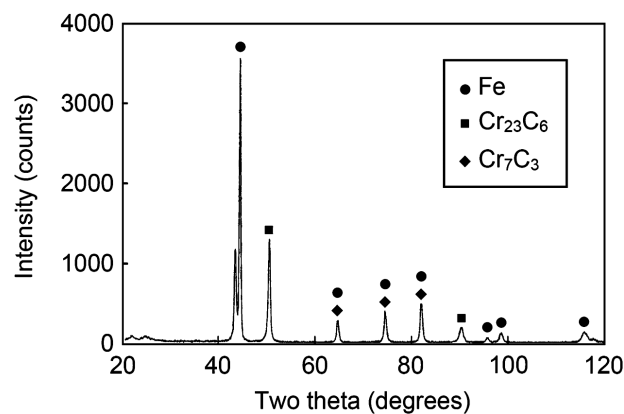


Figure 4: XRD pattern of the AW specimen indicating the presence of chromium carbides

Slika 4: Rentgenski (XRD) posnetek, ki kaže prisotnost kroma v vzorcu AW

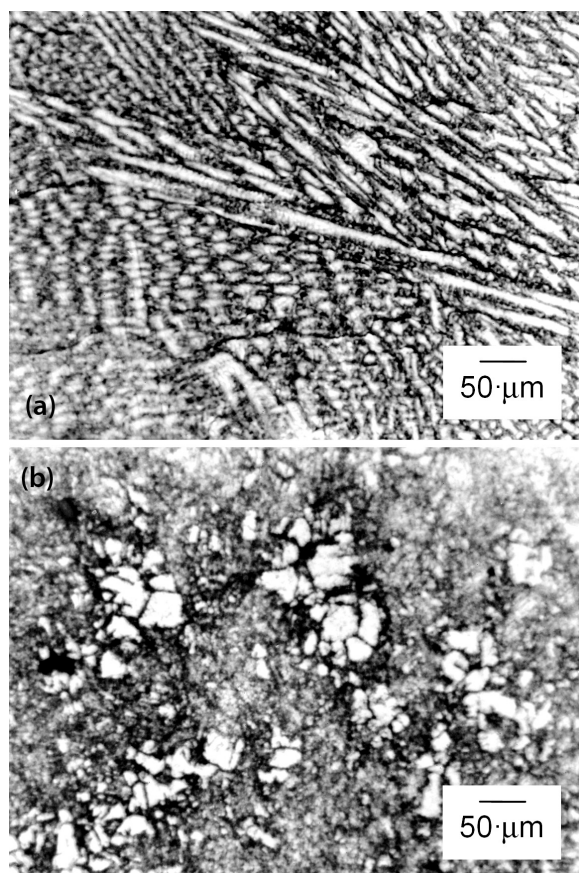


Figure 5: Microstructure of the PH specimen: a) weld metal; b) HAZ
Slika 5: Mikrostruktura PH-vzorca: a) zvar, b) toplotno vplivana cona (HAZ)

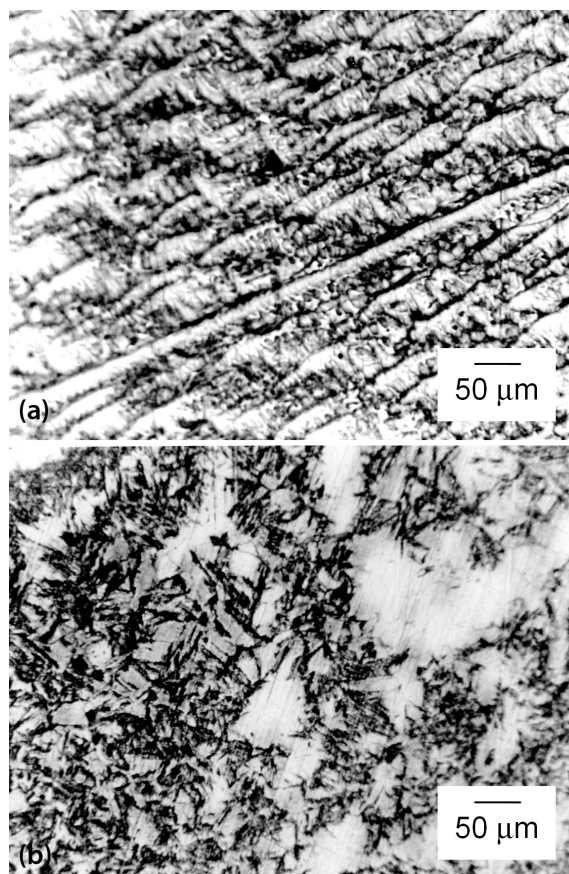


Figure 6: Microstructure of the TP specimen: a) weld metal; b) HAZ
Slika 6: Mikrostruktura TP-vzorca: a) zvar, b) toplotno vplivana cona (HAZ)

The heat affected zone (HAZ) between the weld and the base metal again reveals a microstructure consisting of martensite and austenite phases (**Figure 6b**). Compared to the AW and PH specimens, the martensite phase in the TP specimen has a coarser appearance due to the effects of tempering.

The hardness test results are summarized in **Figure 7**. Microhardness measurements were made both across and along the weld centerline. **Figure 7a** indicates a decrease in the microhardness towards the weld metal for all the welded joints. This is expected, since the base metal consists of martensite and the weld metal consists of either austenite or a mixture of austenite and some delta ferrite. **Figure 7b** shows the microhardness distribution for the weld from top to bottom. While the microhardness distribution for the AW specimen is more or less constant, a steady decrease is observed for the PH and TP specimens. As welding was carried out in 13 passes, each pass resulted in a tempering treatment on the previous pass, which led to the softening of the underlying layers.

The tensile-test results for the welded specimens are listed in **Table 5**. Failures occurred within the weld metal. The YS showed no change with preheating and remained constant at 490 MPa. The tempering treatment

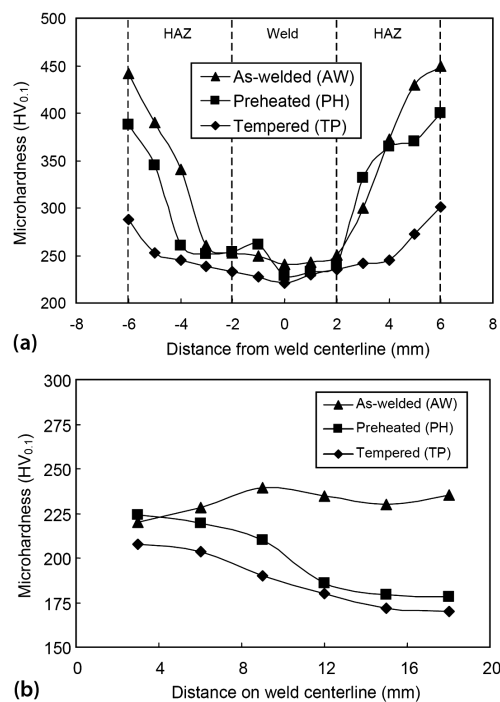


Figure 7: Microhardness distribution for the welded joints: a) across the weld centerline and b) on the weld centerline from top to bottom
Slika 7: Razporeditev mikrotrdot v varjenih spojnih: a) preko sredine zvara in b) na sredini zvara od vrha do dna

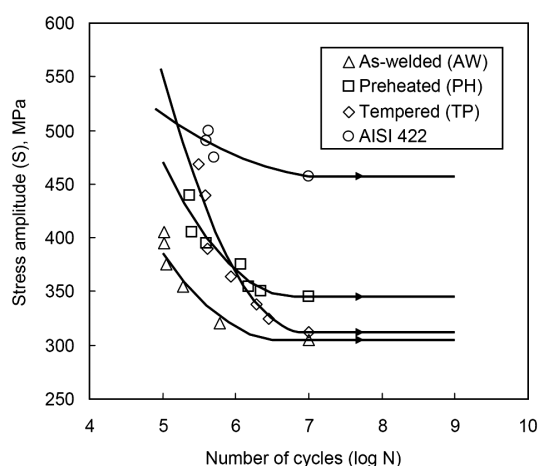


Figure 8: Wöhler (S – N) diagram showing fatigue test results

Slika 8: Wöhlerjeva krivulja (S – N) prikazuje rezultate preizkusov utrujenosti

resulted in a decrease in the YS to 467 MPa. The UTS increased from 630 MPa to 660 MPa with preheating. The tempering further increased the UTS to 683 MPa. The elongation values increased with preheating and tempering treatments. With preheating, the fraction of EL values increased from 12.5 % to 18.8 %. With tempering, the fraction of EL values increased to 25 %.

Table 5: Tensile-test results for the welded AISI 422 alloy for three different heat treatments

Tabela 5: Rezultati nateznih preizkusov varjene AISI 422 zlitine pri treh različnih toplotnih obdelavah

Specimen	Yield strength YS	Ultimate tensile strength UTS	Percent elongation %
AW	490	630	12.5
PH	490	660	18.8
TP	467	683	25.0

The fatigue-test results are given in Figure 8. Despite its lower tensile strength (Figure 5), the unwelded specimen shows a superior fatigue strength compared to its welded counterparts. The fatigue limit of the unwelded specimen lies at 458 MPa, where the PH, TP and AW specimens display the fatigue limits at (345, 312 and 305) MPa, respectively. These results indicate that the fatigue strength is more dependent on the hardness of a weld. The unwelded specimen is completely martensitic and therefore displays the highest fatigue limit. The AW specimen has the highest hardness among the welded specimens, but it displays the lowest fatigue limit which is probably due to residual stresses. The TP specimen has the lowest hardness distribution among the welded specimens displaying a fatigue limit which is only slightly higher than that of the AW specimen. The PH specimen, on the other hand, displays the highest fatigue limit among the welded specimens, which is due to its moderate hardness and also due to the stress relief provided by the preheating.

4 CONCLUSIONS

The effect of preheating and post-weld tempering on the microstructure and mechanical properties of welded martensitic stainless steels was studied. The conclusions drawn from this study are as follows:

1) The grain boundary precipitation of chromium carbides was observed in the welded joints. The precipitation was mainly caused by the diffusion of carbon into the austenitic stainless steel during the welding.

2) A decrease in the microhardness was observed moving from the base metal to the weld. The decrease in and absence of the martensite phase in the HAZ and the weld, respectively, were the main causes for a decreased hardness.

3) An increase in the tensile strength and percent elongation was observed after the preheating and tempering heat treatments.

4) Preheating provided the best fatigue results for the welded specimens. The fatigue limits observed for the tempered specimens were slightly lower than those found in the preheated specimens.

5 REFERENCES

- Welding Handbook, 9th ed., Vol. 1, Welding Science and Technology, American Welding Society, Miami 2007
- S. J. Maddox, Recent advances in the fatigue assessment of weld imperfections, *Weld. J.*, 7 (1992), 42–50
- G. S. Booth, J. G. Wylde, Procedural considerations relating to the fatigue testing of steel weldments, in *Fatigue and Fracture Testing of Weldments*, ASTM STP 1058, Eds., H. I. McHenry, J. M. Potter, American Society for Testing and Materials, Philadelphia 1990, 3–15
- T. N. Nguyen, M. A. Wahab, The effect of weld geometry and residual stresses on the fatigue of welded joints under combined loading, *J. Mater. Proc. Technol.*, 77 (1998), 201–208
- G. Linnert, Common welding problems: Fatigue, *Weld. J.*, 75 (1996), 59–60
- A. Ohta, Y. Maeda, N. Suzuki, Fatigue strength of butt-welded joints under constant maximum stress and random minimum stress conditions, *Fatigue Fract. Eng. M.*, 19 (1996) 19, 265–275
- J. A. Ferreira, C. M. Branco, Fatigue analysis and prediction in fillet welded joints in the low thickness range, *Fatigue Fract. Eng. M.*, 13 (1990), 201–212
- G. Magudeeswaran, V. Balasubramanian, G. Madhusudhan Reddy, T. S. Balasubramanian, Effect of welding processes and consumables on tensile and impact properties of high strength quenched and tempered steel joints, *J. Iron Steel Res. Int.*, 15 (2008), 87–94
- L. R. Link, Fatigue crack growth of weldments, in *Fatigue and Fracture Testing of Weldments*, ASTM STP 1058, Eds., H. I. McHenry, J. M. Potter, American Society for Testing and Materials, Philadelphia 1990, 16–33
- M. Ghosh, K. Kumar, R. S. Mishra, Friction stir lap welded advanced high strength steels: Microstructure and mechanical properties, *Mater. Sci. Eng., A* 528 (2011), 8111–8119
- ASM Handbook, Vol. 6, Welding, Brazing and Soldering, 2nd ed., Metals Park, ASM International, Ohio 1993
- A. J. Williams, P. J. Rieppel, C. B. Voldrich, Literature survey on weld-metal cracking, WADC Technical Report, 52–143, Ohio 1952

NEW COMBINED BIO-SCOURING AND BIO-BLEACHING PROCESS OF COTTON FABRICS

NOV, ZDRUŽENI POSTOPEK BIOIZKUHAVANJA IN BIOBELJENJA BOMBAŽNIH TKANIN

Nina Špička, Petra Forte Tavčer

University of Ljubljana, Faculty of Natural Sciences and Engineering, Department of Textiles, Snežniška 5, 1101 Ljubljana, Slovenia
nina.spicka@ntf.uni-lj.si

Prejem rokopisa – received: 2012-08-27; sprejem za objavo – accepted for publication: 2013-01-03

A new commercial bio-bleaching process for cellulose fibres was investigated in this study. The process runs enzymatically with arylesterase enzymes (EC 3.1.1.2) and hydrogen peroxide. The enzyme system catalyses the perhydrolysis of propylene glycol diacetate. During the reaction propylene glycol and peracetic acid as a bleaching agent are formed in situ. The main advantage of the bleaching with peracetic acid is that a satisfactory degree of whiteness of a cotton fabric can be obtained at 65 °C at a neutral pH. The bleaching performance of the new bio-bleaching process on a traditionally alkaline-scoured and bio-scoured 100 % cotton fabric and the feasibility of a one-bath bio-scouring/bio-bleaching pre-treatment were investigated. The whiteness degrees, tenacities at maximum loads and water absorbencies of the treated cotton fabrics were compared. The hydrogen peroxide and peracetic acid concentrations, pH and TOC values of the remaining treatment solutions were measured. The research showed that the new bio-bleaching system has a powerful bleaching ability under mild process conditions and that bio-scouring and bio-bleaching can be efficiently combined in a one-bath process.

Keywords: cotton, bio-scouring, bio-bleaching, peracetic acid

V študiji je bil raziskan nov komercialni postopek biobeljenja celuloznih vlaken. Proces poteka encimsko z encimi arilesterazami (EC 3.1.1.2) in vodikovim peroksidom. Med reakcijo se v kopeli tvori propilen glikol in perocetna kislina kot belilno sredstvo. Poglavitna prednost beljenja s perocetno kislino je zadostna stopnja beline bombažne tkanine, dosežena pri 65 °C v nevtralnem pH. Raziskana je bila belilna sposobnost novega biobelilnega postopka na tradicionalno alkalno izkuhani in bioizkuhani 100 % bombažni tkanini in možnost enokopelnega procesa bioizkuhavanja in biobeljenja. Pri obdelanih bombažnih tkaninah je bila izmerjena stopnja beline, natezna trdnost ob maksimalni obremenitvi in vodovpojnost. Pri odpadnih obdelovalnih kopelih je bila izmerjena koncentracija vodikovega peroksida in perocetne kisline, pH in TOC-vrednost. Raziskava je pokazala, da ima nov biobelilni postopek močno belilno sposobnost v blagih procesnih razmerah in da sta lahko postopka bioizkuhavanja in biobeljenja uspešno združena v enokopelni proces.

Ključne besede: bombaž, bioizkuhavanje, biobeljenje, perocetna kislina

1 INTRODUCTION

The most important natural cellulose fibre is cotton, whose use is constantly increasing. Natural cotton is highly hydrophobic and slightly coloured. To prepare the fibres for further treatment and use, pretreatment processes are needed. With scouring, non-cellulose substances (wax, pectin, proteins, hemicelluloses, etc.) that surround the fibre cellulose core are removed and, as a result, fibres become hydrophilic. With bleaching the natural pigments of cotton fibres are removed and fibres become white. Traditionally, scouring and bleaching processes are conducted at the temperatures up to 120 °C in a very alkaline medium at a pH of 10 to 12. In these treatments large amounts of auxiliary agents are added. Due to the high working temperatures, a lot of energy is consumed. Large amounts of water are used to rinse and neutralise the alkaline-scoured and bleached fabrics. Consequently, the textile industry is considered to be one of the biggest water, energy, and chemical consumers. To comply with the increasingly more rigorous environmental regulations and to save water and energy, biotechnology and several types of enzymes have entered the textile sector. Bio-scouring with enzyme pectinases is an

alternative to sodium hydroxide scouring in the removal of non-cellulose substances from the cotton-fibre surface. The process occurs at moderate temperatures in a slightly acidic or alkaline medium which is dependent on the type of pectinases.^{1,2}

Some of the alternatives to bleaching with hydrogen peroxide (HP) have been explored in the textile, and pulp and paper industries, i.e., the enzymatic bleaching using peroxidases,³ laccase/mediator system and glucose oxidases⁴⁻⁶ and bleaching with the peracids either produced industrially⁷ or generated *in situ* from different bleach activators.⁸

A new commercial bio-bleaching product, Gentle Power Bleach from Huntsman, is available on the market. It functions enzymatically with arylesterase enzymes (EC 3.1.1.2) and HP. The enzyme system catalyses the perhydrolysis of propylene glycol diacetate. During the reaction propylene glycol and peracetic acid (PAA) as the bleaching agents are formed in situ. If bio-scouring and bio-bleaching could be combined into one process, large amounts of water, energy, time and auxiliary agents would be saved.

The objective of our work was to investigate the bleaching performance of the new bio-bleaching process

on a traditionally alkaline-scoured and bio-scoured 100 % cotton fabric. Secondly, the feasibility of a one-bath process combining bio-scouring and bio-bleaching pre-treatments was investigated. The whiteness degree, tenacity at maximum load and water absorbency of the treated cotton fabrics were evaluated. After the treatments, the pH and TOC (total organic carbon) values of the remaining baths were measured. The quantities of HP and PAA in the remaining bleaching baths were also measured.

2 EXPERIMENTAL WORK

2.1 Materials

Desized cotton fabric, 100 g/m², was obtained from Tekstina, Slovenia. Beisol PRO (a commercial pectinase solution), Felosan RG-N (a non-ionic wetting agent), Cotoblanc HTD-N (an anionic wetting and dispersing agent) and Lawotan RWS (a non-ionic wetting agent) were supplied from CHT, Germany. The Gentle Power Bleach chemicals (CLARITE[®] LTC, INVATEX[®] LTA, INVAZYME[®] LTE) were supplied from Huntsman, Switzerland. H₂O₂ 35 % (HP) was obtained from Belinka, Slovenia and Stabilizer SIFA from Clariant. NaOH and Na₂CO₃ were purchased from Sigma Aldrich.

2.2 Treatment methods

The desized cotton fabric was treated according to the procedures presented in **Table 1**. Two parallel sets of experiments were undertaken. The treatments were performed in a laboratory dyeing machine DL-6000 Plus from Starlet in the 500 ml bakers at a liquor ratio of 1 : 20. After each treatment the samples were washed in hot water, rinsed twice in cold water and air dried.

Table 1: Abbreviations of the treatments and treated samples with treatment descriptions

Tabela 1: Okrajšava obdelave in obdelanega vzorca z opisom obdelave

Treatment/sample abbreviation	Treatment description
AS	alkaline scouring
TB (AS)	two-bath alkaline scouring and traditional bleaching with HP
BB (AS)	two-bath alkaline scouring and bio-bleaching
BS	bio-scouring
BB (BS)	two-bath bio-scouring and bio-bleaching
BS/BB	one-bath bio-scouring and bio-bleaching
BS/BB+	one-bath bio-scouring and bio-bleaching with an additional final temperature rise

Alkaline scouring (AS) was carried out in a bath containing 2 g/l of Cotoblanc HTD-N and 3 g/l of NaOH at 95 °C for 40 min. Traditional bleaching (TB) was carried out in a bath containing 10 ml/l of H₂O₂ (35 %), 0.1 g/l of Lawotan RWS, 0.5 g/l of Stabilizer SIFA and 4 g/l of NaOH at 90 °C for 60 min. The ingredients and

data conditions for bio-treatments are presented in **Tables 2** and **3**.

Table 2: Ingredients of bio-treatments

Tabela 2: Sestavine bioobdelav

Ingredient	Bio-treatment				
	BB (AS)	BS	BB (BS)	BS/BB	BS/BB+
1 g/l Felosan RG-N	–	+	+	–	–
2 g/l Beisol PRO	–	+	+	+	+
1.5 g/l CLARITE [®] LTC	+	–	+	+	+
3 g/l INVATEX [®] LTA	+	–	+	+	+
6 ml/l H ₂ O ₂ 35 %	+	–	+	+	+
1 g/l INVAZYME [®] LTE	+	–	+	+	+
2 g/l Na ₂ CO ₃	+	–	+	+	+

+ the ingredient is included in the treatment bath

– the ingredient is not included in the treatment bath

Table 3: Data conditions for bio-treatments

Tabela 3: Podatki pogojev bioobdelave

	Bio-treatment conditions				
	BB (AS)	BS	BB (BS)	BS/BB	BS/BB+
Bio-scouring	–	55 °C, 15 min 85 °C, 15 min	55 °C, 15 min 85 °C, 15 min	–	–
Bio-bleaching	65 °C, 60 min	–	65 °C, 60 min	65 °C, 60 min	65 °C, 60 min
Final treatment	–	–	–	–	85 °C, 15 min

– the treatment step was not included

2.3 Analytical methods

Prior to the measurements, samples were conditioned for 24 h at 20 °C and 65 % relative humidity. The pH was measured using a pH meter MA5740 (Iskra, Slovenia). The rates of PAA and HP were measured with iodometric titrations.⁵ The degree of whiteness was measured with a spectrophotometer Spectraflash SF600 Plus (Datacolor, Switzerland) using the CIE method, according to EN ISO 105-J02:1997(E). The water absorbency was measured according to DIN 53 924 (the velocity of the soaking water for textile fabrics, the method for determining the wicking height). The measurements of the tenacity at maximum load were performed on a Tensile Tester Model 5567 (Instron, USA). The total organic carbon (TOC) was measured with a TOC-5000A (Shimadzu, Japan) according to ISO 8245.

3 RESULTS AND DISCUSSION

3.1 Concentration of oxidants during the bio-bleaching process

The measurements confirmed that during the bio-bleaching process HP is converted into PAA (**Figure 1**). Almost 0.02 mol/l of PAA was produced and con-

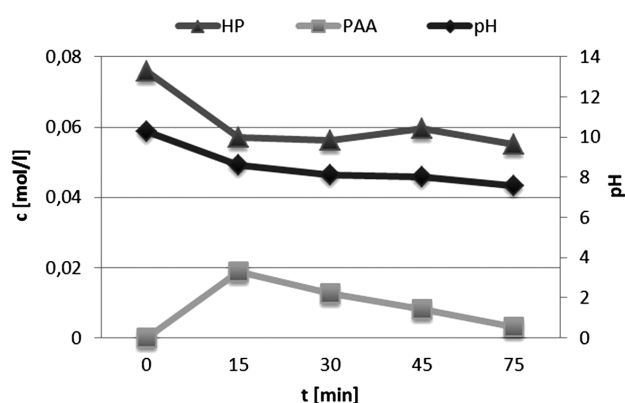


Figure 1: Changes in the concentrations of hydrogen peroxide (HP) and peracetic acid (PAA) and change in the pH during bio-bleaching of an alkaline-scoured sample (during the first 15 min the bath was heated to 65 °C)

Slika 1: Sprememba koncentracije vodikovega peroksida (HP) in perocetne kisline (PAA) ter sprememba pH med biobeljenjem alkalno izkuhanega vzorca (začetnih 15 min je bila kopel ogrevana na 65 °C)

sumed during the bleaching process. During the bleaching with PAA, acetic acid is formed and the pH decreases. For this reason the starting pH was set to be highly alkaline (pH 10.3). During the process the pH decreased to 7.6.

3.2 Fabric analysis

3.2.1 Whiteness

The achieved degrees of whiteness (W) are presented in **Table 4**. The alkaline-scoured sample (AS) had a whiteness of 20.7 and the bio-scoured sample (BS) had a whiteness of 10. After the alkaline scouring, the fibres swelled, became smoother and clean of non-cellulose impurities and the degree of whiteness increased. Alkaline scouring is more intensive and removes some of the coloured substances from the fibre that the bio-scouring does not. The whiteness degrees of both samples increased significantly after the bleaching process. The highest whiteness (84.5) was obtained on the HP-bleached and alkaline-scoured sample (TB (AS)). Not much less (81.7) was obtained on the alkaline-scoured and bio-bleached sample (BB (AS)), while the whiteness degrees of bio-scoured and bio-bleached samples were lower: 73.5 on the separately bio-scoured and bio-bleached sample (BB (BS)), 67.8 on the one-bath bio-scoured and bio-bleached sample (BS/BB) and 72.8 on the one-bath bio-scoured and bio-bleached sample with the final temperature rise. As it can be seen in **Figure 1**, a high quantity of HP remains in the bio-bleaching bath. At a pH below 10 °C and at 65 °C HP is very stable and does not contribute to the bleaching of the fibres. The rising of the temperature at the end of the bio-bleaching process activated the remaining HP, which further increased the degree of whiteness.

3.2.2 Tenacity at maximum load

There were no significant differences in the tenacity values among all the treated samples in the weft directions whereas the tenacity values in the warp directions were very different. The highest value was measured on the alkaline-scoured sample (AS) and on most of the bio-bleached samples. The high tenacity of the AS sample is a result of the contraction of the fabric exposed to a high process temperature. After the HP bleaching of the alkaline-scoured sample (TB (AS)) the tenacity at maximum load decreased significantly. On the other hand, the tenacity after the bio-bleaching of the alkaline-scoured sample remained similar (BB (AS)). These results confirm that during a bio-bleaching process the fabric does not get damaged.

3.2.3 Water absorbency

The remaining substances influence the water absorbency. All the treated samples revealed very good absorption properties. The highest rising height was measured on the traditionally alkaline-scoured and HP-bleached sample (TB (AS)). The rising height of the bio-scoured samples was a bit lower but the differences among all the treated samples were not significant. All the samples could be considered to be absorbent.

Table 4: Whiteness degree (W), tenacity at maximum load (σ_s) and wicking height after 300 s of various sample treatments

Tabela 4: Stopnja beline (W), trdnost ob maksimalni obremenitvi (σ_s) in višina kapilarnega dviga v času 300 s različno obdelanih vzorcev

Sample	W	σ_s (cN/10 ⁻⁶ kg m ⁻¹)		Wicking height (cm)	
		warp	weft	warp	weft
AS	20.68	26.41	16.09	–	–
TB (AS)	84.51	18.36	13.01	6.27	5.67
BB (AS)	81.68	25.50	13.57	–	–
BS	10.11	22.08	13.20	5.62	4.75
BB (BS)	73.47	19.86	12.87	5.12	4.62
BS/BB	67.84	25.99	14.01	5.00	4.15
BS/BB+	72.77	25.52	15.93	5.10	4.27

3.3 Ecological parameters of the remaining treatment baths

The ecological parameters – the remaining concentrations of HP and PAA, the final pH and TOC values – are presented in **Table 5**. High quantities of the unconsumed HP remained in all the bleaching baths, especially in the traditional one. In all the bio-bleaching baths PAA was detected, but the concentrations were low, meaning the PAA was consumed for the bleaching of the cotton fabric.

Traditional alkaline scouring and bleaching are conducted in an alkaline environment. These baths should be neutralised prior to drainage into the sewage system. During the neutralisation, salts that additionally load wastewaters are produced. The final pH value of the bio-scouring bath was 6 and it was around 7.5 for the

bio-bleaching baths. Since none of these treatment processes requires a neutralisation of the fabric, the treatment process can be shorter and less expensive.

Bio-scouring, traditional bleaching and alkaline scouring baths had low TOC values and all the bio-bleaching baths had significantly higher values. A bio-bleaching bath includes more additives than other processes; especially enzymes contribute a lot of organic carbon. On the other hand, enzymatic processes require much less water, energy and time, which compensate for high TOC values from the ecological point of view. Nevertheless, all the treatments exceeded the limit TOC values (60 mg C/l) for direct drainage into the sewage system.

Table 5: Ecological parameters of the remaining treatment baths (concentrations of hydrogen peroxide – HP and peracetic acid – PAA, final pH and TOC values)

Tabela 5: Ekološki parametri odpadnih obdelovalnih kopeli (koncentracija vodikovega peroksida – HP in perocetne kisline – PAA, končni pH in vrednosti TOC)

Treatment	<i>c</i> (HP)/ (mol/l)	<i>c</i> (PAA)/ (mol/l)	pH	TOC (mg/l)
AS	–	–	11.0	1096
TB (AS)	0.1084	–	11.7	558
BB (AS)	0.0542	0.0032	7.6	2372
BS	–	–	5.7	510
BB (BS)	0.0531	0.0034	7.4	2510
BS/BB	0.0588	0.0042	7.6	2673
BS/BB+	0.0608	0.0012	7.4	2842

4 CONCLUSIONS

The research showed that the new bio-bleaching system with enzymatically gained peracetic acid has a powerful bleaching ability under mild process conditions, i.e., a neutral pH and a temperature of 65 °C. With the new bio-bleaching process the fabrics with a high whiteness degree, good water absorbency and high tenacity at maximum load were obtained having properties comparable to the results of the traditional process.

During the bio-bleaching process the cotton fabric did not get damaged as during the traditional pre-treatment. A slightly higher degree of whiteness was obtained on the alkaline-scoured cotton fabric compared to the bio-scoured one. Bio-scouring and bio-bleaching can be efficiently combined in a one-bath process. The final temperature rise of the one-bath process contributes to a higher whiteness degree. This kind of a one-bath process is shorter, consuming less energy and hence being less expensive.

Acknowledgements

This work was supported by the Slovenian Research Agency (P2-0213). N. Š. thanks the Ministry of Higher Education, Science and Technology for a Ph.D. grant (1000-10-310153).

5 REFERENCES

- ¹ P. Preša, P. Forte Tavčer, Low water and energy saving process for cotton pretreatment, *Textile Research Journal*, 79 (2009), 76–88
- ² P. Preša, P. Forte Tavčer, Bioscouring and bleaching of cotton with pectinase enzyme and peracetic acid in one bath, *Color Technol.*, 124 (2008), 36–42
- ³ K. Opwis, D. Knittel, E. Schollmeyer, P. Hoferichter, A. Cordes, Simultaneous Application of Glucose Oxidases and Peroxidases in Bleaching Process, *Eng. Life. Sci.*, 8 (2008), 175–178
- ⁴ T. Tzanov, S. Costa, G. Gübitz, A. Cavaco-Paulo, Hydrogen peroxide generation with immobilized glucose oxidase for textile bleaching, *Journal of Biotechnology*, 93 (2002), 87–94
- ⁵ G. Buschle-Diller, X. D. Yang, Enzymatic Bleaching of Cotton Fabric with Glucose Oxidase, *Textile Research Journal*, 71 (2001), 388–394
- ⁶ P. Forte Tavčer, Low-temperature bleaching of cotton induced by glucose oxidase enzymes and hydrogen peroxide activators, *Biocatal. biotransform.*, 30 (2012), 20–26
- ⁷ P. Križman, F. Kovač, P. Forte Tavčer, Bleaching of cotton fabric with peracetic acid in the presence of different activators, *Coloration Technology*, 121 (2005), 304–309
- ⁸ S. H. Lim, N. C. Gürsoy, P. Hauser, D. Hinks, Performance of a new cationic bleach activator on a hydrogen peroxide bleaching system, *Coloration Technology*, 120 (2004), 114–118

EFFECT OF MECHANICAL ACTIVATION ON MULLITE FORMATION IN AN ALUMINA-QUARTZ CERAMICS SYSTEM

VPLIV MEHANSKE AKTIVACIJE NA NASTANEK MULLITA V KERAMIČNEM SISTEMU GLINICA-KREMEN

Eda Elmas¹, Kenan Yildiz², Nil Toplan², H. Özkan Toplan²

¹Kaleseramik, Çanakkale Kalebodur Ceramic Ind. Inc., 17430 Çan, Çanakkale, Turkey
²Sakarya University, Metallurgy and Materials Engineering Dept., 54187 Sakarya, Turkey
toplano@sakarya.edu.tr

Prejem rokopisa – received: 2012-08-31; sprejem za objavo – accepted for publication: 2013-01-04

Powder mixtures of alumina and quartz were being mechanically activated in a planetary mill for 2 h. Both non-activated and activated samples were sintered at different temperatures (1250, 1300, 1325, 1350 and 1375) °C for (1, 2, 3 and 5) h and the formation of a mullite phase was examined with an X-ray diffraction analysis. It was determined that the mechanical activation increased the quantity of the mullite phase.

Keywords: mullite, mechanical activation, amorphization, X-ray diffraction, alumina, quartz

Mešanice prahov glinice in kremena so bile 2 h mehansko aktivirane v planetarnem mlinu. Neaktivirani in aktivirani vzorci so bili sintrani (1, 2, 3 in 5) h pri različnih temperaturah (1250, 1300, 1325, 1350 in 1375) °C), z rentgensko difrakcijsko analizo pa je bil preiskovan nastanek mullitne faze. Ugotovljeno je bilo, da mehanska aktivacija poveča količino mullitne faze.

Gljučne besede: mullit, mehanska aktivacija, amorfizacija, rentgenska difrakcija, glinica, kremen

1 INTRODUCTION

Mullite ($3\text{Al}_2\text{O}_3 \cdot 2\text{SiO}_2$) is an important ceramic phase in conventional ceramics (such as tableware, construction ceramics and refractories), advanced high-temperature structural materials, heat exchangers, catalysator convertors, filters, optical devices and electronic packaging materials. However, mullite suffers from its relatively low fracture toughness which limits its application in industrial use. The conventional route for the preparation of mullite is the solid-state reaction between alumina and silica, which is controlled with diffusion. The mullite formation with this method takes place at a relatively high temperature (>1500 °C). The mullitization temperature and the morphology of mullite particles depend on the particle size of the initial raw materials and the preparation of the precursors before sintering. Mullite has been synthesized in many ways like simple sintering of alumina and silica powders, sol-gel method, co-precipitation, hydrothermal and chemical-vapor-deposition processes. The mullitization temperature is as high as 1600 °C for the conventional fabrication method, i.e., the solid-state reaction of high-purity alumina and quartz.¹⁻³

Mechanical activation of starting materials is a promising method for a precursor preparation. The particle-size reduction, which increases the contact surfaces between the particles, is a direct consequence of milling. Also, the energy of the system increases resulting in a decrease in the reaction temperature.⁴ Different pro-

cesses can remarkably influence the reactivity of the solids. Particularly, the mechanical treatments are important as long as they can help to produce the changes in the texture and structure of the solids. In many cases, these alterations in the structure cause certain modifications in the phases formed with a thermal treatment of the solids that were mechanochemically treated.^{5,6}

In this work, the effects of mechanical activation on structural disordering (amorphization) in an alumina and quartz ceramics system and a formation of mullite were analyzed using X-ray diffraction (XRD) and scanning electron microscopy (SEM).

2 EXPERIMENTAL METHODS

Alumina and quartz were supplied from the Çelvit Ceramic Company, Turkey. The chemical composition of alumina is 99.425 % Al_2O_3 , 0.52 % SiO_2 and 0.055 % Na_2O . The composition of quartz is 99.1 % SiO_2 , 0.28 % Al_2O_3 , 0.16 % $\text{CaO} + \text{MgO}$, 0.17 % $\text{K}_2\text{O} + \text{Na}_2\text{O}$, 0.05 % Fe_2O_3 , 0.05 % TiO_2 and 0.19 % LOI. Alumina and quartz were mixed to obtain the appropriate stoichiometric ratio according to the chemical formula of mullite ($3\text{Al}_2\text{O}_3 \cdot 2\text{SiO}_2$) in ashless rubber-lined ceramic jars for 2 h using zirconia balls and distilled water as the milling media. After drying, the mixture was made in a high-energy planetary ball mill (Fristch) with a rotation speed of 600 r/min. The ball-to-powder weight ratio was adjusted to 20. The precursor milling was carried out for 2 h. An

X-ray diffraction analysis was performed using a Rigaku Ultima X-ray diffractometer and CuK α radiation. A Joel 6060 LV scanning electron microscope was used for the morphological analysis of non-activated and activated mixed powders. The degree of amorphization ($A/\%$) of the mechanically activated powder was calculated from equation (1):^{7,8}

$$\%A = \left[1 - \frac{B_0 I_x}{B_x I_0} \right] \times 100 \quad (1)$$

where I_0 is the integral intensity of the diffraction peak for the non-activated mixture, B_0 is the background of the diffraction peak for the non-activated mixture and I_x and B_x are the equivalent values for the mechanically activated mixture. After the activation, both non-activated and activated powders were sintered in an electrical furnace with a heating rate of 10 °C/min at (1250, 1300, 1325, 1350 and 1375) °C for (1, 2, 3 and 5) h and the formulation of the mullite phase was examined with XRD. In addition, the degree of mullite crystallization ($C/\%$) of non-activated and activated powders at different firing temperatures and times was calculated from equation (2):

$$\%C = \left[\frac{B_0 I_x}{B_x I_0} \right] \times 100 \quad (2)$$

where I_0 is the integral intensity of the diffraction peak for the reference mullite powders, B_0 is the background of the diffraction peak for the non-activated mixture and I_x and B_x are the equivalent values for the mullite crystallization (the reference mullite is Nabaltec mullite and the JCPDS card number is 01-079-1454). The integrated intensity of the (121) XRD reflection (2θ from 40.5° to 41.5°) was measured to determine to content of the mullite phase.

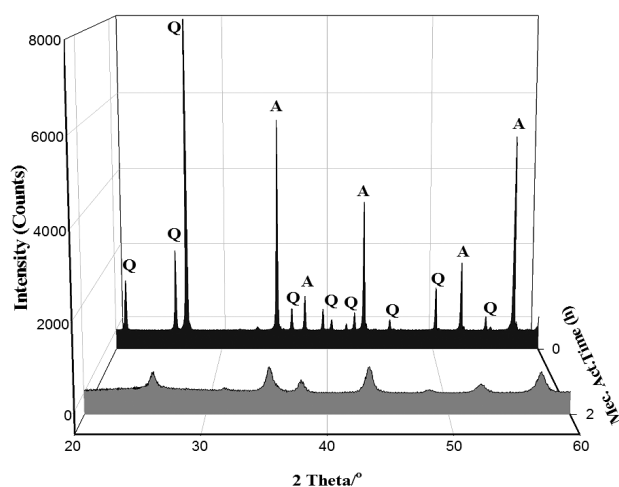


Figure 1: XRD patterns of non-activated and activated alumina-quartz powders (A: alumina, Q: quartz)

Slika 1: XRD-posnetek neaktiviranega in aktiviranega prahu glinica-kremen (A: glinica, Q: kremen)

3 RESULTS

3.1 Structural changes in the activated alumina-quartz mixture powders

The X-ray diffraction analysis of non-activated and activated mixture powders is given in **Figure 1**. A comparison of the peaks from the two diffraction patterns shows that all the diffraction peaks get shorter after a mechanical activation. This reflects the partial amorphization and structural disordering in alumina and quartz. Mechanical activation has already been reported to amorphize materials.⁸

The scanning electron micrographs (SEM) of non-activated and activated alumina and quartz mixture powders can be observed in **Figure 2a, b**. The particle size in the non-activated mixture is over 5 μm (**Figure 2a**). After the mechanical activation, the mixture of the powders is agglomerated. The degrees of amorphization of alumina and quartz were founded to be approximately 70 % and 85 %, respectively.

3.2 Mullite formation

Figure 3a, b shows the XRD patterns of non-activated and activated quartz-alumina mixture powders fired at 1250 °C and 1375 °C for 60 min. It is found that the intensity of the mullite phase in the activated sample increases. **Figure 4a, b** shows the mullite content of the non-activated and activated quartz-alumina mixture powders sintered at 1250–1375 °C for different times. In the samples sintered at 1250 °C for 60 min, the mullite content gradually increased from mass fraction 8.13 % to 45 % during the activation. On the other hand, when they

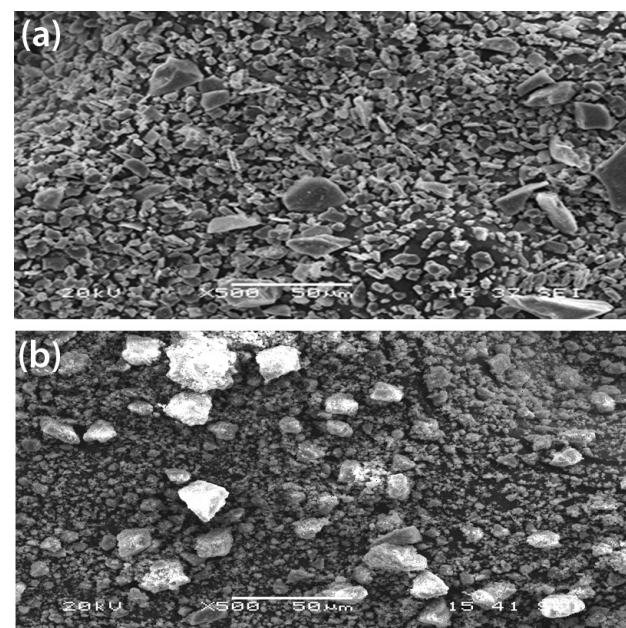


Figure 2: SEM micrographs of: a) non-activated and b) activated alumina-quartz powders

Slika 2: SEM-posnetek: a) neaktiviranega in b) aktiviranega prahu glinica-kremen

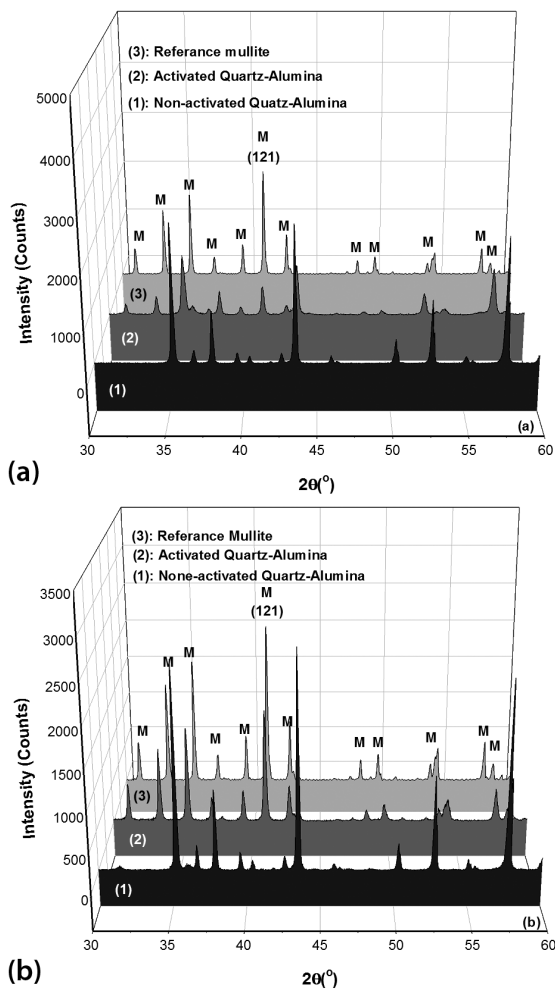


Figure 3: Comparison of the XRD patterns for the reference mullite with the XRD patterns for non-activated and activated quartz-alumina mixtures fired at: a) 1250 °C for 60 min and b) 1375 °C for 60 min
Slika 3: Primerjava XRD-posnetkov referenčnega mullita z XRD-posnetki neaktivirane in aktivirane mešanice kremenca in glinice: a) 60 min segrevanega na 1250 °C in b) 60 min segrevanega na 1375 °C

were sintered at 1375 °C for 60 min, the mullite content increased from 14.2 % to 92.3 % during the activation.

Mechanical treatment in a high-energy mill generates a stress field within the solids. Stress relaxation can occur via several mechanisms: (1) heat release, (2) development of a surface area as a result of the brittle fracture of the particles, (3) generation of various sorts of structural defects and (4) stimulation of chemical reactions within the solids. All of the relaxation channels cause changes in the reactivity of the solid substance that is under treatment, which is why the resulting action is called mechanical activation.⁹ The concentration of the mechanically induced defects and their spatial distribution depend upon the condition of the energy transfer in the mill. The creation of defects enhances the stored energy in the solids and consequently causes a decrease in the activation barrier to further processing of the solids.¹⁰

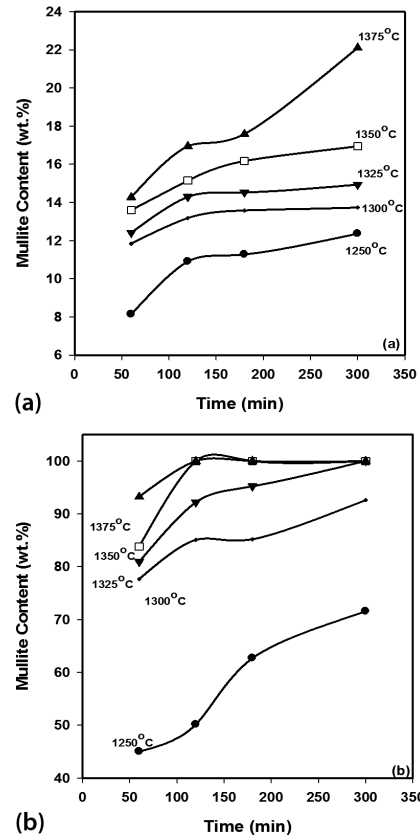


Figure 4: Mass fractions of the mullite content in: a) non-activated and b) activated sintered samples

Slika 4: Masni deleži mullita v: a) neaktiviranih in b) aktiviranih sintiranih vzorcih

4 CONCLUSION

The effect of mechanical activation on mullite formation in a quartz-alumina ceramics system was studied by using XRD and SEM. The mechanical activation caused amorphization and structural disordering of the quartz-alumina mixture. The degree of amorphization of quartz and alumina were found to be approximately 70 % and 85 %, respectively. The application of high-energy milling allowed a dramatic change in the structure and surface performance of alumina and quartz, so the content of mullite was increased with mechanical activation.

5 REFERENCES

- P. M. Souto, R. R. Menezes, R. H. G. A. Kiminami, Sintering of commercial mullite powder: Effect of MgO dopant, *J. Mater. Process Tech.*, 209 (2009), 548–53
- Y. Dong, X. Feng, X. Feng, Y. Ding, X. Liu, G. Meng, Preparation of Low-Cost Mullite Ceramics From natural Bauxite and Industrial Waste Fly Ash, *Journal of Alloys and Compounds*, 460 (2008), 599–606
- V. Viswabaskaran, F. D. Gnanam, M. Balasubramanian, Mullitisation Behaviour of South Indian Clays, *Ceramics International*, 28 (2002), 557–564

- ⁴ N. Behmanesh, S. Heshmati-Manesh, A. Ataie, Role of mechanical activation of precursors in solid state processing of nano-structured mullite phase, *J. Alloy. Compd.*, 450 (2008), 421–5
- ⁵ S. Tamborenea, A. D. Mazzoni, E. F. Aglietti, Mechanochemical activation of minerals on the cordierite synthesis, *Thermochimica Acta*, 411 (2004), 219–24
- ⁶ A. D. Mazzoni, E. F. Aglietti, E. Pereira, Preparation of Spinel Powders at low temperature by mechanical activation, *Latin. Am. Res.*, 21 (1991), 63–8
- ⁷ S. M. Ohlberg, D. W. Strickler, Determination of percent crystallinity of partly devitrified glass by X-ray diffraction, *J. Am. Ceram. Soc.*, 45 (1962), 170–171
- ⁸ P. Balaz, *Mechanochemistry in nanoscience and minerals engineering*, Springer-Verlag, Berlin 2008
- ⁹ V. V. Boldyrev, T. Tkacova, Mechanochemistry of solids: past, present, and prospects, *J. Mater. Synt. Proc.*, 8 (2000) 3/4, 121–32
- ¹⁰ U. Steinike, K. Tkacova, Mechanochemistry of solids-real structure and reactivity, *J. Mater. Synt. Proc.*, 8 (2000) 3/4, 197–203

DETERMINATION OF THE MECHANICAL PARAMETERS OF A BONDED JOINT BETWEEN A METAL AND A COMPOSITE BY COMPARING EXPERIMENTS WITH A FINITE-ELEMENT MODEL

DOLOČANJE MEHANSKIH PARAMETROV SPOJA MED KOVINO IN KOMPOZITOM S PRIMERJAVO PREIZKUSOV IN MODELOM KONČNIH ELEMENTOV

Petr Bernardin¹, Josef Vacík¹, Tomáš Kroupa², Radek Kottner³

¹University of West Bohemia in Pilsen, Department of Machine Design, Univerzitní 22, 306 14 Plzeň, Czech Republic

²University of West Bohemia in Pilsen, Department of Mechanics, Univerzitní 22, 306 14, Plzeň, Czech Republic

³University of West Bohemia in Pilsen, European Centre of Excellence, NTIS – New Technologies for Information Society, Faculty of Applied Sciences, Univerzitní 22, 306 14, Plzeň, Czech Republic
berny@kks.zcu.cz

Prejem rokopisa – received: 2012-09-01; sprejem za objavo – accepted for publication: 2012-11-16

The main goal of this work was to evaluate the application of a cohesive surface-based contact for bonded joints between rotational parts. The numerical simulations were realized using the commercial finite-element software Abaqus. The mechanical properties of the joint were identified using the gradient-optimization method implemented in the OptiSLang software. The identification was performed by minimizing the difference between the force-displacement diagram obtained from the numerical analyses and from the experiments. The shapes of the specimen and the bonded joint were designed in accordance with joints commonly used in the machine industry.

Keywords: joint, bond, composite, metal, finite element, optimization, damage modelling, identification

Glavni cilj tega dela je oceniti uporabo spoja na osnovi kohezivnega stika površin med rotacijskimi deli. Numerične simulacije so bile izvršene z uporabo komercialne programske opreme končnih elementov Abaqus. Mehanske lastnosti spoja pa so bile ugotovljene z uporabo gradientne optimizacijske metode, uporabljene s programsko opremo OptiSLang. Ugotavljanje je bilo izvršeno z zmanjšanjem razlike med vrednostmi na diagramu sila-raztezek, dobljenem z numerično analizo, in preizkusi. Oblike vzorcev in spojev so bile izvedene skladno s spoji, ki se pogosto uporabljajo v strojništvu.

Ključne besede: stik, vez, kompozit, kovina, končni element, optimizacija, modeliranje poškodb, identifikacija

1 INTRODUCTION

Composite materials are being used in different industrial fields. The number of applications in the machinery industry is also increasing very quickly. Most constructions usually consist of more than one material, which places severe demands on the inter-part connections, for example, a metal-to-composite joint. Adhesive bonding is a suitable option for such joints. For the purpose of numerical simulations, the proper finite-element model should be selected. There are many possibilities for bonded joint modelling. The components of the joint can be represented by 3D elements, whereas the adhesive layer substitutes the system of spring elements with a specific stiffness for each direction.¹ The most innovative and recently the most used approach utilizes cohesive elements, i.e., the damage and cohesive surface behaviour² (stiffness and maximum nominal stress), to define the material properties.³ These parameters are not usually provided by the manufacturers of adhesives, since the parameters strongly depend on the type of the bonded joint. The main goal of this work is the determination of the specific values of these para-

meters on the basis of tensile tests. A special optimization cycle compares the results of the experiments and the FE analyses and minimizes the difference.⁴

2 EXPERIMENT

The experiments were performed on specimens consisting of two parts made of steel (**Figure 1** – part #1 and #3) and composite material (**Figure 1** – part #2). The shape of the specimens and the bonded joint was designed by respecting the normal joints used in the machinery industry. The outer diameter of the composite

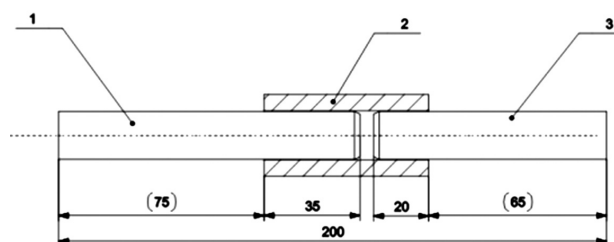


Figure 1: Sketch of specimen

Slika 1: Skica vzorca

Table 1: Material properties of the composite pipe

Tabela 1: Lastnosti materiala kompozitne cevi

Matrix		V_m
Epoxy resin		0.29
Fibre		V_f
T700		0.71
E_1/MPa	E_2/MPa	E_3/MPa
167662	6627	6627
ν_{12}	ν_{23}	ν_{31}
0.329	0.326	0.013
G_{12}/MPa	G_{23}/MPa	G_{31}/MPa
5116	2498	5116

pipe was $D = 30.32$ mm and the thickness was $t = 6.328$ mm. The properties of the composite pipe are shown in **Table 1**.

The assembly arrangement is shown in **Figure 1**.

The description of the layers, the fibre orientation and the thickness of particular layers in the composite pipe are shown in **Table 2**.

Table 2: Description of layers

Tabela 2: Opis plasti

Layer number	Thickness (mm)	Fibre Orientation ($^\circ$)
1	0.677	18.79
2	0.638	-20.09
3	1.320	0.00
4	1.320	0.00
5	0.577	0.00
6	0.228	87.17
7	0.228	87.22
8	0.453	87.26
9	0.453	87.35
10	0.454	87.43

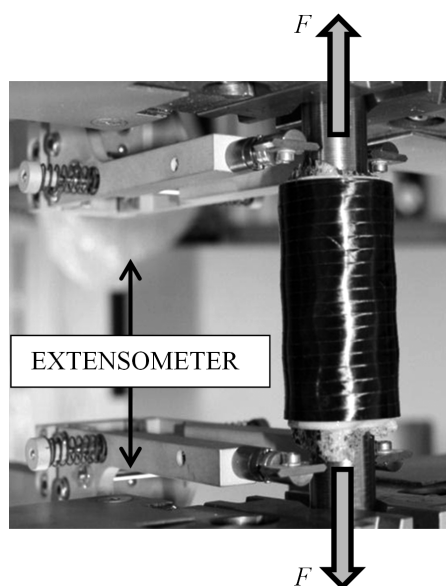


Figure 2: Specimen testing using the Zwick Roell Z050 (Load in F direction)

Slika 2: Preizkus vzorca z Zwick Roell Z050 (obremenitev v smeri F)

Four specimens were analyzed during the determination of the cohesive parameters. An epoxy adhesive Spabond 345 LV⁵ was used to join the two cylindrical surfaces of the specimens. The specimens were then tensile loaded until failure using a Zwick Roell Z050 universal testing machine. The method of loading and the location of the extensometer are shown in **Figure 2**.

2.1 Finite-element analysis

The finite-element models were created in the commercial software Abaqus/CAE 6.11-1. All the parts were modelled in accordance with the sketch in **Figure 1**. They were uniformly meshed except for the contact surfaces. These surfaces were covered with a finer mesh. Parts #1 and #3 were made of steel. Part #2 was made of composite material. The idealization of the adhesive layer was realized using surface-to-surface contact with defined cohesive and damage behaviour. To simulate the loading, the coupling function on both frontal surfaces and the reference points was applied. The boundary conditions were set on the reference points. The loading was defined by the velocity $v_y = 0.033$ mm/s. The 3-D finite-element model is shown in **Figure 3**. Four particular specimens were modelled because of the different size of the active surface of the bonded joint.

The surface-to-surface-contact with the defined cohesive and damage properties was used for the modelling. The cohesive properties of the bonded joint are characterized by the cohesive stiffness in three directions (k_{nm}, k_{ss}, k_{tt}). A damage-modelling option was used for the simulation of the degradation and the eventual failure of the joint. The mechanism of failure consists of a damage-initiation criterion and the damage-evolution law.

The damage initiation refers to the beginning of the degradation when the maximum contact stress defined by user (t_n, t_s, t_t) and the nominal traction stress are equal, and the maximum contact stress ratio reaches the value of one. This state describes the equation:²

$$\max \left\{ \frac{\langle t_n \rangle}{t_n^0}, \frac{t_s}{t_s^0}, \frac{t_t}{t_t^0} \right\} = 1 \tag{1}$$

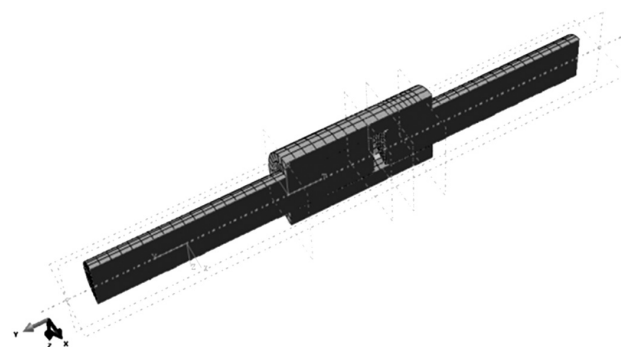


Figure 3: 3-D meshed model

Slika 3: 3-D model mreže

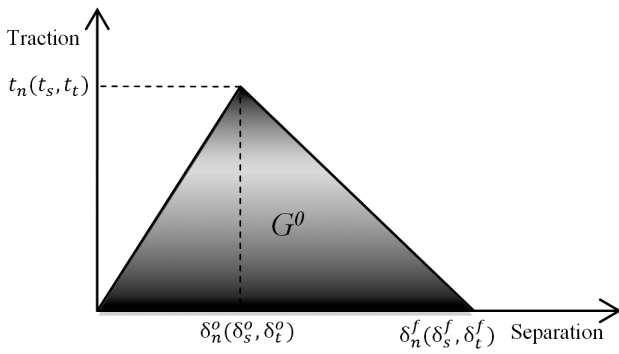


Figure 4: Linear damage parameters

Slika 4: Linearni parametri poškodbe

The damage evolution can be defined either by an effective separation during complete failure or by the energy that dissipates during the failure. The separation (δ) is described in Figure 4, while the energy (G^0) is represented by the area under the curve in Figure 4.

The relationship between the above-mentioned parameters is described by equation:³

$$t = \begin{Bmatrix} t_n \\ t_s \\ t_t \end{Bmatrix} = \begin{Bmatrix} K_{nn} & K_{ns} & K_{nt} \\ K_{ns} & K_{ss} & K_{st} \\ K_{nt} & K_{st} & K_{tt} \end{Bmatrix} \begin{Bmatrix} \delta_n \\ \delta_s \\ \delta_t \end{Bmatrix} = K\delta \quad (2)$$

2.2 Identification

The cohesive and damage properties of the bonded joint were identified using the optimization method implemented in OptiSLang software. The cohesive and damage parameters (δ , k_{nn} , k_{ss} , k_{tt} , t_n , t_s , t_t) were set as the input parameters. The identification was performed by minimizing the difference between the force-displacement diagram obtained from the numerical analysis and the experiment:

$$r_g = \sum_{i=0}^n \frac{(F_{FEA}^i - F_{exp}^i)^2}{\max(F_{exp}^i)} \quad (3)$$

where F_{FEA}^i is the force obtained by the experiment and F_{exp}^i is the force obtained by the analysis. The difference marked as r_g is the objective function and was tracked at particular points of two curves. This is the model parameter to be minimized.

3 DISCUSSION

The curves shown in Figure 5 describe the relationship between the force and the displacement of all four specimens. These values were obtained during the testing. The reason for the disagreement between the curves was the different area of the active bonding surface. The real bonding surface area was influenced by the shrinkage of the adhesive, which occurs within the curing process. Another reason could be the errors caused by the imperfect manual preparation of the test

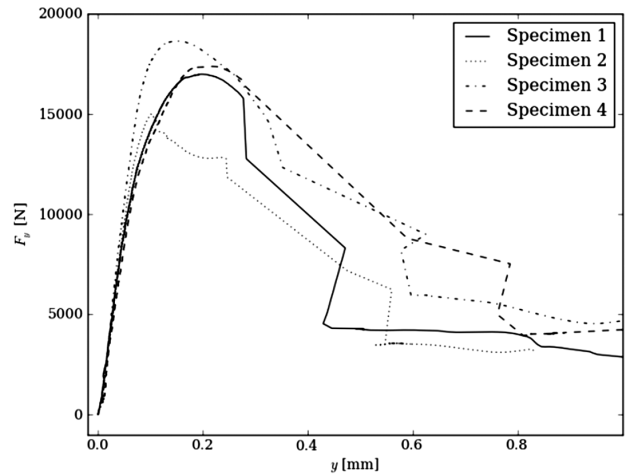


Figure 5: Comparison between four tested specimens

Slika 5: Primerjava med štirimi preizkušenimi vzorci

specimens. Thanks to the particular ruptured specimens it was possible to find the different widths of the bonded joint surface, which was implemented in the 3D-model.

Using the optimization process, the necessary parameters for all the bonded joints were found for the tested specimens (Table 3).

Table 3: Cohesive and damage parameters

Tabela 3: Parametri kohezije in poškodbe

Parameters	1	2	3	4
δ /mm	0.75	0.89	0.95	0.97
K_{nn} /N/mm	1254.0	1158.0	1193.0	1194.0
K_{ss} /N/mm	1212.0	1179.0	1112.0	1112.6
K_{tt} /N/mm	1000.0	6648.0	6007.0	850.9
t_n /MPa	30.0	30.0	30.0	30.0
t_s /MPa	30.0	30.0	30.0	30.0
t_t /MPa	30.1	27.8	30.6	31.2
r_g	41.19	11.7	4.1	16.8

Table 3 describes the cohesive and damage parameters obtained during the optimization process for four specimens. In the ideal state, the found parameters had to be the same, but some differences emerged, especially in the value of K_{tt} . The specimens #1 and #4 show similar values, as well as #2 and #3. This might be caused by a different mechanism of failure during the test. With the 1st and 4th specimens, the pull-up of the fibre, not the

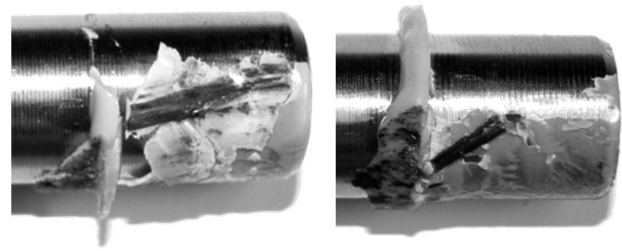


Figure 6: Specimens 1 and 4

Slika 6: Vzorca 1 in 4

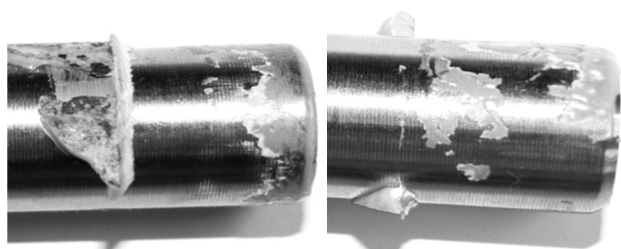


Figure 7: Specimens 2 and 3
Slika 7: Vzorca 2 in 3

adhesive failure, occurred. The failures of the specimens #2 and #3 were located in the layer of the adhesive. The properties gained from these specimens (bold text in Table 3) are really describing the cohesive and damage behaviour of the adhesive. These parameters do not differ by more than 10 % and the r_g ratio is also low. The mechanism of the failure is shown in Figures 6 and 7.

The fitting of the interpolation curves of the experiment and the FE analyses are shown from Figures 8 to 11.

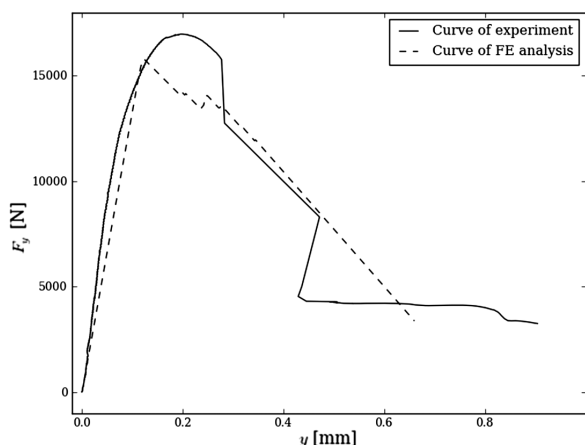


Figure 8: Specimen 1
Slika 8: Vzorec 1

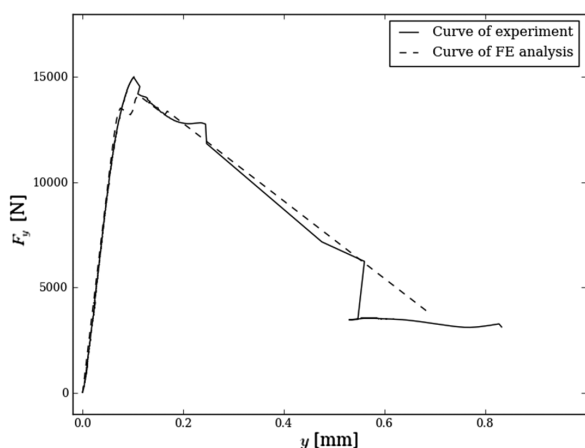


Figure 9: Specimen 2
Slika 9: Vzorec 2

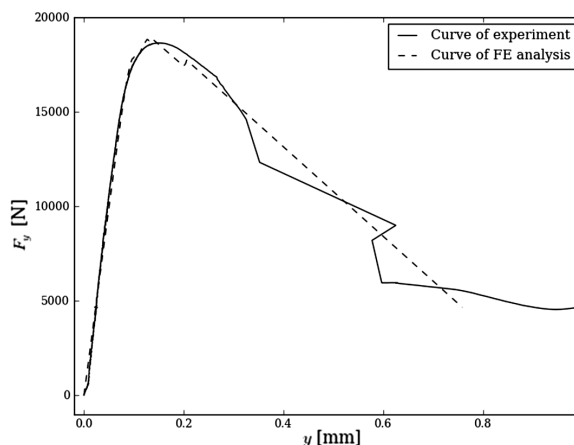


Figure 10: Specimen 3
Slika 10: Vzorec 3

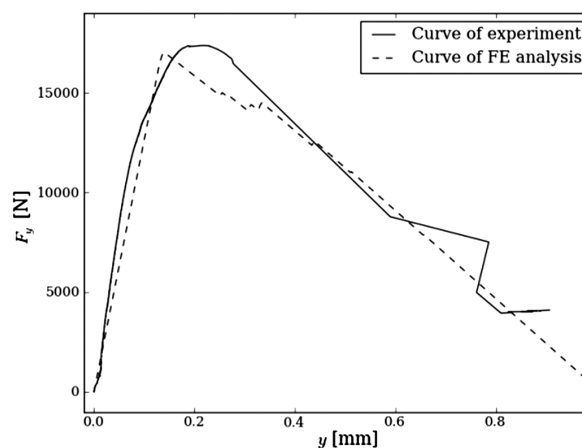


Figure 11: Specimen 4
Slika 11: Vzorec 4

The behaviour of the curves of the experiment and the FE analyses differs after the 0.8 mm value of the displacement and the curves were fitted up to this value. After this value, the force obtained by the experiment had a constant value, which was caused by the friction, although the adhesive was already ruptured. The friction was not taken into account in the FE models; therefore, the force decreased to zero in the numerical simulations. As is implied by the optimization process, the parameters of δ , k_n , t_i have the largest influence on the shape of the curve, while the other parameters have smaller influences (k_{nm} , k_{ss} , t_n , t_s). The datasheet shear stress value of the Spabond 345 LV⁵ is in the range between 29 MPa and 37 MPa, which corresponds well with the observed values.

4 CONCLUSION

A series of tensile tests was performed on specimens consisting of steel and composite material. Particular parts of the specimens were joined by the Spabond 345 LV⁵ adhesive and loaded using the Zwick Roell Z050

universal testing machine. The objective function was minimized with the help of the OptiSLang software. The damage and cohesive parameters of the cohesive surface-based contact were determined. The analyses successfully confirmed the suitability of the experimental data fitting for the identification of the cohesive parameters. Nevertheless, further investigations should follow in order to optimise the parameters, e.g., testing according to ASTM standards.

Acknowledgement

The work has been supported by projects ME 10074 and GA P101/11/0288.

5 REFERENCES

- ¹ F. P. Tahmasebi, Finite Element Modeling of an Adhesive in a Bonded Joint, NASA Goggard Space Flight Center, 1999
- ² M. L. Benzeggagh, M. Kenane, Measurement of Mixed-Mode Delamination Fracture Toughness of Unidirectional Glass/Epoxy Composites with Mixed-Mode Bending Apparatus, *Composites Science and Technology*, 56 (1996) 4, 439–449
- ³ P. P. Camanho, C. G. Davila, Mixed-Mode Decohesion Finite Elements for the Simulation of Delamination in Composite Materials, NASA/TM-2002-211737, 2002
- ⁴ P. Janda, M. Kosnar, T. Kroupa, V. Lašová, J. Vacík, Využití programů ANSYS a OPTISLANG v konstrukci výrobních strojů, Frymburk: ANSYS konference, 2010
- ⁵ Spabond, Epoxy Adhesive System, Newport Isle of Weight, 2004, Available: http://www.gurit.com/files/documents/Spabond_345_v7.pdf. [cited 12 June 2012]

DETERMINATION OF THE METAL CONCENTRATIONS IN AN ANODE MATERIAL FOR SOLID-OXIDE FUEL CELLS

DOLOČITEV VSEBNOSTI KOVIN V ANODNEM MATERIALU ZA GORIVNE CELICE S TRDNIM ELEKTROLITOM

Tina Skalar^{1,2}, Amalija Golobič¹, Marjan Marinšek^{1,2}, Jadran Maček^{1,2}

¹University of Ljubljana, Faculty of Chemistry and Chemical Technology, Aškerčeva 5, 1000 Ljubljana, Slovenia

²Center of Excellence for Low-Carbon Technologies (CO-NOT), Hajdrihova 19, 1000 Ljubljana, Slovenia
tina.skalar@fkk.uni-lj.si

Prejem rokopisa – received: 2012-09-25; sprejem za objavo – accepted for publication: 2013-01-03

Ni-SDC is a very promising new anode material for SOFC systems. It exhibits a superb ionic and electronic conductivity at intermediate temperatures (400–700 °C) in comparison to Ni-YSZ. Ni-SDC is a composite material requiring careful microstructural and compositional tailoring during the preparation of the material. Ni-SDC was synthesized using a simplified Pechini method with a reaction between metal acetates and ethylene glycol, the latter serving as a chelating agent, and a reaction medium. The molar ratio between cerium and samarium in the ceramic part was 83 : 17 and the overall nickel content in the final product was set to 38 %. During the preparation of the material, several different intermediates were synthesized (i.e., a powdered product after the synthesis, an oxide mixture after the calcination and a mechanically ground powder after the milling), which may differ according to their chemical and morphological properties. In this respect, the material chemical composition expressed as concentrations of nickel, cerium and samarium was followed through the preparation sequence using various analytical techniques, i.e., the volumetric and gravimetric methods, ICP-OES, SEM-EDS and XRD. It appears that the obtained results diverge consistently with the analytical techniques used. Volumetry and gravimetry were used only for the nickel-content determination. Additionally, all the metals were simultaneously determined with ICP-OES and XRD Rietveld refinement in a bulk sample and with SEM-EDS for a point analysis. There is no unique answer as to which analytical method should be used at various preparation steps. Instead, suitable analytical methods or their combinations were chosen with respect to the analyzed material's appearance and its morphological and microstructural characteristics.

Keywords: NiO-SDC powders, gravimetric method, volumetric method, SEM-EDS, XRD, ICP analysis

Kermet Ni-SDC se uporablja kot anodni material v SOFC gorivnih celicah (gorivne celice s trdnim elektrolitom). V primerjavi z navadno uporabljenim anodnim materialom Ni-YSZ ima Ni-SDC višjo ionsko in elektronsko prevodnost pri temperaturah od 400 °C do 700 °C. Kermet Ni-SDC zahteva pazljivo prilagajanje mikrostrukture in sestave med svojo pripravo. Ni-SDC je bil sintetiziran s poenostavljeno Pechinijevo metodo, kjer poteka reakcija med kovinskimi acetati in etilen glikolom. V končnem produktu je bilo molsko razmerje med cerijem in samarijem 83 : 17, volumenski delež niklja pa 38 %. Za ustrezen anodni material je potrebnih več stopenj obdelave, sinteza prekursorja Ni-SDC, kalcinacija in mletje v atritorju. V vsaki stopnji se pri materialu lahko spreminjata ali sestava ali morfologija. Kemijska sestava vseh treh materialov je bila izražena s koncentracijami niklja, cerija in samarija. Za določitev teh koncentracij so bile uporabljene različne analize metode: volumetrija, gravimetrija, ICP-OES, SEM-EDS in XRD. Med dobljenimi rezultati se glede na uporabljeno metodo pokažejo razlike. Volumetrijo in gravimetrijo smo uporabili za določanje koncentracije niklja v vzorcih. Vsebnost vseh treh kovin istočasno pa smo določili z ICP-OES, XRD in SEM-EDS, kjer se s slednjo točkovno določi koncentracije, s prvima dvema metodama pa v večjem volumnu. Unikatnega odgovora, katera analitska metoda je najbolj primerna, ni. Najprimernejšo metodo oziroma njihovo kombinacijo izberemo glede na morfološke in mikrostrukturne lastnosti analiziranega materiala.

Ključne besede: NiO-SDC-prahovi, gravimetrična metoda, volumetrična metoda, SEM-EDS, XRD, ICP-analiza

1 INTRODUCTION

The solid-oxide fuel cell (SOFC) is one source of alternative energy. These cells have a more efficient and pollution-free transformation of fuel into electrical power than the traditional combustion engines, which is the reason for the growing research in this field. A SOFC is typically composed of an anode, a cathode and electrolytes, which should each have their specific properties. The anode should have a high ionic and electronic conductivity for the transportation of oxide ions to the reaction site and electrons from it. Its microstructure should provide a good contact between the reactive gas, electronic and ionic conductors (the triple-phase boundary; hereafter: TPB). Finally, the desired molar ratio of the metals in the cermet^{1,2} is also very important. The

volume content of nickel in the cermet influences the open porosity of the material, which enables a contact between the gasses and the anode.³ The electronic conductivity increases with the increasing nickel content; meanwhile, the ionic conductivities of the cermet decrease due to the weak connections among the SDC grains.⁴ Furthermore, the ceramic phase of the cermet (samaria-doped ceria; hereafter: SDC) should have a proper composition of samarium and cerium. It is experimentally determined that the best ionic conductivity is achieved when the molar ratio of Ce : Sm is 80 : 20, and the samarium is distributed homogeneously in the cerium.⁵ It is necessary to fulfill all these conditions to provide a high-efficiency material for SOFCs. Previous contributions^{6–8} mostly stress the importance of the metal content in such materials, but this was rarely determined,

even partially. The value of the metal content has the highest importance when developing the materials for SOFCs.

This report describes the material's composition expressed as concentrations of nickel, cerium and samarium, which are followed through the preparation steps, using several analytical techniques, such as the volumetric and gravimetric methods, ICP-OES, SEM-EDS and XRD.

2 EXPERIMENTAL WORK

2.1 Sample preparation

A mixture of 17.68 g of $\text{Ce}(\text{C}_2\text{H}_3\text{O}_2)_3 \cdot x\text{H}_2\text{O}$ (Sigma Aldrich, 99.9 % pure, metals basis) and 3.65 g of $\text{Sm}(\text{C}_2\text{H}_3\text{O}_2)_3 \cdot x\text{H}_2\text{O}$ (Sigma Aldrich 99.9 % pure, metals basis) was dissolved in 150 mL of deionized water. After the acetates dissolved 100 mL of ethylene glycol ($\text{C}_2\text{H}_6\text{O}_2$, Sigma Aldrich, puriss. p. a. 99.5 %) was added. The mixture was heated to 50 °C for 30 min, then the temperature was raised to 80 °C and 32.93 g of nickel acetate $\text{Ni}(\text{CH}_3\text{COO})_2 \cdot 4\text{H}_2\text{O}$ (Riedel-de Haën, min 98 % purity) was added. The metal molar ratio in the reaction mixture was 5.0 : 4.6 : 1. This mixture was heated and vacuum dried for two and half hours in a vacuum dryer (Büchi Heating bath B-490 Rotavapor R-200), equipped with a vacuum pump (PC 2003 VARIO). Afterwards, the product was dried at 80 °C for three days until the final crystals were formed, which were then used as an intermediate (Sample 1) to produce the anode material. This intermediate was calcined at 900 °C in air for 1 h to form a mixture of metal oxides (Sample 2). Sample 2 was homogenized in an attritor mill by wet milling in isopropanol for one hour which resulted in Sample 3.

Nickel concentrations in the NiO-SDC material were determined with the gravimetric method, using dimethylglyoxime, and the volumetric method with the EDTA titration. To determine cerium and samarium, and the nickel weight content, SEM-EDS, XRD method and ICP-OES analysis were used.

The samples that were used for gravimetry, volumetry and the ICP analysis were dissolved in different solvents. The intermediate after the synthesis (Sample 1), which was a water-soluble product, was dissolved with distilled water. Sample 2 was a cermet composed of nickel oxide, samarium oxide and cerium oxide. It was dissolved in concentrated (96–98 %) sulfuric (VI) acid and evaporated to form the sulfates of the metals present. The residue of metallic sulfates was then dissolved in 37 % hydrochloric acid and diluted in distilled water. Sample 3 was dissolved using the same acid procedure as for the Sample 2.

2.2 Analytical procedures

2.2.1 Thermal decomposition of Sample 1

Thermal decomposition of Sample 1 was analyzed in the range from room temperature to 1000 °C in air with a

heat rate of 10 K min⁻¹ with the TG/DTA analysis using a Netzsch STA 449 F3 Jupiter apparatus.

2.2.2 Gravimetric determination with dimethylglyoxime

The nickel content was determined in 10 mL aliquots of dissolved samples diluted with distilled water in an Erlenmeyer flask. The pH level was adjusted to between 4 to 5 with an ammonia or hydrochloric solution, depending on the pH value of the previous solution. Then, 0.5 mL of NaCOOCH_3 and 20 mL of CH_3COOH were added to form an acetate buffer. The solution was then boiled with an electric heater. After the mixture cooled down slightly, 10 mL of dimethylglyoxime (1 % ethanol solution) was added and the red nickel precipitate was filtered through the ceramic filter and washed with hot water. The precipitate containing nickel was dried at 120 °C for 1 h, cooled down in a desiccator and weighed. This was repeated at least three times. The weight percentage was calculated from the weight of the complex.⁹ It is recommended that the analysis of the standard sample be carried out in the same method of analysis that was used for our samples. Therefore, the gravimetric method was also used for the nickel (II) oxide (NiO), the Aldrich nanopowder that was taken as the standard material.

2.2.3 Volumetric method using EDTA as a titration reagent

For a determination of nickel, 10 mL aliquots of dissolved samples were diluted with distilled water in an Erlenmeyer flask to 100 mL. The pH value was adjusted to 10 with an ammonia solution. Then a solid murexide indicator was added that formed a bright yellow color. The sample was titrated with the standard 0.01 M EDTA until the yellow color of the nickel-murexide complex started to change to the purple color of a free indicator. The volumetric-determination procedure was repeated ten times for each sample. The weight percentage was calculated from the EDTA volume used for the titration of the nickel ions.^{9–11} Using this method, the nickel content was also determined for the nickel (II) oxide (NiO), the Aldrich nanopowder that was taken as the standard material.

2.2.4 SEM-EDS

All the samples were characterized on an FE-SEM Zeiss Ultra Plus microscope equipped with EDS (an Oxford X-Max SDD 50 mm² detector and INCA 4.14 X-ray microanalysis software). The sample preparation included a fixation onto a conductive C tape and a subsequent sputtering with platinum, without any polishing. The detector was calibrated just before the analysis with the Co-standard under operating conditions. The EDS spectra were recorded on the flat regions of the samples using a process time of 5, a lifetime of 120 s and an accelerating voltage of 14 kV, which is an acceptable compromise between the analyzing volume and the overvoltage needed to excite the Ce, Sm and Ni X-rays,

whose emission lines are found in the interval between 4.84 ($L\alpha_1$) keV, 5.64 ($L\alpha_1$) keV and 7.48 ($K\alpha_1$) keV, respectively. Using the Anderson-Halser estimation,¹² the X-ray production depth was approximately 0.6 μm . The quantification of the X-ray spectra was performed with respect to the standard procedure provided by the software manufacturer (ZAF-based method¹³). For the statistically reliable data in each case, five to seven different fields of view in various regions of interest were analyzed.

2.2.5 XRD analysis

The X-ray powder-diffraction data for Samples 1, 2 and 3 were collected using a PANalytical X'Pert PRO MPD diffractometer with the θ - 2θ reflection geometry, a primary-side Johansson-type monochromator and the $\text{CuK}\alpha_1$ ($\lambda = 0.154\ 059\ \text{nm}$) radiation. The room-temperature-reflection data were acquired from the 2θ angles of 5° to 90° in the steps of 0.034° . A quantitative XRD analysis with the Rietveld method using the *TOPAS2.1* program suite¹⁴ was performed for Samples 2 and 3. The background was modeled with a third-order polynomial. We also refined zero error, scale factor, lattice parameter a and one profile parameter (the crystallite size) for NiO and SDC. The atom parameters were fixed, taken from the published structures of SDC and NiO.^{15,16} The final match between the observed and calculated profiles is shown in **Figures 1** and **2**. The agreement factor R_{wp} was 0.094 5 and 0.078 5 for Samples 2 and 3, respectively.

2.2.6 ICP-OES

An analysis of nickel, samarium and cerium was carried out with an inductively coupled plasma-optical emission spectrometer (Varian 715-ES ICP-OES Spectrometer). The ICP-OES spectrometer is used to define concentrations of several elements in the solution. The ICP-OES method was already used to detect the metals (Ni, Ce, Gd, Ag) in the materials used for SOFCs.^{1,17-20} Details about the instruments' operating conditions are depicted in **Table 1**.

3 RESULTS AND DISCUSSION

The results for the metal contents in Samples 1, 2 and 3 are shown in **Tables 2**, **3** and **4**, respectively. The calculated concentrations of cations for Samples 2 and 3 were determined according to the initial amounts of added cations. It was assumed that during the process there were no losses of the metals and that the entire chemical reaction took place in line with the expectations, meaning that Samples 2 and 3 consist of oxides only. The calculated metal mass fractions for Sample 1 were calculated by considering its thermal decomposition into oxides (**Figure 3**). The concentration range of the elements that are in the samples is in the detection range of the classical analytical methods (gravimetry, volumetry). The systematic error in the gravimetric determination of nickel had to do with the specific characteristics of the

precipitated nickel dimethylglyoxime (the voluminosity of the formed complex).²¹ The values obtained with the complexometric titration of nickel deviate more from the expected calculated values than in the case of gravimetry. It was difficult to determine the color leap of the organic indicator that provided the endpoint of titration. The pH value of the prepared solution had a significant influence on the results, as did the absence of oxidants in the analyte.²¹ The rare elements showed a great similarity in the chemical properties; therefore, the concentration of these elements (cerium and samarium) was determined only with instrumental methods.

Determination of the chemical compositions of the samples was quite a challenge with regard to the quantification of the collected EDS spectra. The main difficulty was found in the fact that the Ce and Sm characteristic X-ray peaks in the EDS spectra mostly overlap. This problem was particularly pronounced in the case of Sm, since the superimposed Ce peaks on all the main Sm peaks made a consistent quantitative compositional calculation rather difficult. From this point of view, the related WDS analysis seems to be more suitable for a compositional investigation of such samples. However, when compared to WDS, EDS has its advantages: it is more available, quicker, simpler and easier to perform. In fact, in material science, the EDS analysis is one of the basic tools for compositional investigations and, as such, it is very popular.

EDS and XRD are nondestructive approaches to a material investigation, but both are less accurate than the other three used analytical methods. Additionally, EDS and XRD are both based on a similar physical phenomenon; however, there is one distinguishable difference between them. The XRD quantitative analysis always refers to the bulk-sample composition, while EDS denotes the chemical composition in a much smaller sample region. For this reason, EDS results always depend upon the specimen surface preparation and are also influenced by the sample topography.

From this point of view, the three investigated samples were somewhat dissimilar. After the synthesis, the sample was composed of tiny crystals (**Figure 4**). To determine the homogeneity of this sample, an X-ray sur-

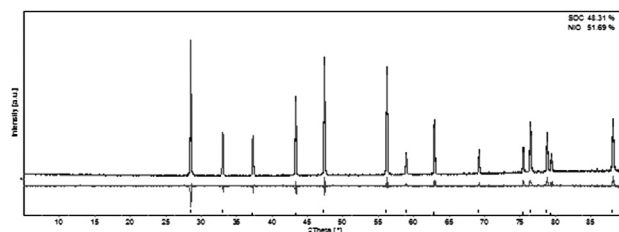


Figure 1: Rietveld refinement for Sample 2: experimental and calculated (upper curves) and difference (lower curve) profiles. Vertical bars denote the position of reflections for SDC (upper) and NiO (lower).

Slika 1: Rietveldovo prilaganje za vzorec 2: izmerjena in izračunana krivulja (zgoraj) ter diferenčna (spodaj). Pokončne črtice označujejo lego uklonov za SDC (zgoranje) in NiO (spodnje).

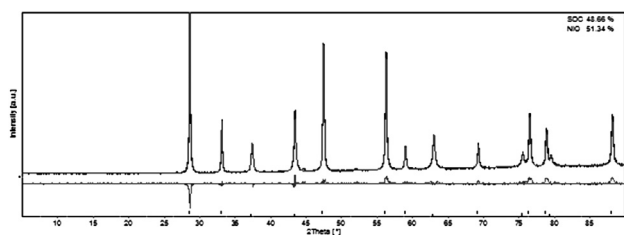


Figure 2: Rietveld refinement for Sample 3: experimental and calculated (upper curves) and difference (lower curve) profiles. Vertical bars denote the position of reflections for SDC (upper) and NiO (lower).

Slika 2: Rietveldovo prilaganje za vzorec 3: izmerjena in izračunana krivulja (zgoraj) ter diferenčna (spodaj). Pokončne črtice označujejo lego uklonov za SDC (zgoranje) in NiO (spodnje).

face mapping was performed (**Figure 5**). As expected, Ce, Sm, Ni, O and C were the only elements detected in the sample. From the element maps it could be seen that the specimen was rather inhomogeneous. Some variations in the grayscale maps may be associated with the specimen topography; however, it was evident that the sample contains two separate phases. The elongated crystals, typically 20–40 μm long and $\approx 5 \mu\text{m}$ wide, were Ce- and Sm-rich, while smaller particles (3–10 μm in diameter) of an undefined shape were Ni-rich. This was also supported by the XRD diffraction pattern of Sample 1, presented in **Figure 6**. The qualitative XRD analysis revealed that the sample consisted of an SDC metal-organic precursor with a known structure and formula²² and of at least one additional crystalline phase with an unknown composition and structure. The positions of the first reflections of the unknown phase were at the angles lower than $10^\circ 2\theta$. They also had significantly lower intensities in comparison with the SDC precursor phase. Both facts indicated that the unknown phase could be a metal-organic nickel complex, i.e., a precursor of NiO. The XRD quantitative analysis using Rietveld refinement was not possible for this sample, since it requires the knowledge of the composition and the structure of all the crystalline phases. Due to the observed inhomogeneity, the only practical way of performing a quantitative EDS analysis was by collecting the X-ray signals from the regions of interest (ROI) of approximately 0.25 mm^2 in

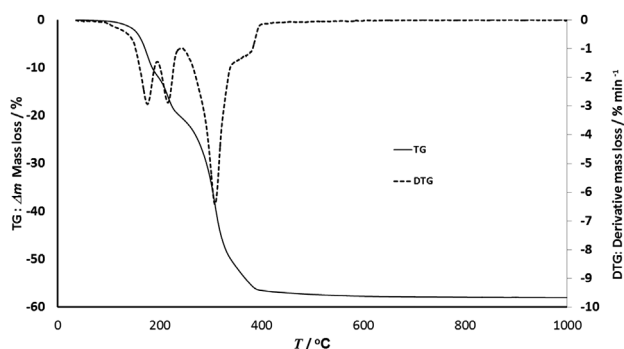


Figure 3: Thermal decomposition of Sample 1 to Sample 2 in air
Slika 3: Termični razpad vzorca 1 do vzorca 2 na zraku

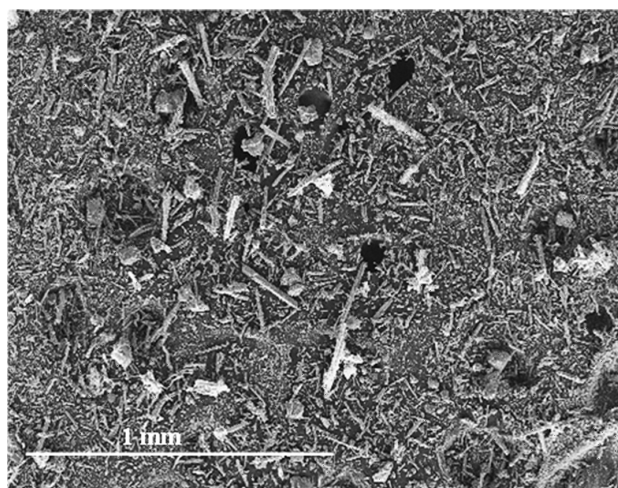


Figure 4: Tiny crystals in Sample 1 after the synthesis
Slika 4: Kristalčki vzorca 1 po sintezi

Table 1: Operating conditions for the ICP-OES analysis

Tabela 1: Pogoji merjenja za ICP-OES analize

Parameter	Value
RF generator power / kW	1.2
Frequency of RF generator / MHz	40
Plasma-gas flow rate / L min ⁻¹	15.0
Auxiliary-gas flow rate / L min ⁻¹	1.50
Nebulization-gas flow pressure / kPa	200
Gas	Argon
Sample-uptake rate / mL min ⁻¹	1.9
Type of detector	CCD
Type of spray chamber	Sturman-Masters double pass
Type of nebulizer	V-groove
Element λ/nm^{-1}	Ce: 418.659 446.021
	Sm: 359.259 360.949
	Ni: 216.555 231.604

Table 2: Results of metal mass fractions for Sample 1 obtained with different analytical methods

Tabela 2: Masni deleži treh kovin v vzorcu 1, določeni z različnimi analitskimi metodami

Used method	w(Ni)/%	w(Ce)/%	w(Sm)/%	w(Ni) : w(Ce) : w(Sm)
Calculated value	16.1	14.6	3.2	5.0 : 4.6 : 1.0
Gravimetric method	16.5 ± 0.3	/	/	/
Volumetric method	15.47 ± 0.02	/	/	/
SEM-EDS	12.3 ± 0.5	12.6 ± 1.5	2.5 ± 0.5	5.0 : 5.1 : 1.0
ICP-OES	14.9	13.5	2.8	5.4 : 4.9 : 1.0

w/% – mass fraction, w/% – masni delež

size (6–7 ROIs on each field of view). According to the results summarized in **Table 2**, the determined element-content ratio (ECR) among Ni, Ce and Sm (w(Ni):w(Ce):w(Sm) = 5.0 : 5.1 : 1.0) was not in good accordance with

the calculated ratio $w(\text{Ni}) : w(\text{Ce}) : w(\text{Sm}) = 5.0 : 4.6 : 1.0$. The highest deviations were observed for the Ce-content determination, which was estimated to be too high and the Sm-content determination, which was estimated to be too low. The reason for the inaccurate Ce- and Sm-content determinations was probably a poor deconvolution of the overlapping peaks in the EDS spectra.

The EDS spectra of Sample 1 also exhibited a characteristic carbon peak, which made the absolute quantitative analysis unrealistic. The C peak was attributed to two origins; i) carbon was contained in the structure of the metal-organic intermediate in Sample 1, and ii) the characteristic C peak was partially a consequence of a sample contamination due to its exposure to air (CO_2) before the analysis, as well as some cracking of the hydrocarbons in the vacuum system of the electron microscope under the electron beam.²³

Sample 2 was obtained with the subsequent thermal treatment of Sample 1 without performing any other mechanical operation. Such a preparation path for Sample 2 also meant that the ECR for the metals should be the same as for Sample 1. However, the absolute

values of the Ni, Ce, Sm and O element contents should increase during the thermal treatment due to a mass loss when the metal-organic compound in Sample 1 was transformed into an oxide mixture of NiO and SDC.

After the thermal decomposition, the sample retained its degree of homogeneity (Figure 7). For that reason, the X-ray signals for the quantitative EDS analysis of Sample 2 were repeatedly collected from ROIs of approximately 0.25 mm^2 in size (6–7 regions of interest on each field of view), similarly to the EDS analysis of Sample 1. Since the treatment at $900 \text{ }^\circ\text{C}$ transformed the sample into a mixture of oxides, the summation of the Ni, Ce, Sm and O contents was normalized to 100%. The EDS spectra of Sample 2 also exhibited a characteristic C peak, which was attributed only to the sample contamination and subsequently entirely omitted in the quantitative calculations. The average absolute values for the Ni, Ce and Sm contents as obtained by the EDS measurements are given in Table 3. The errors were estimated on the basis of the variations of the data. The results of the quantitative EDS analysis of the Ni, Ce and Sm contents (38.7 %, 39.7 % and 7.0 %, respectively) were in a relatively good agreement with the expected calculated values for Sample 2. However, due to the local inhomogeneity, the measured absolute values of the element contents may differ substantially between ROIs, resulting in a relatively high standard deviation ($\pm 4.8 \%$ for Ni). The calculated ECR for Sample 2 implied that the Sm content was again estimated too low.

The quantitative XRD phase analysis with the Rietveld method resulted in $(48.3 \pm 3.0) \%$ of SDC and

Table 3: Results of metal mass fractions for Sample 2 obtained with different analytical methods

Tabela 3: Masni deleži treh kovin v vzorcu 2, določeni z različnimi analitskimi metodami

Used method	$w(\text{Ni})/\%$	$w(\text{Ce})/\%$	$w(\text{Sm})/\%$	$w(\text{Ni}) : w(\text{Ce}) : w(\text{Sm})$
Calculated value	38.2	34.7	7.6	5.0 : 4.6 : 1.0
Gravimetric method	38.58 ± 0.09	/	/	/
Volumetric method	36.8 ± 0.2	/	/	/
SEM-EDS	38.7 ± 4.8	39.7 ± 4.1	7.0 ± 1.5	5.5 : 5.7 : 1.0
XRD	40.6 ± 3.0	32.9 ± 3.0	7.2 ± 2.0	5.6 : 4.6 : 1.0
ICP-OES	37.4	36.5	7.6	4.9 : 4.8 : 1.0

$w/\%$ – mass fraction, $w/\%$ – masni delež

Table 4: Results of metal mass fractions for Sample 3 obtained with different analytical methods

Tabela 4: Masni deleži treh kovin v vzorcu 3, določeni z različnimi analitskimi metodami

Used method	$w(\text{Ni})/\%$	$w(\text{Ce})/\%$	$w(\text{Sm})/\%$	$w(\text{Ni}) : w(\text{Ce}) : w(\text{Sm})$
Calculated value	38.2	34.7	7.6	5.0 : 4.6 : 1.0
Gravimetric method	38.5 ± 0.2	/	/	/
Volumetric method	36.45 ± 0.09	/	/	/
SEM-EDS	37.6 ± 2.3	38.9 ± 2.1	7.0 ± 0.7	5.4 : 5.6 : 1.0
XRD	40.3 ± 2.0	33.1 ± 2.0	7.3 ± 2.0	5.5 : 4.5 : 1.0
ICP-OES	38.0	36.7	7.5	5.1 : 4.9 : 1.0

$w/\%$ – mass fraction, $w/\%$ – masni delež

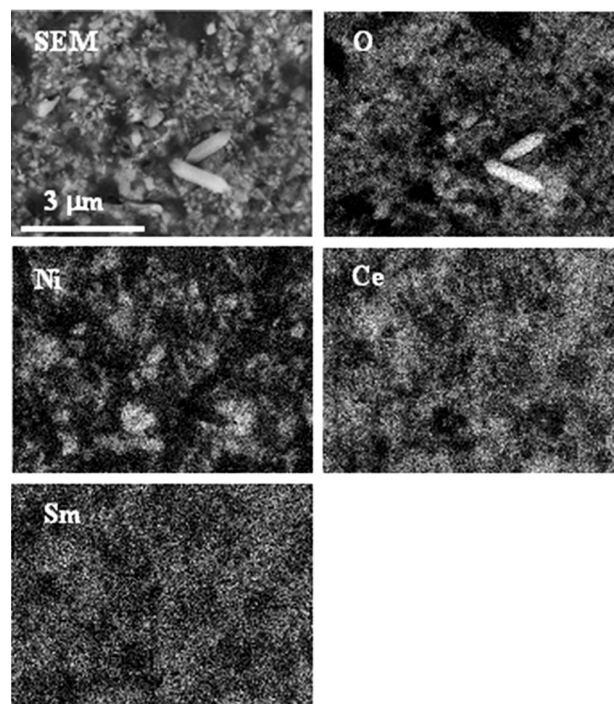


Figure 5: X-ray surface mapping of Sample 1
Slika 5: Elementna porazdelitev vzorca 1

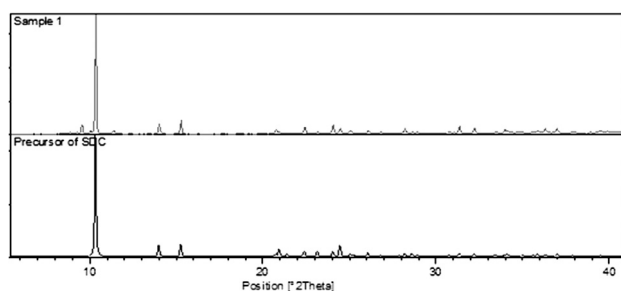


Figure 6: XRD patterns at low angles of Sample 1 (upper) and of pure precursor of SDC (bottom)

Slika 6: Rentgenski praškovni posnetek pri nizkih kotih: vzorec 1 (zgoraj), čisti prekurzor SDC-ja (spodaj)

(51.7 ± 3.0) % of NiO. From these results, the mass fractions of the metals, given in **Table 3**, are calculated; they are close to the expected calculated values (within the experimental error). Sample 3 was prepared by attritor milling of Sample 2. Such milling results in an increased homogeneity of the sample. The region of the one-phase dominance (either a NiO or SDC phase) was estimated on the basis of the morphological characteristics of Sample 3 and expected to be in the sub-micrometer range. Collecting the X-ray spectra of Sample 3 and the subsequent calculations were performed identically to the previous analyses by investigating several ROIs (C was omitted in the quantitative calculations). According to **Table 4**, the consequence of the increased homogeneity in Sample 3 was reflected through a relatively accurate determination of the Ni and Ce contents with a much smaller deviation, practically halved in comparison to Sample 2. The key problem of processing the EDS spectra of the selected system still remains in the fact that the main Sm peaks overlap with the Ce peaks, resulting again in a too low Sm-content and a too high Ce-content estimation and thus making the EDS quantification heavily dependent on the method used to deconvolute the spectrum. The quantitative XRD phase analysis using the Rietveld method of Sample 3 resulted in (48.7 ± 2.0) % of SDC and (51.3 ± 2.0) % of NiO. From these results, the mass fractions of the metals, given in **Table 4**, were calculated, which were close to the expected calculated values (within the experimental error). It has to be emphasized that the Rietveld method gave us the mass fractions for NiO and SDC in the crystalline part of the sample. Consequently, in the case of the presence of a significant amount of an amorphous phase the resulted mass fractions may not be representative for the whole sample (especially if the metal content in the amorphous phase differs significantly in comparison to the crystalline part). Rietveld-refinement results also confirmed that Samples 2 and 3 contained only NiO and SDC with the desired compositions where the lattice parameter a for SDC is 0.543 2(1) and 0.543 3(1) nm,²² respectively. The width of the reflections of Sample 3 was larger in comparison with those of Sample 2. Consequently, the crystallite-size parameters resulting

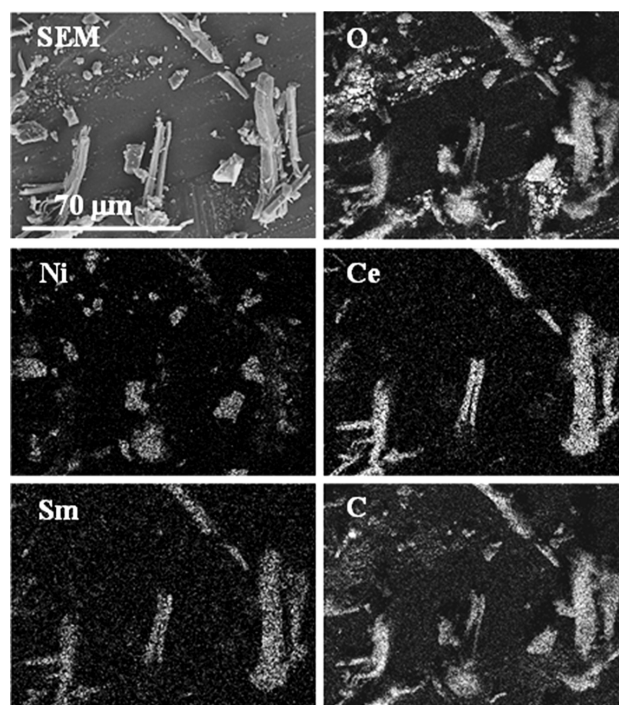


Figure 7: X-ray surface mapping of Sample 2

Slika 7: Elementna porazdelitev vzorca 2

from Rietveld refinement for both NiO and SDC were larger in Sample 2 than in Sample 3. This was evidently caused by the milling in the attritor. On the other hand, the milling of Sample 3 improved the fit between the calculated and measured curves (**Figures 1 and 2**) due to the grinding of larger grains.

The results of the ICP analysis depend on the treatment of the material before the analysis. This includes homogenization, weighing, dissolving and diluting.

Consequently, if the element contents in the samples submitted to the ICP analysis were higher than the recommended concentrations, multiple diluting was necessary, which eventually caused a deviation from the calculated values. Furthermore, the standard deviation of the ICP results for the analyzed samples could not be defined due to an insufficient number of the analysis repeats. Such repeats of the ICP analyses would have increased the costs.

4 CONCLUSION

Based on various analytical approaches to the analyzed samples used in the process of the final-material development, the following conclusions can be drawn:

The gravimetry and volumetry methods are rather time-consuming showing fairly accurate values in the chosen concentration range; however, both methods can be used only for determining the Ni content. The gravimetry shows better results.

Although the topographies of the prepared samples were not ideal for an X-ray microanalysis, one of the

aims of this work was to demonstrate the feasibility of the quantitative EDS analysis of the selected system. While the Ni content could be determined accurately, the Sm content was generally estimated too low and the Ce content too high due to the overlapping of the Ce and Sm peaks, making the EDS quantification heavily dependent on the method used for deconvoluting the spectrum.

The XRD quantitative analysis using the Rietveld method gave us, in a fast, easy and relatively inexpensive way, the mass contents for all three metals that are in agreement with the expected calculated values within the experimental error. The standard deviations are comparable to those of SEM-EDS and higher in comparison with the volumetry or gravimetry. The advantage of this method was also that the effect of milling on the crystallite-size parameter could be observed and the qualitative-phase analysis checked. The disadvantages of this method are that it requires the knowledge of the structures of all the present crystalline phases and that the obtained mass contents may not be representative for the whole sample, when a significant amount of an amorphous phase is present in the sample.

The instrumental ICP-OES method may be considered to be accurate for all three samples. However, the possibility of an analytical error becomes greater if the concentration of the components is higher than 1 % due to the necessary sample dilution. In addition, ICP-OES is a rather costly method.

In general, to reliably determine the contents of all three metals, we recommend a combination of gravimetry with the alternative instrumental methods (ICP, SEM-EDS and XRD) that also determine cerium and samarium.

Acknowledgement

We thank the Ministry of Education, Science, Culture and Sport of the Republic of Slovenia for the financial support provided through grants P1-0175-103, P1-0A5-103 and the Center of Excellence for Low-Carbon Technologies (CO NOT).

5 REFERENCES

- ¹ H. Uchida, S. Suzuki, M. Watanabe, *Electrochemical and Solid State Letters*, 6 (2003), A174–A177
- ² M. Backhus-Ricoult, *Solid State Sciences*, 10 (2008), 670–688
- ³ M. Chen, B. H. Kim, Q. Xu, B. G. Ahn, D. P. Huang, *Solid State Ionics*, 181 (2010), 1119–1124
- ⁴ Z. Wang, M. Mori, T. Itoh, *ECS Transactions*, 35 (2011), 1631–1640
- ⁵ H. Yoshida, H. Deguchi, M. Kawano, K. Hashino, T. Inagaki, H. Ijichi, M. Horiuchi, K. Kawahara, S. Suda, *Solid State Ionics*, 178 (2007), 399–405
- ⁶ J. B. Wang, J. C. Jang, T. J. Huang, *Journal of Power Sources*, 122 (2003), 122–131
- ⁷ R. Maric, S. Ohara, T. Fukui, T. Inagaki, J. Fujita, *Electrochemical and Solid-State Letters*, 1 (1998), 201–203
- ⁸ Y. Okawa, Y. Hirata, *Journal of the European Ceramic Society*, 25 (2005), 473–480
- ⁹ I. M. Kolthoff, P. J. Elving, *Treatise on analytical chemistry, Part II, Analytical chemistry of the elements, Vol. 2, Ga-In-Tl, Si, Ge, Fe, Co, Ni*, John Wiley & Sons, New York- London 1962, 377–440
- ¹⁰ E. Merck, *Complexometric Assay Methods with Titriplex[®]*, 3rd ed., Darmstadt 1979, 46–47
- ¹¹ H. A. Flaschka, *EDTA titrations: An introduction to theory and practice*, Pergamon Press, New York 1959
- ¹² J. J. Friel, C. E. Lyman, *Microscopy and Microanalysis*, 12 (2006), 2–25
- ¹³ J. Goldstein, *Scanning Electron Microscopy and X-Ray Microanalysis*, Springer, New York 2003
- ¹⁴ Topas2.1: *Advanced X-Ray solutions*, Bruker AXS, Karlsruhe, Germany 2003
- ¹⁵ G. Brauer, H. Gradinger, *Zeitschrift fuer Anorganische und Allgemeine Chemie*, 276 (1954), 209–226
- ¹⁶ N. G. Schmahl, J. Barthel, G. F. Eikerling, *Zeitschrift fuer Anorganische und Allgemeine Chemie*, 332 (1964), 230–237
- ¹⁷ A. J. Darbandi, T. Enz, H. Hahn, *Solid State Ionics*, 180 (2009), 424–430
- ¹⁸ V. A. C. Haanappel, J. Mertens, J. Malzbender, *Short communication, Journal of Power Sources*, 171 (2007), 789–792
- ¹⁹ M. Stanislawski, J. Froitzheim, L. Niewolak, W. J. Quadackers, K. Hilpert, T. Markus, L. Singheiser, *Journal of Power Sources*, 164 (2007), 578–589
- ²⁰ L. Saravanan, A. Pandurangan, R. Jayavel, *Materials Letters*, 66 (2012), 343–345
- ²¹ D. A. Skoog, D. M. West, E. J. Holler, S. R. Crouch, *Fundamentals of Analytical Chemistry*, 8th ed., Brooks/Cole, USA 2004
- ²² T. Skalar, J. Maček, A. Golobič, *Journal of the European Ceramic Society*, 32 (2012), 2333–2339
- ²³ D. Lau, A. E. Hughes, T. H. Muster, T. J. Davis, A. M. Glenn, *Microscopy and Microanalysis*, 16 (2010), 13–20

PRODUCING ANTIBACTERIAL SILVER-DOPED HYDROXYAPATITE POWDERS WITH CHEMICAL PRECIPITATION AND RESHAPING IN A SPRAY DRYER

IZDELAVA S SREBROM DOPIRANEGA PROTIBAKTERIJSKEGA PRAHU HIDROKSIAPATITA S KEMIJSKIM IZLOČANJEM IN PREOBLIKOVANJEM V RAZPRŠILNEM SUŠILNIKU

Fatih Erdem Baştan, Yıldız Yaralı Özbek

Sakarya University, Engineering Faculty, Department of Metallurgy and Materials Engineering, 54187 Esentepe-Sakarya, Turkey
febastian@sakarya.edu.tr

Prejem rokopisa – received: 2012-09-28; sprejem za objavo – accepted for publication: 2012-12-18

Hydroxyapatite is used for fixing orthopedic prostheses and it has reached a significant level of clinical application. It is important to prevent the initial bacterial colonization of the existing colonies. Silver has been known to exhibit a strong cytotoxicity towards a broad range of microorganisms. In this study, the aim was to produce antibacterial silver-doped hydroxyapatite powders and to reshape them in a spray dryer. Mole fraction of silver 1 % was added to the hydroxyapatite structure with the ion-exchange technique. *E. coli* bacteria were used for investigating the powder antibacterial specimens. Different temperatures and a pressure of 1.5 bar were used for shaping them in a spray dryer. Scanning electron microscopy (SEM), X-ray diffraction (XRD), Energy-dispersive X-ray spectroscopy (EDX) and a bacterial test were used to characterize the powder specimens.

Keywords: hydroxyapatite, spray dryer, silver-doped hydroxyapatite, antibacterial HAP

Hidroksiapatit se uporablja za pritrditev ortopedskih protez in se množično uporablja na klinikah. Pomembno je preprečiti začetno bakterijsko kolonizacijo obstoječih kolonij. Za srebro je poznano, da izkazuje močno citotoksičnost v širokem spektru mikroorganizmov. Namen te študije je bila izdelava protibakterijskega, s srebrom dopiranega prahu iz hidroksiapatita in njegovo preoblikovanje v pršilnem sušilniku. Molski delež srebra 1 % je bil dodan v strukturo hidroksiapatita z metodo izmenjave ionov. Za preiskavo protibakterijskega prahu je bila uporabljena bakterija *E. coli*. Za preoblikovanje v pršilnem sušilniku so bile uporabljene različne temperature in tlak 1,5 bar. Za karakterizacijo vzorcev prahu so bile uporabljene: vrstična elektronska mikroskopija (SEM), rentgenska difrakcija (XRD), energijsko disperzijska rentgenska spektroskopija (EDX) in bakterijski preizkus.

Ključne besede: hidroksiapatit, razpršilni sušilnik, s srebrom dopiran hidroksiapatit, protiobakterijski sintetični hidroksiapatit

1 INTRODUCTION

Inorganic biomaterials based on calcium orthophosphate have a wide range of applications in medicine. Among them, synthetic hydroxyapatite (HAP, $\text{Ca}_{10}(\text{PO}_4)_6(\text{OH})_2$) is the most promising one because of its biocompatibility, bioactivity and osteoconductivity. Hydroxyapatite has been used to fill a variety of bone defects in orthopedic and maxillofacial surgeries and in dentistry.¹ Hydroxyapatite [HAP, $\text{Ca}_{10}(\text{PO}_4)_6(\text{OH})_2$] is the main mineral constituent of a human bone.² This material does not possess acceptable mechanical properties to be used as a bulk biomaterial; however, it does demonstrate a significant potential to be used as a coating on metallic orthopedic and dental prostheses.³

Post-surgical infections associated with the presence of implant materials are found with up to 5 % of patients; the problem usually requires their removal. Microorganism adhesions on implant surfaces represent the initial crucial reason for an infection and lead to the formation of a biofilm, whose microorganisms are more resistant to antimicrobial agents. To solve the problem of contaminating the hydroxyapatite, it has been proposed

to use antimicrobial agents such as antibiotics, fluoride and biocide metal ions. The main concerns with antibiotics are the development of resistant microorganisms and the fact that the adsorbed antibiotics are quickly washed out by the body fluids so that they cannot prevent post-surgical infections in the long term. Metal ions (Ag^+ , Cu^{2+} and Zn^{2+}) are widely used in medicine as antimicrobial agents. Silver ions, in particular, show an oligodynamic effect with a minimum development of the microorganism resistance.⁴⁻⁶

Compared with the other heavy-metal ions, silver has demonstrated a high antimicrobial activity while maintaining a relatively low cytotoxicity.⁶⁻⁸ Silver ions are highly active ions that are strongly bound to the electron donor groups containing sulphur, oxygen or nitrogen. In the case of the biological molecule components such as thio, amino, imidazole, carboxylate and phosphate, the groups contain these electron donors.⁷ Studies have shown that Ag^+ ions are able to penetrate a bacterial cell wall and cause DNA to transform to a condensed form that reacts with the thiol-group proteins resulting in a cell death. It was also found that silver ions are able to interfere with the replication process. It has been demon-

strated that the higher the level of silver incorporated into a material, the better is the antimicrobial effect, but it comes at the cost of an increased cytotoxicity.⁸ Therefore, it is a good idea to incorporate a secondary chemical to alleviate the potential negative effects, while maintaining optimum antimicrobial properties of Ag.⁷ Silver-doped ceramics have a high chemical durability and antibacterial activity.³ Several *in vitro* studies reported that the silver ions in the HAP coatings play an important role in preventing or minimizing the initial bacterial adhesion.⁷

Spray drying can be defined as a transformation of a material from the fluid state into a dried particulate form by spraying the feed into a hot-drying gas medium.⁹ The uniformity of the shape and the diameter of the particles is the main advantage of spray drying.¹⁰ The aims of spray drying are the granulation of the solid phase in spherical, monodispersed, high-density aggregates and a quick, effective recovery of the production.¹¹

In this study, we have produced antibacterial silver-doped hydroxyapatite powders and reshaped them in a spray dryer. 1 % silver was added to the hydroxyapatite structure with the ion-exchange technique. We have investigated the effect of adding silver to a hydroxyapatite powder.

2 EXPERIMENTAL PROCEDURE

In this study, the chemical-precipitation method was chosen for producing silver-doped hydroxyapatite. Calcium nitrate tetra hydrate ($\text{Ca}(\text{NO}_3)_2 \cdot 4\text{H}_2\text{O}$, extra pure, Merck), orthophosphoric acid (H_3PO_4 , 85 %, Merck), ammonium hydroxide (NH_4OH , 28–30 %, Merck) and silver nitrate (AgNO_3 , crystalline, 99.9+ %, Alfa Aesar) were used as raw materials. Calcium nitrate, orthophosphoric acid and silver nitrate were dissolved separately in deionised water. Dissolved silver nitrate was added into the calcium nitrate solution. Finally, orthophosphoric acid was added. Ammonium hydroxide was added to fix the pH to 10–11. The pH affected the hydroxyapatite crystallinity.¹² The solution was mixed for 24 hours. After the precipitation, hydroxyapatite was washed with deionised water when filtered from the solution, then it was dried in a furnace at the temperature of 105 °C. The powders were sintered at the temperature

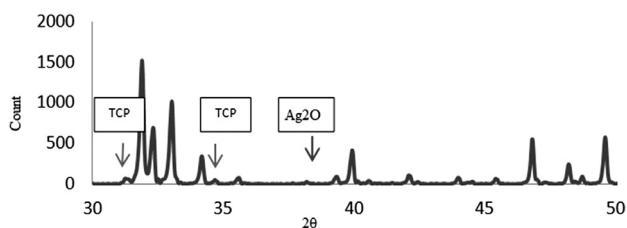


Figure 1: XRD peaks after sintering (TCP: tricalcium phosphate, Ag_2O : silver oxide)

Slika 1: XRD-vrhovi po sintranju (TCP: trikalcij fosfat, Ag_2O : srebrov oksid)

of 1050 °C for 1 h under the 10 °C/min sintering regime. Dried powders were prepared for drying with deionised water. The inlet temperatures of 175 °C, 190 °C and 205 °C and a pressure of 1.5 bar were used for drying. 1 % silver was added to the hydroxyapatite structure. The plate-count test and *E. coli* colonies were used for the antibacterial activity.

3 RESULT AND DISCUSSION

3.1 XRD results

It is seen in **Figure 1** that tricalcium phosphate and silver oxide were in the powder structure. Hydroxyapatite decomposes when heated to form β -TCP.¹¹ The

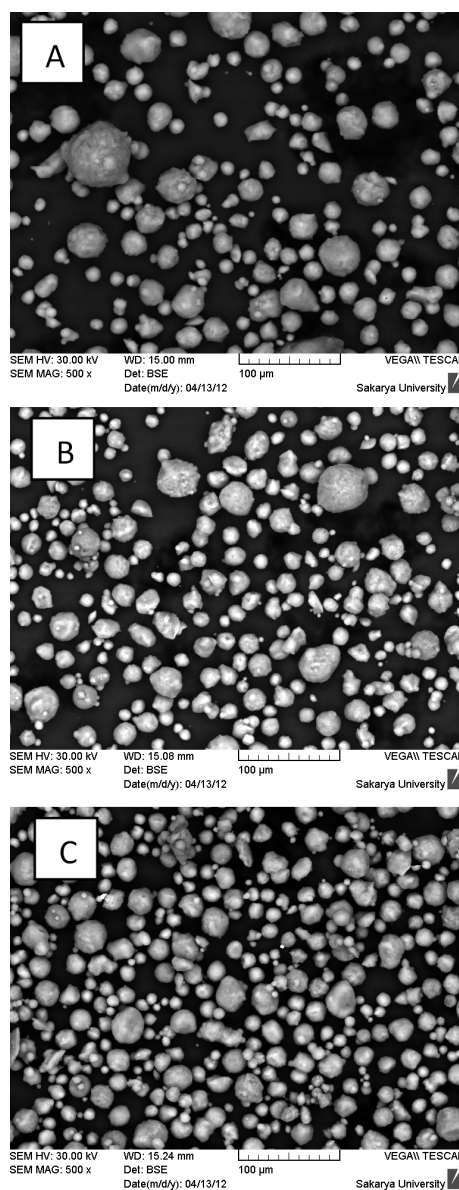


Figure 2: SEM images of the powders after spray drying at the inlet temperatures: a) 175 °C, b) 190 °C, c) 205 °C

Slika 2: SEM-posnetki prahov po razpršilnem sušenju pri vstopni temperaturi: a) 175 °C, b) 190 °C, c) 205 °C

secondary phases such as α -tricalcium phosphate and β -tricalcium phosphate were also found in the coatings to a small extent. The phases that are undesired such as tetra-tricalcium phosphate (TTCP) and calcium oxide (CaO) were absent. In the samples that contained Ag_2O , a characteristic Ag_2O (101) peak was observed as well as the peak shifts, indicating an effective incorporation of Ag_2O into the apatite structure.^{13,14}

Metallic silver precipitates silver oxide according to the potential-pH diagram in an aqueous solution.¹⁵ All the other peaks are hydroxyapatite peaks.

3.2 SEM results

However, the shapes of the powders are not totally spherical, though they are close to a spherical shape. The shape is an important phenomenon for the flowability and apparent density. When the inlet temperature was 205 °C, all the products were dried with the heat energy. At the other temperatures (175 °C and 190 °C), the problem was that the powders tended to stick together because of the moisture. It is seen in **Figure 2** that the temperature is an important factor affecting the particle size. Using high heat energy, particles were dried very quickly. Hence, the particle size decreased.

3.3 Particle-size-analysis results

It is seen in **Figure 3** that the average particle size was 37 μm for A and 28 μm for B. The particle size decreased with the increasing temperature. High energy

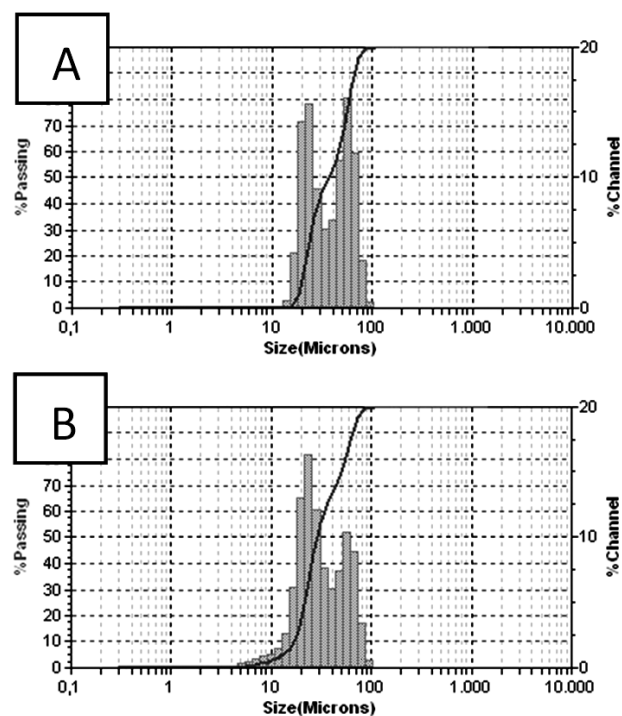


Figure 3: Analysis of the particle-size distribution after spray drying (inlet temperatures: a) 190 °C, b) 205 °C)

Slika 3: Šušenje po razprševanju. Analiza razporeditve velikosti zrn (vstopna temperatura: a) 190 °C, b) 205 °C).

provided quick drying and small particles were produced. Powder diameters after spray drying were recorded in **Table 1**.

Table 1: Mean diameters after spray drying (analyzed with a Microtrac S3500)

Tabela 1: Srednji premer zrn po razpršilnem sušenju (analizirano z Microtrac S3500)

Mean diameters	190 °C inlet temperature	205 °C inlet temperature
d10	19.89 μm	16.91 μm
d50	37.08 μm	28.52 μm
d90	67.13 μm	65.40 μm

It is clear from **Table 1** that the higher temperature led to a smaller particle size for all the mean diameters (d10, d50, d90).

3.4 Antibacterial-test results

Figure 4a shows that there are 63+ bacterial colonies in the medium and there are no bacterial colonies in the medium in **Figure 4b**. The hydroxyapatite powders with a 1 % silver addition show a 100 % antibacterial activity. Silver inhibited the growth of bacterial colonies. On the other hand, the amount of silver is important with respect to biocompatibility as an increased amount of silver

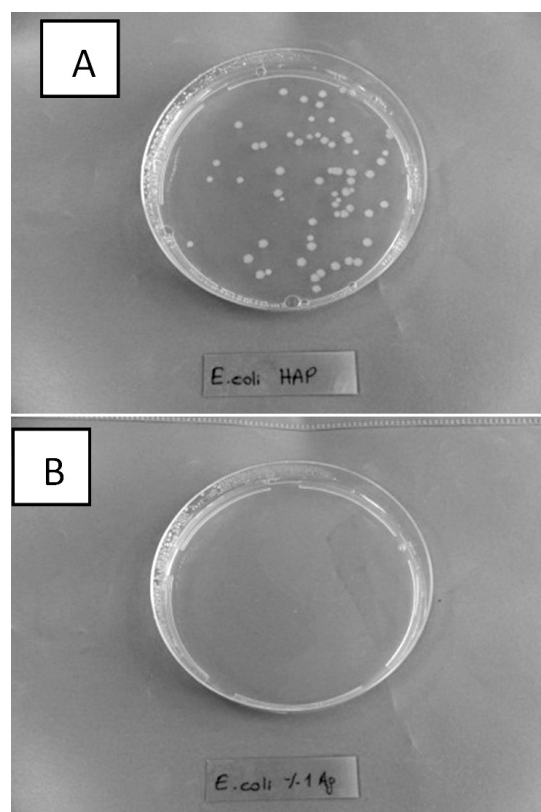


Figure 4: After the antibacterial test: a) no additive to hydroxyapatite, b) 1 % mol fraction Ag added to hydroxyapatite

Slika 4: Po protibakterijskem preizkusu: a) hidroksiapatit brez dodatkov, b) hidroksiapatit z dodanim molskim deležem 1 % Ag

causes a decrease in biocompatibility. A high content of silver leads to a poor biocompatibility because the alkaline phosphatase activity of osteoblasts increases.^{16,17}

It was reported that the toxicity of Ag ions affected the basic metabolic cellular functions common to all the specialized mammalian cells. A concentration- and time-dependent depletion of the intracellular ATP content was attributed to the presence of Ag ions, thereby compromising the cell energy charge that precedes the cell death. Therefore, it is prudent to incorporate a minimum amount of Ag on the implant surfaces to adequately reduce the bacterial adhesion as well as minimizing the tissue cytotoxicity.¹⁸

4 CONCLUSION

HA coating materials have been well studied as osteogenic enhancing materials and are effectively used in several medical and dental applications. In this study, the silver-doped hydroxyapatite was produced and reshaped in a spray dryer. The shaping is very important in the coating application because the shape affects the fluidity.

The hydroxyapatite structure decomposed into hydroxyapatite and tricalcium phosphate phases at a high temperature. It was seen that the hydroxyapatite powders including silver show a 100 % antibacterial effect. So, we were able to effectively enhance the coating with sustainable, long-term antimicrobial properties, while minimizing the negative cytoplasmic effects on the osteoblast cells.

5 REFERENCES

- ¹ H. F. Lin, L. Chun-Jen, C. Ko-Shao, Thermal reconstruction behavior of the quenched hydroxyapatite powder during reheating in air, *Materials Science and Engineering: C*, 13 (2000) 1–2, 97–104
- ² C. F. Koch, S. Johnson, D. Kumar, Pulsed laser deposition of hydroxyapatite thin films, *Materials Science and Engineering: C*, 27 (2007) 3, 484–494
- ³ S. Johnson, M. Haluska, R. J. Narayan, In situ annealing of hydroxyapatite thin films, *Materials Science and Engineering: C*, 26 (2006) 8, 1312–1316
- ⁴ V. Stanić, D. Janačković, S. Dimitrijević, S. B. Tanasković, M. Mitić, M. S. Pavlović, A. Krstić, D. Jovanović, S. Raičević, Synthesis of Antimicrobial Monophase Silver-Doped Hydroxyapatite Nanopowders for Bone Tissue Engineering, *Applied Surface Science*, 257 (2011) 9, 4510–4518
- ⁵ L. Harris, R. Richards, Staphylococci and implant surfaces: a review, *Injury*, 37 (2006), S3–S14
- ⁶ A. Montali, Antibacterial coating systems, *Injury*, 37 (2006), S81–S86
- ⁷ G. A. Fielding, M. R. Bandyopadhyay, A. S. Bose, Antibacterial and biological characteristics of silver containing and strontium doped plasma sprayed hydroxyapatite coatings, *Acta Biomaterialia*, 8 (2012) 8, 3144–3152
- ⁸ K. Gross, Hydroxyapatite – Synthesis of Hydroxyapatite Powders, *Journal of Biomedical Materials Research*, 62 (2002) 2, 228–236
- ⁹ V. Stanic, D. Janackovic, S. Dimitrijevic, Synthesis of antimicrobial monophase silver-doped hydroxyapatite nanopowders for bone tissue engineering, *Applied Surface Science*, 257 (2011) 9, 4510–4518
- ¹⁰ H. Jeon, S. Yi, S. Oh, Preparation and antibacterial effects of Ag-SiO₂ thin films by sol-gel method, *Journal of Materials Science*, 42 (2007) 24, 10085–10089
- ¹¹ A. L. R. Rattes, W. P. Oliveira, Spray drying conditions and encapsulating composition effects on formation and properties of sodium diclofenac microparticles, *Powder Technology*, 171 (2007) 1, 7–14
- ¹² J. M. Gac, L. Gradon, A distributed parameter model for the spray drying of multicomponent droplets with a crust formation, *Advanced Powder Technology*, 24 (2013) 1, 324–330
- ¹³ M. Serantoni, P. Piancastelli, A. L. Costa, L. Esposito, Improvements in the production of Yb:YAG transparent ceramic materials: Spray drying optimisation, *Optical Materials*, 34 (2012) 6, 995–1001
- ¹⁴ A. K. Nayak, Hydroxyapatite Synthesis Methodologies: An Overview, *International Journal of ChemTech Research*, 2 (2010) 2, 903–907
- ¹⁵ V. V. Skorokhod, S. M. Solonin, V. A. Dubok, L. L. Kolomiets, Decomposition Activation of Hydroxyapatite in Contact with β -Tricalcium Phosphate, *Powder Metallurgy and Metal Ceramics*, 49 (2010), 324–329
- ¹⁶ M. Diaz, F. Barba, M. Miranda, F. Guitian, R. Torrecillas, J. S. Moya, Synthesis and Antimicrobial Activity of a Silver-Hydroxyapatite Nanocomposite, *Journal of Nanomaterials*, (2009), doi: 10.1155/2009/498505
- ¹⁷ J. Qu, X. Lu, D. Li, Silver/hydroxyapatite composite coatings on porous titanium surfaces by sol-gel method, *Journal of Biomedical Materials Research Part B: Applied Biomaterials*, 97B (2011) 1, 4048
- ¹⁸ W. Chen, Y. Liu, H. S. Courtney, M. Bettenga, C. M. Agrawal, In vitro anti-bacterial and biological properties of magnetron co-sputtered silver-containing hydroxyapatite coating, *Biomaterials*, 27 (2006) 32, 5512–5517

TRIBOCORROSION DEGRADATION OF PROTECTIVE COATINGS ON STAINLESS STEEL

TRIBOKOROZIJSKA DEGRADACIJA ZAŠČITNIH PREVLEK NA NERJAVNEM JEKLU

Darja Kek Merl, Peter Panjan, Miha Čekada, Peter Gselman, Srečko Paskvale

Jožef Stefan Institute, Jamova 39, 1000 Ljubljana, Slovenia
darja.kek@ijs.si

Prejem rokopisa – received: 2012-10-12; sprejem za objavo – accepted for publication: 2012-12-18

Wear, erosion, corrosion and other forms of material deterioration lead to a significant decrease in the performance of industrial production and thus increase the production cost. The PVD protective coatings based on nitrides, carbides and oxides of transitional metals have been developed in order to reduce these problems. Further progress in this field, however, depends on the understanding of the surface and interface effects, especially in the case of tribocorrosion when degradation of materials results from a combination of tribological and electrochemical processes.

This work focuses on the methodology that allows one to conduct the sliding wear and corrosion tests simultaneously and to follow in situ the degradation processes of the coating systems by controlling (in real time) the friction coefficient, corrosion current and corrosion potential. Using practical examples from the area of biomedical applications, i.e., the stainless-steel 316L substrate and the stainless-steel substrate protected with the TiAgN and TiSiN hard coatings, it is shown that tribocorrosion experiments can be used to design and predict the properties of new coatings with an enhanced performance and stability.

Keywords: tribocorrosion, PVD coatings, stainless steel, ball-on-disc, electrochemical method

Obraba, erozija, korozija in druge oblike degradacije materiala vodijo do manjše produktivnosti in s tem do večjih stroškov proizvodnje. Da bi zmanjšali omenjene težave, so bile razvite različne PVD-prevleke. Nadaljnji napredek na tem področju je odvisen od razumevanja procesov na površinah in faznih mejah, še posebej v primeru tribokorozijske degradacije materiala zaradi triboloških in elektrokemijskih procesov.

V delu se osredinjamo na metodologijo, ki omogoča hkrati merjenje parametrov drsne obrabe (npr. koeficienta trenja) in elektrokemijskih parametrov (korozijski potencial, korozijski tok). Tako lahko in-situ spremljamo degradacijo prevlek ali pasivne plasti na pasivnih kovinah. Na praktičnih primerih tribokorozijskih preizkusov (dveh prevlek TiAgN in TiSiN ter podlage 316L) smo pokazali, da je mogoče tribokorozijske preizkuse uporabljati za načrtovanje in napovedovanje lastnosti prevlek z optimalnimi lastnostmi.

Ključne besede: tribokorozijska, PVD-prevleke, nerjavno jeklo, pin-on-disc, elektrokemijske metode

1 INTRODUCTION

Wear and corrosion of materials are the most important failure mechanisms in industry.¹ Significant efforts have been made to combat wear and corrosion. Hard coatings such as nitrides and carbides are successful examples in protecting surface against dry wear.^{1,2} Passivation techniques were shown to improve significantly the corrosion properties of passive materials.^{3,4} However, when wear and corrosion are involved simultaneously, the synergistic action of wear and corrosion may deteriorate the performance of the materials. For instance, hard coatings may perform poorly in a corrosive medium due to defect growth.⁵⁻⁷ On the other hand, corrosion-resistant materials, such as stainless steels and titanium alloys, may lose their corrosion resistance and corrosive-wear conditions as the passive layer continuously abrades away by wear.⁸⁻¹⁰

In general, tribocorrosion is defined as a degradation of materials that results from a combination of tribological and electrochemical processes.^{11,12} The material-degradation rate, whether expressed as a loss in the component performance or a loss in the material, is very often higher than the sum of the rates of corrosion and

wear acting separately. The synergy of corrosion and wear is still poorly understood due to the complexity of the problem and a lack of appropriate experimental techniques. The material resistance to tribocorrosion is very often evaluated using the conventional wear testers such as pin-on-disc and simply immersing the contact in a specific electrolyte. These testers can be used to rank the materials but not to investigate the mechanism responsible for tribocorrosion. Until recently, no effective analytic methods have been available to investigate the separate roles of the wear and corrosion in the corrosive wear, which are crucial for understanding the corrosive-wear synergy. Currently, in industry, the selection of the material to resist corrosive wear is mainly based on experience and trial-and-error testing. Therefore, it is useful to develop the guidelines for materials selection and design.

In this paper, we present the characterization of material resistance to tribocorrosion. Electrochemical techniques are combined with tribological testing in order to assess the roles of wear and corrosion. Additionally, microhardness was measured.

2 EXPERIMENTAL WORK

Tribocorrosion experiments were conducted using a CSM tribometer with a pin-on-disc configuration. A special configuration of a cell (**Figure 1**) allowed us simultaneous measurements of the wear (the friction coefficient) and electrochemical parameters (open-circuit potential – OCP). The ball-sample contact was fully immersed in the test electrolyte. The sample served as the working electrode and its potential was measured with respect to a standard Ag/AgCl electrode. A platinum wire was used as the counter electrode.

The test electrolyte was Hank's solution which simulates the body fluid environment with the composition of NaCl 8 g/L, Na₂HPO₄ 0.0475 g/L, NaHCO₃ 0.35 g/L, KCl 0.5 g/L, KH₂PO₄ 0.06 g/L, MgCl₂ · 6H₂O 0.1 g/L, MgSO₄ · 7H₂O 0.10 g/L, CaCl₂ 0.18 g/L and 1 g/L glucose at pH = 7.2. As the test samples stainless-steel AISI 316L discs were used as the substrates with two types of coatings (TiAgN and TiSiN) deposited on the AISI 316L substrates.

The coatings (with the thickness of 1.6 μm for TiSiN and 1.9 μm for TiAgN) were deposited with the plasma-beam-sputtering technique in a Sputron (Balzers) apparatus. The polished stainless-steel samples (*R_a* = 25 nm) were used as substrates. The vacuum chamber was evacuated to the base pressure of approximately 2 mPa. The nitrogen (with the purity of 99.995 %) flow remained constant at 5 sccm. During the deposition the bias voltage was –30 V and the temperature not did not exceed 130 °C. For enhancement an adhesion layer of pure titanium (around 100 nm) was sputtered on the substrate at the beginning of the deposition.

The wear tests were conducted with an alumina ball sliding on the plate of a sample at a fixed normal load of 8 N. The sliding was performed for 1800 laps at a sliding radius of 2 mm. The corresponding Hertz contact pressure was around 1.5 GPa.

The hardness was measured using a Fischerscope H100 indenter with the loads of 10 mN to 1000 mN.

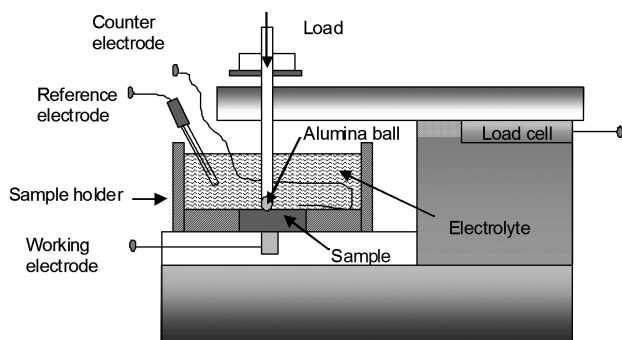


Figure 1: Scheme of the experimental cell that allowed us simultaneous measurements of wear (friction coefficient) and electrochemical parameters (open-circuit-potential – OCP)

Slika 1: Shema eksperimentalne celice, ki omogoča hkratno merjenje obrabnih in elektrokemijskih parametrov

3 RESULTS AND DISCUSSION

Tribocorrosion involves tribological and corrosion processes. Due to the synergistic interaction between them, the material loss can be larger than the sum of the losses due to the wear and corrosion acting separately. The total mass loss is expressed as:

$$M_{\text{tot}} = M_{\text{mech}} + M_c + M_{\text{syn}} \quad (1)$$

where M_{tot} is the total mass loss, M_{mech} is the mass loss due to the pure mechanical wear in the absence of corrosion, M_c is the mass loss due to the static corrosion in the absence of wear and M_{syn} is the mass loss due to the synergy effect. Friction and wear change the corrosion behavior of a material and vice-versa; corrosion may change the condition of friction.¹³ Therefore, M_{syn} can be expressed as the sum of the two components, M_{c-w} and M_{w-c} , where M_{c-w} is the increase in the corrosion loss due to a tribological action, called the wear-enhanced corrosion, and M_{w-c} is the increase in the mechanical wear due to the corrosion, called the corrosion-enhanced wear. Therefore, equation (1) can be expressed as:

$$M_{\text{tot}} = M_{\text{mech}} + M_c + M_{c-w} + M_{w-c} \quad (2)$$

M_{w-c} could be attributed to the inhomogeneous distribution of strain, defect and surface irregularities caused by the mechanical wear. In such a way micro-electrodes (cathodic and anodic places) are generated at the surface. This leads to an increase in the material dissolution. A destruction of the passive film by wear can also lead to the material dissolution. M_{c-w} is more relevant in coated substrates, where the electrolyte penetrates through the pores and defects in the coatings. These can lead to a reduction of the tribological properties of the substrate/coating system.

The tribocorrosion experiments were performed on the bare stainless-steel AISI316L substrate and on the samples coated with two nitride-based coatings. The

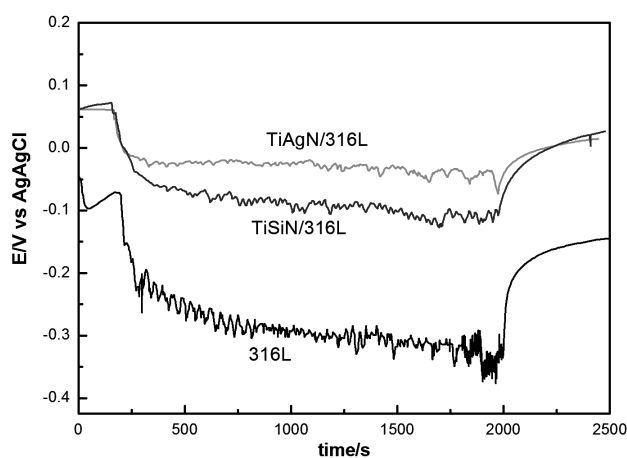


Figure 2: Evolution of the corrosion potential before, during and after the wear of the bare substrate and both coatings (TiAgN, TiSiN)

Slika 2: Spreminjanje korozijskega potenciala (OCP) pred obrabo, med njo in po njej za samo podlago in obe prevleki (TiAgN, TiSiN)

measurement consisted of monitoring the OCP before, during and after the sliding wear. The drop in the potential can be the result of the destruction of the protective passive layer due to the wear mechanism. After the sliding was stopped the corrosion potential increased. Therefore, the repassivation of the passive layer occurred.

Figure 2 shows the corrosion potential (OCP) evolution of the two coated stainless-steel samples and of the bare stainless-steel substrate in Hank's solution. For the bare substrate, the OCP dropped gradually to the lowest value of -375 mV vs Ag/AgCl after almost 1700 cycles of sliding. This gradual drop in the potential suggests a gradual removal of the oxide passive layer. When the sliding ceased, the OCP increased and progressively returned to its original value. Thus, the repassivation of the passive layer occurred. For the coated samples, the OCP dropped to reach the potential values of -80 mV vs Ag/AgCl for the TiAgN and of -110 mV vs Ag/AgCl for the TiSiN coatings. The drop in the potential on the bare substrate is the result of the destruction of the protective passive layer due to the wear mechanism. After the sliding was stopped the corrosion potential increased.

The explanation for the drop and increase in the potential for the coated substrates is not as straightforward as in the case of the bare substrate. In this case there is no formation of a passive layer on the inert nitride coating. The drop in the potential suggests a reduction in the corrosion properties of the substrate/coating system due to the penetration of the electrolyte through the pores and defects in the coatings, as explained before in equation (2) (M_{c-w} part). However, more data are needed to support this statement.

The evolution of the friction coefficient was analyzed during the sliding in Hank's solution for both coatings and the bare substrate. **Figure 3** shows the representative

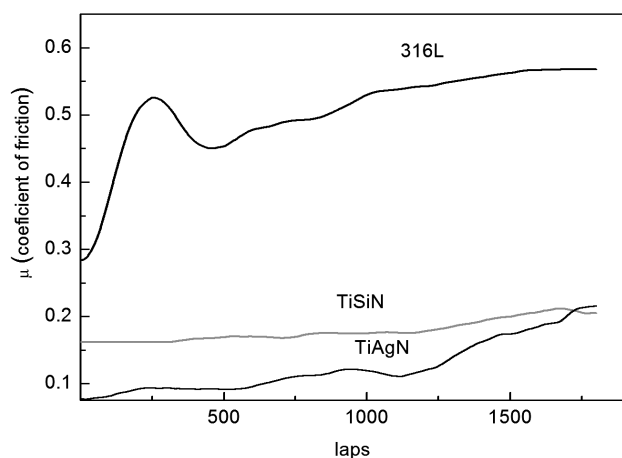


Figure 3: Evolution of the friction coefficient during the sliding in Hank's solution of the bare substrate and both coatings (TiAgN, TiSiN)

Slika 3: Spreminjanje koeficienta trenja med razenjem v Hankovi raztopini za podlago in obe prevleki (TiAgN, TiSiN)

curves of the observed trends. For the bare substrate, there was an increment in the values of the friction coefficients at the beginning of the sliding process (250 laps). After the initial running-in period, the value of the friction coefficient remains stable at around 0.6. The fluctuation in the value of the friction coefficient corresponds to the removal and regrowth of the passive layer.¹³ When the substrate was coated with TiSiN or TiAgN, the friction coefficient dropped by about five times to about 0.15. However, it should be pointed out, that for the TiAgN coatings the friction coefficient did not converge to a stable value during 1800 laps. An increase in the friction coefficient during the sliding was observed (**Figure 3**) for the TiAgN coating. Such behavior may be due to the formation of the corrosion products and wear debris during the sliding process, as also reported in literature.¹³ In general, the tribocorrosion parameters are not the material properties, but the properties of the system. Therefore, the friction coefficient depends on the sliding processes (i.e., parameters, electrolyte).

After the tribocorrosion test, the wear track was analyzed by a profilometer (**Figures 4 and 5**). **Figure 4** shows the average depths of the worn profiles on both coatings, TiAgN and TiSiN, and on the bare substrate. The depth of the worn profile was estimated and compared to the thickness of the coatings. The wear-track depth is around 0.70 μm for the bare substrate, 0.33 μm for the TiSiN coatings and 0.15 μm for the TiAgN coatings. Based on the results, we can find out if the coatings were removed completely or not after the tribocorrosion test. In the case of the TiSiN coatings 20 % was removed, while only 8 % of the TiAgN coatings were removed. This shows that the current systems (when the coating and the substrate are considered) exhibit good tribocorrosion properties.

Hardness is one of the key mechanical properties of the protective coatings. However, the result obtained with the measurement strongly depends on the load

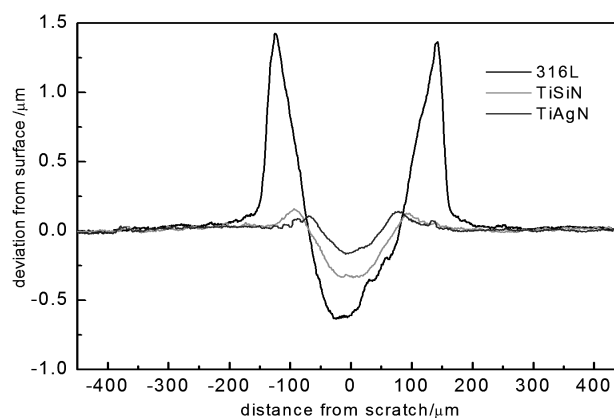


Figure 4: Average depth profile after the tribocorrosion experiment of the bare substrate and both coatings (TiAgN, TiSiN)

Slika 4: Povprečni globinski profil podlage in obeh prevlek (TiAgN, TiSiN) po tribokorozijskem preizkušanju

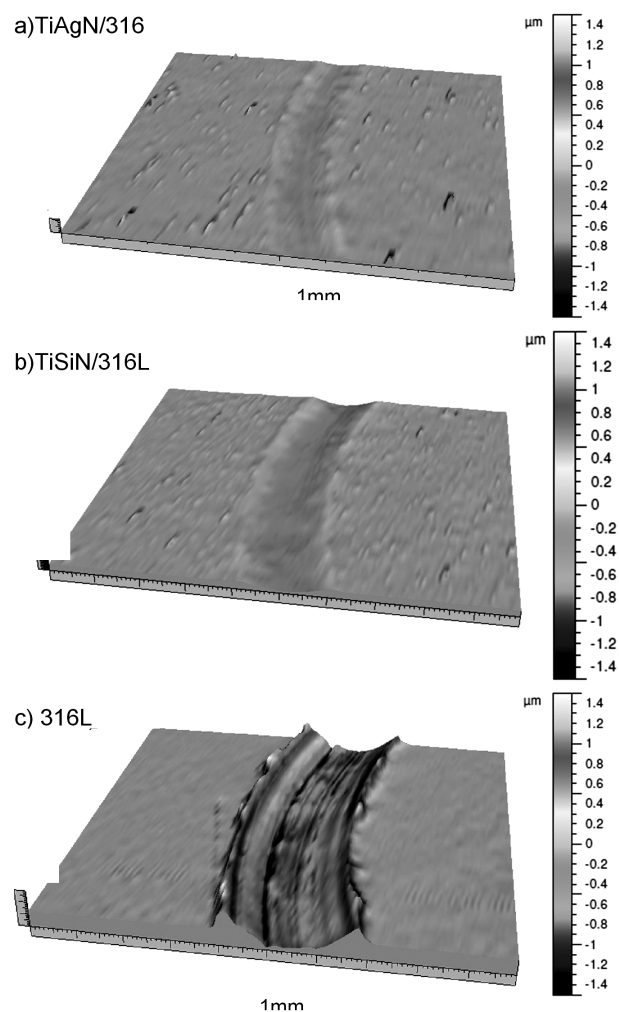


Figure 5: 3D micrographs of the wear tracks after tribocorrosion experiments for the bare substrate and both coatings

Slika 5: 3D globinski profil raze podlage in obeh prevlek (TiAgN, TiSiN) po tribokorozijskem preizkušanju

applied, as well as on the sample preparation. At smaller loads there is no substrate influence on the hardness (when the indentation depth is less than about 10 % of the coating thickness). Therefore, only the coating properties are measured. At higher loads, on the other hand, the substrate influence comes into sight. In our case, the measurements were taken at the applied loads from 10 mN to 100 mN. It should be noted, that, at a lower load, the error of the measurement grows because of various surface affects (roughness, defects, inhomogeneities, tip irregularities, etc.).

Figure 6 presents the hardness in dependence of the relative indentation depth (RID) for both coatings in the load range from 10 mN to 100 mN. The relative indentation depth is computed by dividing the indentation depth by the coating thickness of the corresponding system.¹⁴ The hardness of the bulk substrate was determined to be 200 HV. The hardness, measured at the 10 mN load reached the value of around 3800 HV for the TiSiN coating, and 2900 HV for the TiAgN coatings.

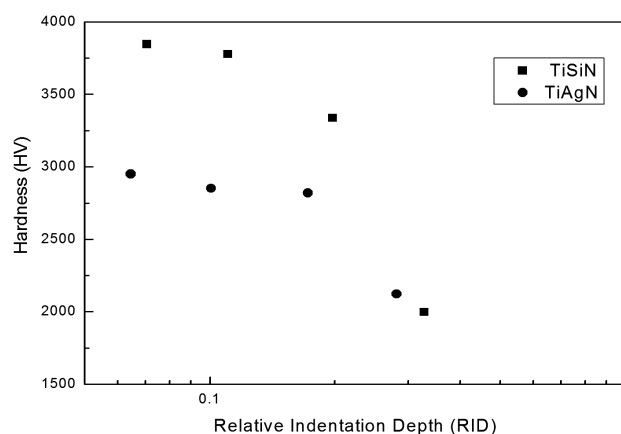


Figure 6: Vickers hardness as a function of the relative indentation depth (RID) for both coatings at the loads from 10 mN to 100 mN

Slika 6: Trodota po Vikersu v odvisnosti od relativnega globinskega profila (RID) za obe prevleki (TiAgN, TiSiN) pri obremenitvi od 10 mN do 100 mN

Thus, with a coating deposition the surface hardness increases by almost 20-fold. However, the highest value of the surface hardness does not imply the best wear resistance. One possible reason why TiSiN exhibits a lower wear resistance than TiAgN is the presence of the hard Si_3N_4 particles that increase the wear.

4 CONCLUSION

In this paper, the hardness and tribocorrosion characterization of the TiAgN and TiSiN coatings and bare stainless-steel substrate was performed. Electrochemical techniques were combined with friction tests to understand the synergy between wear and corrosion.

For the bare substrate, the drop in the potential is the result of the destruction of the protective passive layer due to the wear mechanism. After the sliding was stopped the corrosion potential increased. Therefore, a repassivation of the oxide layer occurred. The friction coefficient of the bare substrate and the depth of the wear track exhibit the wear resistance that is five times lower than that of the coated substrate.

For the TiAgN and TiSiN coatings, the drop in the potential during the wear suggests a reduction in the corrosion properties of the substrate/coating system due to the penetration of the electrolyte through the pores and defects in the coatings. Both coatings improved the tribocorrosion and mechanical stability compared to the bare stainless-steel substrate. The TiAgN coating exhibits a better wear resistance than the TiSiN coating, although the surface hardness of the TiSiN coating is higher than that of the TiAgN coatings.

Acknowledgements

The work was supported by the Slovenian Research Agency – ARRS (project L2-4173 and research program P2-0082).

5 REFERENCES

- ¹ P. Panjan, M. Cekada, D. K. Merl, M. Macek, B. Navinsek, A. Jesih, A. Zalar, M. Jenko, *Vacuum*, 71 (2003), 261
- ² P. Panjan, I. Boncina, J. Bevk, M. Cekada, *Surf. Coat. Tech.*, 200 (2005), 133
- ³ Z. Bou-Saleh, A. Shahryari, S. Omanovic, *Thin Solid Films*, 515 (2007), 4727
- ⁴ A. Shahryari, F. Azari, H. Vali, S. Omanovic, *Acta Biomater.*, 6 (2010), 695
- ⁵ D. K. Merl, P. Panjan, M. Panjan, M. Cekada, *Plasma Process Polym.*, 4 (2007), S613
- ⁶ P. Gselman, T. Boncina, F. Zupanic, P. Panjan, D. K. Merl, M. Cekada, *Mater. Tehnol.*, 46 (2012) 4, 351–354
- ⁷ D. K. Merl, I. Milosev, P. Panjan, F. Zupanic, *Mater. Tehnol.*, 45 (2011) 6, 593–597
- ⁸ Y. Yan, A. Neville, D. Dowson, S. Williams, *Tribol. Int.*, 39 (2006), 1509
- ⁹ A. Igual Munoz, J. L. Casaban, *Electrochimica acta*, 55 (2010), 5428
- ¹⁰ N. Papageorio, S. Mishler, *Tribology Letter*, 48 (2012), 271
- ¹¹ J. P. Celis, P. Ponthiaux, F. Wenger, *Wear*, 261 (2006), 939
- ¹² D. Landolt, S. Mischler, M. Stemp, S. Barril, *Wear*, 256 (2004), 517
- ¹³ S. Mischler, *Tribol. Int.*, 41 (2008), 573
- ¹⁴ D. Beegan, S. Chowdhury, M. T. Laugier, *Thin Solid Films*, 516 (2008), 3813

BEHAVIOUR OF SHORT CRACKS EMANATING FROM TINY DRILLED HOLES

VEDENJE KRATKIH RAZPOK, KI NASTANEJO IZ MAJHNIH IZVRTIN

Vladimir Gliha¹, Pavlo Maruschak², Tomaž Vuherer¹

¹University of Maribor, Faculty of Mechanical Engineering, Smetanova 17, 2000 Maribor, Slovenia

²Ternopil Ivan Pul'uj National Technical University, Ruska 56, 46001 Ternopil, Ukraine
vladimir.gliha@um.si

Prejem rokopisa – received: 2012-10-15; sprejem za objavo – accepted for publication: 2012-11-27

Specimens with martensitic microstructure were defected by tiny drilled holes with the existing local residual stresses induced by drilling and without them. The objective of this research was to determine the cyclic stress level for the crack initiation and fatigue limit of the defected and smooth specimens' dependence upon the residual-stress field. Compressive residual stresses retarded the crack initiation. Immediately after the crack initiation, residual stresses decelerated the short-crack propagation, but later, when the residual-stress sign was changed, they accelerated it. Non-propagating short-crack size and fatigue limit also depend on the residual-stress field.

Keywords: small defect, drilled hole, crack initiation, crack propagation, short crack, long crack, anomalous fast-crack propagation

Pri preizkušanjih z martenzitno mikrostrukturo smo naredili majhne izvrtine z obstoječimi lokalnimi zaostalimi napetostmi zaradi vrtnanja in brez njih. Namen te raziskave je bilo določiti odvisnost ciklične napetosti, ki je potrebna za nastanek razpoke, in odvisnost trajne dinamične trdnosti z izvrtino oslabljenih in gladkih preizkušancev, od polja zaostalnih napetosti. Tlačne zaostale napetosti so zavrlje nastanek razpoke. Takoj po nastanku razpoke so zaostale napetosti upočasnile širjenje kratke razpoke, pozneje, ko se je predznak napetosti spremenil, pa so ga pospešile. Velikost kratke razpoke, ki se ne širi več, in trajna dinamična trdnost sta prav tako odvisni od polja zaostalnih napetosti.

Ključne besede: majhne napake, izvrtina, nastanek razpoke, širjenje razpoke, kratka razpoka, dolga razpoka, nenormalno hitro širjenje razpoke

1 INTRODUCTION

The phenomenon of crack initiation from small defects in metals caused by cyclic stress at a level lower than the fatigue limit, in connection with the initial fatigue-crack propagation to the size when it becomes a non-propagating crack is now well understood.¹⁻³ The hardness and the defect size are crucial for the fatigue limit of the metals with small defects.^{4,5} The measure of the defect size is the square root of its projection onto the plane of cyclic stress, i.e., the parameter $\sqrt{\text{area}}$. The measure of hardness is the HV number.

However, most of the experiments confirming the above-mentioned relation have been performed on specimens with small, three-dimensional, artificial surface defects. The effects of the eventual residual stresses due to the artificial defect preparation have not been taken into account. Of course, the local residual stresses induced by drilling, scratching, impressing, etc., affect the crack initiation and the initial fatigue-crack propagation. The latter is known as the short-crack propagation. Acceleration or retardation of a crack initiation and assistance or obstruction of the short-crack propagation are reflected in the sizes of the largest non-propagating cracks emanating from small defects.^{5,6}

The influence of the local residual stresses caused by Vickers-pyramid indenting in an artificially prepared martensitic microstructure on the crack initiation and subsequent propagation was the matter of our previous paper.⁷ We have found that these stresses play an important role in the crack initiation from Vickers indentations and its initial propagation. Actually, at the very beginning, the tensile residual stresses around both exposed corners of an indentation accelerate the initiation of two cracks along the edges. Later on, the compressive residual stresses around the top of the indentation retard the short-crack propagation along the edges in the direction towards the top. When both cracks are linked and become a single crack, which is larger than individual short cracks, it starts to behave as a long crack. Now, the tensile residual stresses around the corners accelerate the crack propagation at the surface. This large crack also assists the crack penetration into the depth. As a result, the indentations with present local residual stresses seem to be smaller than expected.^{4,7}

The experimental results of the crack initiation from tiny drilled holes, instead of Vickers indentations, as well as the fatigue limits of smooth and defected specimens with identical microstructures are shown in the present article. The stress level for the crack initiation was experimentally assessed. On the specimens in the as-drilled

condition, crack sizes at different stress levels were measured in order to analyse the effects of the residual-stress field on the short-crack-propagation rate.

2 EXPERIMENTAL WORK

2.1 Samples and specimen preparation

Samples of the material with martensite microstructure were used for experimental work. The chemical composition and the mechanical properties of this material are given in **Tables 1** and **2**.

Table 1: Chemical composition of the material (mass fractions, w%)

Tabela 1: Kemijska sestava materiala (masni deleži, w%)

C	Si	Mn	P	S	Cr	Ni	Cu	Mo	Al
0.18	0.22	0.43	0.012	0.028	1.56	1.48	0.15	0.28	0.023

Table 2: Mechanical properties of the material

Tabela 2: Mehanske lastnosti materiala

$R_{p0.2}$ / MPa	R_m / MPa	A_5 / %	Z / %	Impact toughness (at +20 °C)/J	Hardness/ (HV10)
1042	1431	15	56	72	463

A two-step heat treatment was used to create the microstructure of the samples. It is schematically shown in **Figure 1** (the solid line). The first stage of the heat treatment is long-lasting high-temperature annealing and water quenching (mark b), while the second stage is hardening by water quenching (d). The grains have grown during the annealing. The martensite transformation was a result of water quenching (**Figure 2**).

Cylinders were machined from the as-delivered steel 17CrNiMo7 (mark a). In the first sequence of the specimen preparation high-temperature annealing and quenching were applied (b), and then the cylinders were turned to produce grooved cylinders (c). The grooved area was fine polished.

The first sequence of the specimen preparation was the same for all the specimens. In the second sequence of

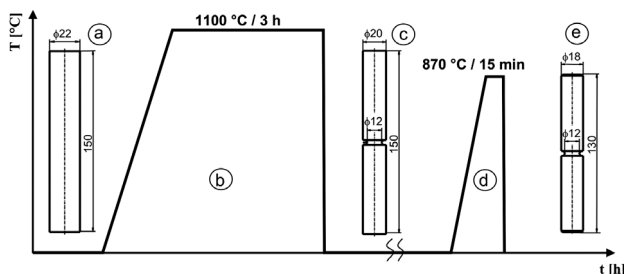


Figure 1: Procedure for the specimen preparation: a) cylinder machining, b) high-temperature annealing and quenching, c) thinning and machining a groove with $\rho = 2$ mm, d) hardening, e) specimen aligning by thinning and shortening

Slika 1: Postopek priprave preizkušancev: a) izdelava valja, b) visokotemperaturno žarjenje in kaljenje, c) tanjšanje in izdelava žleba z $\rho = 2$ mm, d) kaljenje, e) poravnavanje preizkušancev s tanjšanjem in krajšanjem

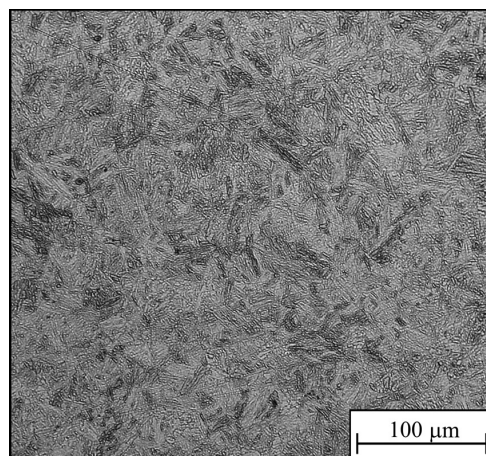


Figure 2: Microstructure of the material samples

Slika 2: Mikrostruktura vzorcev materiala

the specimen preparation, three different types of grooved cylinders were produced, i.e., type-I, type-II and type-III specimens.

- I. The grooved cylinders were hardened (d), while the surface at the bottom of the groove remained intact. The type I-specimens were smooth and in the residual-stress-free condition.
- II. Before hardening the cylinders were hole-drilled at the bottom of the groove. The diameter of the hole was 90 μm , while the depth was 45 μm . The local residual stresses induced by hole-drilling were relaxed due to heating over the A_{c3} temperature during the hardening (d). The type-II specimens were defect-free in the residual-stress-free condition.
- III. The hardening (d) was followed by groove polishing and hole drilling. Therefore, the local residual-stress field induced by drilling existed in the specimens. The type-III specimens were defect-free and were in the as-drilled condition.

The cylinders were slightly distorted after the second sequence of the specimen preparation. In order to avoid any possible influence on the stress level during the loading, the cylinders were turned, in the third sequence of the specimen preparation, to the final size and shape (mark e). The axis of the specimens was adjusted to the centre of the existing groove. The final stress-concentration coefficient was 1.73.⁸ At the end of the specimen preparation the grooves were cleaned to make the surface suitable for observations.

The specimens were loaded, at room temperature, onto the rotary bending machine with a ratio $R = -1$. The levels, at which the crack initiated from the tiny drilled hole and began to propagate, were determined experimentally. The bottom of the groove was analysed after every stop using a light microscope mounted on the loading machine. SEM was used on the dismantled specimens. The fatigue limit was defined as 10^7 cycles strength.

2.2 Cracks registration

The type-I specimens were smooth at the bottom of the groove, i.e., without small defects:

A photograph of small cracks in the type-I specimen at the stress level lower than the fatigue limit is shown in **Figure 3a**. The cracks are non-propagating. Their size is $2a = 50\text{--}60\ \mu\text{m}$.

A photograph of larger non-propagating cracks at the stress level higher than the former one and equal to the fatigue limit is shown in **Figure 3b**. A net of small individual cracks can be seen. The size of the largest one is $2a \cong 300\ \mu\text{m}$. All the other ones are minor cracks.

The type-II specimens were defected by tiny holes. They were in the residual-stress-relaxed condition:

A photograph of the specimen with the drilled hole at the bottom of the groove at the stress level lower than the level for the crack initiation is shown in **Figure 4a**. There is no crack initiated.

A photograph of the specimen at the stress level above the level for the crack initiation is shown in **Figure 4b**. The cracks on both sides of the hole are non-propagating. The cracks including the hole behave

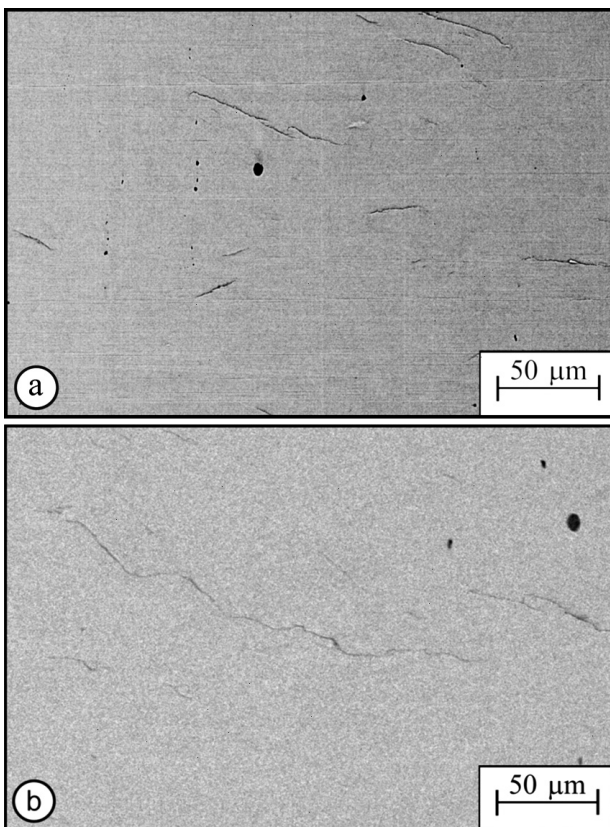


Figure 3: Non-propagating short cracks in the type-I specimens after 10^7 cycles: a) individual cracks at the stress level of 708 MPa, b) a net of cracks at the stress level of 760 MPa

Slika 3: Kratke razpoke, ki se ne širijo, pri preizkušanjih tipa I po 10^7 ciklih: a) posamezne razpoke na nivoju napetosti 708 MPa, b) mreža razpok na nivoju napetosti 760 MPa

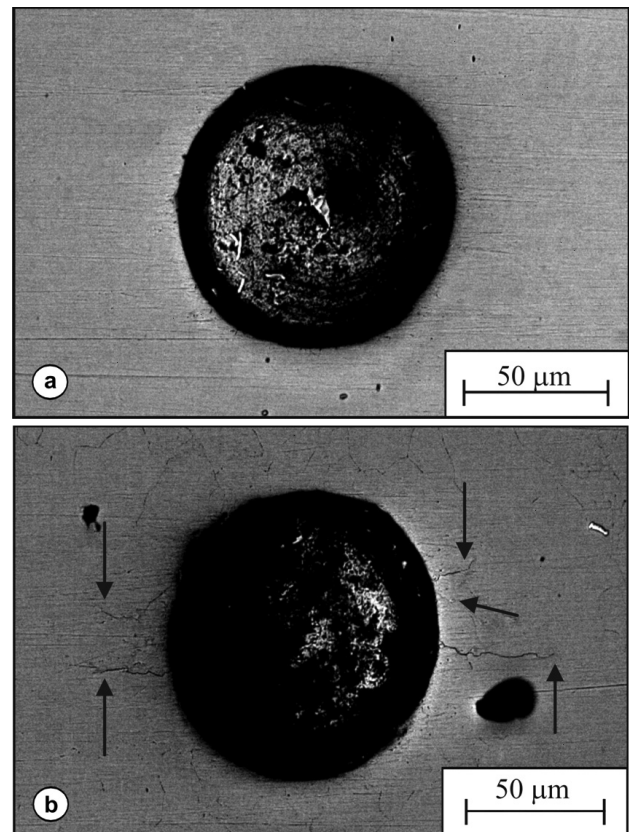


Figure 4: Two different stages at the bottom of the groove in the type-II specimens after 10^7 cycles: a) no cracks at the stress level of 357 MPa, b) non-propagating cracks at the stress level of 405 MPa

Slika 4: Dve različni stanji na dnu žleba pri preizkušanjih tipa II: a) brez razpok na nivoju napetosti 357 MPa, b) razpoke, ki se ne širijo na nivoju napetosti 405 MPa

as a single short, non-propagating crack. Its size is $2a = 165\ \mu\text{m}$.

The type-III specimens were in the as-drilled condition, i.e., with the existing residual stresses:

A photograph of the initiated crack is shown in **Figure 5a**. Only one extremely short crack is registered. The crack including the hole behaves as a single short, non-propagating crack. Its length is $2a = 109.5\ \mu\text{m}$.

A photograph of the cracks at the stress level slightly higher than the fatigue limit is shown in **Figure 5b**. Two cracks were initiated at each side of the hole. The cracks including the hole behave as a single, but propagating crack. In this moment its size is $2a = 202\ \mu\text{m}$. Afterwards, the loading was continued. The specimen finally fractured before 10^7 cycles.

2.3 Short-crack analysis

In order to register the short-crack propagation in the specimens with the existing residual-stress field induced by hole-drilling and evaluate short-crack-propagation rate, some of the specimens were tested in detail at the stress levels between the levels for the crack initiation and the fatigue limit. One of the specimens was tested a

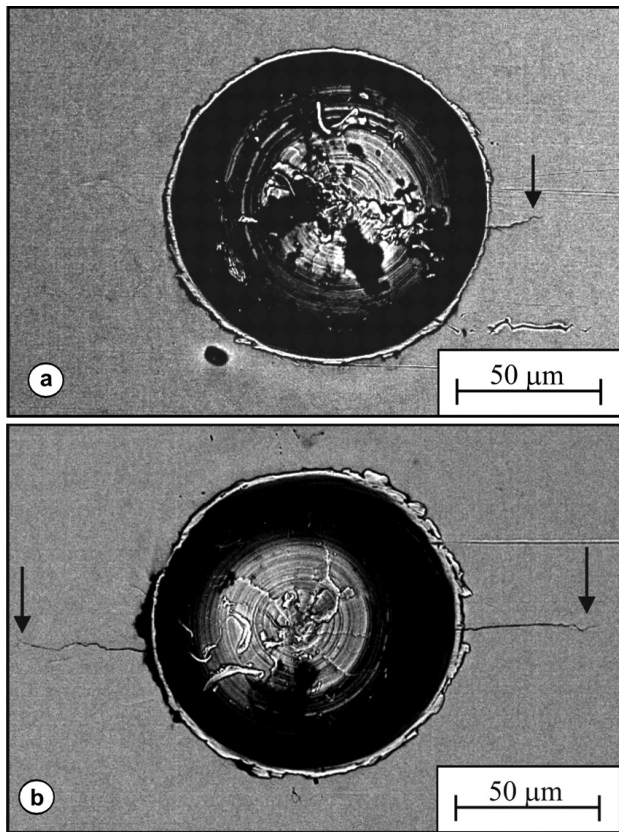


Figure 5: Two different stress levels applied to the type-III specimens: a) non-propagating crack at the stress level of 565 MPa after 10^7 cycles, b) propagating cracks at the stress level of 685 MPa after $1.27 \cdot 10^6$ cycles

Slika 5: Dva različna nivoja napetosti pri preizkušancih tipa III: a) razpoka, ki se ne širi, na nivoju napetosti 565 MPa po 10^7 ciklov, b) razpoki, ki se širita, na nivoju napetosti 685 MPa po $1,27 \cdot 10^6$ ciklov

bit above the fatigue limit. The crack lengths at different stress levels and at different numbers of stress cycles were measured using microscopes.

The registered crack lengths, i.e., the sum of the single crack and the hole diameter or the sum of two cracks and the hole diameter are presented in **Figure 6** depending on the specific number of the cycles.

3 RESULTS AND DISCUSSION

3.1 Fatigue limit

The summarized data on the fatigue limit, the stress level for the crack initiation and the non-propagating crack size registered during the testing as well as the parameter $\sqrt{\text{area}}$ of the drilled holes and the information about the local residual-stress field are listed in **Table 3**. The surface stress at the bottom of the groove corresponds to the nominal bending stress multiplied by the stress-concentration coefficient.

The fatigue limit of defected specimens is lower than the fatigue limit of smooth specimens. Tiny holes help crack initiation. Cracks appear at lower stress levels. The reason for it is the stress concentration caused by a hole.

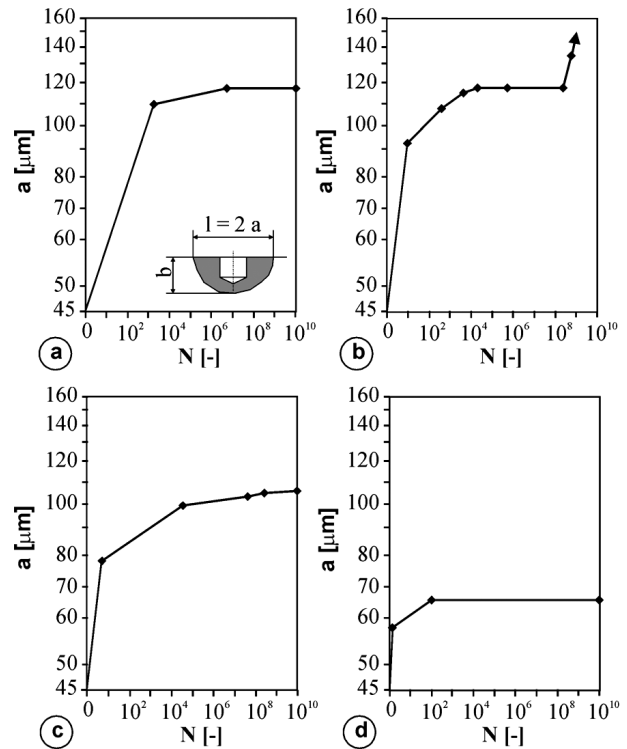


Figure 6: Dependences of crack lengths, a , upon the number of stress cycles, N , at different stress levels, σ : a) 697 MPa, b) 678 MPa, c) 677 MPa, d) 522 MPa

Slika 6: Odvisnost dolžin razpoke a od števila ciklov napetosti N na različnih nivojih napetosti σ : a) 697 MPa, b) 678 MPa, c) 677 MPa, d) 522 MPa

Table 3: Test results

Tabela 3: Rezultati preizkušanja

Specimen	Fatigue limit (MPa)	Stress level for initiation (MPa)	Non-propagating crack size (μm)	Parameter $\sqrt{\text{area}}$ (μm)	Residual stress
Type I	760	691	>150	0	none
Type II	706	381	136	56.2	none
Type III	678	517	112	58.0	present

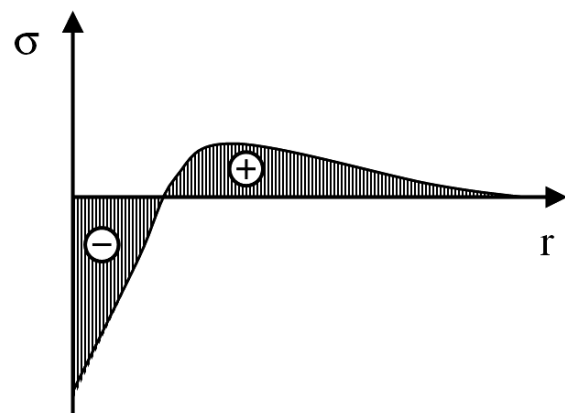


Figure 7: Course of the circular stress induced by drilling σ , against the distance, r (schematically)

Slika 7: Potek krožne napetosti σ , ki je nastala z vrtnjem, glede na razdaljo r (shematsko)

In respect to the residual-stress field induced by drilling the defected specimens behave differently. Namely, the residual stresses are compressive adjacent to the hole. Residual stresses are self-balancing forces. Compressive stresses are in the equilibrium with tensile ones. Therefore, the compressive residual stress decreases with the distance and turns to the tensile stress. The tensile stress attains its maximum at a certain distance and then it decreases. The sketch of the residual stresses induced by hole-drilling is shown in **Figure 7**.

The stress level for the crack initiation is the lowest for the type-III specimens. The largest non-propagating crack is the shortest in the type-III specimens, too. The reason can only be the existing residual-stress field. Compressive stresses retard the crack initiation.

3.2 Anomalous fast short-crack propagation

After the initiation, the short-crack propagation is anomalous fast, much faster than the propagation of the long cracks close to the threshold.

Between two successive moments during the cyclic loading of the specimens when the crack-length measurement was performed (**Figure 6**), the average crack-propagation rate was calculated as:

$$\frac{da}{dN} = \frac{a_i - a_{i-1}}{N_i - N_{i-1}} \quad (1)$$

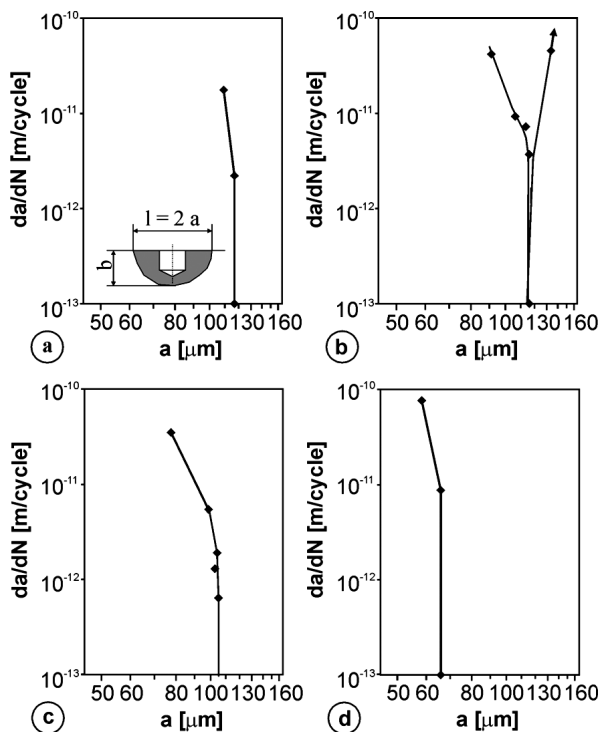


Figure 8: Dependences of the crack-propagation rate, da/dN , upon the crack size, a , for different stress levels, σ : a) $\sigma = 697$ MPa, b) $\sigma = 678$ MPa, c) $\sigma = 677$ MPa, d) $\sigma = 522$ MPa

Slika 8: Odvisnost hitrosti širjenja razpoke da/dN od velikosti razpoke a pri različnih nivojih napetosti σ : a) 697 MPa, b) 678 MPa, c) 677 MPa, d) 522 MPa

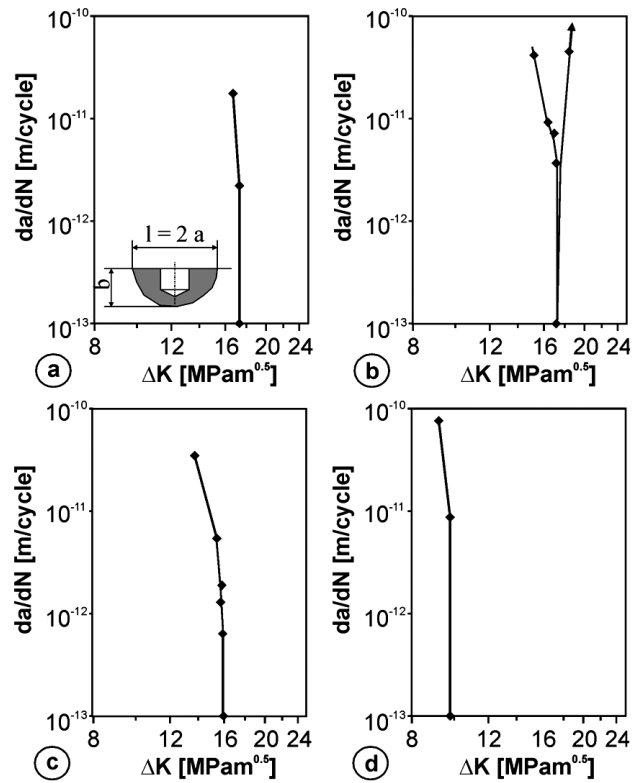


Figure 9: Dependences of the crack-propagation rate, da/dN , upon the stress-intensity-factor range, ΔK , for different stress levels, σ : a) 697 MPa, b) 678 MPa, c) 677 MPa, d) 522 MPa

Slika 9: Odvisnost hitrosti širjenja razpoke da/dN od razpona faktorja intenzitete napetosti ΔK pri različnih nivojih napetosti σ : a) 697 MPa, b) 678 MPa, c) 677 MPa, d) 522 MPa

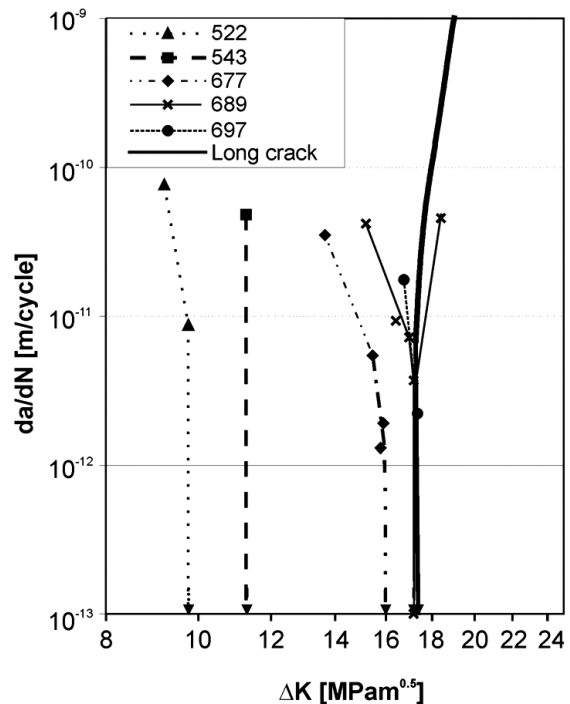


Figure 10: Comparison of short-crack and long-crack propagation rates

Slika 10: Primerjava hitrosti širjenja kratkih in dolgih razpok

The results of the calculations shown against the crack size are presented in **Figure 8**.

As expected, the short-crack-propagation rate decreases with the crack length. At the stress levels lower than the fatigue limit, the cracks sooner or later stop propagating. The crack at the stress level equal to the fatigue limit is the largest non-propagating crack.

However, the driving force for the crack propagation is the stress-intensity-factor range, ΔK :^{4,6}

$$\Delta K = 0.65 \cdot \Delta \sigma \cdot \sqrt{\pi \cdot a} \quad (2)$$

The crack-propagation rates against the stress-intensity-factor range are plotted in **Figure 9**.

The comparison of all the short-crack-propagation rates with the long-crack-propagation rate^{7,8} close to the threshold value for the long-crack propagation and above it are shown in **Figure 10**. The largest non-propagating crack in the type-III specimens is 112 μm long (the sum of the cracks and the hole diameter is 224 μm).

4 CONCLUSIONS

Immediately after the initiation the driving force for the short-crack propagation is not equal to the whole stress-intensity-factor range, ΔK , but to its effective range, ΔK_{eff} . The reason is the crack-closure effect. As a short crack approaches the grain boundary, the propagation rate is gradually retarded because ΔK_{eff} decreases. If the stress level of the applied cyclic stress is lower than the fatigue limit, i.e., ΔK_{eff} is smaller than the threshold stress-intensity-factor range, the crack stops propagating and becomes a non-propagating crack.⁹ In contrast, if ΔK_{eff} is bigger than the threshold value, the crack will continue to propagate as a long crack after retardation during the short-crack propagation.

The largest non-propagating crack in the type-I specimens is longer than in the type-II specimens. Both specimen types are in the residual-stress-free condition. A drilled hole makes a crack initiation easy. The registered crack in a type-I specimen is the largest crack spreading along the whole circumference of the specimen, while the crack in a type-II specimen was forced to emanate from the drilled hole. It is expected that the condition for the unimpeded short-crack propagation is not so convenient in the type-II specimens because short-crack propagation depends on the grain composition (size, orientation etc).

The reason why the non-propagating cracks in the type-III specimens are not as large as the ones in the type-II specimens is the stress field induced by hole-drilling. At the stress levels much lower than the fatigue limit, a short crack begins to propagate through the domain of compressive residual stresses. These levels lower ΔK_{eff} as well as the short-crack propagation rate. Due to the decreasing compressive residual stress during the crack propagation, the crack closure decreases and ΔK_{eff} increases. The result is the quickly increasing short-crack propagation. Despite the decelerated initial crack propagation due to the compressive residual-stress field, the crack, sooner or later, propagates to the domain of the tensile residual stress. Then the crack propagates faster. The largest non-propagating crack in the type-III specimens is therefore smaller than in the type-II specimens.

5 REFERENCES

- ¹ K. J. Miller, The behavior of short fatigue cracks and their initiation 1. A review of 2 recent books, *Fatigue & Fracture of Engineering Materials & Structures*, 10 (1987) 1, 75–91
- ² K. J. Miller, The behavior of short fatigue cracks and their initiation 2. A general summary, *Fatigue & Fracture of Engineering Materials & Structures*, 10 (1987) 2, 93–113
- ³ Y. Murakami, M. Endo, Effects of defects, inclusions and inhomogeneities on fatigue-strength, *International Journal of Fatigue*, 16 (1994) 3, 163–182
- ⁴ Y. Murakami, M. Endo, Quantitative evaluation of fatigue strength of metals containing various small defects or cracks, *Engineering Fracture Mechanics*, 17 (1983), 1–15
- ⁵ Y. Murakami, M. Endo, Effect of hardness and Crack geometries on ΔK_{th} of small cracks estimating from small defect, In K. J. Miller, E. R. de los Rios, editors, *Proceedings, The behaviour of short fatigue cracks*, Mechanical Engineering Publications, London 1986, 275–294
- ⁶ Y. Murakami, K. J. Miller, What is fatigue damage? A view point from the observation of low cycle fatigue process, *International Journal of Fatigue*, 27 (2005) 3, 991–1005
- ⁷ T. Vuherer, L. Milović, V. Gliha, Behaviour of small cracks during their propagation from Vickers indentations in coarse-grain steel: An experimental investigation, *International Journal of Fatigue*, 33 (2011) 12, 1505–1513
- ⁸ T. Vuherer, Analysis of influence of micro defects on fatigue strength of coarse grain HAZ in welds, Doctor Thesis, University of Maribor, Faculty of Mechanical Engineering, 2008
- ⁹ S. Suresh, *Fatigue of materials*, second edition, Cambridge University Press, Cambridge 1998, 343–345, 541–569

INTERNAL-OXIDATION KINETICS OF Ag-Cd ALLOYS

KINETIKA NOTRANJE OKSIDACIJE ZLITIN Ag-Cd

Ljubiša Balanović¹, Vladan Čosović², Nadežda Talijan², Dragana Živković¹

¹University of Belgrade, Technical Faculty, Bor, Serbia

²Institute of Chemistry, Technology and Metallurgy, University of Belgrade, Belgrade, Serbia
ljbalanovic@tf.bor.ac.rs

Prejem rokopisa – received: 2012-10-15; sprejem za objavo – accepted for publication: 2012-12-11

The oxidation kinetics of the Ag-Cd alloys with different Cd contents in mass fractions (9.5, 11, 12 and 16) % at (670, 750 and 795) °C during the production of Ag-CdO electrical-contact materials was investigated. It was found that the internal oxidation of the investigated Ag-Cd alloys generally follows the parabolic-rate law for all the applied oxidation times (5, 9.5, 20.5, 36 and 48) h. The parabolic-rate-law constant for the measured oxide-thickness gain was evaluated at every examined temperature and the Arrhenius-type equations were determined in order to describe the temperature dependence of the rate constants. Microstructures of the obtained Ag-CdO electrical-contact materials were investigated using a SEM-EDS analysis and the microstructure of a sample produced under the optimum process conditions is illustrated with the corresponding micrographs and chemical compositions.

Keywords: Ag-Cd oxidation kinetics, internal oxidation, electrical-contact materials, microstructure

Med proizvodnjo materialov Ag-CdO za električne kontakte je bila preiskovana kinetika oksidacije zlitin Ag-Cd z različno vsebnostjo masnih deležev Cd (9,5, 11, 12 in 16) % pri (670, 750 in 795) °C. Ugotovljeno je bilo, da se notranja oksidacija preiskovanih zlitin Ag-Cd ujema z zakonom parabolične odvisnosti hitrosti pri vseh časih oksidacije (5; 9,5; 20,5; 36 in 48) h. Konstanta parabolične odvisnosti hitrosti naraščanja debeline oksida je bila določena pri vsaki temperaturi preizkusa, prav tako je bila določena Arrheniusova vrsta enačbe za opis temperaturne odvisnosti konstant hitrosti. Mikrostruktura dobljenega materiala Ag-CdO za električne kontakte je bila preiskovana s SEM-EDS-analizami. Prikazana je bila mikrostruktura in narejena kemijska analiza vzorca, izdelanega v optimalnih razmerah.

Ključne besede: kinetika oksidacije Ag-Cd, notranja oksidacija, materiali za električne kontakte, mikrostruktura

1 INTRODUCTION

In the electrical industry most of the contact applications use the materials based on silver that include a combination of pure metals, alloys and metal powders. Silver is also used as a plated, brazed, or mechanically bonded overlay on copper and copper-based materials due to its high thermal and electrical conductivities.

When considering that electrical-contact materials are used in diverse service conditions and also that no metal has all the properties required to accomplish the objectives of different contact applications, in addition to the silver-type contacts, other types of contacts based on platinum-group metals, tungsten, molybdenum, copper, copper alloys and mercury can be found in the electrical industry.

The usefulness of an electrical-contact material also depends on a variety of electrical and mechanical properties, service life, load conditions and economical reasons.¹⁻⁵

The Ag-Cd groups of the contact alloys are widely used in tonnage quantities in the electrical and electronics industries because of their high electrical and thermal conductivities, high resistance to arcing, high welding-adhesion resistance, low-contact resistance, high hardness and strength. Cadmium improves the arc-quenching ability of silver and also increases its resistivity and mechanical strength.⁶⁻⁸

Silver cadmium oxide can be obtained using internal oxidation and powder metallurgy, and the manufacturing method has a significant influence on the properties and microstructure of this material.⁹

In the case of the internal-oxidation process, oxygen diffuses into an alloy and causes a sub-surface precipitation of the oxides of one or more alloying elements, which was the subject of the reviews by Birks et al.¹⁰

The process of internal oxidation occurs in the following manner: oxygen dissolves in the base metal and diffuses inward through the metal matrix containing previously precipitated oxide particles. The critical activity product for the nucleation of the precipitates is established at the reaction front (parallel to the specimen surface) with the inward-diffusing oxygen and the outward diffusion of the solute. When the rate-controlling step in the oxidation process is the diffusion of ions through a compact barrier layer of the oxide with the chemical potential gradient as the driving force, the parabolic-rate law is usually observed.¹¹ As the oxide grows thicker, the diffusion distance increases and the oxidation rate slows down.

The results of the investigation of the oxidation-layer-thickness dependence on the temperature and time of the oxidation for the Ag-Cd alloys with different contents of Cd are presented in this paper. Previous investigations have shown that the oxidation process in this alloy has a parabolic behavior according to the

theoretical relation between the parabolic-rate constant of the metal oxidation and the self-diffusion coefficients in the oxide layer growing on the metal surface, given by Wagner.¹² But, Wagner's general equation in its original form could only be applied to the cases, in which the dependence of the self-diffusion coefficient on the equilibrium partial pressure of the oxidizer was known a priori.

Therefore, since the thickness of the oxide layer depends on the oxidation rate and the oxidation rate is directly correlated with the temperature, the oxidation time and the oxygen pressure, the Arrhenius equation, being widely used to describe the temperature dependence of the kinetic constants, was used for determining the activation energy for the oxidation processes in the studied Ag-Cd alloys.

2 EXPERIMENTAL PROCEDURE

Silver cadmium alloys with mass fractions (9.5, 11, 12 and 16) % of Cd were prepared using the Ag and Cd metals of 99.99 % purity. The alloys were first cast into ingots and then plastically deformed, at low temperatures, into the strips with a thickness of 2 mm. The prepared silver cadmium alloys were heated in an electro-resistive oven in air atmosphere under natural convection at the temperatures of 670 °C, 750 °C and 795 °C during (5; 9.5; 20.5; 36 and 48) h. The micro-structure observation and measurements of the thickness of the oxidized layer were done on the polished cross-sections of the investigated samples using a scanning electron microscope JEOL-JSM-6610LV with an energy dispersive spectrometer (EDS) and a metallographic microscope REICHAART of the POLYVAR – MET type.

3 RESULTS AND DISCUSSION

3.1 Oxidation rate

The samples were measured before and after the internal oxidation. The graphic dependence of the relative change in the weight after (5, 9.5, 20.5, 36 and 48) h of the oxidation of the silver cadmium alloys with mass fractions (9.5, 11, 12 and 16) % of Cd is presented in **Figure 1a**. The inner oxidation of the Ag alloys with different Cd contents generally follows the parabolic-rate law for the examined time range up to 48 h at the temperature of 750 °C. In **Figure 1b** it can be seen that 60 % of Cd was oxidized after a 20.5 h oxidation of the silver cadmium alloy with 9 % Cd.

3.2 Oxidation kinetics

During the internal oxidation of the silver cadmium alloy, the cadmium species become depleted in the zones when the oxygen front moves into the silver cadmium alloy. As the oxidation front moves from the surface of

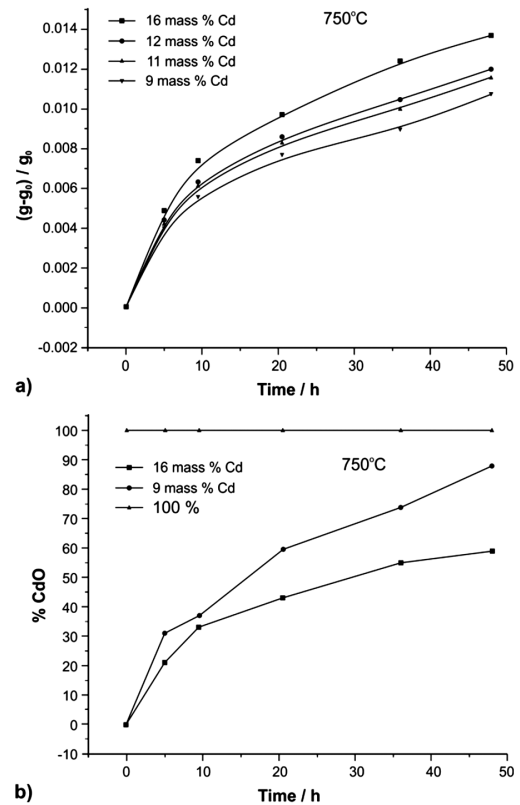


Figure 1: a) Dependence of the relative mass change during the oxidizing for the Ag-Cd alloys with different Cd contents at 750 °C; b) extent of the Cd oxidation for the Ag-Cd alloys with 9 % and 16 % Cd at 750 °C

Slika 1: a) Odvisnost relativne spremembe mase med oksidacijou zlitin Ag-Cd z različno vsebnostjo Cd pri 750 °C, b) delež oksidacije Cd v Ag-Cd zlitinah z 9 % in 16 % Cd pri 750 °C

the strip toward the center, the concentration of the cadmium species becomes increasingly dilute as compared to the original composition. Hence, after the oxidation is completed, the cross-section will display a significant oxide-deficient or oxide-depleted zone in the center of the contact body. For some applications the presence of the depletion zone is detrimental, requiring its removal or displacement from the center. There are two common methods to achieve such a result. The first method takes account of the fact that an oxidation barrier, such as a ceramic glaze, is applied to one surface so that the oxidation can proceed only from one side. The second method is to laminate two silver cadmium sheets of the same size and to form a package by welding them along all four edges. After the oxidation, the sheets are separated. The oxide-deficient zone will appear on one side (the inner side of the package) of each sheet.^{5,12}

Figure 2 shows the dependence of the thickness of an oxidized layer for different Cd contents in the Ag-Cd alloys. After comparing the changes in the thickness of the oxidized layer with the temperature and time, it is obvious that the oxidation rate is the highest for the alloy with the smallest amount of Cd and the lowest for the alloy with largest amount of Cd.

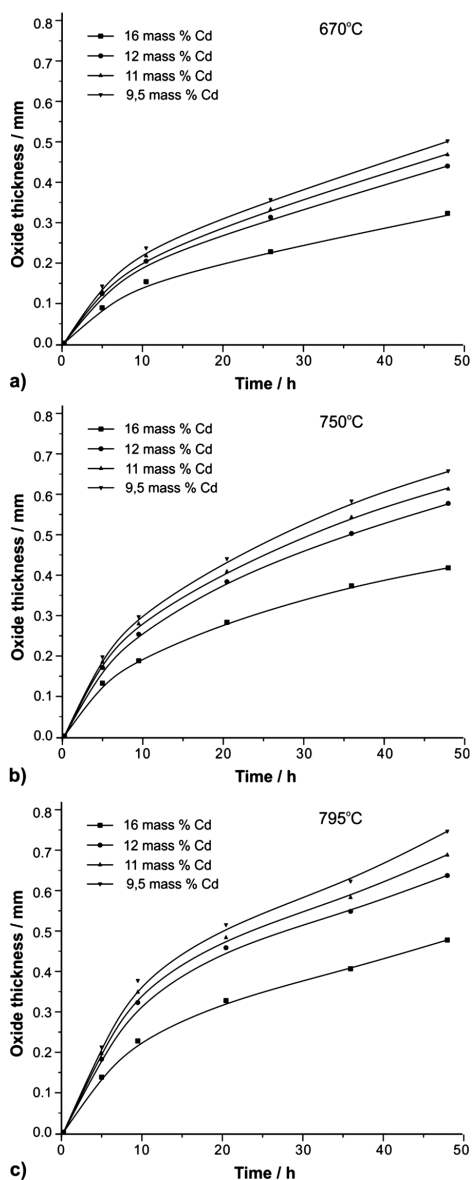


Figure 2: Dependence of the thickness of an oxidized layer for Ag-Cd alloys with different Cd contents; inner oxidation at: a) 670 °C, b) 750 °C and c) 795 °C

Slika 2: Odvisnost debeline oksidirane plasti pri zlitinah Ag-Cd z različno vsebnostjo Cd; notranja oksidacija pri: a) 670 °C, b) 750 °C in c) 795 °C

A mass content of 9–12 % of CdO in the Ag-CdO alloys successfully creates a decrease in the deformation and devastation of electrical contacts. With the concentrations of CdO above 12 %, an inner break is possible due to an intension caused by an increase in the grain diameter after the oxidation. The main difference is that the elevated temperatures promote ionic diffusion and, thus, the oxide formation can proceed to a much greater extent than at the low temperatures where only thin layers are formed.

The dependence of the scale thickness on the time can be used for determining the kinetic law for the oxidation rate. As the oxidized layer grows thicker, the

diffusion distance increases and the oxidation rate slows down. The rate (dx/dt) is inversely proportional to the oxide thickness (x) or:

$$\frac{dx}{dt} = \frac{k_p}{x} \quad (1)$$

Equation (1) can be rewritten as:

$$x dx = k_p dt \quad (2)$$

Upon an integration of equation (2):

$$\int_{x=0}^{x=x} x dx = \int_{t=0}^{t=t} k_p dt \quad (3)$$

On integration, the parabolic equation is obtained:

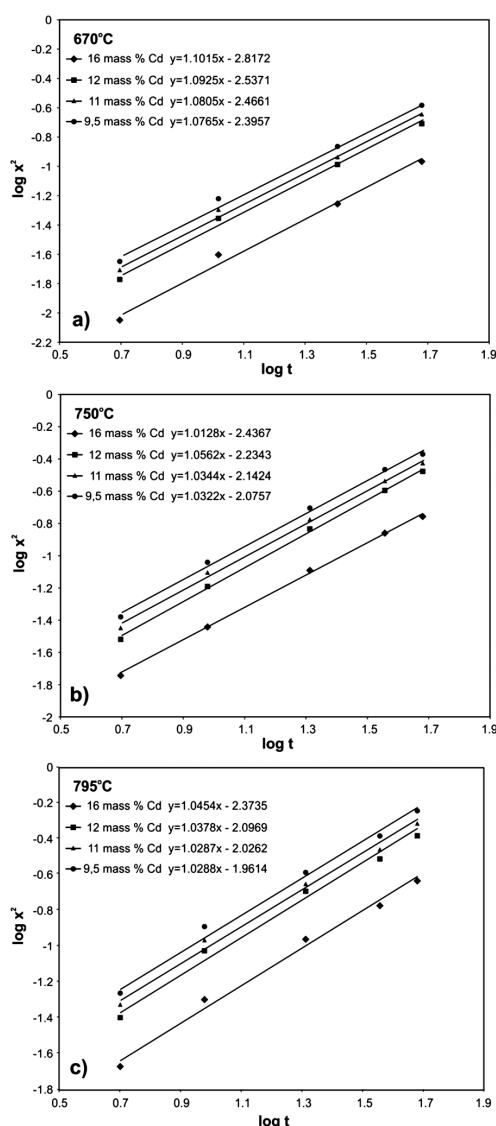


Figure 3: Logarithm of the oxide thickness versus the logarithm of the oxidation time for the Ag-Cd alloys with different Cd contents at: a) 670 °C, b) 750 °C and c) 795 °C

Slika 3: Logaritmem debeline oksida v primerjavi z logaritmom časa oksidacije za zlitine Ag-Cd z različno vsebnostjo Cd pri: a) 670 °C, b) 750 °C in c) 795 °C

$$x^2 = 2k_p t + c \tag{4}$$

and the parabolic-rate constant, k_p , can be determined from the experiment in the units of $\text{cm}^2 \text{s}^{-1}$ or a similar length squared per time units:^{12,13}

If one takes the logarithm of both sides of equation (4), the following is obtained:

$$\lg x^2 = \lg k_p + \lg t \tag{5}$$

A plot of $\lg x^2$ versus $\lg t$ can be done linearly and the parabolic-rate constants can be determined for the reaction carried out at several temperatures. The intercept of the line is $\lg k_p$.

The logarithm of the oxide thickness as a function of the logarithm of the oxidation time for the Ag-Cd alloys with different Cd contents at the investigated temperatures is presented in **Figure 3**, while the dependence of the parabolic-rate constant as a function of the inverse temperature oxidation of the Ag-Cd alloys with different Cd contents is shown in **Figure 4**.

This indicates that the thermal diffusion process is rate controlling, with oxygen or cations or both diffusing through a compact layer. The rate of diffusion through an oxide film depends on a number of factors, such as the temperature, oxygen partial pressure and structure of the oxide.¹²⁻¹⁴

At the temperatures higher than the melting point of a metal, the lattice diffusion dominates through the crystalline oxide formed on the metal and, at the lower temperatures, the diffusion via the oxide-grain boundaries is predominant. In this case, the rate of oxidation of a metal or alloy depends on the oxide-grain size, which is often dictated by the substrate-grain orientation, surface pretreatment, etc.⁹ A deviation from the parabolic-oxidation behavior is often observed and can be a result of the oxide-grain-size change with time and at a particular temperature. In this case, the number of oxide-grain-boundary 'easy diffusion paths' decreases

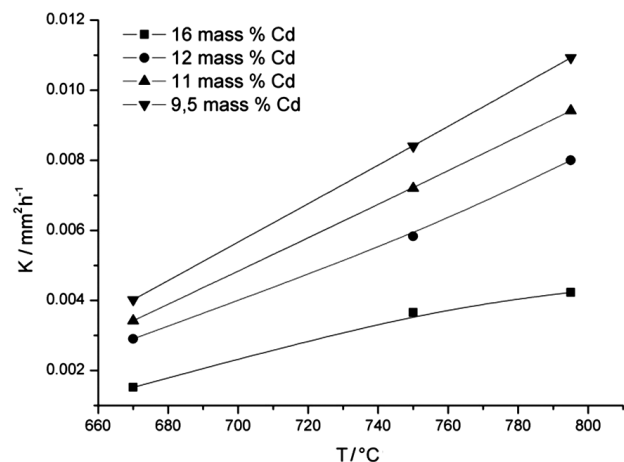


Figure 4: Dependence of parabolic-rate constants versus temperature oxidation of the Ag-Cd alloys with different Cd contents

Slika 4: Odvisnost konstant paraboličnih hitrosti od temperature oksidacije zlitin Ag-Cd z različno vsebnostjo Cd

with time, causing an apparent decrease in the oxidation rate. When the rate-controlling step in the oxidation process is a diffusion of ions through a compact barrier layer of oxide with the chemical potential gradient as the driving force, the parabolic-rate law is usually observed¹⁵ and then the change in the oxidation rate with the temperature will follow the Arrhenius equation:^{11,16-18}

$$k_p = A e^{-\frac{E_a}{RT}} \tag{6}$$

where k is the rate constant, A is the frequency factor (or pre-exponential factor), R is the molar gas constant, E_a is the activation energy, and T is the temperature (K). If we take the natural logarithm of both sides and the rearrangement, this equation can be put in the linear form:

$$\ln k_p = \ln A - \frac{E_a}{RT} \tag{7}$$

so that the constants can be calculated using a linear regression. This type of linearization, which allows fitting a straight line into the transformed experimental data, has been used for nearly a century.¹⁹⁻²³ Most of the constants reported in the literature were obtained using this method. And therefore, a plot of $\ln k_p$ versus $1/T$ can be made, or a linear regression performed, after the rate constants have been determined for a reaction carried out at several temperatures. The Arrhenius plot is shown in **Figure 5**. For a particular reaction, the following rate constants were obtained when the reaction was studied at a series of temperatures.

Using the data presented in **Figure 4** and the Arrhenius plot of the parabolic-rate constants for the oxidation of the Ag-Cd alloy, shown in **Figure 5**, the activation energy was calculated as $36 \pm 2 \text{ kJ/mol}$ and shown in **Table 1**.

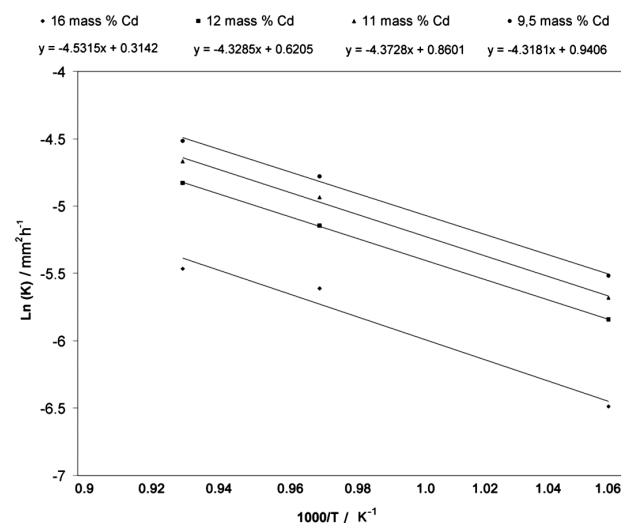


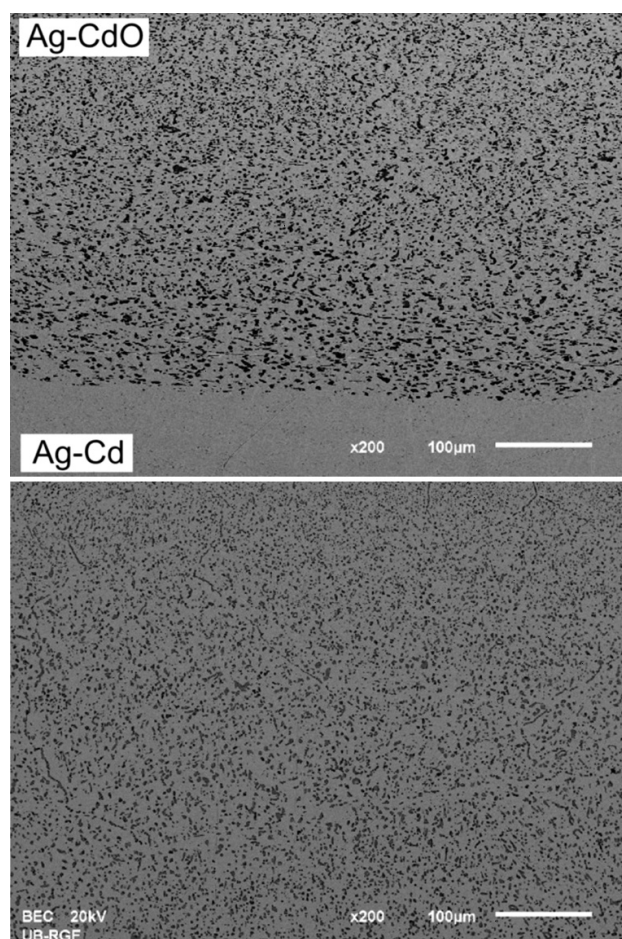
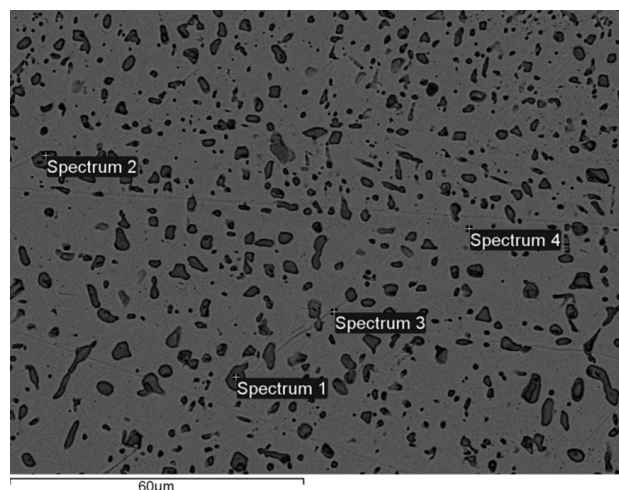
Figure 5: Logarithm of the parabolic-rate constants versus the inverse temperature for the oxidation of the Ag-Cd alloys

Slika 5: Logaritem konstant paraboličnih hitrosti v primerjavi z inverzno vrednostjo temperature pri oksidaciji zlitin Ag-Cd

Table 1: Parabolic-rate constants and activation energy of the oxidation of the Ag-Cd alloys with different Cd contents**Tabela 1:** Konstante parabolične hitrosti in aktivacijska energija zlitin Ag-Cd z različno vsebnostjo Cd

Material composition in mass fractions	K/(mm ² h)			Activation energy of oxidation kJ/mol
	670 °C	750 °C	795 °C	
16 % Cd	$1.52 \cdot 10^{-3}$	$3.66 \cdot 10^{-3}$	$4.23 \cdot 10^{-3}$	38
12 % Cd	$2.90 \cdot 10^{-3}$	$5.83 \cdot 10^{-3}$	$8.00 \cdot 10^{-3}$	36
11 % Cd	$3.41 \cdot 10^{-3}$	$7.20 \cdot 10^{-3}$	$9.41 \cdot 10^{-3}$	38
9.5 % Cd	$4.02 \cdot 10^{-3}$	$8.40 \cdot 10^{-3}$	$10.92 \cdot 10^{-3}$	36

Considering that the anti-welding behavior and wear resistance of the electrical-contact materials can be improved with a uniform dispersion of the metal oxide particles in a soft silver matrix, the ultimate goal of the investigations is an optimization of the internal-oxidation process parameters that promote the formation of the optimum microstructure, i.e., obtaining of a good and homogeneous oxide dispersion within the silver matrix.

**Figure 6:** SEM micrograph of an Ag-CdO composite obtained with the internal oxidation of the Ag-11 % Cd alloy (Ag-CdO11); a) pure Ag-Cd and an oxide layer of Ag-CdO; b) oxide layer of Ag-CdO**Slika 6:** SEM-posnetek kompozita Ag-CdO, dobljenega z notranjo oksidacijo zlitine Ag-11 % Cd (Ag-CdO11); a) čisti Ag-Cd in oksidna plast Ag-CdO; b) oksidna plast Ag-CdO**Figure 7:** SEM micrograph of a cross-section of the Ag-11 mass % Cd alloy (Ag-CdO11) with the annotated points of the EDS analysis**Slika 7:** SEM-posnetek preseka zlitine Ag-11 % Cd (Ag-CdO11) z označenimi točkami, kjer je bila izvršena EDS-analiza

As an illustration of the optimum microstructure of the Ag-CdO electrical-contact materials obtained in the process investigating the internal oxidation, a characteristic SEM micrograph of the Ag-CdO composite obtained with the internal oxidation of the Ag-11 % Cd alloy (Ag-CdO11) is given in **Figure 6**.

The results of a further microstructural analysis using EDS are presented in **Table 2** and the selected points used for the analysis are marked in **Figure 7**.

Table 2: Results of the EDS analysis of the Ag-11 % Cd alloy (Ag-CdO11) for the electrical-contact material**Tabela 2:** Rezultati EDS-analize zlitine Ag-11 % Cd (Ag-CdO11) za električne kontakte

Spectrum	w(Ag)/%	w(Cd)/ %	w(O)/ %
1	0	83.55	16.45
2	4.99	78.76	16.25
3	97.92	2.08	0
4	97.91	2.09	0

Figures 6 and 7 display a microstructure of the material upon the completion of the oxidation process, which consists of the CdO particles embedded in a silver matrix. It should be noted that in order to provide a good bond between the contact material and the contact holder by soldering, about 25 % of the total thickness of the electrical-contact material must not be oxidized, as illustrated in **Figure 6**. The presented EDS results (**Table 2**) corroborate the observed microstructure and illustrate the Ag and CdO-rich regions.

4 CONCLUSION

The present study on the oxidation behavior of the Ag-Cd alloys with different contents of Cd, carried out in the air environment at the temperatures of 670 °C, 750 °C and 795 °C during (5, 9.5, 20.5, 36 and 48) h using a

microstructure observation and measurements of the thickness of the oxidized layer revealed the following:

The thickness of the oxidized layer during the heating depends on the following process conditions: the temperature and duration of oxidation, the amount of cadmium in the Ag-Cd alloys and the oxygen pressure on the surface of the alloy.

The oxidation kinetics of the alloys follows the parabolic-rate law suggesting a diffusion-controlled growth of the oxide film.

The activation energy, E_a , and the pre-exponential factor were determined using the Arrhenius equation, fitting $\ln k_p$ vs $1/T$ at the temperatures of 670 °C, 750 °C and 795 °C. The activation-energy value of 36 ± 2 kJ/mol indicates a mixed effect of diffusion and temperature on the kinetics of the mentioned process of the internal oxidation of Ag-Cd alloys. This is in accordance with the observation given in⁵ that the temperature has the highest influence on the process of an inner oxidation⁵ because, at higher temperatures, the inner oxidation is faster according to Wagner's expression of the parabolic-rate constant for an internal oxidation where the solute element is part of the denominator.¹²

The aim of this study is to gain a better basic understanding of the controlling processes in the coarsening of the cadmium oxide phase in the internally oxidized silver cadmium alloys.

Acknowledgement

This paper was done under the financial support of the Ministry of Education and Science, Republic of Serbia – project No 172037.

5 REFERENCES

- ¹ J. R. Davis, ASM Materials Engineering Dictionary, ASM International, Materials Park, OH 1992
- ² Y. S. Shen, P. Lattari, J. Gardner, H. Wiegard, ASM Handbook, Powder Metal Technologies and Applications, 7 (1998), 1025
- ³ R. Holm, Electrical Contacts - Theory and applications, 4th ed., Springer, 2000
- ⁴ M. Braunović, N. K. Myshkin, V. V. Konchits, Electrical contacts – Fundamentals, Applications and Technology, CRC Press, Taylor and Francis Group, 2007
- ⁵ N. Talijan, J. Stajić-Trosić, V. Čosović, A. Grujić, E. Romhanji, Electrical and mechanical properties of silver based electrical contact materials, Proceedings of the 4th Balkan Conference on Metallurgy, Zlatibor, 2006, 445
- ⁶ P. G. Slade, ed., Electrical Contacts: Principles and Applications, CRC Press, 1999, 684
- ⁷ N. Talijan, J. Stajić-Trosić, V. Čosović, A. Grujić, E. Romhanji, Composite electrical contacts based on silver, Proceedings of the 10th International Research/Expert Conference Trends in the Development of Machinery and Associated Technology, Barcelona, 2006, 1339
- ⁸ V. Čosović, N. Talijan, D. Živković, D. Minić, Ž. Živković, Comparison of properties of silver-metal oxide electrical contact materials, J. Min. Metall. Sect. B-Metall., B 48 (2012), 131–141
- ⁹ ASTM Standards, Standard Guide for Silver-Cadmium Oxide Contact Material, B781–93a, 1999
- ¹⁰ N. Birks, G. H. Meier, F. S. Pettit, Introduction to the High Temperature Oxidation of Metals, Cambridge University Press, New York 2006
- ¹¹ J. R. Davis, Heat-resistant materials, ASM International, Handbook Committee, Materials Park, OH 1997
- ¹² C. Wagner, Z. Phys. Chem. B, (1933), 21
- ¹³ D. J. Young, High Temperature Oxidation and Corrosion of Metals, Elsevier, Cambridge 2008
- ¹⁴ J. H. Moore, N. D. Spencer, Encyclopedia of Chemical Physics and Physical Chemistry, Volumes 1–3, Institute of Physics, 2001
- ¹⁵ A. M. Huntz, Journal of materials science letters, 18 (1999), 1981–1984
- ¹⁶ M. J. Graham, R. J. Hussey, Oxid. Met., 44 (1995), 339
- ¹⁷ S. Arrhenius, Zur Theorie der chemischen Reaktionsgeschwindigkeiten, Z. Physik. Chem., 7 (1899)
- ¹⁸ W. Jaenicke, S. Leistikow, A. Sadler, J. Electrochem. Soc., 111 (1964), 1031
- ¹⁹ N. B. Pilling, R. E. Bedworth, J. Inst. Met., 29 (1923), 529
- ²⁰ W. K. Appleby, R. F. Tylecote, Corros. Sci., 10 (1970), 325
- ²¹ J. Stringer, Werkstoffe Korros., 23 (1972), 747
- ²² N. H. Chen, R. Aris, Determination of Arrhenius constants by linear and nonlinear fitting, AIChE J., 38 (1992) 4, 626–628
- ²³ J. Šesták, A. Kozmidis-Petrović, Ž. Živković, Crystallization kinetics accountability and the correspondingly developed glass-forming criteria – A personal recollection at the forty years anniversaries, J. Min. Metall. Sect. B-Metall. B, 47 (2011) 2, 229–239

EFFECTS OF THE AGEING TREATMENT ON THE SUPERELASTIC BEHAVIOR OF A NITINOL STENT FOR AN APPLICATION IN THE ESOPHAGEAL DUCT: A FINITE-ELEMENT ANALYSIS

UČINEK STARANJA NA SUPERELASTIČNO VEDENJE NITINOLNE OPORE PRI UPORABI V CEVI POŽIRALNIKA: ANALIZA KONČNIH ELEMENTOV

Fardin Nematzadeh¹, Seyed K. Sadrnezhaad²

¹Materials and Energy Research Center, (MERC), P.O. Box 14155-4777, Tehran, Iran

²Department of Materials Science and Engineering, Sharif University of Technology, P.O. Box 11155-9466, Tehran, Iran
fardinnematzadeh@gmail.com

Prejem rokopisa – received: 2012-10-23; sprejem za objavo – accepted for publication: 2012-12-18

The effects of design parameters and material properties obtained with the ageing treatment on the mechanical performance of a z-shaped esophageal-duct nitinol wire stent under the crushing tests for clinical applications are investigated with a finite-element simulation. With 90 % crushing, low chronic outward force, high radial resistive strength and favorable superelastic behavior are attained at the segment angle of 65° and the A_f temperature of 24 °C. The performance of the stent is seen to drastically vary with a change of only 1° in the segment angle.

Keywords: finite-element analysis, esophageal duct, nitinol stent, ageing treatment, mechanical performance

Z metodo končnih elementov so bili preučevani učinek konstrukcijskih parametrov in mehanske lastnosti materiala pri tlačnih preizkusih starane nitinolne žične opornice z-oblike za klinično uporabo v cevi požiralnika. Z 90-odstotnim tlačenjem, nizko stalno silo navzven, veliko radialno silo upornosti in zeleno superplastično vedenje je bilo doseženo pri segmentu s kotom 65° in temperaturi A_f 24 °C. Opazi se, da se vedenje opore občutno spremeni že pri spremembi kota segmenta za 1°.

Ključne besede: analiza končnih elementov, cev požiralnika, nitinolna opora, staranje, mehansko delovanje

1 INTRODUCTION

Gastrointestinal disease is an important cause of death these days. Renteln et al. have referred to the esophageal cancer as a worldwide source of gastrointestinal malignancies.¹ The majority of patients with esophageal cancer suffers from dysphagia and undergoes death.¹ The primary aim of treating these patients is to reduce dysphagia with a minimum morbidity and mortality and to improve the quality of their lives.¹ With respect to this type of illness, Renteln et al.² have stated that an endoscopic stenting is better than a surgical repair. A stent placement has, therefore, been one of the main remedies for these types of diseases in the last decade.

The use of a stent has two main objectives: (1) a short-term effect of avoiding intimal dissection and an elastic recoil and (2) a long-term effect of avoiding restenosis caused by neointimal hyperplasia mentioned by Stoeckel et al.³ A nitinol-stent placement was developed to introduce a behavioral modality of the palliation of malignant dysphagia. Nitinol stents for the esophageal duct are easily implanted with a low risk of a severe complication. They provide a successful palliation of malignant esophageal obstructions, too. They also help

relieve dysphagia for the patients with inoperable carcinoma esophagus.¹

A stent placement has been the major approach to solving gastrointestinal diseases like esophageal malignancy during the past decade. Nitinol superelastic stents have been considered a solution to the problems such as restenosis after an implantation, a low twisting ability, an unsatisfactory radial mechanical strength and improper dynamic behaviors associated with the ducts.

Owing to a good retrievability and flexibility, the z-shaped wire stents are most widely used in the stent designs.⁴ They can be used to fabricate custom-made stents with preselected values exerting the radial forces for the clinical use. The Z-shaped models are also desirable as, even in a laboratory, they can be easily manufactured by hand. The Z-shaped models also allow various designs with different amounts of radial forces as described by Patrick et al.⁵ Important parameters like the length, diameter of the wire, number of bends, segment angle, stent inner diameter and radial contraction should be determined with analytical equations associated with the geometry of a stent.

The first report about a numerical study of the fatigue behavior of a nitinol stent was presented by Whitcher et al.⁶ A good agreement of their numerical results, calcu-

lated for the crushing tests, with the other researchers' experimental data was assessed by Petrini et al.⁷, Kleinstreuer et al.⁸ have offered a computational analysis of different nitinol stent-graft combinations for the support of the abdominal aortic aneurysm (AAA). Beule et al.⁹ have developed the strategies to investigate and optimize the mechanics of braided stents. Silber et al.¹⁰ have shown the effect of changing geometrical characteristics on the mechanical properties of the nitinol wire stents. The finite-element method is useful for designing the knitted nitinol meshes utilized in a prospective external vein reinforcement.¹¹

Liu et al.¹² have performed critical testing for determining the pseudoelastic behavior and transformation temperatures of the near-equiatomic NiTi shape-memory alloys. Duerig et al.⁴ have compared the mechanical performance of self-expanding stents usable for the treatment of a vascular disease. It has been shown that the NiTi A_f temperature has a great influence on the mechanical performance of self-expandable stents. Yeung et al.¹³ have shown that the A_f temperature of a nitinol alloy can be controlled by manipulating the heat-treatment parameters. This is important for the production of the nitinol stents with favorable superelastic behavior. Patel et al.¹⁴ have studied the effect of the active A_f temperatures on the fatigue properties of nitinol. They have shown that a low A_f temperature has a short fatigue-life consequence. Liu et al.¹⁵ have evaluated the effect of age treatment on the shape-setting and superelasticity of the Ti-50.7 % Ni stents. They have shown that the optimum ageing temperature for the production of the expected shape of a stent is 500 °C with an ageing time of no more than 60 min resulting in an excellent non-linear superelasticity with the maximum recoverability at the body temperature. To achieve the superelastic behavior of a stent, A_f should be lower than the body temperature. Its optimum value depends on the stiffness needed for a removal of a duct obstruction. A low A_f causes problems like high stiffness and augmented radial forces that can lead to an injury and scars on the duct.

Although there is some information available on the nitinol wire stents, to the best of our knowledge, the z-shaped wire stents for esophageal ducts have not been

studied before. The purpose of this investigation is, hence, an application of the finite-element method for an elucidation of the effects of the design parameters and material properties obtained from the ageing treatment on the mechanical performance of the nitinol stents designed for esophageal ducts. The effects of important parameters are predicted via the model calculations and are verified with the experimental information available in the literature. The model is developed on the basis of the nonlinear 3D finite-element method. An application of the results can help diminish dysphagia, improving the quality of patients' life.

2 MODELING AND METHODS

2.1 Geometric models

Micro-CT can be used for obtaining the optimum geometry of the commercial stents available on the market. This instrument is, however, not useful for designing innovative new designs. The geometry of the stent used in this research was, therefore, generated by a computer-aided three-dimensional interactive application (Catia v.5 (Dassault Systèmes, USA)) and transformed into a finite-element-analysis code. The geometric parameters of the esophageal stent are sketched in **Figure 1** and quantified in **Table 1**. The geometric parameters shown in **Figure 1** and **Table 1** were based on the age treatment of the Ti-50.7 % Ni alloy at 500 °C for respective durations of 60 min and 30 min according to the clinical reports given in the literature.^{1,15}

Table 1: Geometric values for the stents of this research (unit of length is mm)

Tabela 1: Geometrijske vrednosti za opore v tej raziskavi (enota dolžine je mm)

Sample	Internal diameter of stent (D)	Radius of curvature (ρ)	Segment length (L)	Diameter of wire (d)	Bending angle (ϕ)
Sample 1	25.0	0.3	10.03	0.2	66°
Sample 2	25.0	0.3	10.80	0.2	65°

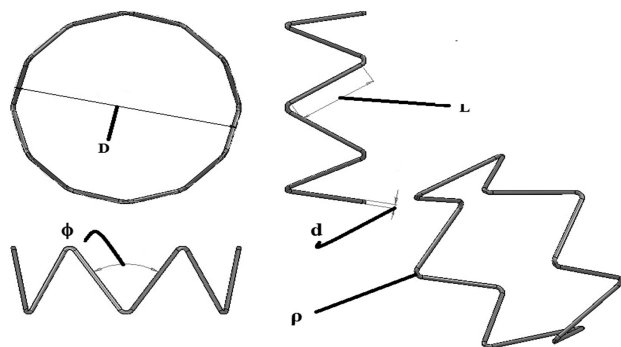


Figure 1: Geometric parameters of a Z-shaped esophageal stent
Slika 1: Geometrijski parametri Z-oblike opornice za cev požiralnika

2.2 Material properties

The properties of the nitinol stents considered for esophageal ducts are evaluated with a crushing test. Superelastic wire properties are merely considered in an evaluation of the clinical behavior of the nitinol stents used in this research. The model first developed by Auricchio et al.¹⁶ and Lubliner et al.¹⁷ and then significantly extended by Rebelo et al.¹⁸ is used for the simulation of the nitinol superelastic behavior. The model is based on a generalization of the theory of plasticity and the second law of thermodynamics written in terms of Helmholtz free energy. In this theory, the strain is decomposed into two components:

$$\Delta \epsilon = \Delta \epsilon^{el} + \Delta \epsilon^{tr} \quad (1)$$

in which $\Delta\epsilon^{el}$ is the elastic strain and $\Delta\epsilon^{tr}$ is the transformation strain. The transformation of austenite to twinned martensite occurs due to the motion of the shear forces taking place in the stress-threshold range of the superelastic material according to the following equations:

$$F^S \leq F \leq F^F \tag{2}$$

in which F is the transformation potential and S and F denote the martensite transformation start and finish, respectively;

$$\Delta\epsilon^{tr} = a\Delta\zeta \frac{\partial F}{\partial \sigma} \tag{3}$$

$$\Delta\zeta = f(\sigma, \zeta)\Delta F \tag{4}$$

$$F = \bar{\sigma} - p \tan \beta + CT \tag{5}$$

in which a is the coefficient of strain, ζ is the martensite percentage, σ is the von Mises stress, $\bar{\sigma}$ is the von Mises equivalent stress, p is the pressure, β and C are the material constants and T is the temperature. A similar approach is applied to define the reverse transformation which takes into account different stress

thresholds. Equations 3 and 4 define the transformation intensity. Any change in the stress direction generates a martensite reorientation with a negligible additional attempt. Furthermore, the model includes a linear shifting of the stress thresholds with the temperature. In view of the fact that there is a volume increase associated with the transformation, less stress is needed to generate a transformation in tension and, specifically, in compression. This effect is modeled with the linear Drucker-Prager approach for the transformation potential shown in equation 5 and referred to by Rebelo et al.¹⁸ The parameters required in the Abaqus 6.10 (Dassault Systèmes, Providence, RI, USA) user-material subroutine for the nitinol material based on the Auricchio model for opening the esophageal duct are summarized in **Table 2**.^{12,15,19} The basis for the material-property selection of the stents is the age treatment results of the Ti-50.7 % Ni alloy at 500 °C for 30 min and 60 min. The data given for the sample No. 1 from **Table 2** is based on the age treatment of the Ti-50.7 % Ni alloy at 500 °C for 30 min. The data for the sample No. 2 from **Table 2** is based on the age treatment of the Ti-50.7 % Ni alloy at 500 °C for 60 min. A typical nitinol superelastic behavior employed in this research is illustrated in **Figure 2**. Before testing, a cubic element of nitinol is considered and its results are compared with the experimental data. Based on the comparative experimental and mathematical curves plotted in **Figure 3**, it is recognized that the Auricchio model is in reasonable agreement with the empirical data and, consequently, hereafter, the properties of the materials are defined in a subroutine based on the aforementioned numerical model.

Table 2: Material properties used in the simulation of an esophageal-duct opening with a nitinol stent. The data are based on the Auricchio model.^{12,15,19}

Tabela 2: Lastnosti materiala, uporabljene v simulaciji odpiranja nitinolne opore požiralnika. Podatki temeljijo na Auricchiovem modelu.^{12,15,19}

Symbol	Description	Sample No. 1	Sample No. 2
E_A	Austenite elasticity	24100 MPa	20700 MPa
ν_A	Austenite Poisson's ratio	0.33	0.33
E_M	Martensite elasticity	17800 MPa	11700 MPa
ν_M	Martensite Poisson's ratio	0.33	0.33
ϵ^L	Transformation strain	0.054	0.055
$\left(\frac{\partial \sigma}{\partial T}\right)_L$	stress/temperature ratio during loading	5.32 MPa T ⁻¹	5.32 MPa T ⁻¹
σ_L^S	Start of transformation loading	390 MPa	344 MPa
σ_L^E	End of transformation loading	401 MPa	363 MPa
T_0	Reference temperature	37 °C	37 °C
$\left(\frac{\partial \sigma}{\partial T}\right)_U$	Stress/temperature ratio during unloading	5.32 MPa T ⁻¹	5.32 MPa T ⁻¹
σ_U^S	Start of transformation unloading	112 MPa	58 MPa
σ_U^E	End of transformation unloading	93 MPa	42 MPa
σ_{CL}^S	Start of transformation stress in compression	-	-
ϵ_V^L	Volumetric transformation strain	0.054	0.055
A_f	Austenite finish transformation temperature	22 °C	24 °C
ϕ	Segment bending angle	66°	65°

2.3 Meshing and boundary conditions

Hypermesh (Altair® Hypermesh® v. 6.0) is a high-performance finite-element preprocessor that provides highly interactive software for the performance analysis of a product design. It is noticeable that due to the meshing problems caused by a small section of the nitinol wire and a relatively complex geometry of the stents, the hypermesh software is used to mesh the samples. The

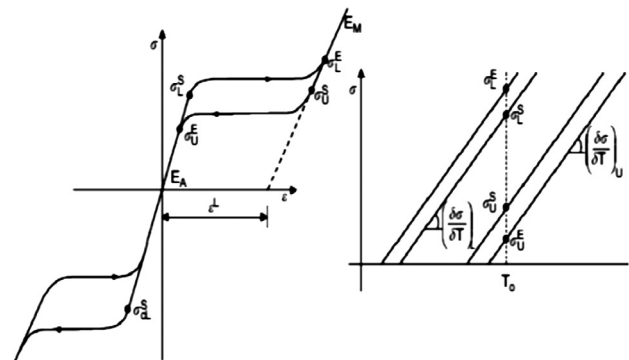


Figure 2: Typical behavior of superelastic nitinol
Slika 2: Značilno vedenje superelastičnega nitinola

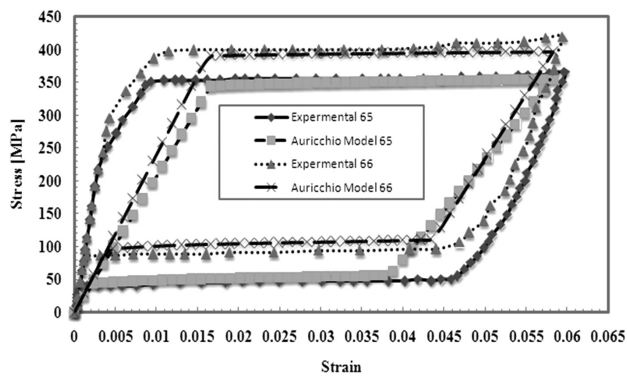


Figure 3: Comparison of the Auricchio-model calculations with the experimental data obtained for the superelastic nitinol samples No. 1 (66°) and 2 (65°) from **Table 2**

Slika 3: Primerjava izračunov po Auricchiovem modelu z eksperimentalnimi podatki za superelastične vzorce nitinola št. 1 (66°) in št. 2 (65°) iz **tabele 2**

mesh parameters for the esophageal stent during crushing are listed in **Table 3**. Using the Abaqus contact module, only the contact between the outer stent surface and the inner plane surfaces is activated. In this contact algorithm, the master surface for the rigid planes and the slave surface for the stent are concurrently applied. A penalty interaction property is employed to enforce the impermeable boundaries. Two inflexible similar plates are applied for the pressure on the stent. The distance between the two planes is 25 mm (equal to the stent nominal diameter value in the expanded configuration). The rigid-flexible contact pairs are formed between the planes and the surfaces of the stent and no friction is considered for any contact pair. According to Petrini et al.,⁷ the lower plane is fixed in all directions and the higher plane can just move in the Y direction. Four stent nodes close to the planes are fixed in the X and Z directions. As a result, the stent can be compressed just in the Y direction. Displacement loading is thus applied on the higher plane: the higher plane compresses the stent and reduces the distance between the two planes to 7.5 mm (a 70 % reduction in the diameters of the stents) and 2.5

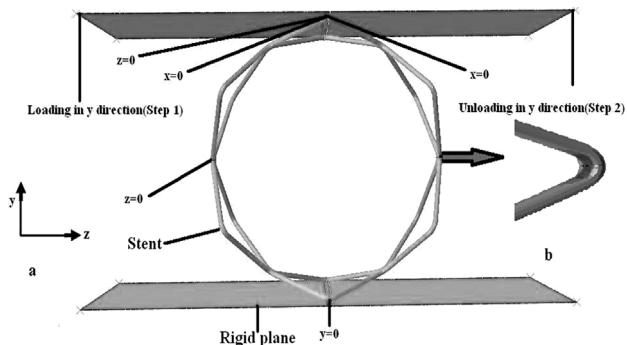


Figure 4: a) Schematic representation of the boundary conditions for the crushing of the esophageal stent, b) exact position of the stent, for which numerical calculations have been performed

Slika 4: a) Shematski prikaz robnih pogojev za tlačenje opore požiralnika, b) točen položaj opore, kjer so bili izvršeni numerični izračuni

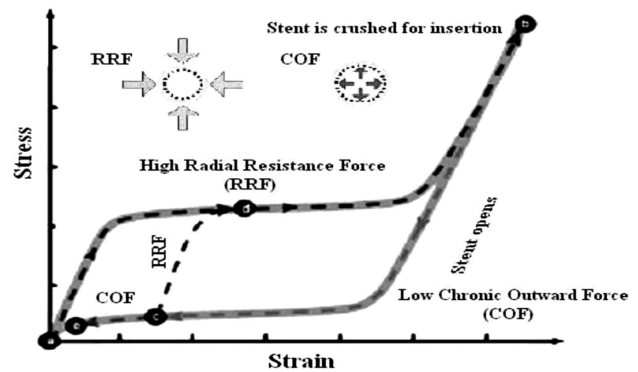


Figure 5: RRF and COF of a typical superelastic hysteresis loop¹⁵
Slika 5: RRF in COF značilne superelastične histerezne zanke¹⁵

mm (a 90 % reduction in the diameters of the stents). The higher plane then moves back to its first location and recovers the stent. The reaction force on the plane is collected during the compression and recovers the process. The boundary conditions for the crushing of the esophageal-duct stent are shown in **Figure 4**. To decrease the calculation time and use the benefits of the axis symmetry, only one-quarter of the geometrical model is analyzed. The temperature is adjusted to 37 °C (the body temperature) during the simulation.

3 RESULTS AND DISCUSSION

Duerig et al.⁴ have shown a favorable clinical performance of the nitinol stents used for esophageal application due to a complete superelastic hysteresis loop, the lowest chronic outward force (COF), the highest radial resistive force (RRF) and the long plateau stress. Gideon et al.²⁰ have shown that a lower stress and a higher strain on the critical points of a stent allow a suitable clinical performance. COF and RRF are related to the superelastic behavior of a nitinol stent. A typical superelastic stress-strain curve for a self-expanding stent is shown in **Figure 5**.¹⁵ The stent is crushed by two rigid planes (path a-b) and later deployed, reaching stress equilibrium with the duct at point c. The force against the duct is controlled with the unloading curve (COF) and the force resisting deformation is controlled with the loading curve (RRF). Generally, stent designers aim for as high an RRF as possible, with as low a COF as possible.⁴ Furthermore, two particular points should be considered so that the stents are never in the elastic region. In addition, the stents are known for having a satisfactory superelastic behavior. Moreover, the stents should be in the failure-safe domain from mechanical strength and strain.²¹ Beule et al.⁹ have shown that an increase in the segment angles, radial contraction of the stent and decrease in the length of the segments improve the performance of the stent. Their study indicates, however, that due to the transformation-temperature (A_T) effects, in the case of a lower angle and longer segments, a better superelastic performance is gained with the nitinol stent.

Table 3: Mesh parameters for the esophageal stent during crushing
Tabela 3: Parametri mreže za oporo požiralnika med stiskanjem

Material	Element type	Number of elements	Number of nodes
Stent	C3D8I	3600	14400
Rigid plane	R3D4	20000	20402

Table 4: Results for stress, strain and displacement of the esophageal stent under 70 % crushing

Tabela 4: Rezultati napetosti, raztezka in radialnega raztezka opore požiralnika pri 70-odstotnem stiskanju

Stent model	Maximum stress (MPa)	Maximum strain	Radial displacement
Sample 1 from Table 2	269.9	0.00862	0.00642
Sample 2 from Table 2	229.9	0.00850	0.011

Table 5: Results for stress, strain and displacement of the esophageal stent under 90 % crushing

Tabela 5: Rezultati napetosti, raztezka in radialnega raztezka opore požiralnika pri 90-odstotnem stiskanju

Stent model	Maximum stress (MPa)	Maximum strain	Radial displacement
Sample 1 from Table 2	486.8	0.0152	0.00246
Sample 2 from Table 2	373.5	0.0146	0.00340

This advantage is consistent with the observations of Beule et al.⁹ Every nitinol stent with a high A_f temperature (close to the body temperature) will be in the lower COF range with a better fatigue life. A nitinol stent of an acceptable performance does not require a high RRF for a low obstruction of esophageal ducts. With a high obstruction of esophageal ducts, the A_f temperature of nitinol should be much lower than the body temperature due to the need for a high RRF.

With respect to the nitinol stents illustrated in **Figure 1** and quantified in **Table 1**, this paper first discusses the results of the 70 % standard crushing according to Petrini et al.⁷ and then the results of the 90 % crushing. According to **Table 4**, the maximum stress, strain and displacement during the 70 % crushing show an elastic behavior of the esophageal stents. A comparison of sample No. 1 from **Table 2** and sample No. 2 from **Table 2** indicates that a decrease in the maximum stress from 269.9 MPa to 229.9 MPa results in an insignificant reduction in the maximum strain from 0.00862 to 0.00850. The maximum radial displacement increases from 0.00642 to 0.011 under the same conditions. This increasing ratio is about 71.3 %. Also, these stents, owing to the non-superelastic behavior, are not suitable for esophageal applications. According to the stent shown in **Figure 1** and **Table 1** (sample No. 1 from **Table 2**), the minimum stress to initiate a martensitic transformation is 390 MPa. The stress level of this stent is not sufficient for achieving the superelastic behavior.

Consequently, this stent is not appropriate for an esophageal application. Therefore, discussing other test results of the stent has no meaning. As a result, the desired superelastic behavior is not achieved. Finally, considering the non-superelastic behavior, the stent would not be suitable for an esophageal-stent application. With the material properties of sample No. 2 from **Table 2**, the minimum stress to initiate a martensite transformation is 344 MPa. Discussing the test results for the stents with unacceptable stress levels is not necessary, even if they can provide a normal spring behavior. As a result, the desired superelastic behavior is not achieved with the stents that have very low stresses. According to **Table 5**, a comparison of sample No. 1 from **Table 2** and sample No. 2 from **Table 2** indicates that a decrease in the maximum stress from 486.8 MPa to 373.5 MPa results in a insignificant reduction in the maximum strain from 0.0152 to 0.0146. The maximum radial displacement increases from 0.00246 to 0.00340 under the same conditions. This increasing ratio is about 38.2 %. The maximum stress on the internal curvature of the stent of sample No. 2 from **Table 2** is lower than that of sample No. 1 from **Table 2**. The former is, hence, preferred to the latter. The maximum strain on the internal curvature of the stent of sample No. 1 from **Table 2** is slightly higher than that of sample No. 2 from **Table 2**. Consequently, the former helps the dynamic motion of the stent to be in harmony with the duct. In summary, despite the fact that the standard crushing level is 70 %, the stents showed no superelastic behavior at this crushing level. An increase in the crushing from 70 % to 90 % results in an appearance of the superelastic behavior and produces a favorable condition for fabricating esophageal stents. This indicates that the designed stents are capable of withstanding higher strain forces of up to 90 % while preserving the superelastic behavior. In addition, a failure of a stent with this value is safe.²¹ With 90 % crushing, the stent shown in **Figure 1** and quantified in **Table 1** (sample No. 2 from **Table 2**) exhibits a more acceptable mechanical performance as far as the material properties are concerned. Considering the properties of the materials used in **Table 2** (samples 1 and 2) at 22 °C and 24 °C, respectively, there should be a different range of loading and unloading plateau stress. A lower A_f temperature of nitinol and extensive loading and unloading stress levels of the mechanical hysteresis are related to the superelastic behavior. Duerig et al.⁴ have shown that a difference of 7 °C in the A_f temperature results in about a 50 % variation in the stress level. Patel et al.¹⁴ have shown that a decreasing A_f temperature results in a higher upper plateau stress. **Figure 6** shows an increase in the upper plateau stress due to the difference between the A_f temperatures of 22 °C and 24 °C. For a difference of 2 °C, the expected 15 % variation has been confirmed with the experimental and numerical results⁴. The angular difference between the stent geometries illustrated in **Figure 1** and **Table 1** is

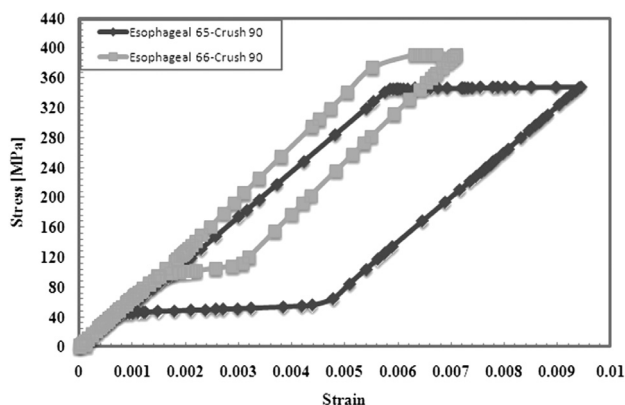


Figure 6: Comparison of the superelastic behavior of the 90 % crushed esophageal-duct stent with the material properties of sample No. 1 (66°) and 2 (65°) from **Table 2**

Slika 6: Primerjava superelastičnega vedenja 90-odstotno stisnjene opornice požiralne cevi z lastnostmi materiala vzorca št. 1 (66°) in št. 2 (65°) iz **tabele 2**

only 1 degree. The basis for the aforementioned geometric design results from the age treatment of the Ti-50.7 % Ni alloy at 500 °C and the time intervals of 30 min and 60 min.¹⁵ However, the stent shown in **Figure 1** and **Table 1** (sample No. 2 from **Table 2**) reveals a more acceptable mechanical and practical performance in comparison with that illustrated in **Figure 1** and **Table 1** (sample No. 1 from **Table 2**). Nevertheless, according to **Figure 1** and **Table 1** (sample No. 1 from **Table 2**) and considering the short segments of the stent and a wider angle between the stent segments, better geometric conditions for the crushing test are achieved and a more reasonable mechanical performance is expected as described by Beule et al.⁹ The acceptable mechanical performance of the stent from **Figure 1** and **Table 1** (sample No. 2 from **Table 2**) is mainly rooted in its material properties obtained by the ageing treatment of the Ti-50.7 % Ni alloy at 500 °C, the time interval of 60 min and the optimum angle of 65°.¹⁵ The results of the numerical calculations performed for the curve of the stent in **Figure 4b** obtained with crushing under a high pressure are demonstrated in **Figure 6**. Consequently, based on the desired mechanical standards of the stents and according to **Figure 6**, the stent shown in **Figure 1** and quantified in **Table 1** (sample No. 2 from **Table 2**) with a low COF, high RRF, superelastic behavior related to the hysteresis loop and no stress concentration at the internal curvature of the stent is preferred to the other types.

4 LIMITATIONS

This simulation is complex because of the contacts, non-linear geometry, the material nonlinearity, large deformation, additional buckling and bending of the stent. On the other hand, during crushing, the self-contact phenomenon (the contact between the edges of the

stent) is anticipated and it can cause additional stress at the contact points. However, according to Wu et al.,²² owing to the superelasticity behavior of the stent, these types of stress can be neglected. The crushing tests have only been performed in the longitudinal orientations. It is obvious that more experiments and simulation results related to the stenosis degree of ducts are needed to reach to a comprehensive conclusion.

5 CONCLUSIONS

The effects of design parameters and material properties obtained from the ageing treatment on the mechanical performance of the z-shaped nitinol stents for esophageal ducts are investigated. A nitinol stent shows a better mechanical and practical performance owing to only a 1-degree angular difference between the segments of the stent. The material is the Ti-50.7 % Ni alloy, age treated at 500 °C for a 30 min to 60 min time interval. The nitinol stent with the segment angle of 65°, crushing of 90 % and the A_f temperature of 24 °C having a low COF and high RRF shows a favorable superelastic behavior and a low stress concentration on the internal curvature. The superelasticity and hysteresis behavior of nitinol are proven to be promising properties for the z-shaped wire stents used for fabricating esophageal ducts.

Acknowledgments

The authors would like to thank Dr. Amir R. Khoei, professor at Civil Engineering Department, Sharif University of Technology and Mr. Ehsan Haghghat, research assistant at McMaster University for assisting with the implementation of the simulation program to model the samples. We would also like to thank Mr. Seyed M. Seyed Salehi, PhD student at Material Science and Engineering Department, Sharif University of Technology for many helpful discussions on the numerical analysis of the stents.

6 REFERENCES

- ¹ K. Hameed, H. Khan, R. Din, J. Khan, A. Rehman, M. Rashid, Self-Expandable metal stents in palliation of malignant esophageal obstruction, *Gomal J. Med. Sci.*, 8 (2010), 39–43
- ² D. Renteln, B. Walz, B. Riecken, T. Kayser, K. Caca, Endoscopic management of acute esophageal dissection by using a covered self-expanding metal stent, *Gastro. Endoscopy*, 69 (2009), 577–580
- ³ D. Stoeckel, A. R. Pelton, T. Duerig, Self-expanding Nitinol stents: material and design considerations, *Eur. Radio*, 14 (2004), 292–301
- ⁴ T. Duerig, D. Tolomeo, M. Wholey, An overview of superelastic stent Design, *Min. Invas. Ther. and Allied Technol.*, 9 (2000), 235–246
- ⁵ B. Patrick, B. Snowhill, L. John, L. Randall, H. Frederick, Characterization of Radial Forces in Z Stents, *Inves. Radiology*, 36 (2001), 521–530
- ⁶ F. D. Whitcher, Simulation of in vivo loading conditions of Nitinol vascular stent structures, *Comput. Struct.*, 64 (1997), 1005–1011

- ⁷ L. Petrini, F. Migliavacca, P. Massarotti, S. Schievano, G. Dubini, F. Auricchio, Computational studies of shape memory alloy behavior in biomedical applications, *J. Biomech. Eng.*, 127 (2005), 716–725
- ⁸ C. Kleinstreuer, Z. Li, C. Basciano, S. Seelecke, M. Farber, Computational mechanics of Nitinol stent grafts, *J. Biomech.*, 41 (2008), 2370–2378
- ⁹ M. Beule, S. Cauter, P. Mortier, D. Loo, R. Impec, P. Verdonck, B. Verheghe, Virtual optimization of self-expandable braided wire stents, *Med. Eng. Phys.*, 31 (2009), 448–453
- ¹⁰ G. Silber, M. Alizadeh, A. Aghajani, Finite element analysis for the design of Self-expandable Nitinol stent in an artery, *I. J. Energ. Tech.*, 2 (2010), 1–7
- ¹¹ H. V. D. Merwe, B. D. Reddy, P. Zilla, D. Bezuidenhout, T. A. Franz, Computational study of knitted Nitinol meshes for their prospective use as external vein reinforcement, *J. Biomech.*, 41 (2008), 1302–1309
- ¹² Y. Liu, S. P. Galvin, Criteria for pseudoelasticity in near-equiatomic NiTi shape memory alloys, *Acta Materialia*, 45 (1997) 11, 4431–4439
- ¹³ K. Yeung, K. Cheung, W. Lu, C. Chung, Optimization of thermal treatment parameters to alter austenitic phase transition temperature of NiTi alloy for medical implant, *Mater. Sci. Eng. A*, 383 (2004), 213–218
- ¹⁴ M. Patel, D. Plumley, R. Bouthot, The Effects of Varying Active A_f temperatures on the Fatigue Properties of Nitinol Wire, *Proc. of ASM Conf.*, Boston, 2005, 1–8
- ¹⁵ X. Liu, Y. Wang, D. Yang, M. Qi, The effect of ageing treatment on shape-setting and superelasticity of a Nitinol stent, *Mater. Charact.*, 59 (2008), 402–406
- ¹⁶ F. Auricchio, R. Taylor, Shape-memory alloys: Modeling and numerical simulations of the finite-strain superelastic behavior, *Comput. Methods Appl. Mech. Engrg.*, 143 (1997), 175–194
- ¹⁷ J. Lubliner, F. Auricchio, Generalized plasticity and shape memory alloy, *I. J. Solid. Struct.*, 33 (1996), 991–1003
- ¹⁸ N. Rebelo, N. Walker, H. Foadian, Simulation of implantable stents, *Abaqus user's conf.*, 143 (2001), 421–434
- ¹⁹ A. G. Prince, G. L. Quarini, J. E. Morgan, J. Finlay, Thermomechanical response of 50.7 % Ni-Ti alloy in the pseudoelastic regime, *Mater. Sci. Tech.*, 19 (2003), 561–565
- ²⁰ V. Gideon, P. Kumar, L. Mathew, Finite Element Analysis of the Mechanical Performance of Aortic Valve Stent Designs, *Trends Biomater. Artif. Organs*, 23 (2009), 16–20
- ²¹ A. R. Pelton, V. Schroeder, M. Mitchell, X. Gong, M. Barneya, S. Robertson, Fatigue and durability of Nitinol stents, *J. Mech. Behav. Biomed. Mater.*, 1 (2008), 153–164
- ²² W. Wu, M. Qi, X. Liu, D. Yang, W. Wang, Delivery and release of Nitinol stent in carotid artery and their interactions: a finite element analysis, *J. Biomech.*, 40 (2007), 3034–3040

INVESTIGATION OF THE EFFECT OF SKIN-PASS ROLLING ON THE FORMABILITY OF LOW-CARBON STEEL SHEETS

PREISKAVA UČINKA DRESIRNEGA VALJANJA NA PREOBLIKOVALNOST MALOGLJIČNE JEKLENE PLOČEVINE

Davoud Asefi, Hussein Monajatizadeh, Amir Ansaripour, Ahmadreza Salimi

Department of Materials Engineering, Najafabad Branch, Islamic Azad University, P.O.Box 517, Isfahan, Iran
h_monajati@iaun.ac.ir

Prejem rokopisa – received: 2012-10-26; sprejem za objavo – accepted for publication: 2012-12-11

In the present survey, the effects of skin-pass elongation and cold-rolling reduction on the formability parameters are studied. For this reason, three sets of samples, including those from industry and laboratory, were evaluated. In the first set, samples with different hot-rolling conditions were submitted to the same amount of skin reduction and their final mechanical properties were compared. In the second set, samples with similar conditions were tested with different amounts of laboratory cold reduction after full annealing and, finally, in the third set, fully annealed samples went through different amounts of industrial elongations in a skin-pass line. The results showed that skin reduction has a significant effect on the work-hardening coefficient and it should be kept at the minimum value required to prevent the yield-drop phenomenon. This value was observed to be around 0.5 % for St14 sheets with a thickness of 0.7 mm.

Keywords: ferritic steels, plastic behavior, destructive testing, cold rolling

Preiskovan je bil učinek raztezka in redukcije prereza pri hladnem preoblikovanju na parameter preoblikovanja. Zato so bile ocenjene tri skupine industrijskih in laboratorijskih vzorcev. V prvi skupini so bili v različnih razmerah vroče valjani vzorci dresirno valjani z enako redukcijo, primerjane pa so bile tudi njihove končne mehanske lastnosti. V drugi skupini so bili preizkušeni laboratorijski vzorci z različnimi stopnjami hladne redukcije po predhodnem mehkem žarjenju, v tretji skupini pa mehko žarjeni vzorci izpostavljeni različnim stopnjam raztezka na industrijski liniji za dresiranje. Rezultati so pokazali, da ima redukcija pri dresiranju pomemben vpliv na koeficient hladnega utrjevanja, ki naj bi imel najmanjšo vrednost, da bi se preprečil pojav zmanjšanja plastičnosti. Ugotovljeno je bilo, da je pri pločevini iz jekla St14 z debelino 0,7 mm ta vrednost okrog 0,5 %.

Ključne besede: feritna jekla, plastičnost, porušni preizkusi, hladno valjanje

1 INTRODUCTION

Complex stamping is an important stage in forming automotive body parts and various other products. The steel industry has made many attempts to enhance the quality of their products so that they would lead to easier and faster metal-forming processes. The formability is defined as the resistance of a material to necking and thinning in the thickness direction. The former is known to be related to the work-hardening exponent (n) and the latter to the average plastic-strain ratio (r).^{1,2} Drawability, on the other hand, is the ability of a material to easily flow in the plane of the sheet without thinning in the thickness direction, and stretchability represents the ability of the material to resist localized necking.^{3,4} In a combined forming operation, r , the normal anisotropy and n , the work-hardening coefficient can be representatives of the drawability and stretchability, respectively. They are obtained with a uniaxial tensile test. Industrial steel sheets with typical values of (\bar{r}) in the range 1.6–2.0 and n in the range 0.22–0.24 are known as deep-drawing-quality (DDQ) products.⁵

In recent years, the effects of process conditions and metallurgical microstructure on the quality of low-carbon steel sheets have been studied by mathematical

models that use experimental observations as their database. The formability is affected by all the process parameters, such as hot rolling, annealing and the skin-pass conditions.^{6,7} Numerous studies have been published regarding the influence of the processing parameters on the microstructure and formability of low-carbon steel.^{8–10} However, little has been published on the effect of the skin-pass parameters on the formability.¹¹

Skin pass or temper rolling is the last stage in thin-strips production, introducing a small plastic strain in the sheet to bypass the non-uniform deformation region and erase the yield-point jogs. It also improves the flatness of the strip and makes a certain surface roughness and smoothness.¹² The reduction percentage of temper rolling has a significant effect on its mechanical properties. Therefore, the preset of the reduction percentage is restricted not only by the flatness and the surface roughness of the strip steel, but also by the mechanical properties. The mechanical properties of low-carbon steels are influenced by a small strain processing treatment.^{13,14} But the effects of a little cold strain and the reduction percentage of skin pass on the formability parameters of steel sheets still need to be investigated. This important issue is the purpose of the present study.

2 EXPERIMENTAL PROCEDURE

2.1 Materials

Three kinds of samples were used in this study. The chemical composition of each is shown in **Table 1**. The first set, prefixed by A from 1 to 5, had a different Al-to-N ratio and coiling temperature (CT), as shown in **Table 1**. All of them received the same amount of 0.7 % industrial skin reduction and their properties were measured before and after the skin-pass process.

The effect of the skin-pass strain on the final formability of the sheets was studied in set B. For this reason, different amounts of cold reduction were applied using a laboratory rolling machine on 40 cm × 60 cm samples obtained from a longitudinal section of a coil after an industrial box anneal and near each other. Again, their properties were measured before and after the skin pass (**Table 2**).

It should be noted that there are two operations in skin pass rolling: a stretching that is applied using a tension leveler and a compression applied from rolls. As it was not possible to apply the stretching load on laboratory skin rolling, a separate set of samples, set C, was imposed on a different amount of reductions using an industrial skin machine to investigate the effect of the real skin process on the final properties.

2.2 Experiments

Standard uniaxial tensile tests were carried out on the samples in three directions, i.e., 0°, 45° and 90°, corresponding to the rolling direction, to obtain the strength and ductility of the specimens as well as the r and n coefficients. The normal anisotropy was calculated according to the equation:

$$\bar{r} = (r_0 + 2r_{45} + r_{90})/4 \quad (1)$$

\bar{n} was also calculated in a similar way to reach an average value.²

The average grain sizes (d) of the samples were measured according to ASTM E112-96 (Jeffries method) and the optical micrograph of the samples was prepared by a standard metallographic technique. As the grain structure in low-carbon steel sheets after cold rolling and box annealing is generally pancaked, the aspect ratio of the elongated grains was also evaluated using measurements of the large and small diameters of the grains, separately.

3 RESULTS AND DISCUSSION

3.1 Effects of the process parameters on the final properties under similar skin-pass conditions

The magnitudes of \bar{r} and \bar{n} for the samples of set A, before and after the skin pass, are illustrated in **Figure 1**. Although \bar{r} does not demonstrate any large change before and after the skin pass, the variations of \bar{n} are drastic, clearly showing a significant decrease after the treatment.

In accordance with **Figure 1a**, the skin pass does not have any significant effect on \bar{r} . This parameter is mostly affected by grain orientation or texture.² It has been shown that high \bar{r} values are displayed by materials that have a high proportion of grains oriented with {111} planes parallel to the sheet plane. The {111} fiber texture is particularly beneficial for imparting good deep drawability.¹⁵ It has also been shown that the morphology of cementite particles and the precipitation of fine AlN precipitates control the texture of low-carbon steel

Table 1: Chemical composition of the investigated samples in mass fractions, w/%

Tabela 1: Kemijska sestava preiskovanih vzorcev v masnih deležih, w/%

NUM	w(C)	w(Si)	w(Mn)	w(Al)	w(N)/(μg/g)	w(Al)/w(N)	CT/°C
A1	0.045	0.009	0.209	0.049	19	25.7	560
A2	0.049	0.01	0.204	0.047	30	15.6	560
A3	0.039	0.009	0.209	0.049	19	25.7	620
A4	0.05	0.01	0.0220	0.055	58	9.4	625
A5	0.05	0.01	0.220	0.055	58	9.4	625
B	0.036	0.012	0.27	0.043	25	17.2	–
C	0.034	0.009	0.215	0.045	35	12.8	–

CT – Coiling Temperature

Table 2: Normal anisotropy, work hardening values, applied reduction and grain size and aspect ratio for the samples in set B

Tabela 2: Normalna anizotropija, vrednosti utrjevanja pri preoblikovanju, uporabljena redukcija, velikost zrn in razmerje širina proti debelini vzorcev iz skupine B

NUM	Cold reduction (%)	\bar{r}	\bar{n}	Grain size $d/(\mu\text{m})$	Aspect ratio
B0	0	1.60	0.24	26	2.26
B1	2.5	1.60	0.19	24	2.9
B2	3.8	1.62	0.19	26	3.1
B3	4.8	1.59	0.15	27	3.6

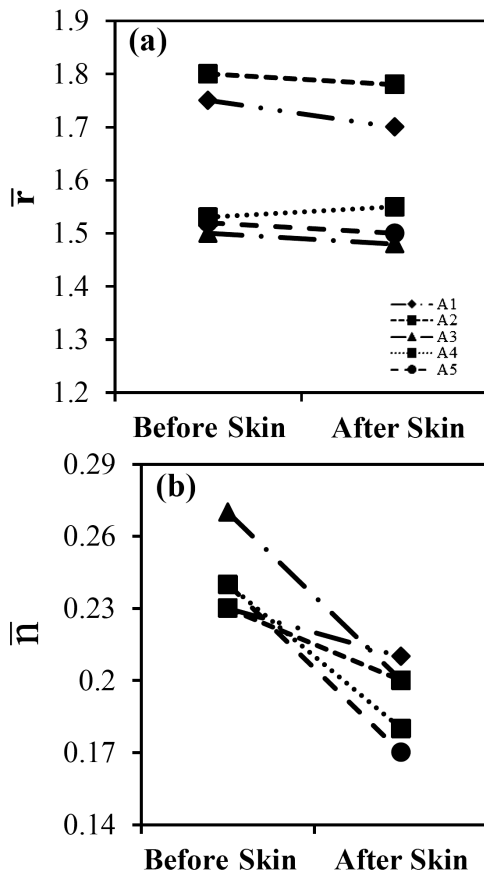


Figure 1: Variation of: a) \bar{r} and b) \bar{n} before and after the skin-pass rolling for samples in set A
Slika 1: Spreminjanje: a) \bar{r} in b) \bar{n} pred dresirnim valjanjem vzorcev iz skupine A in po njem

sheets.^{15,16} The most important process parameters affecting these microstructural features are hot and cold. The rolling parameters and subsequent annealing parameters, such as the heating rate and soaking time are important.^{6,10} The most important microstructural effect exerted by the limited strain in skin-pass rolling, except the very small strain near the surface, is releasing dislocations from short-range local locks of carbon and nitrogen atoms and eliminating the yield drop and heterogeneous deformation.^{8,9} Therefore, cold deformation due to the skin-pass process has a slight effect on the volume fraction of $\{111\}$ fiber and its influence on \bar{r} is almost negligible.¹

Figure 1b implies that for all samples of set A, \bar{n} is decreased considerably after the skin-pass process.

The variation percentage of \bar{n} in each sample is shown in **Figure 2**. It can also be seen that the drop value is not the same for all the samples, varying in the range of 8.7 % to 30 % for different samples. This reduction is due to the direct relationship between the work-hardening coefficient and the microstructure variations. The relationship between the microstructure and the work-hardening coefficient can be explained by Eq 1, which was first expressed by Antoine:^{8,9}

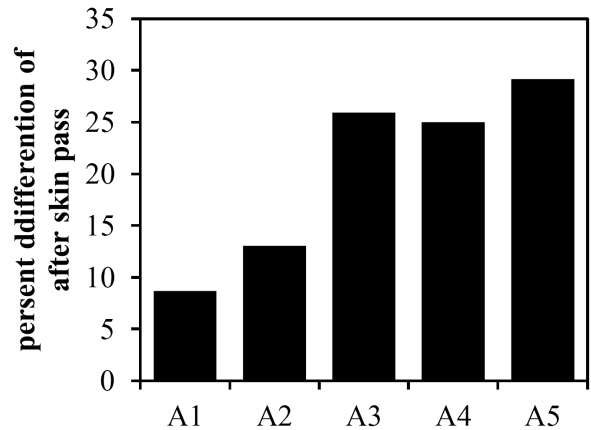


Figure 2: Variation percentage of \bar{n} after skin pass in the samples of set A
Slika 2: Spreminjanje deleža \bar{n} pri dresirnem valjanju vzorcev iz skupine A

$$n = 0.450 - 0.001(\sigma_p + \sigma_{SA} + \sigma_{GB} + \sigma_{PCT} + \sigma_{F0.2}) \quad (2)$$

The stresses in this equation are the strengthening contribution of Peierls (σ_p), the solid solution (σ_{SA}) (both affected by the chemical composition), the precipitates (σ_{PCT}), the grain boundaries (σ_{GB}) and the dislocation density ($\sigma_{F0.2}$). The above equation shows that all the mentioned microstructural factors affect n directly. Among them, the dislocation density and the grain-boundary characters (in the form of the shape and the aspect ratio) may be changed during the skin-pass rolling, while the chemical composition's and the precipitates' contributions remain unchanged.

The study of the grain characteristics in these samples implied a very negligible difference between the grain elongations. Therefore, the only influential microstructure factor would be the variation of the dislocation density in the various samples.

Among the microstructural parameters that may affect the dislocation density during cold work, the precipitates are of paramount importance. They can play the role of an obstacle preventing dislocation movement and increase the work-hardening rate. Hence, the work-hardening coefficient decreases. This can be explained better by referring to the results of Antoine's work. **Figure 3** illustrates the dislocation density calculated for the samples with a different volume percentage of TiC precipitates after 0.02 % strain. These data are derived from the results of Antoine's work. It can be seen from the figure that by increasing the volume fraction of the precipitates, the dislocation density is increased and n is decreased.^{8,9}

The difference in the amount of work hardening coefficient for the samples in set A, therefore, may be attributed to the volume fraction of the precipitates before the skin pass, which in the case of St14 steels, and in absence of carbide-forming elements like Ti, are mostly AlN particles. The volume fraction and the size of the AlN precipitates are influenced by various pro-

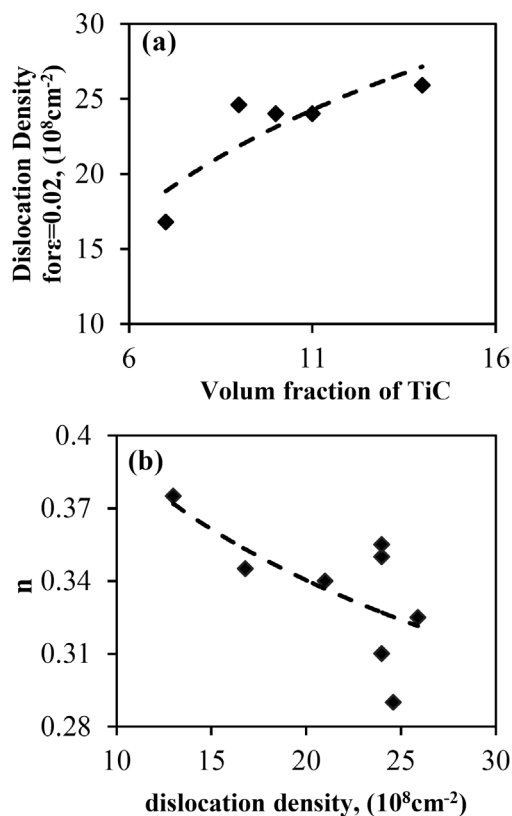


Figure 3: The dependence of: a) dislocation density on volume fraction of TiC precipitates and b) work-hardening coefficient on the dislocation density, calculated and drawn from Antoine's results^{9,10}
Slika 3: Odvisnost: a) gostote dislokacij od volumenskega deleža izločkov TiC in b) koeficient utrjevanja pri hladni predelavi na gostoto dislokacij, izračunano in vzeto iz rezultatov Antoina^{9,10}

duction parameters, with the most important ones being the cooling rate and the coiling temperature after hot rolling,¹⁰ and the heating rate during annealing.¹ The reported CTs for the samples in set A are shown in **Table 1**. It is clear that A3, A4 and A5 experienced the highest CT.

Coiling above 600 °C can promote the precipitation of AlN precipitates and affect the microstructural features during the following annealing process.¹⁰ As all the samples in set A have experienced the same annealing conditions, it can be concluded that the differences in the CT have led to a different amount of work-hardening coefficient due to the different volume fraction of AlN under the same conditions of the skin-pass process.

3.2 Effect of experimental cold reduction on the formability parameters of fully annealed samples

Figure 4 shows the dependences of \bar{r} and \bar{n} on the percentage of cold reduction (after full annealing) for the samples in set B. It is implied that while increasing the cold reduction the percentage does not have any obvious effect on \bar{r} in the examined range,¹ it decreases \bar{n} in a discernible manner. For instance, in the case of the sample without cold work, the amount of \bar{n} is almost 0.25,

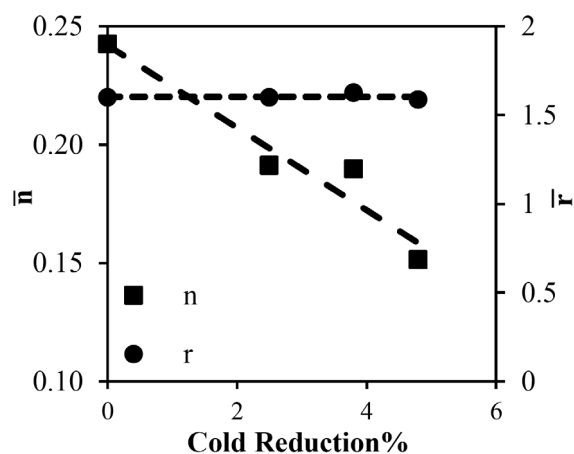


Figure 4: Variation of \bar{r} and \bar{n} with cold reduction in samples of set B
Slika 4: Spreminjanje \bar{r} in \bar{n} z redukcijo v hladnem vzorcev iz skupine B

whereas it reaches 0.15 after 4.8 % cold reduction. As mentioned in the previous section, the variations of \bar{n} with the percentage of cold work may be related to variations in the dislocation density. On the other hand, the slip distance of dislocations, which is in relation to the grain size, is expected to affect \bar{n} due to the increasingly homogeneous strain region.^{8,9} To examine this parameter, the variations of the grain size with applied elongation were characterized and illustrated in **Figure 5**.

As can be seen, the variation of grain size with increasing cold-work percentage in the examined range is not considerable. However, the grains' aspect ratio is increased in proportion to cold reduction percentage, due to the elongation along the rolling direction. This confirms that the most influential factor in decreasing \bar{n} with cold reduction is increasing the dislocation density. It suggests that the limitation of cold reduction in the skin-pass rolling can prevent an excess drop of \bar{n} . However, the amount of the reduction should be in such a range that would guarantee the elimination of the heterogeneous deformation region (yield drop phenomenon).

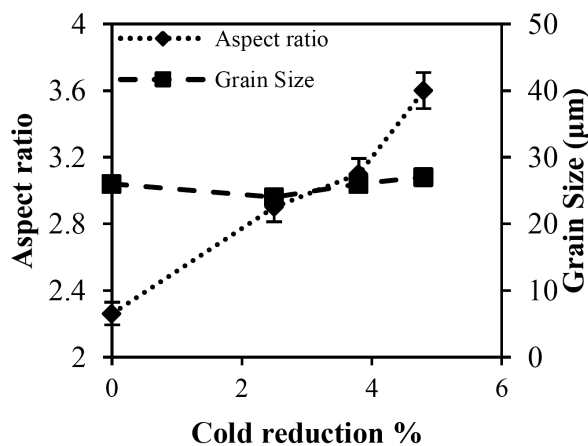


Figure 5: The relation of grain sizes and their aspect ratio to cold reduction in the samples of set B

Slika 5: Odvisnost velikosti zrn in njihovega razmerja širina-debelina, pri hladni redukciji vzorcev iz skupine B

3.3 Effect of skin-pass elongation on the formability properties of industrial samples

The effects of the skin-pass elongation on the \bar{r} and \bar{n} values in the samples of set C are shown in **Figure 6**. These samples had the same chemical composition (**Table 1**) and the same processing conditions, except the amount of elongation in the skin-pass step.

As can be seen in **Figure 6**, and as can be expected from the results of the previous section, the elongation percentage of the skin pass does not have any influence on \bar{n} , whereas it severely decreases \bar{r} . It should be noted that although the strain path in experimental skin rolling (compression from rolls and the tension applied on the whole line between the feeding and coiling rolls) is different from the laboratory rolling experiments (just compression from the rolls) in the previous section, it does not have any influence on the variation of the work-hardening coefficient. This is due to the fact that \bar{n} is mostly affected by the dislocation density, which is similar in the experimental range of strain in both laboratory and industrial experiments.

Figure 6 shows that the elongation percentage of 0.5 % in the skin pass has led to the highest amount of work-hardening coefficient. Laboratory tests showed that lower amounts of elongation percentage do not prevent the occurrence of yield-drop phenomenon. It may be concluded that the most suitable elongation percentage in the skin-pass step for the sheet thickness studied (0.7 mm) is 0.5 %.

4 CONCLUSIONS

In this study, low-carbon steel sheets were investigated from a formability point of view.

The following results were obtained. The work-hardening coefficient is mostly affected by the dislocation density. Any microstructural feature that can increase the dislocation density can decrease \bar{n} . While the skin-pass

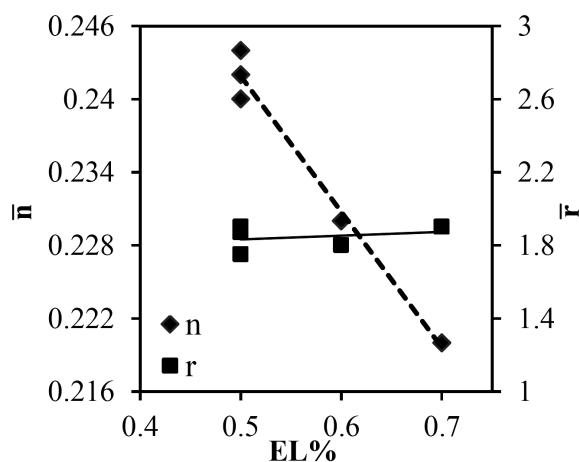


Figure 6: Variation of \bar{r} and \bar{n} with elongation percentage in skin-pass rolling for samples in set C

Slika 6: Spreminjanje \bar{r} in \bar{n} z deležem raztezka pri dresirnem valjanju vzorcev iz skupine C

reduction after full annealing does not have any large effect on \bar{r} , it may change \bar{n} drastically. Therefore, the limitation of skin reduction to a minimum value is required to prevent yield drop, which is an important process parameter that can preserve \bar{n} at an appropriate level after it reaches its maximum value during the annealing process. This value was observed in this study to be around 0.5 % for St14 sheets with a thickness of 0.7 mm.

Acknowledgements

This research was conducted under a contract with the Mobarakeh steel company, Isfahan, Iran. The support from the research & development management, MPT, and skin-pass and product laboratory personnel are gratefully appreciated.

5 REFERENCES

- Y. Jia, H. Guo, R. Li, H. Li, Effects of Rolling Processes on Yield Ratio and Formability of Hot Rolled Gas Cylinder Steel, *Journal of Iron and Steel Research, International*, 19 (2012) 3, 52–55
- M. Safavi, S. M. Abbasi, R. Mahdavi, Influence of Aluminum Content on Mechanical Properties and Cold Workability of Fe-33Ni-15Co Alloy, *Journal of Iron and Steel Research, International*, 19 (2012) 2, 67–72
- M. A. Akoy, E. S. Kayali, H. Cimenoglu, The influence of microstructural features and mechanical properties on the cold formability of ferritic steel sheets, *ISIJ Int*, 44 (2004), 422–428
- H. Monajati, D. Asefi, A. Parsapour, S. Abbasi, Analysis of the effects of processing parameters on mechanical properties and formability of cold rolled low carbon steel sheets using neural networks, *Comput Mater Sci*, 49 (2010), 876–81
- C. Capdevila, C. Garcia-Mateo, F. G. Caballero, C. Garcia de Andres, Neural network analysis of the influence of processing on strength and ductility of automotive low carbon sheet steels, *Comput Mater Sci*, 38 (2006), 192–201
- P. Antoine, S. Vandeputte, J. B. Vogt, Effect of microstructure on strain-hardening behavior of a Ti-IF steel grade, *ISIJ Int*, 45 (2005), 399–404
- P. Antoine, S. Vandeputte, J. B. Empirical model predicting the value of the strain-hardening exponent of a Ti-IF steel grade, *Mater Sci Eng A*, 433 (2006), 55–63
- C. Capdevila, J. P. Ferrer, F. G. Caballero, C. Garcia De Andres, Influence of processing parameters on the recrystallized microstructure of extra-low-carbon steels, *Metal Mater Trans A*, 37 (2006), 2059–2068
- H. Monajati, D. Asefi, Investigation of the effect of Work Hardening coefficient on Formability of low carbon Steel sheets and the improvement methods for its enhancement, Technical Report, Mobarakeh Steel Co, 2008
- H. Kijima, N. Bay, Influence of tool roughness and lubrication on contact conditions in skin-pass rolling, *J Mater Proc Tech*, 125 (2009) 48, 38–41
- Q. L. Ma, W. D. Cheng, L. H. Min, Effect of temper rolling on tensile properties of low-Si Al-killed sheet steel, *Journal of Iron and Steel Research, International*, 16 (2009) 3, 64–67
- E. J. Hoggan, R. I. Scott, M. R. Barnett, P. D. Hodgson, Mechanical properties of tension leveled and skin passed steels, *J Mater Proc Tech*, 125 (2002), 55–63
- R. K. Ray, J. J. Jonas, R. E. Hook, Cold rolling and annealing textures in low carbon and extra low carbon steels, *Int Mater Rev*, 39 (1994), 129–71

- ¹⁴ T. De Cock, C. Capdevila, F. C. Caballero, Global recrystallization model of low carbon sheet steels with different cementite contents, *Mater Sci Eng A*, 519 (2009), 9–18
- ¹⁵ J. Pero-Sanz, M. Ruiz-Delgado, V. Martinez, J. I. Verdeja, Annealing textures for drawability: influence of the degree of cold rolling reduction for low-carbon and extra low-carbon ferritic steels, *Mater Charact*, 43 (1999), 303–309
- ¹⁶ J. P. Ferrer, T. D. Cock, C. Capdevila, F. G Caballero, C. Garcia de Andres, Comparison of the annealing behavior between cold and warm rolled ELC steels by thermoelectric power measurements, *Acta Mater*, 55 (2007), 2075–83

SYNTHESIS, CHARACTERIZATION AND SENSING APPLICATION OF A SOLID ALUM/FLY ASH COMPOSITE ELECTROLYTE

SINTEZA, KARAKTERIZACIJA IN MOŽNOST UPORABE TRDNEGA KOMPOZITNEGA ELEKTROLITA GALUN-LETEČI PEPEL

Amit Sachdeva¹, Roja Singh², Pramod K. Singh², Bhaskar Bhattacharya²

¹Department of Nanotechnology, School of Bioscience and Biotechnology, Lovely Professional University, Phagwara-144411, Punjab, India

²Material Research Laboratory, School of Engineering and Technology, Sharda University, Greater Noida-201310, India
b.bhattacharya@sharda.ac.in

Prejem rokopisa – received: 2012-11-16; sprejem za objavo – accepted for publication: 2013-01-03

A new composite system using low-cost materials, potash alum and fly ash, was prepared and characterized using various techniques. Complex impedance spectroscopy was used for the conductivity measurement. A conductivity enhancement due to an addition of fly ash was observed and the maximum value was obtained with the 65 : 35 compositions. The maxima in conductivity can be explained with the percolation theory. Infrared spectroscopy (IR) as well as X-ray diffraction (XRD) confirmed the composite nature of the samples. Scanning electron microscopy (SEM) shows a good homogeneous mixture of the composite material which is essential for the conductivity enhancement. Based on the maximum-conductivity composition, a humidity sensor was fabricated which showed a good sensing behavior.

Keywords: composite, conductivity, IR, XRD, humidity sensor

Pripravljen in karakteriziran z različnimi tehnikami je bil nov kompozitni sistem iz poceni kalijevega galuna in letečega pepela. Za meritve prevodnosti je bila uporabljena kompleksna impedančna spektroskopija. Opaženo je bilo maksimalno povečanje prevodnosti zaradi dodatka letečega pepela pri razmerju sestave 65 : 35. Maksimum prevodnosti lahko razložimo s teorijo pronicanja. Infrardeča spektroskopija (IR) in rentgenska difrakcija (XRD) sta potrdili kompozitno osnovo vzorcev. Vrščna elektronska mikroskopija (SEM) je pokazala homogeno mešanico kompozitnih materialov, ki je ključna za povečanje prevodnosti. Na osnovi sestave z največjo prevodnostjo je bil izdelan senzor vlage, ki je pokazal dobro občutljivost.

Ključne besede: kompozit, prevodnost, IR, XRD, senzor vlage

1 INTRODUCTION

Composite materials are well known materials playing a dominant role in the industrial areas such as sport, aerospace, automotive industry and transportation. Due to the pioneering work of Liang and the subsequent efforts of many researchers, solid-composite electrolytes have been widely studied for their attractive behavior.¹ A significant enhancement in the conductivity has been observed in the multiphase materials with very small amounts of dispersoids. Fly ash, one of the dispersoids, has led to a multifold increase in the ionic conductivity when together with alumina. Several theoretical approaches have also been made to explain such a behavior. A comparison of a pure system and a two-phase mixture reveals that the two-phase mixtures in general exhibit a higher conductivity than those of the starting materials.²⁻⁵ In this paper we report on an increase in the conductivity for a new composite using two low-cost materials, i.e., potash alum and fly ash.

Fly ash is a waste product produced from coal-fired thermal-power stations during the combustion of coal. It is an alkaline grey powder which causes serious environmental problems. Due to the environmental regu-

lations, new ways of utilizing fly ash have to be explored in order to safeguard the environment and provide useful ways for its disposal. Hence, there is a considerable interest in utilizing fly ash as a raw material. More recently, materials scientists and engineers have suggested and devised various methods of using this waste product for the synthesis of some useful composites.⁶⁻⁸ Raw fly ash consists of quartz and mullite as the crystalline phases and an amount of a glassy phase.⁹ Efforts have been made to understand the electrical conductivity and dielectric behavior of fly ash and it was observed that this material possesses a very high relative dielectric constant of the order of 10^4 . Such a high dielectric constant is one of the important parameters in a capacitor fabrication and microwave absorption applications.⁸⁻¹⁴ The common alum is a double sulphate of potassium and aluminum, $K_2Al_2(SO_4)_4 \cdot 24H_2O$, which is a white crystalline powder readily soluble in water.

Through this work we have made a successful effort in preparing potash alum/fly ash composites and develop a humidity sensor which gives newer ways of a better utility of fly ash.

2 EXPERIMENTS

2.1 Preparation of the sample

Potash alum was purchased and used without any further purification while fly ash of an unknown purity and composition was collected from a local supplier. Appropriate amounts of potash alum and fly ash were weighed and thoroughly mixed in an agate mortar and pestle (≈ 2 h) and this was followed by a pulverization and pelletization in a nickel-plated steel die at the pressure of 2.5 t using a hydraulic pelletizer machine. The circular-shaped pellets thus obtained were 0.15 cm² in area and 4–6 mm in thickness. Infrared spectroscopy (Perkin Elmer 883) was carried out to study the composite nature and the functional groups present in the composite electrolyte. For further confirmation, X-ray diffraction was obtained using a Rigaku D/max-2500 in the range of $2\theta = 20\text{--}55^\circ$ with a scan rate of 1° min^{-1} . Scanning electron microscopy (SEM) was used to check the surface morphology. SEM micrographs were recorded using SEM (Hitachi S-570). For all the electrical measurements, a conductive silver paste was coated onto both surfaces of the pellets and dried under room environment. The complex impedance spectroscopy was used to calculate the bulk electrical conductivity of the polymer electrolyte films. In our laboratory we used pressure-contacted stainless-steel electrodes and connected them with a CH instruments electrochemical workstation (Model CHI604D) with a frequency range of 0.00001 Hz to 100 kHz. The electrical conductivity (σ) was evaluated using the following formula:

$$\sigma = R_b (l/A)$$

where σ is the ionic conductivity, R_b is the bulk resistance, l is the thickness of the pellet and A is the area of a given sample.

3 RESULTS AND DISCUSSION

3.1 Complex impedance spectroscopy

The ionic conductivity of pure potash alum and the alum doped with fly ash pellets were measured using the complex impedance spectroscopy. The bulk resistance (R_b) was determined from an intersection at a high frequency with the real axis in the impedance plots. The complex impedance plot of a typical potash alum/fly ash composition is shown in **Figure 1**. The ionic conductivity values were calculated from the impedance spectroscopic data and are listed in **Table 1** and plotted in **Figure 2**.

It is observed that initially the electrical conductivity of the composite increases with the increasing content of fly ash. It attains its maximum at 65 % fly ash and then decreases gradually. To interpret such variations in conductivity, several theoretical models have been proposed in the literature. The percolation model considers the highly conducting paths that were created along the

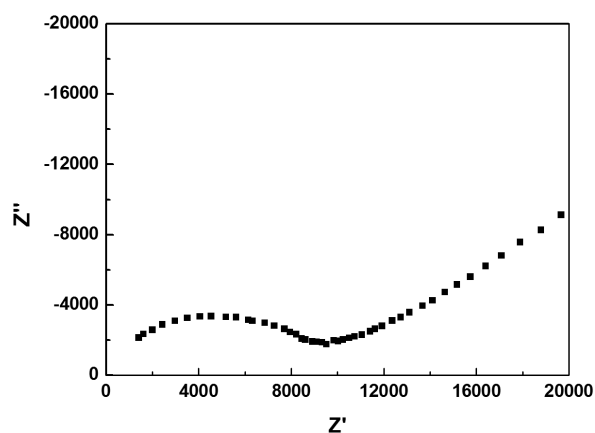


Figure 1: Complex impedance plot of a typical potash alum/fly ash solid electrolyte system

Slika 1: Kompleksno impedančno področje značilnega trdnega elektrolita kalijev galun-leteči pepel

Table 1: Room-temperature electrical conductivity of a potash alum/fly ash composite system

Tabela 1: Električna prevodnost kompozitnega sistema kalijev galun-leteči pepel pri sobni temperaturi

Composition, mass fraction, w/% Potash alum/fly ash	Electrical conductivity $\sigma/(S/cm)$
95 : 5	3.2×10^{-6}
85 : 15	5.3×10^{-6}
75 : 25	9.2×10^{-6}
65 : 35	1.5×10^{-5}
60 : 40	1.2×10^{-5}
40 : 60	5.4×10^{-6}
10 : 90	4.6×10^{-6}

interface between the host electrolyte and the dispersoid. In the present system the conductivity maxima could be explained with the percolation model.⁹ The maximum is obtained for the composition, with which the percolation threshold is achieved. The water of crystallization

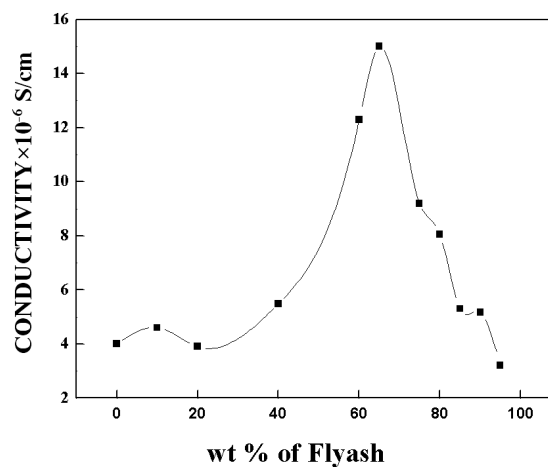


Figure 2: Variation in conductivity with the concentration of fly ash in a potash alum/fly ash composite system

Slika 2: Spreminjanje prevodnosti s koncentracijo letečega pepela in kalijevega galuna v kompozitnem sistemu

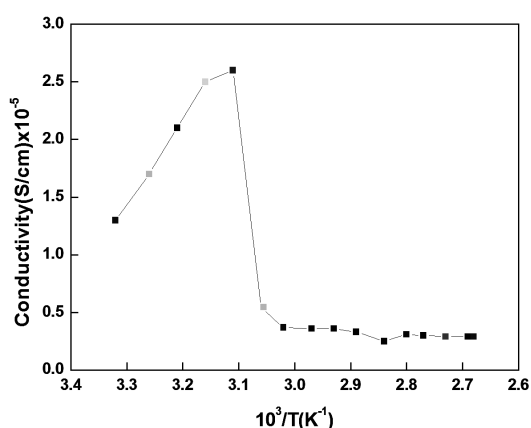


Figure 3: Variation in conductivity with temperature (maximum conductivity)

Slika 3: Spreminjanje prevodnosti s temperaturo (maksimalna prevodnost)

present in the alum gets adsorbed on the surface of the composite, in which the movement of H^+ and OH^- ions is responsible for an increase in the conductivity. The decrease in the conductivity after the maximum is similar to those obtained in similar composite systems.¹⁵⁻¹⁷

3.2 Temperature dependence of conductivity

Figure 3 shows the variation in conductivity with the temperature of the maximum conductivity composition of the composite. The variation in conductivity indicates that the physisorbed water present in potash alum plays an important role in the conductivity enhancement. The conductivity rises with an increase in the temperature up to $\approx 50^\circ C$ and then begins to fall; after this a constant value is attained. This is because the physisorbed water present in potash alum is lost between $45^\circ C$ to $50^\circ C$ leading to a loss of the H^+ and OH^- ions that were responsible for the conductivity of the composite sample.

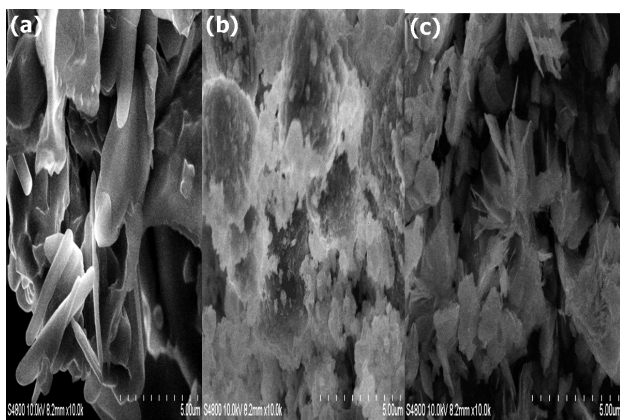


Figure 4: SEM micrographs of: a) pure potash alum, b) potash alum/fly ash composite and c) pure fly ash

Slika 4: SEM-posnetki: a) čisti kalijev galun, b) kompozit kalijev galun-leteči pepel in c) čisti leteči pepel

3.3 Scanning electron microscopy

Scanning electron microscopy (SEM) was used to check the surface morphology of composite electrolytes. We have recorded the SEM micrographs using a SEM instrument (SEM, Hitachi S-570) and the micrographs are shown in **Figure 4**.

It is clear from this figure that potash alum shows a needle-like morphology (**Figure 4a**) while fly ash (of an unknown purity) shows a more or less irregular structure when seen under SEM (**Figure 4c**). From the potash alum/fly ash composite SEM micrograph it is clear that the composite system shows a mixed morphology where the white-colored fly ash is uniformly mixed with the light-blackish potash-alum grains (**Figure 4b**).

3.4 Infrared spectroscopy

Infrared spectroscopy (Perkin Elmer 883) was carried out to study the composite nature and the functional groups present in the composite electrolyte. **Figure 5** shows the recorded IR spectra of pure potash alum, pure fly ash and the potash alum doped with fly ash (the maximum σ composition).

It is obvious that the IR spectrum of the composite material (**Figure 5c**) contains the peaks related to either pure potash alum (**Figure 5a**) or to alum (**Figure 5b**). An absence of any new peaks in the composite electrolyte other than those of the host materials clearly confirms the composite nature. The IR spectrum of potash alum (**Figure 4a**) based on one monovalent and one trivalent cation has been published.¹⁸ Ross gave an interpretation of the infrared spectrum of potassium alum as $(981, 1200, 1105, 618 \text{ and } 600) \text{ cm}^{-1}$ for $(SO_4)^{2-}$. The water stretching modes were reported at 3400 cm^{-1} and 3000 cm^{-1} , the bending modes at 1645 cm^{-1} and the vibrational modes at 930 cm^{-1} and 700 cm^{-1} .¹⁹

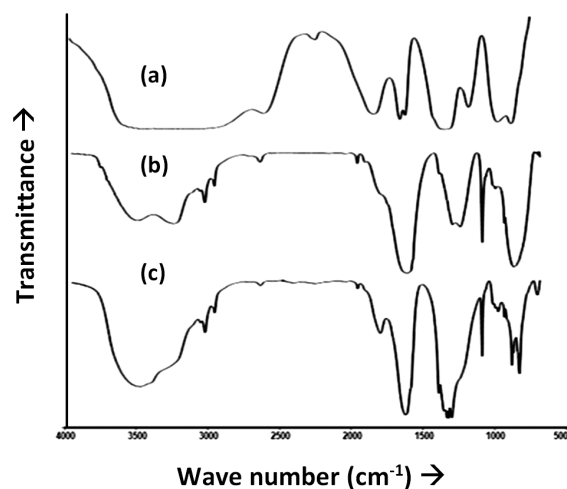


Figure 5: IR spectra of: a) pure potash alum, b) pure fly ash, c) potash alum/fly ash composite

Slika 5: IR-spektri: a) čisti kalijev galun, b) čisti leteči pepel, c) kompozit kalijev galun-leteči pepel

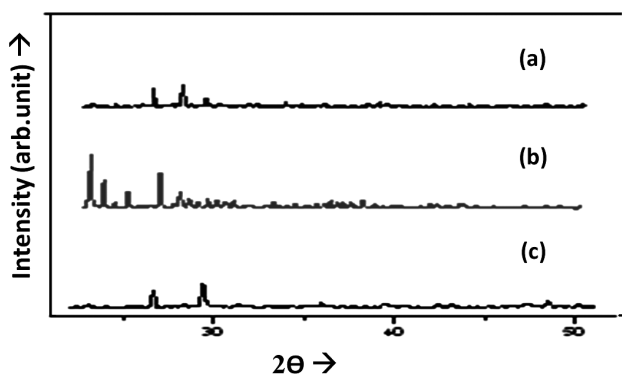


Figure 6: XRD patterns of: a) pure fly ash, b) potash alum and c) potash alum/fly ash composite

Slika 6: XRD-posnetki: a) čisti leteči pepel, b) kalijev galun in c) kompozit kalijev galun-leteči pepel

Figure 5b shows the IR spectrum of fly ash, in which the characteristic IR peak observed at 1094 cm^{-1} may be attributed to the presence of silica.¹⁷ This peak confirms the highest % of silica in fly ash, which is confirmed by a chemical analysis.⁸ Several absorption peaks are observed in the range from 1400 cm^{-1} to 1300 cm^{-1} , which correspond to the various metal oxides present in fly ash. A characteristic broad band at 3422 cm^{-1} in the spectrum of the composite is due to the N-H stretching of aniline (**Figure 4b**). The absorptions at $(1297.49 \pm 10, 1139.71 \pm 10, 1089.48 \pm 10$ and $794.81 \pm 20)\text{ cm}^{-1}$ correspond to the fly-ash constituents in the potash alum/fly ash composite (**Figure 5c**).

3.5 X-ray diffraction

To further investigate the composite nature, we recorded the XRD patterns of the composite electrolytes along with the host materials and the recorded patterns are shown in **Figure 6**. It was noted that the peaks that appear in the XRD pattern of the composite material (**Figure 6c**) also appear in the XRD patterns of fly ash



Figure 7: Photograph of developed humidity sensor based on the potash alum/fly ash composite

Slika 7: Posnetek razvitega senzorja vlage, ki temelji na kompozitu kalijev galun-leteči pepel

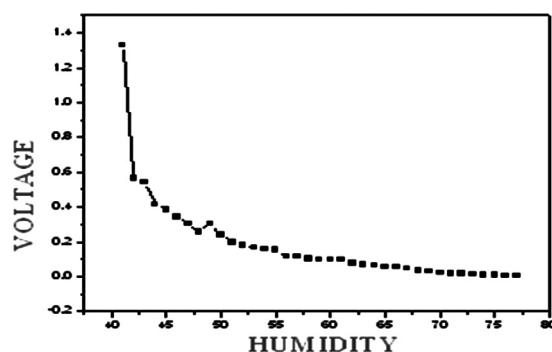


Figure 8: Response of the humidity sensor based on the potash alum/fly ash composite (the maximum conductivity sample)

Slika 8: Odziv na vlago senzorja na osnovi kompozita kalijev galun-leteči pepel

(**Figure 6a**) or potash alum (**Figure 6b**) affirming the composite nature that we have already found with the IR data.

4 APPLICATIONS

4.1 Humidity sensor

On the basis of the maximum electrical conductivity sample we tried to fabricate a humidity sensor in our laboratory. The optical photograph of the sensor is shown in **Figure 7**. To develop it we made a finger-type electrode on the surface of the composite pellet using vacuum-coated silver paint as the electrode material and deposited the pattern using the vacuum coating unit (Hind High Vacuum, India) at a pressure of 1.33×10^{-3} mbar. A conducting copper wire was used for the contact and sensing behavior. To measure the response of the humidity sensor we also developed a constant-humidity chamber in our laboratory as designed by Chandra et al²⁰. A very simple approach was adopted for creating different constant humidities for an in-situ measurement inside the chamber. It is known that the water-vapor pressure in over-saturated solutions of 'different salts' give different relative humidities. We applied different humidities inside the close chamber developed by us and measured the sensor response. The response of the sensor (voltage vs. humidities) is shown in **Figure 8**. It is clear from this figure that the developed sensor shows a good sensing behavior with a quick response. Within a short period the developed sensor shows an exponential decrease in the voltage with an increase in the humidity level.

5 CONCLUSION

A solid-state composite based on potash alum/fly ash has been developed and well characterized using various techniques. The electrical-conductivity measurement shows that by adding fly ash the electrical conductivity enhances the attained maxima at 65 % of fly ash in the composition to the conductivity value of $1.5 \times 10^{-5}\text{ S/cm}$

and this is followed by a decrease. IR as well as XRD confirmed the composite nature, while SEM affirmed the homogeneous mixing of potash alum/fly ash. A humidity sensor has been fabricated (with the maximum conductivity sample) and it shows a stable and good performance.

Acknowledgments

This work was supported by the DST project (SR/S2/CMP-0065/2010) of the government of India.

6 REFERENCES

- ¹ C. C. Liang, *J. Electrochem. Soc.*, 120 (1973), 1289
- ² T. Jow, J. B. Wagner, *J. Electrochem. Soc.*, 126 (1979), 1963
- ³ R. C. Agrawal, R. K. Gupta, *J. Mat. Sci.*, 34 (1999), 1131
- ⁴ N. Vaidehi, R. Akila, A. K. Shukla, K. T. Jacob, *Mater. Res. Bull.*, 21 (1986), 909
- ⁵ N. J. Dudney, *Annu. Rev. Mater. Sci.*, 19 (1989), 103
- ⁶ B. B. Owens, P. M. Skarstad, *Solid State Ionics*, 53–56 (1992), 665
- ⁷ K. K. Nanda, S. N. Sahu, *Adv. Mater.*, 13 (2001), 280
- ⁸ D. N. Bose, D. Majumdar, *Bull. Mater. Sci.*, 6 (1984), 223
- ⁹ A. Bunde, W. Dietrich, E. Roman, *Phys. Rev. Lett.*, 55 (1985), 5
- ¹⁰ K. Ahmad, W. Pan, S. L. Shi, *Appl. Phys. Lett.*, 89 (2006), 133122
- ¹¹ D. Rout, V. Subramanian, K. Hariharan, V. Sivasubramanian, V. R. K. Murthy, *J. Phys. Chem. Solids*, 67 (2006), 1629
- ¹² J. Maier, *J. Phys. Chem. Solids*, 46 (1985), 309
- ¹³ J. Maier, *Mater. Chem. Phys.*, 17 (1987), 485
- ¹⁴ B. K. Money, K. Hariharan, *Solid State Ionics*, 179 (2008), 1273
- ¹⁵ P. Kumar, P. K. Singh, B. Bhattacharya, *Ionics*, 17 (2011), 721
- ¹⁶ P. K. Singh, B. Bhattacharya, R. M. Mehra, H. W. Rhee, *Current Applied Physics*, 11 (2011), 616
- ¹⁷ M. Sotelo-Lerma, M. A. Quevedo-Lopez, R. A. Orozco-Teran, R. Ramirez-Bon, F. J. Espinoza-Beltran, *J. Phys. Chem. Solids*, 59 (1998), 145
- ¹⁸ P. K. Singh, P. Kumar, T. Seth, H. W. Rhee, B. Bhattacharya, *J. Phys. Chem. Solids*, 73 (2012), 1159
- ¹⁹ S. D. Ross, *Inorganic Infrared and Raman Spectra*, McGraw-Hill Book Company Ltd, London 1972
- ²⁰ N. Srivastava, S. Chandra, *European Polymer Journal*, 36 (2000), 421

DIFFERENT SOURCE ATELOCOLLAGEN THIN FILMS: PREPARATION, PROCESS OPTIMISATION AND ITS INFLUENCE ON THE INTERACTION WITH EUKARYOTIC CELLS

RAZLIČEN IZVIR ATELOKOLAGENSKIH TANKIH PLASTI: PRIPRAVA, OPTIMIZACIJA PROCESA IN VPLIV NA INTERAKCIJE Z EVKARIONTIČNIMI CELICAMI

Jorge López García¹, Petr Humpolíček¹, Marián Lehocký¹, Ita Junkar², Miran Mozetič²

¹Centre of Polymer Systems, Tomas Bata University in Zlín, nám. T. G. Masaryka 5555, 760 01 Zlín, Czech Republic

²Department of Surface Engineering, Plasma Laboratory, Jožef Stefan Institute, Jamova cesta 39, 1000 Ljubljana, Slovenia
lehocky@post.cz

Prejem rokopisa – received: 2012-11-16; sprejem za objavo – accepted for publication: 2013-01-09

Collagen thin films were prepared via bovine atelocollagen matrices. The film casting was carried out by using different culture dishes, concentrations, equipment, drying processes and periods of time. In order to optimise the repeatability and reproducibility, microscopic analyses were utilised to explore the film quality and topographical patterning. In addition, the human immortalised non-tumorigenic keratinocyte cell line (HaCaT) was seeded onto the obtained specimens, and the cell proliferation was determined by using the MTT assay. These results indicated how the substrate, its concentration and processing conditions influence the cellular response. The attempted technique shows itself to be an excellent procedure for continuous collagen film preparation with optimal cell-proliferation rates, which may potentially be used in tissue engineering or wound-healing applications.

Keywords: atelocollagen thin films, film optimisation, film quality, surface topography, eukaryotic cell response

Kolagenska tanka plast je bila narejena z govejo atelokolagensko matriko. Priprava plasti je potekala na različnih gojiščih, pri različnih koncentracijah, opremi, postopkih sušenja in pri različnih časih. Za doseganje optimalne ponovljivosti in obnovljivosti so bile uporabljene mikroskopske analize, s katerimi je bila ugotovljena kakovost plasti in njihov topografski vzorec. Poleg tega so bile na vzorce nanese neimortalizirane nekancerogene celice linije keratinocita (HaCaT), njihova proliferacija pa je bila ugotovljena z MTT-preizkusom. Rezultati prikazujejo, kako podlaga, njena koncentracija ter procesne razmere vplivajo na biološki odziv. Tovrstna tehnika je edinstven postopek za izdelavo kontinuirnih kolagenskih plasti za optimalno proliferacijo celic, ki je potencialno uporabna v tkivnem inženirstvu ali za celjenje ran.

Ključne besede: atelokolagenske tanke plasti, optimizacija plasti, kvaliteta plasti, topografija površine, odziv evkariontičnih celic

1 INTRODUCTION

Collagen is a fibrous protein that is present in nearly all mammalian tissues. It constitutes approximately 25 % of the whole-body protein content¹ and its abundance is mainly centred on connective tissues, such as tendons, ligaments and cartilage. Skin also contains this protein, which is involved in prime biological functions, such as tissue formation, cell attachment and proliferation.² Around 19 proteins are classified as collagen. Moreover, there are several proteins that have collagen domains.³ Although the 20 standard amino acids are encoded in collagen biosynthesis, the general sequence is (X-Y-Glycine)_n, where proline is recurrently in the X-position, and 4-hydroxyproline, which is almost unique to collagen, in the Y-position of the sequence (**Figure 1a**).^{4,5}

This protein is made up of three polypeptide strands, each chain is a left-handed helix, and the three chains are coiled around each other in a right-handed super-helix.^{6,7} As a biomaterial for industrial applications, collagen has been widely used in many fields, such as cell cultures, cosmetic and food products and medical devices.⁸

As for medical applications, this protein is considered as a primary source in biomedical applications and one of the most useful biomaterials because of its excellent biocompatibility, immunogenicity and biodegradability.⁹⁻¹¹ Unfortunately, native collagen has some difficulties with its tractability. For example, it may not be processed by injection moulding or any conventional extrusion technique.¹²

Collagen treated either by enzymatic digestion or by salt/acid extraction is so-called atelocollagen. This treatment leads towards crosslinks breaking amongst the collagen molecules, resulting in soluble triple helices lacking of telopeptides, which has the same physical properties as untreated collagen (**Figure 1b**).¹³

Atelocollagen possesses enormous assets; for instance, it is soluble in an acid pH, and its liquid form is tractable and free of telopeptides, which guaranties a low immunogenicity. Thus, it is employed for a wide range of purposes, including wound healing, vessel prostheses, haemostatic agent and tissue engineering.¹⁴⁻¹⁸

Despite the plethora of collagen-related publications, and to the best of our knowledge, there is no general

description of the preparation of atelocollagen thin films. Therefore, the aim of this contribution is the preparation and optimisation of collagen thin films. These findings seek to enlighten some of the issues involved in collagen sheet forming, film casting and the use of atelocollagen as a biomaterial.

2 PREPARATION OF ATELOCOLLAGEN FILMS

Selecting a proper collagen source is the most important issue before preparing collagen films. Four sorts of atelocollagen were employed across the trial, i.e., an emulsion of atelocollagen from bovine Achilles tendon, which contains 1.4 % of atelocollagen with a pH of 3.5; a gel of atelocollagen from bovine splits, 16.2 % of atelocollagen, pH 5.16 (Splits 1); a gel of atelocollagen from bovine splits, 11.8 % of atelocollagen, pH 3.7 (Splits 2) and an emulsion of atelocollagen from bovine tendons, 3.6 % of atelocollagen, pH 3.3. These starting materials were provided by Vipo A. S., and all of them were produced by trypsin enzymatic digestion. Three main factors were taken into account: atelocollagen concentration, processing factors such as mixing and casting solution volume. Each atelocollagen source was solubilised in a aqueous acetic acid solution 0.1M to finally obtain the mass fractions (0.5, 0.25, 0.1 and 0.05) %. A solution of acetic acid 0.1M was used as a solvent throughout this study; on account of it being recommended and employed in previous researches.¹⁹⁻²¹ It is because pH values within 1.0 and 4.0 have the best collagen-solubility yields.^{22,23} The measured pH of the experimental solution was between 3.5 and 4.0.

The tested samples were homogenised and casted in culture dishes by using stirring machines with distinct rotational frequencies and pouring volumes. An IKA RCT stirring machine (IKA® works, Inc, Germany) and Merci 1500 (Merci S. R. O, Czech Republic) were used for the experiments.

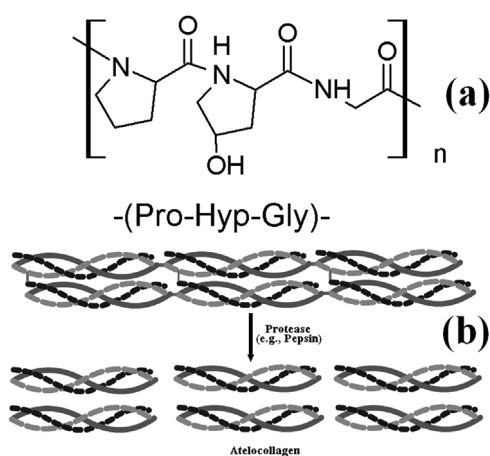


Figure 1: a) Collagen typical primary sequence; b) atelocollagen via enzymatic digestion

Slika 1: a) Značilno primarno zaporedje kolagena; b) atelokolagen z encimsko razgradnja

A rotational frequency of 1000 r/min was set as the appropriate one, since this speed provided an efficient flock reduction. Higher frequencies may cause sample spilling, whereas lower frequencies are insufficient for the appropriate preparation of films within a reasonable processing time. The mixture is referred as the state formed by a complex of two or more ingredients, whilst mixing is an operation intended to reduce the non-uniformity of a mixture and it may be achieved by inducing the physical motion of the ingredients. The mixing time was a crucial factor; ensuring 4 h of mixing, the solution was homogeneous and without atelocollagen flocks. After an hour of mixing, medium-size flocks were visible in the solution, and those were progressively reducing their sizes. Nevertheless, the turbidimetry assay that measures transmitted light, and is directly proportional to the concentration and depth of the dispersion, indicates that approximately one hour is enough for serving, since the transmittance started to be constant (**Figure 2**).

This information may be corroborated either with Scanning Electron Microscopy (SEM) images, which illustrate the relation between surface-quality and mixing time (**Figure 3**), or in **Table 1**, which lists the percentage of transmittance before beginning the enquiry.

Table 1: Mass fractions of transmittance with respect to concentration (w/w%)

Tabela 1: Delež prepustnosti glede na koncentracijo v masni deležih (w/w%)

Source	0.5 %	0.25 %	0.1 %	0.05 %
Atelocollagen from bovine splits 1	80.1	73.4	51.2	28.5
Atelocollagen from bovine splits 2	91.2	73.6	56.5	32.0
Atelocollagen from bovine tendons	87.7	72.7	50.4	27.8

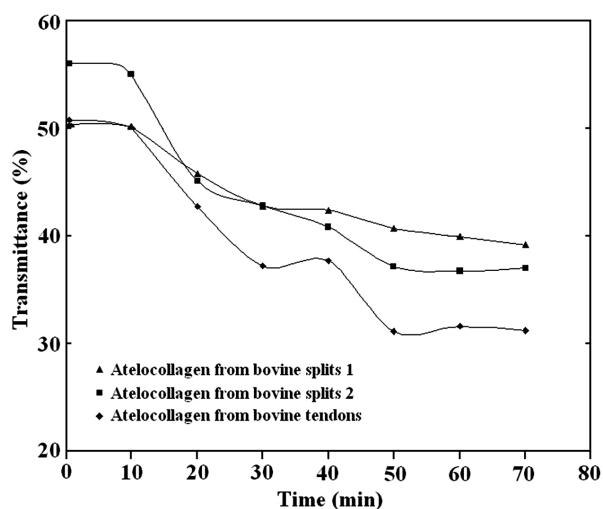


Figure 2: Turbidimetry assay of different atelocollagen solutions, studied concentration 0.1 %

Slika 2: Preizkus turbidimetrije različnih atelokolagenskih raztopin; raziskovana koncentracija 0,1 %

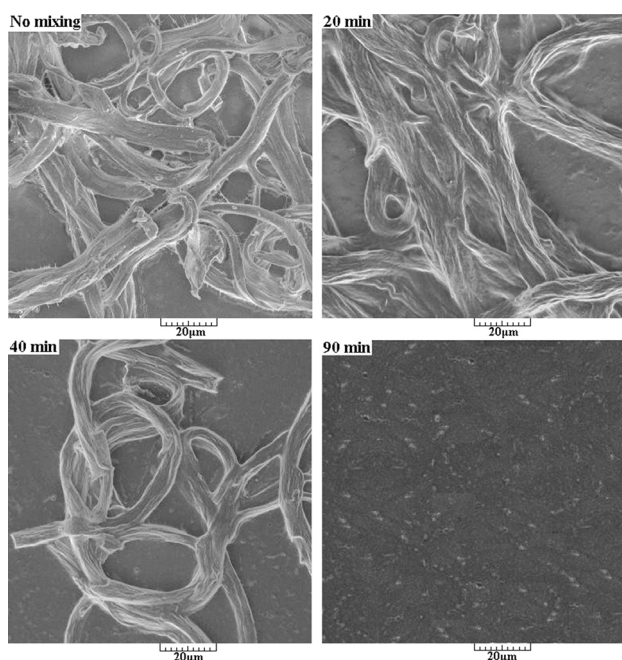


Figure 3: Mixing progress: emulsion 0.1 % of atelocollagen from bovine tendons. SEM images taken at different mixing times.

Slika 3: Proces mešanja: emulzija 0,1 % atelokolagena iz goveje kite. SEM-posnetki po različnih časih mešanja.

The turbidimetry assay was carried out on a Helios γ -spectrophotometer (Thermo scientific, USA) at 422 nm.

All the atelocollagen solutions were disposed into the culture dishes (TPP, Switzerland) 30 min after mixing, to avoid bubbles coming from the solution stirring, which alter surface texture. When the solutions were casted immediately, the subsequent films had a rough appearance, along with collagen congregates, which indeed deteriorate the surface quality (**Figure 4a**).

The employed culture dishes were of (9.0, 6.0 and 4.0) cm diameter. The first attempt involved the 9.0 cm ones and volumes of (30, 20, 10 and 5) mL of the

solution were casted into. The casted films were kept standing at lab temperature (20–24 °C) for three days to evaporate the excess solvent.

Casted solutions of 20 mL and 30 mL are also suitable for making collagen films; nonetheless, those volumes need more time for optimal solvent evaporation. If 10 mL is casted, its films get their shapes in two days, but the solvent still remains (eye observation and sensory evaluation). The extra day is for completing the solvent evaporation.

A total of 5 mL was discarded as a pouring volume, because it scarcely took the shape of the 9.0 cm Petri dishes. Then, it was decided that 10 mL should be the starting volume for the culture dishes of this diameter.

The vacuum and the temperature may be utilised for film drying, thereby reducing the evaporation time. However, fast solvent evaporation and vacuum influence the surface smoothness (**Figures 4b** and **4c**).

With reference to temperature, it may not exceed 30–35°C, which is on average the denaturation temperature of collagen acid solutions, and refers to the collapse of the collagen triple helix to a random coil configuration.^{24–27} As the vapour pressure rises, the surface roughness increases, and to render smooth films, it is extremely important to focus on the employed solvent and its evaporation. Solvents with low evaporation rates tend to produce better quality films than fast evaporating ones.^{28,29}

3 SURFACE MORPHOLOGY

The specimens made from 10 mL had the best film appearance (dry, smooth, resilient and the solvent seemed to be thoroughly evaporated). For example, the digital camera images depict a surface that apparently has neither any eye-visible damage nor scratches (**Figure 5**). This assessment is reinforced by the SEM images, where the surfaces are relatively smooth, except for some

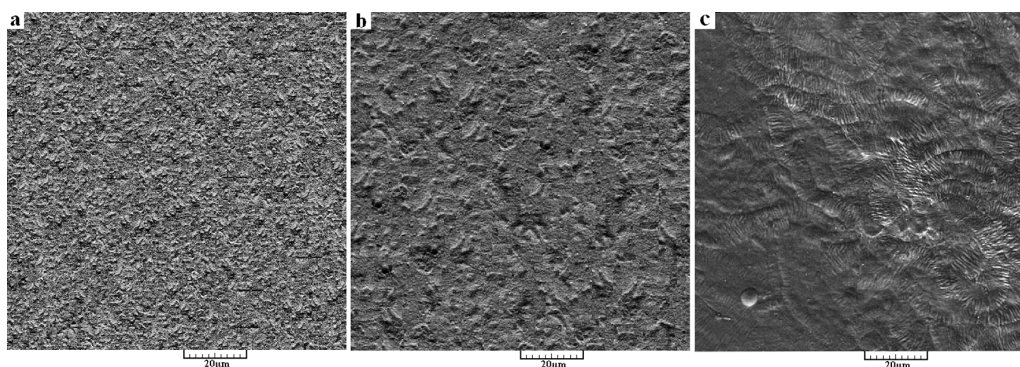


Figure 4: a) Atelocollagen film obtained from a solution of 0.1 % of the mass fraction atelocollagen from bovine tendons that was poured immediately after mixing; b) atelocollagen films cast and dried at 30 °C of 0.1 % atelocollagen from bovine tendons; c) by using a desiccator of 0.1 % atelocollagen from bovine splits 1

Slika 4: a) Atelokolagenske plasti, pridobljene iz 0,1 % masnega deleža raztopine atelokolagena iz goveje kite, ki je bil nanosen takoj po mešanju; b) ulita in sušena atelokolagenska plast pri 30 °C iz 0,1 % atelokolagena iz goveje kite; c) z uporabo eksikatorja iz 0,1 % atelokolagena iz govejega dela 1

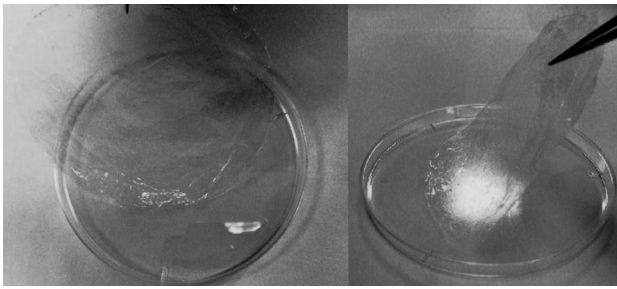


Figure 5: Glimpse at the thin films of 0.1 % of the mass fraction of atelocollagen from bovine splits 2 by a standard camera with the corresponding brightness and contrast adjustments

Slika 5: Pogled na tanko plast 0,1 % masnega deleža atelokolagena iz govejega dela 2 s standardno kamero s primerno nastavljeno svetlostjo in kontrastom

wavy areas, which may result either from small collagen flocks or a product of solvent evaporation (**Figure 6**).

Scanning electron microscopy (SEM) was performed in a VEGA II LMU microscope (Tescan s. r. o, Czech Republic) operated in high vacuum/secondary electron imaging mode at an accelerating voltage of 5 kV. The specimens were coated with a thin layer of gold/palladium alloy and tilted at 30° to attain a better observation of the surface topography. The images were taken at a magnification of 2000-times.

4 THIN-FILM NORMALISATION

To normalise the procedure for multiple diameters, the height of served solutions in the Petri dishes was ascertained by means of an equation that signifies the

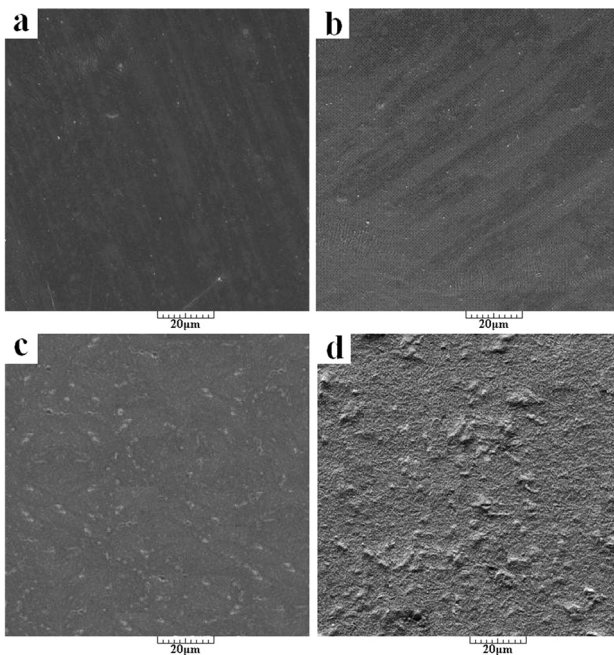


Figure 6: Surface morphology of the atelocollagen thin films from: a) bovine splits 1; b) bovine splits 2; c) bovine tendons; d) bovine tendons

Slika 6: Morfologija površine atelokolagenske plasti iz: a) govejega dela 1; b) govejega dela 2; c) goveje kite; d) goveje kite

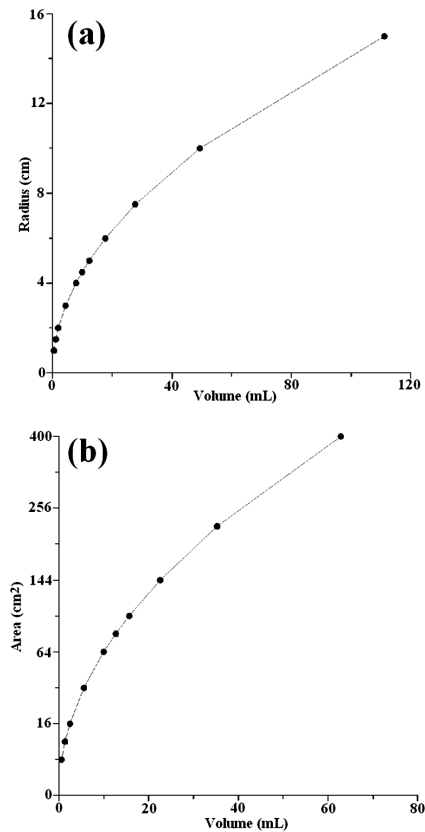


Figure 7: a) Model for Petri dishes; b) model for rectangular cuboids sheets

Slika 7: a) Model za petrijevke; b) model za pravokotne kubične liste

volume of a cylinder $v = \pi r^2 h$, where v is the volume, r is the radius and h is the height. The idea was to keep the same height no matter the diameter (twice the radius) of the culture dishes, *i.e.*, same height, distinct radii and thus, different volumes. The height was calculated by using 10 cm³ as an initial volume. As was mentioned, 10 mL (equivalent to 10 cm³) was the selected volume for the 9.0 cm diameter. The obtained volumes from the previously calculated height were 4.5 mL and 2.0 mL for the 6.0 cm and 4.0 cm diameters, respectively.

In order to get the same film thickness, the height has to be settled as a constant. The model may be applied to any Petri dish, as it is described in **Figure 7a** or numerous forms that have a known area. **Figure 7b** shows the model that may be used for rectangular sheets. In any rectangular cuboid form, the volume is defined as $v = lwh$, where l is the length, w is the width and h is the height. If the height (film thickness) remains steady and the length and width (area) are known, the volume may be ascertained.

This trial was conducted by following two fundamental concepts: repeatability and reproducibility. The former is the effort to keep constant conditions by using the same instruments in a short period of time; and the latter is the one with different instruments and other periods of time.

5 CELL RESPONSE

A human immortalised non-tumorigenic keratinocyte cell line was supplied by Cell Lines Service (Catalogue No. 300493, Germany). Dulbecco's modified eagle medium-high glucose, supplemented with 10 % foetal bovine serum and Penicillin/Streptomycin, 100 U/mL (100 µg/mL) respectively (PAA Laboratories GmbH, Austria) was used as a culture medium.³⁰ HaCaT cells in the exponential growth phase were seeded onto the thin films at a concentration of cells $1 \times 10^5 \text{ mL}^{-1}$ and incubated at 37 °C with 5 % CO₂ in humidified air.

The cell proliferation was determined after 4 d in the culture with the MTT cell proliferation assay kit (Invitrogen Corporation, USA). The formazan concentration was measured in a Sunrise microplate absorbance reader (Tecan, Switzerland) at 570 nm. The photomicrographs were taken by using an inverted phase-contrast microscope Olympus CKX41 (Olympus, Germany) with an optical zoom of 40-times.

The HaCaT keratinocyte cells behaviour on the prepared films was evaluated with the MTT assay and the results are given in **Figure 8**. It was found that after four days of cultivation, in terms of cost-effectiveness the films made from 0.1 % were the most suitable. Regardless of the atelocollagen matrix, the cell proliferation on the films prepared at this concentration exhibits the highest rate. In contrast, higher concentrations of collagen (0.5 % and 0.25 %) seem to be detrimental to the keratinocytes cells.

As far as surface morphology is concerned, the films that were dried at 30 °C, (with faster solvent evaporation and rougher surfaces than the lab temperature ones) also

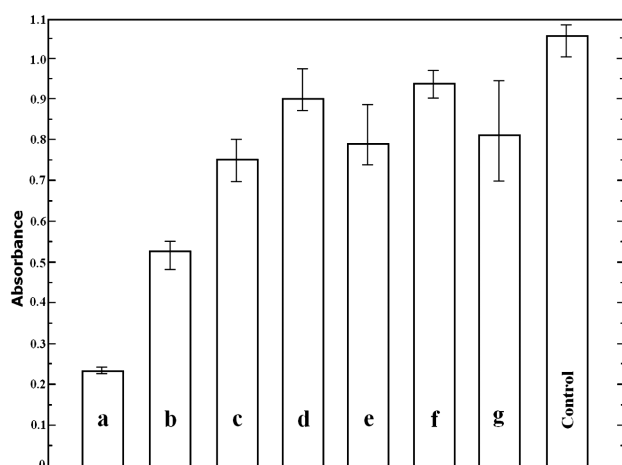


Figure 8: Comparison of HaCaT cell growth measured by MTT assay at 570 nm on: a) 0.5 %; b) 0.25 %; c) 0.05 %; d), e) and f) 0.1 % of the mass fraction of atelocollagen from bovine tendons, atelocollagen from bovine splits 1 and atelocollagen from bovine splits 2 respectively; g) 0.1 % film, dried at 30 °C. Error bars signify standard deviations.

Slika 8: Primerjava rasti celic HaCaT, izmerjene z MTT-preizkusom pri 570 nm: a) 0,5 %; b) 0,25 %; c) 0,05 %; d), e) in f) 0,1 % masnih deležev atelokolagena iz goveje kite, atelokolagena iz govejega dela 1 in atelokolagena iz govejega dela 2; g) 0,1-odstotna plast, sušena pri 30 °C. Odmiki na grafu so prikaz standardne deviacije.

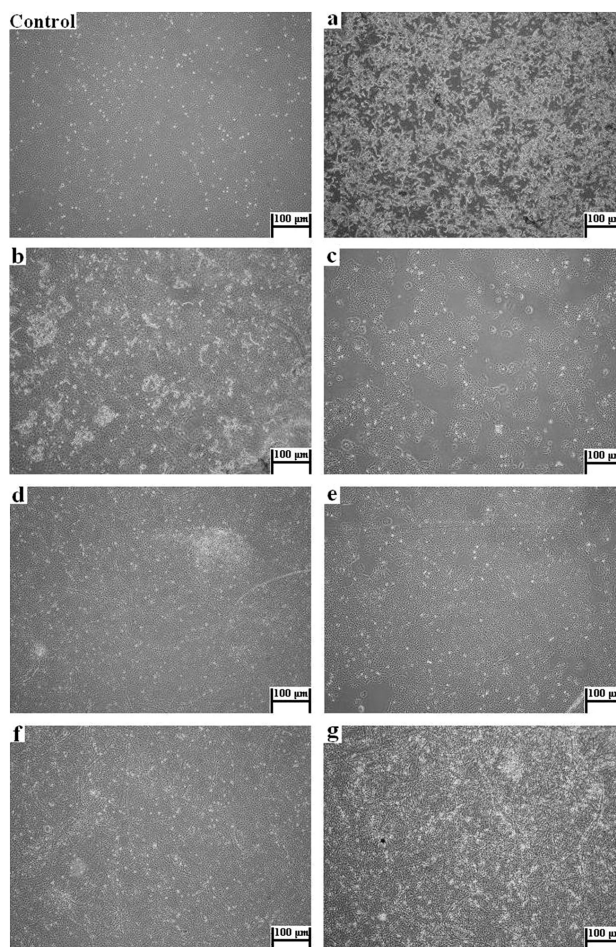


Figure 9: Photomicrographs of human skin HaCaT keratinocytes in culture upon collagen compared with control: a) 0.5 %; b) 0.25 %; c) 0.05 %; d), e) and f) 0.1 % of the mass fraction of atelocollagen from bovine tendons, atelocollagen from bovine splits 1 and atelocollagen from bovine splits 2; g) 0.1 % film, dried at 30 °C

Slika 9: Slike keratinocitov iz človeške kože HaCaT v kulturi s kolagenom v primerjavi s kontrolo: a) 0,5 %; b) 0,25 %; c) 0,05 %; d), e) in f) 0,1 % masnih deležev atelokolagena iz govejega kite, atelokolagena iz govejega dela 1 in atelokolagena iz govejega dela 2; g) 0,1-odstotna plast, sušena pri 30 °C

had thriving cell proliferation rates (**Figure 8g**). Consequently, film drying at this temperature may be used without affecting atelocollagen-scaffold quality at all. It was previously demonstrated that the keratinocyte cells adhere and proliferate satisfactorily on both smooth and rough surfaces, and also the pivotal role of chemistry and topography as cell regulatory factors.^{31–33}

This outcome was also qualitatively appraised by the photomicrographs in **Figure 9**, which show the cell aggregates that are adhered on the film surfaces. It may be seen that the film obtained from 0.5 % has a vast amount of collagen flocks, which presumably hinder the HaCaT cell growth.

Nevertheless, the mechanisms of keratinocytes adhesion and proliferation are still unclear, even though it is well known that hydrophilic surfaces (like these ones) are favourable for HaCaT cell growth.^{34–36} For this reason, a protocol for continuous and effective substrate

preparation is of paramount importance. Atelocollagen is certainly a potential scaffold for cell growth purposes, which also has the advantage of being eliminated by degradation processes similar to the metabolism of endogenous collagen.³⁷

6 CONCLUSIONS

In this contribution, the adopted technique for atelocollagen thin-film preparation was confirmed to be a cost-efficient procedure, independent of the equipment or the time. It increases in importance due to the difficulties that collagen has for its manipulation. The materials referred to herein as 'atelocollagen films' were succinctly characterised by microscopic analysis. In addition, HaCaT keratinocytes cell adhesion was successfully accomplished. This effort may be adjusted to diverse atelocollagen matrices. Hence, the present approach strengthens the knowledge in the use of atelocollagen as a prospective scaffold, and indeed in the development of suitable materials for tissue-engineering and wound-healing applications.

Acknowledgements

The authors would like to express their gratitude to the Ministry of Education, Youth and Sport of the Czech Republic (CZ.1.05/2.1.00/03.0111). The Slovenia Ministry of Higher Education, Science, and Technology (Program P2-0082-2) and Ad Futura L7-4009 are also gratefully acknowledged for the financial support of this research.

7 REFERENCES

- M. D. Shoulders, R. T. Raines, *Annu. Rev. Biochem.*, 78 (2009) 929–958
- D. J. Prockop, K. I. Kivirikko, *Annu. Rev. Biochem.*, 64 (1995) 403–34
- H. W. T. Matthew, *Polymers for Tissue Engineering Scaffolds*, In: S. Dumitriu, editor, *Polymeric biomaterials*, CRC Press, Boca Raton 2001, 167–180
- N. C. Avery, T. J. Sims, C. Karkup, A. J. Bailey, *Meat Sci.*, 42 (1996) 355–369
- R. Berisio, L. Vitagliano, L. Mazzarella, A. Zagari, *Protein Sci.*, 11 (2001), 262–270
- A. Rich, F. H. C., *Nature*, 176 (1955), 915–916
- K. Okuyama, *Connect. Tissue Res.*, 49 (2008), 299–310
- R. Parenteau-Bareil, R. Gauvin, F. Berthod, *Materials*, 3 (2010), 1863–1887
- N. Nambu, S. Kishimoto, S. Nakamura, H. Mizuno, S. Yanagibayashi, N. Yamamoto, R. Azuma, S. Nakamura, T. Kizosawa, M. Ishihara, Y. Kanatani, Accelerated wound healing in healing-impaired db/db mice by autologous adipose tissue-derived stromal cells combined with atelocollagen matrix, *Ann. Plas. Surg.*, 62 (2009), 317–321
- J. L. Garcia, J. Pacherník, M. Lehocký, I. Junkar, P. Humpolíček, P. Sáha, Enhanced keratinocyte cell attachment to atelocollagen thin films through air and nitrogen plasma treatment, *Prog. Colloid Polym. Sci.*, 138 (2011), 89–94
- I. Banerjee, D. Mishra, T. Das, S. Maiti, T. K. Maiti, Caprine (Goat) collagen: A potential biomaterial for skin tissue engineering, *J. Biomater. Sci. Polym. Ed.*, 23 (2012), 355–373
- A. Vesel, K. Eleršič, M. Mozetič, Immobilization of protein streptavidin to the surface of PMMA polymer, *Vacuum*, 86 (2012), 773–775
- H. Fasl, L. F. Zemljic, W. Goessler, K. Stana - Kleinschek, V. Ribitsch, Investigation into amphiphilic chitosan: properties and availability of original and newly introduced functional groups, *Macromolecular Chemistry and Physics*, 15 (2012), 1582–1589
- F. Silver, A. Garg, Collagen: Characterization, processing and medical applications, In: A. Domb, J. Kost, D. Wiserman (editors), *Handbook of biodegradable polymers*, Part of the book series, Drug targeting and delivery, Harwood Academic Publishers, Amsterdam 1997, 319–346
- S. Inaba, S. Nagahara, N. Makita, Y. Tarumi, T. Ishimoto, S. Matsuo, K. Kadomatsu, Y. Takei, Atelocollagen-mediated systemic delivery prevents immunostimulatory adverse effects of siRNA in mammals, *Mol Ther*, 20 (2012), 356–366
- F. Takeshita, Y. Minakuchi, S. Nagahara, K. Honma, H. Sasaki, K. Hirai, T. Teratani, N. Namatame, Y. Yamamoto, K. Hanai, T. Kato, A. Sano, T. Ochiya, I. M. Verma, Efficient delivery of small interfering RNA to bone-metastatic tumors by using atelocollagen in vivo, *Proc. Nat. Acad. Sci. USA*, 102 (2005), 12177–12182
- A. Sano, M. Maeda, S. Nagahara, T. Ochiya, K. Honma, H. Itoh, T. Miyata, K. Fujioka, Atelocollagen for protein and gene delivery, *Adv. Drug Delivery Rev.*, 55 (2003), 1651–1677
- Y. Tanaka, H. Yamaoka, S. Nishizawa, S. Nagata, T. Ogasawara, Y. Asawa, Y. Fujihara, T. Takato, K. Hoshi, The optimization of porous polymeric scaffolds for chondrocyte/atelocollagen based tissue-engineered cartilage, *Biomaterials*, 31 (2010), 4506–4516
- H. Yamaoka, Y. Tanaka, S. Nishizawa, Y. Asawa, T. Takato, K. Hoshi, The application of atelocollagen gel in combination with porous scaffolds for cartilage tissue engineering and its suitable conditions, *J. Biomed. Mater. Res., Part A*, 93 (2010), 123–132
- A. Bernal, R. Balková, I. Kuřitka, P. Sáha, Preparation and characterisation of a new double-sided bio-artificial material prepared by casting of poly(vinyl alcohol) on collagen, *Polym Bull.*, 70 (2013) 2, 431–453
- J. Einbinder, M. Schubert, Binding of mucopolysaccharides and dyes by collagen, *J. Biol. Chem.*, 188 (1951), 335–341
- H. Sage, R. G. Woodbury, P. Bornstein, Structural studies on human type IV collagen, *J. Biol. Chem.*, 254 (1979), 9893–9900
- O. Harada, K. Kadota, T. Yamamoto, Collagen-based new biomedical films: Synthesis, property and cell adhesion, *J. Appl. Polym. Sci.*, 81 (2000), 2433–2438
- F. Vojdani, Solubility, In: G. M. Hall (editor), *Methods of testing protein functionality*, Chapman and Hall, London 1996, 11–60
- H. Tabarestani, Y. Maghsoudlou, A. Motamedzadegan, A. R. Sadeghi, H. Rostamzad, Study on some properties of acid-soluble collagens isolated from fish skin and bones of rainbow trout (*Onchorhynchus mykiss*), *Int. Food Res. J.*, 19 (2012), 251–257
- Y. Nomura, S. Toki, Y. Ishii, K. Shirai, The physicochemical property of shark type I collagen gel and membrane, *J. Agric. Food Chem.*, 48 (2000), 2028–2032
- A. A. S. Machado, V. C. A. Martins, A. M. G. Plepis, Thermal and rheological behavior of collagen chitosan blends, *J. Thermal Anal. Cal.*, 67 (2002), 491–498
- Z. Zhang, G. Li, B. Shi, Physicochemical properties of collagen, gelatin and collagen hydrolysate derived from bovine lamed split wastes, *J. Soc. Leath. Technol. Chem.*, 90 (2005), 23–28
- G. Lai, Y. Li, G. Li, Effect of concentration and temperature on the rheological behavior of collagen solution, *Int. J. Biol. Macromol.*, 42 (2008), 285–2891
- P. Müller-Buschbaum, J. S. Gutmann, M. Wolkenhauer, J. Kraus, M. Stamm, D. Smilgies, W. Petry, Solvent-Induced Surface Morphology of Thin Polymer Films, *Macromolecules*, 34 (2001), 1369–1375

- ³¹ T. To, H. Wang, A. B. Djurišić, M. H. Xie, W. K. Chan, M. H. Xie, W. K. Chan, Z. Xie, C. Wud, S. Y. Tonge, Solvent dependence of the evolution of the surface morphology of thin asymmetric diblock copolymer films, *Thin Solid Films*, 467 (2004), 59–65
- ³² P. Boukamp, R. T. Petrussevska, D. Breitzkreutz, J. Hornung, A. Markham, Normal keratinization in a spontaneously immortalized aneuploid keratinocyte cell line, *J. Cell Biol.*, 106 (1998), 761–771
- ³³ R. G. Flemming, C. J. Murphy, G. A. Abrams, S. L. Goodman, P. F. Nealey, Effects of synthetic micro- and nano-structured surfaces on cell behavior, *Biomaterials*, 20 (1999), 573–588
- ³⁴ J. L. Garcia, A. Asadinezhad, J. Pacherník, M. Lehocký, I. Junkar, P. Humpolíček, P. Sáha, P. Valášek, Cell proliferation of HaCaT keratinocytes on collagen films modified by argon plasma treatment, *Molecules*, 15 (2010), 2845–2856
- ³⁵ N. Roy, N. Saha, T. Kitano, M. Lehocký, E. Vitková, P. Sáha, Significant characteristics of medical-grade polymer sheets and their efficiency in protecting hydrogel wound dressings: A soft polymeric biomaterial, *Int. J. Polym. Mater.*, 61 (2012), 72–88
- ³⁶ S. L. Ishaug-Riley, L. E. Okun, G. Prado, M. A. Applegate, A. Ratcliffe, Human articular chondrocyte adhesion and proliferation on synthetic biodegradable polymer films, *Biomaterials*, 20 (1999), 2245–2256
- ³⁷ M. Lehocký, P. St'ahel, M. Koutný, J. Čech, J. Institoris, A. Mráček, Adhesion of *Rhodococcus* sp S3E2 and *Rhodococcus* sp S3E3 to plasma prepared teflon-like and organosilicon surfaces, *J. Mater. Process. Technol.*, 209 (2009), 2871–2875

EVALUATION OF EQUILIBRIUM ISOTHERM MODELS FOR THE ADSORPTION OF Cu AND Ni FROM WASTEWATER ON BENTONITE CLAY

OCENA MODELOV RAVNOTEŽNIH IZOTERM ZA ADSORPCIJO Cu IN Ni IZ ODPADNIH VOD NA BENTONITNO GLINO

Saad A. Al-Jlil, Mohammad Sajid Latif

National Center for Water Technology (NCWT), King Abdulaziz City for Science and Technology (KACST), P. O. Box 6086, 11442 Riyadh, Kingdom of Saudi Arabia
saljlil@kacst.edu.sa

Prejem rokopisa – received: 2012-12-03; sprejem za objavo – accepted for publication: 2012-12-14

A study was carried out to evaluate equilibrium isotherm models for the adsorption of Cu and Ni on bentonite clay from wastewater. The adsorption of Cu and Ni increased with an increase in the pH and was high at the pH values of around 7. The adsorption capacity of bentonite clay increased with an increase in the temperature. The maximum adsorption capacity of bentonite clay was 11.12 mg g⁻¹ and 6.78 mg g⁻¹ for Cu and Ni, respectively, at 20 °C. Among the three equilibrium isotherm models used, the Langmuir-Freundlich isotherm model described the experimental data well at different temperatures.

Keywords: equilibrium isotherm models, adsorption, copper, nickel, bentonite clay, temperature, wastewaters

Izvršena je bila študija ocene modelov ravnotežnih izoterm pri adsorpciji Cu in Ni iz odpadnih vod na bentonitno glino. Adsorpcija bakra in niklja narašča z naraščanjem pH in je velika pri pH vrednostih okrog 7. Adsorpcijska zmogljivost bentonitne glino se povečuje z naraščanjem temperature. Največja zmogljivost adsorpcije bentonitne glino je bila 11,12 mg g⁻¹ in 6,78 mg g⁻¹ za Cu in Ni pri 20 °C. Med tremi modeli ravnotežnih izoterm pa dobro opisuje eksperimentalne podatke pri različnih temperaturah izotermni model Langmuir-Freundlich.

Ključne besede: modeli ravnotežnih izoterm, adsorpcija, baker, nikelj, bentonitna glina, temperatura, odpadne vode

1 INTRODUCTION

Wastewater is an important resource of water for augmenting the existing inadequate fresh-water supplies for multiple uses other than drinking purposes. Among the different biological, organic and inorganic pollutants in wastewater, the presence of trace elements and heavy-metal ions above the permissible limits pose environmental hazards. According to FAO (1985), the maximum permissible limits of Cu and Ni in drinking water are 1 mg L⁻¹ and 0.015 mg L⁻¹, respectively.¹

Previous studies showed that sewage water in Riyadh contains an appreciable amount of heavy metals.² Frequently, industrial-waste effluents are discharged into the drainage channels.³ The sources of heavy metals in wastewaters, especially the industrial effluents, are metal plating and ceramics photography,⁴ household chemicals in sewage water,⁵ and corrosion of the pipes of drinking-water-supply networks as well as leaching of the chemicals from polyvinyl chloride (PVC) pipes.^{6,7} To minimize the environmental hazards, it is important to remove the heavy-metal ions from the wastewaters and maintain their concentration within the recommended limits before their land disposal as required by the National Regulatory Authority. Currently, among the various technologies for wastewater treatment, the use of bentonite clay is a very common and effective method for the removal of heavy-metal ions, especially Cu and Ni, from wastewaters.

The main objective of this study was to test and evaluate the local, natural, Saudi bentonite clay for the adsorption of copper and nickel ions from wastewaters using three equilibrium isotherm models at different temperatures.

2 METHODOLOGY

2.1 Experimental part

a) Material

Adsorbent: The adsorbent used in this research was the local natural bentonite clay.

Adsorbates: Copper-and-nickel-ion solution prepared from the copper sulfate and nickel nitrate purified and supplied by S. Define-Chem. limited (Laboratory Rasyan) was used in the experiment.

b) Procedures

Preparation of copper-and-nickel-ion samples

Stock solutions of Cu and Ni metal ions with a concentration of 1000 mg L⁻¹ were obtained. A mixture of Cu and Ni ions was prepared by mixing both metal ions having the same concentration and then diluted to obtain the concentrations (50–1000 × 10⁻⁶) required for the use in equilibrium experiments. After that, the initial concentrations of the metal-ion samples and the final concentration of the resultant solution (after the completion of the experiment) were diluted and analyzed

with the atomic-absorption spectroscopy (model AAnalyst 700, PerKin Elmer, an atomic absorption spectrometer).

c) Equilibrium experiments

The equilibrium isotherm was determined by placing a constant mass of clay (1 g) with a solute solution 50 mL in glass bottles in a constantly agitating shaker. In each isotherm run, the solute-solution concentrations ranged from 50–1000 mg L⁻¹ and the temperatures ranged from 0–20 °C during the study.

The equilibrium experiments were run up to the state of equilibrium. After that the samples were filtered using filter papers, then diluted and the absorbance was measured using atomic absorption spectroscopy. The concentration of Cu and Ni ions was calculated from the absorbance using the calibration curve. The amount of metal ions adsorbed on the bentonite clay (adsorbent) was calculated with the mass-balance equation as follows:

$$q_e = \frac{V(C_0 - C_e)}{M} \quad (1)$$

where M is the adsorbent mass (g), V is the solution volume (L), q_e is the adsorbed metal-ion concentration (mg/g), C_0 is the initial concentration of metal ions (mg L⁻¹) and C_e is the metal-ion concentration in a bulk solution at equilibrium (mg L⁻¹).

2.2 Multicomponent Equilibrium Isotherm Models

Three equilibrium isotherm models were applied to interpret the experimental data for bentonite clay as an adsorbent at different temperatures to obtain the optimum values of the equilibrium parameters. These models are:

a) Extended Langmuir isotherm model

The extended Langmuir isotherm model was applied to determine the adsorption of copper and nickel ions on bentonite clay from wastewater. The extended Langmuir isotherm model can be written as follows:⁸

$$q_{e1} = \left(\frac{k_1 C_{e1}}{1 + b_1 C_{e1} + b_2 C_{e2}} \right) \quad (2)$$

$$q_{e2} = \left(\frac{k_2 C_{e2}}{1 + b_1 C_{e1} + b_2 C_{e2}} \right) \quad (3)$$

The extended Langmuir parameters K_1 , b_1 , K_2 and b_2 can be obtained by using the non-linear regression technique with equations 2 and 3.

b) Langmuir-Freundlich isotherm model

A combination of Langmuir and Freundlich isotherm models makes a new model called the Langmuir-Freundlich isotherm model.^{9,10} The Langmuir-Freundlich isotherm parameters K_1 , b_1 , K_2 and b_2 , n_1 and n_2 can be obtained by using the non-linear regression technique

with equations 4 and 5. This form can be written as follows:

$$q_{e1} = \left(\frac{k_1 C_{e1}^{n_1}}{1 + b_1 C_{e1}^{n_1} + b_2 C_{e2}^{n_2}} \right) \quad (4)$$

$$q_{e2} = \left(\frac{k_2 C_{e2}^{n_2}}{1 + b_1 C_{e1}^{n_1} + b_2 C_{e2}^{n_2}} \right) \quad (5)$$

c) Multicomponent isotherm model

The required five parameters of the multicomponent isotherm model are as follows:^{9,11}

$$q_{e1} = \left(\frac{k_1 C_{e1}}{1 + b_1 C_{e1}^{n_1} + b_2 C_{e2}^{n_2}} \right) \quad (6)$$

$$q_{e2} = \left(\frac{k_2 C_{e2}}{1 + b_1 C_{e1}^{n_1} + b_2 C_{e2}^{n_2}} \right) \quad (7)$$

The equilibrium constants K_1 , b_1 , K_2 and b_2 , n_1 and n_2 can be obtained with the non-linear regression technique with equations 6 and 7.

3 RESULTS AND DISCUSSION

3.1 Characterization of Bentonite Clay

Saudi bentonite clay was analyzed with XRF (model JSX-3201, JEOL, an element analyzer). The chemical analysis is presented in **Table 1**. Physical parameters such as the BET surface area, the pore volume and the average pore width of bentonite clay were determined with a surface-area analyzer (model ASAP 2020, Micromeritics). The particle density and porosity of solid materials were measured in the Micromeritics Material Analysis Laboratory (Norcross, Georgia, U.S.A.) using the gas pycnometer method (an Accupc 1330 pycnometer). The results are shown in **Table 2**. The XRD

Table 1: Chemical analysis of the Saudi bentonite clay in mass fractions (w/%)

Tabela 1: Kemijska analiza saudijske bentonitne gline v masnih deležih (w/%)

Compound	w/% (in clay)
SiO ₂	55.0 ± 3.0
Al ₂ O ₃	22.0 ± 2.0
TiO ₂	1.5 ± 0.25
Fe ₂ O ₃	5.67 ± 0.5
MgO	2.30 ± 0.45
CaO	<2.00
Na ₂ O	<2.00
K ₂ O	<1.00
P ₂ O ₅	<0.20
S O ₃	0.002
Cl ⁻	0.2
Cr ₂ O ₃	0.02
Mn ₂ O ₃	0.03
Loss on ignition	9.80

(model D8AD VANCE, BRUKER) analysis of clay showed that the bentonite clay contained 80 % of montmorillonite, 10 % of kaolinite and 10 % of illite and quartz.

Table 2: Characteristics of bentonite clay

Tabela 2: Značilnosti bentonitne gline

Characteristic	Value
BET surface area	62.5671 m ² /g
Pore volume ($p/p_0 = 0.97$)	0.098005 cm ³ /g
Average pore width	6.2656 nm
Average pore diameter	9.5650 nm
Porosity (%)	17
Solid density	2.6253 g/cm ³

3.2 pH Effects

The effect of a changing pH from 1–10 on the adsorption of copper and nickel ions on bentonite clay was studied. The adsorption of Cu and Ni on bentonite clay increased with an increase in the pH and its maximum value was at around 7. At a low pH, the positive charges increased¹² and the adsorption of metal ions decreased due to an increase in the positive charges on the clay (Figure 1).

The main components of the Saudi bentonite clay are SiO₂ and Al₂O₃ (Table 1). The adsorption properties of clay are influenced by the pH of the solution and the Si/Al ratio. The effect of pH can be illustrated as follows.¹²



where M is the Al or Si atoms in the clay. The isoelectric point (PI) is the pH, at which there is no net charge present on the surface of a clay particle. The value of the isoelectric point for silica is 2 and that of

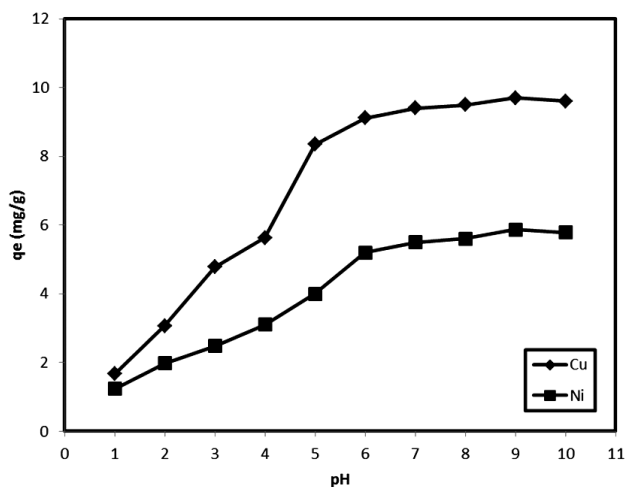


Figure 1: Effect of pH on the adsorption of copper and nickel on bentonite clay

Slika 1: Vpliv pH na adsorpcijo bakra in niklja na bentonitno glino

alumina is 9.¹² However, when the Si/Al ratio is between 1 and 5, the clay will adsorb both the cation and anion ions.¹²

Overall, the adsorption of the Cu and Ni ions with the negative charge on the clay is due to the attraction of the electrostatic force between the negative and positive charges of heavy metals. The negative charges on the clay surface are largely due to the presence of silica. The optimum pH value of 7 was used to analyze the effects of other variables such as temperature.

3.2.1 Equilibrium experiments

A combination of copper and nickel as a multicomponent system was investigated. The equilibrium results are presented in Figures 2 and 3. The results indicate that the adsorption capacity of clay was higher for Cu ions than for Ni ions. The maximum adsorption capacity of clay was 11.12 mg g⁻¹ at 20 °C for Cu and 6.78 mg/g at 20 °C for Ni in the batch solution containing both the

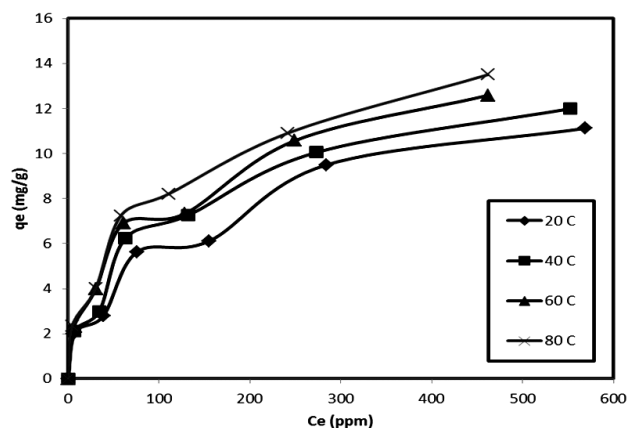


Figure 2: Equilibrium isotherm for the adsorption of Cu from wastewater on bentonite clay at different temperatures

Slika 2: Ravnotežna izoterma za adsorpcijo bakra iz odpadne vode na bentonitno glino pri različnih temperaturah

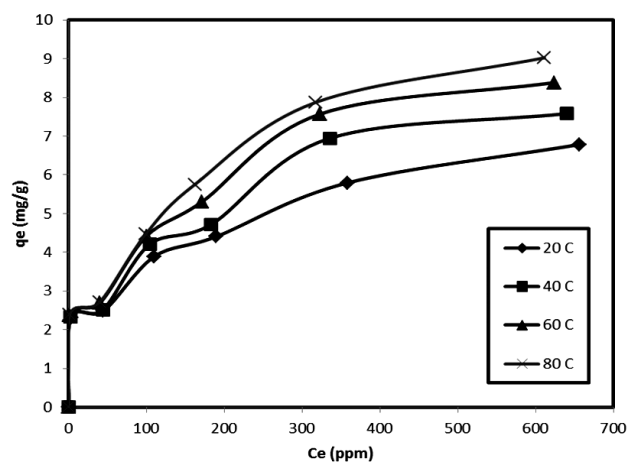


Figure 3: Equilibrium isotherm for the adsorption of Ni from wastewater on bentonite clay at different temperatures

Slika 3: Ravnotežna izoterma za adsorpcijo Ni iz odpadne vode na bentonitno glino pri različnih temperaturah

Cu and Ni ions. This may be attributed to the competition between the Cu and Ni ions on the active site on the clay. Other investigators obtained similar results for a multicomponent adsorption on the orthophosphate-modified kaolinite clay.¹³ The results infer that the selectivity of bentonite clay for the adsorption of various ions is Cu > Ni ion. This can be concluded from the data presented in **Table 3**.

Table 3: Copper and nickel properties^{9,10}**Tabela 3:** Lastnosti bakra in niklja^{9,10}

Property	Copper ion	Nickel ion
Ionic radius (nm)	0.072	0.069
Atomic mass	63.4	57.8
Coordination number	2, 4	4, 5
Electron configuration	[Ar] 3d ⁹	[Ar] 3d ⁸
Electro negativity of the atom	1.90	1.91

This variability for more Cu ion adsorption than Ni on clay is clear from **Table 3**, which shows an unpaired electron for a Cu ion in addition to the Cu ion being paramagnetic.¹⁴ Consequently, the Cu ion can be attracted by a magnetic field resultant from the clay adsorbent¹⁵ because the Ni ion is stable due to the absence of an unpaired electron.

3.3 Equilibrium Experimental Results

a) Extended Langmuir isotherm model

The extended Langmuir parameters K_1 , b_1 , K_2 and b_2 were obtained with the non-linear regression technique from equations 2 and 3. The equilibrium parameters K_1 ,

Table 4: Extended Langmuir constants for the Cu-ion adsorption on clay from a mixture of copper and nickel solution at different temperatures**Tabela 4:** Razširjene Langmuirove konstante za adsorpcijo Cu-ionov na glino iz mešanice raztopine bakra in niklja pri različnih temperaturah

Temperature $T/^\circ\text{C}$	$K_1/(\text{L/g})$	$B_1/(\text{L/mg})$	AARD/%	R^2	X^2
20	0.106	0.007	18.58	0.941	2.41
40	0.1306	0.0089	16.42	0.959	2.06
60	0.167	0.0114	16.88	0.94	2.346
80	0.176	0.012	15.91	0.95	3.41

Table 5: Extended Langmuir constants for the Ni-ion adsorption on clay from a mixture of copper and nickel solution at different temperatures**Tabela 5:** Razširjene Langmuirove konstante za adsorpcijo Ni-ionov na glino iz mešanice raztopine bakra in niklja pri različnih temperaturah

Temperature $T/^\circ\text{C}$	$K_2/(\text{L/g})$	$b_2/(\text{L/mg})$	AARD/%	R^2	X^2
20	0.557	0.0002	22.25	0.672	29.23
40	0.068	0.0002	23.07	0.755	25.92
60	0.0843	0.0001	21.76	0.808	35.15
80	0.0865	0.0001	22.40	0.829	37.32

b_1 , K_2 and b_2 were calculated with the non-linear regression technique and presented in **Tables 4** and **5**.

b) Langmuir-Freundlich isotherm model

The parameters of the Langmuir-Freundlich isotherm model such as K_1 , b_1 , K_2 and b_2 , n_1 and n_2 were obtained applying equations 4 and 5. The equilibrium parameters are presented in **Tables 6** and **7**.

Table 6: Langmuir-Freundlich constants for the Cu-ion adsorption on clay in a mixture of multicomponent from copper and nickel at different temperatures**Tabela 6:** Langmuir-Freundlich konstante za adsorpcijo Cu-ionov na glini iz multikomponentne mešanice za baker in nikelj pri različnih temperaturah

Temperature $T/^\circ\text{C}$	$K_1/(\text{L/g})$	$b_1/(\text{L/mg})$	n_1	AARD/%	R^2	X^2
20	0.662	0.0028	0.482	13.51	0.959	0.526
40	0.9778	0.0093	0.4233	11.31	0.964	0.535
60	0.567	0.0046	0.5799	13.57	0.935	1.16
80	0.4623	0.0066	0.7434	13.002	0.969	0.932

Table 7: Langmuir-Freundlich constants for the Ni-ion adsorption on clay in a mixture of multicomponent from copper and nickel at different temperatures**Tabela 7:** Langmuir-Freundlich konstante za adsorpcijo Ni-ionov na glino v multikomponentni mešanici iz bakra in niklja pri različnih temperaturah

Temperature $T/^\circ\text{C}$	$K_2/(\text{L/g})$	$b_2/(\text{L/mg})$	n_2	AARD/%	R^2	X^2
20	0.722	0.0135	0.375	12.533	0.892	1.5
40	0.879	0.0005	0.355	16.34	0.901	1.23
60	1.101	0.0300	0.3720	20.2412	0.885	1.386
80	0.1928	0.0108	0.788	17.087	0.874	16.08

Table 8: Multicomponent five-parameter isotherm constants for the Cu-ion adsorption on clay in a mixture of copper and nickel at different temperatures**Tabela 8:** Večkomponentna petparametrična izotermna konstanta za adsorpcijo Cu-ionov na glini iz mešanice bakra in niklja pri različnih temperaturah

Temperature $T/^\circ\text{C}$	$K_1/(\text{L/g})$	$b_1/(\text{L/mg})$	n_1	AARD/%	R^2	X^2
20	1.714	18.098	0.0664	20.254	0.918	3.935
40	1.072	5.599	0.1479	16.71	0.947	2.142
60	1.343	4.761	0.0119	15.49	0.938	1.263
80	1.489	1.279	0.0088	9.057	0.958	0.6468

Table 9: Multicomponent five-parameter isotherm constants for the Ni-ion adsorption on clay in a mixture of copper and nickel at different temperatures**Tabela 9:** Večkomponentna petparametrična izotermna konstanta za adsorpcijo Ni-ionov na glini iz mešanice bakra in niklja pri različnih temperaturah

Temperature ($^\circ\text{C}$)	$K_2/(\text{L/g})$	$b_2/(\text{L/mg})$	n_2	AARD/%	R^2	X^2
20	0.9066	0.0048	1.456	26.598	0.614	38.312
40	0.5629	0.0042	1.397	21.79	0.769	24.854
60	0.6829	0.1277	0.909	20.309	0.8252	23.44
80	0.7455	0.4703	0.7206	20.232	0.873	9.521

c) Multicomponent five-parameter isotherm model

The equilibrium constants for the model such as K_1 , b_1 , K_2 and b_2 , n_1 and n_2 were obtained applying equations 6 and 7 as shown in **Tables 8** and **9**.

3.4 Estimation of the Best Fit

The theoretical results and the experimental equilibrium data were compared using the average absolute relative deviation percent (AARD/%), the chi-square method (X^2) and the adjusted coefficient of determination (R^2). The AARD was calculated to determine the best fit between the theoretical and experimental results from the applied equilibrium isotherm models as summarized below.

$$AARD/\% = \frac{100}{N} \sum_{i=1}^N \left| \frac{q_{i_{\text{exp}}} - q_{i_{\text{calc}}}}{q_{i_{\text{exp}}}} \right| \quad (8)$$

where N is the number of data points, $q_{i_{\text{calc}}}$ is the calculated amount of the metal-ion adsorption on clay and $q_{i_{\text{exp}}}$ is the experimental amount of the metal-ion adsorption on clay for a given data point i . Also, the chi-square method (X^2) was applied to evaluate the relationship between the theoretical and the experimental data from the equilibrium experiments. The chi-square (X^2) formula is:

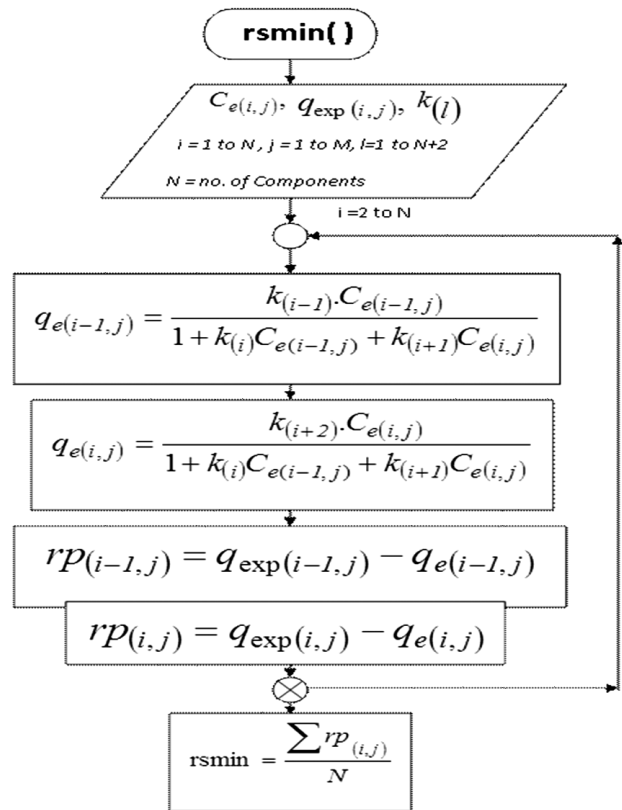
$$(X^2) = \sum_{i=1}^N \frac{(q_{i_{\text{exp}}} - q_{i_{\text{calc}}})^2}{q_{i_{\text{calc}}}} \quad (9)$$

where N is the number of data points, $q_{i_{\text{exp}}}$ is the experimental amount of the metal-ion adsorption on clay and $q_{i_{\text{calc}}}$ is the calculated amount of the metal-ion adsorption on clay for a given data point i . In the case of the chi-square method (X^2), the X^2 has a small value, the result of the model is close to the result of the equilibrium experiment and vice versa. The adjusted coefficient of determination, R^2 , is normally used to evaluate the best fit.

Significant differences were observed between the extended Langmuir isotherm model, the Langmuir-Freundlich isotherm model and the multicomponent five-parameter isotherm model. The Langmuir-Freundlich isotherm model provided the best correlation with the equilibrium data.

3.5 Numerical Solution of the Non-Linear Isotherm Models

A non-linear, least-square, data-fitting algorithm using the `fminsearch` function from MATLAB was used to find the optimum values of the isotherm models. Then the average absolute relative deviation percent (AARD/%), the adjusted coefficient of determination, R^2 , and the chi-square method (X^2) were calculated for the experimental and theoretical values. The program was written using MATLAB and the flow chart is shown below:



4 CONCLUSIONS

The study showed that pH is a significant factor in the adsorption processes as it causes electrostatic changes in the solutions. The optimum pH value for the Cu and Ni adsorption is around 7. The maximum adsorption capacity of clay increased with an increase in the temperature, which was 11.12 mg g⁻¹ for copper and 6.78 mg g⁻¹ for nickel at 20 °C in the experimental solutions. Among the various isotherm models, the Langmuir-Freundlich isotherm model described the experimental data very well.

Acknowledgements

The authors would like to thank King Abdulaziz City for Science and Technology (KACST) for the support and encouragement to carry out the study.

5 REFERENCES

- 1 M. J. Zamzow, J. E. Murphy, Removal of metal cations from water using zeolites, *Separation Science and Technology*, 27 (1992) 14, 1969–1984
- 2 A. S. Mashhady, Heavy metals extractable from a calcareous soil treated with sewage sludge, *Environmental pollution (series B)*, 8 (1984), 51
- 3 A. M. Al-Rehaili, Municipal wastewater treatment and reuse in Saudi Arabia, *The Arabian Journal for Science and Engineering*, 22 (1997), 143

- ⁴ U. Forstner, G. T. Wittmann, Metal pollution in the aquatic environment, Springer verlag, New York 1979
- ⁵ D. Jenkins, Effect of reformulation of household powder laundry detergents on their contribution to heavy metals levels in wastewater, *Water Environment Research*, 70 (1998) 5, 980
- ⁶ A. I. Alabdula'aly, Trace metals in Riyadh public water supplies, *The Arabian Journal for Science and Engineering*, 22 (1997), 165
- ⁷ M. Sadiq, G. Hussain, Drinking water quality in Saudi Arabia- an overview, *The Arabian Journal for Science and Engineering*, 22 (1997), 153
- ⁸ G. McKay, Use of adsorbents for the removal of pollutants from wastewater, CRC, Press, Inc., 1996
- ⁹ W. Fritz, E. U. Schuender, Simulation adsorption equilibria of organic solutes in dilute aqueous solution on activated carbon, *Chemical Engineering Series*, 29 (1974), 1279
- ¹⁰ A. I. Liapis, D. W. T. Rippin, A general model for the simulation of multi-component adsorption from a finite batch, *Chemical Engineering science*, 32 (1977), 619
- ¹¹ C. M. Yon, P. H. Turnock, Multicomponent adsorption equilibria on molecular sieves, *American Institute Chemical Engineers, Symposium*, 67 (1971), 75
- ¹² H. A. Elliott, C. P. Huang, Adsorption characteristics of some Cu(II) complexes on aluminosilicates, *Water research*, 15 (1981), 849-855
- ¹³ K. O. Adebawale, I. E. Unuabonah, B. I. Olu-Owolabi, The effect of some operating variables on the adsorption of lead and cadmium ions on kaolinite clay, *Journal of Hazard Material*, 134 (2006), 130
- ¹⁴ K. F. Purcell, J. C. Kotz, *An Introduction to Inorganic Chemistry*, Saunders College Publishing, Philadelphia 1980
- ¹⁵ K. H. Chong, B. Volesky, Metal biosorption equilibria in a ternary system, *Biotechnology and Bioengineering*, 49 (1996), 629

MODELLING AND OPTIMIZATION OF A LASER DROPLET-FORMATION PROCESS

MODELIRANJE IN OPTIMIZACIJA LASERSKEGA TVORJENJA KAPLJICE

Tadej Kokalj¹, Igor Grabec², Edvard Govekar²

¹Institute of Metals and Technology, Lepi pot 11, 1000 Ljubljana, Slovenia

²Faculty of Mechanical Engineering, University of Ljubljana, Aškerčeva 6, 1000 Ljubljana, Slovenia
tadej.kokalj@imt.si

Prejem rokopisa – received: 2013-04-12; sprejem za objavo – accepted for publication: 2013-05-06

The laser droplet-formation process (LDFP) is a part of the novel joining technology for forming high-temperature joints. The advantages of this technology are: good heat-input control, good control of the added material and limited local heating. A molten metal droplet is used as the basic unit for the filling material, and a determination of the process parameters for the formation of droplets with desired properties is crucial. A physical and numerical model of the process was built to allow a theoretical determination of the process parameters. The numerical model enables a simulation of the process at different sets of parameters and a genetic algorithm optimization was implemented to find the best set. To verify this general procedure for determination and optimization of the parameters, we applied it in a specific case of a nickel wire. On the basis of the numerical model of the process, laser pulses for pendant-droplet formation and droplet detachment were determined and applied in experiments. With numerically determined laser pulses pendant-droplet formation and detachment were accomplished. In most cases, the process showed a very high repeatability. The encouraging experimental verification shows that a numerical approach is a very helpful tool for a determination of the process parameters and a better understanding of the process. It significantly reduces the number of necessary experiments when the laser droplet-formation setup or the target droplet properties are changed.

Keywords: droplet formation, laser, modelling, optimization, experimental verification

Proces laserskega tvorjenja kapljice (LTK) je del nove tehnologije spajanja za tvorjenje visokotemperaturnih spojev. Prednosti te tehnologije so: dobra kontrola vnesene toplote in dodanega materiala ter omejeno lokalno segrevanje podlage. Staljena kovinska kapljica se uporabi kot dodajni material, parametri za tvorjenje kapljice s primernimi lastnostmi pa so bistveni za uspešnost procesa. Zgradili smo fizikalni in numerični model procesa, ki omogoča teoretično določitev optimalnih procesnih parametrov. Numerični model nam omogoča simulacijo procesa pri različnih naborih parametrov, optimizacijo z genetskimi algoritmi pa smo uporabili za iskanje najboljšega nabora. Za eksperimentalno potrditev tega splošnega načina smo metodo uporabili v konkretnem primeru nikljeve žice. Na osnovi teoretičnega modela smo določili laserski blisk za tvorjenje in odlet kapljic ter jih uporabili v poskusih. Z numerično določenimi laserskimi bliski smo uspešno tvorili in ločili kapljico od žice. V večini primerov je proces izredno dobro ponovljiv. Uspešna eksperimentalna potrditev potrjuje pomembnost teoretičnega modela za določitev procesnih parametrov in boljše razumevanje procesa. Numerični model močno zmanjša potrebno število eksperimentov za določitev procesnih parametrov ob spremembi vrste žice ali spremembi ciljnih lastnosti tvorjenih kapljic.

Ključne besede: tvorjenje kapljice, laser, modeliranje, optimizacija, eksperimentalna verifikacija

1 INTRODUCTION

A constant technological advance is increasing the demand for joining new and dissimilar materials, for which conventional technologies are neither appropriate nor convenient. The differences in the thermophysical properties of base materials and the trend of miniaturisation require a better control of the heat input and the amount of a filler material. In order to improve this control, droplet-joining technologies are investigated where a small, molten metal droplet is used as the basic unit of a filling material. The droplet is deposited on a joining spot creating a material-to-material joint or a bridge over a gap in the substrate.^{1,2}

Several droplet-formation technologies have been proposed for the applications in the joining technologies. Individual droplets are generated by different "drop-on-demand" generators.³⁻⁵ In the case of low-melting materials (300 °C to 500 °C), the melted material is provided from a heated reservoir. A droplet is then generated with

a short pressure pulse.^{5,6} Produced joints are not susceptible to high temperatures and usually contain lead that is environmentally disputable. The generation of droplets from a high-melting material (typically over 1000 °C), is usually accomplished with local heating of a wire. The first systems for droplet generation used a pulsed electric arc between the electrodes and the tip of the wire.⁷⁻⁹ A molten metal droplet was then detached from the wire by the electromagnetic force, as a consequence of an increase in the electric current at the end of the pulse^{10,11}, which could be accompanied by mechanical oscillations of the wire.¹² The diameter of a droplet in this technology is limited down to 1 mm.¹³ A system for the arc-droplet formation does not allow for a precise energy control. Besides, an electric arc induces the formation of hot plasma, which strongly heats the surroundings. The system has to be intensely cooled and it is not appropriate in the cases when the heat susceptibility of the substrate is limited.

To avoid the listed deficiencies of the formation of high-temperature joints, a new laser droplet-formation technology was proposed.^{14,15} In this novel technology a laser beam is used for droplet formation and detachment from the feed wire (**Figure 1**). The advantage of this technology is a good heat-input control and limited local heating enabling a formation of smaller droplets.¹⁵⁻¹⁷

The laser droplet-formation process (LDFP) was proposed as part of a new droplet-joining technology in¹⁵ and was first characterized with an IR camera and acoustic emission signals in¹⁴. A detailed characterization of the process on the basis of acoustic emission, where different phases of the process such as heating, melting, droplet formation and droplet detachment are observed, is given in¹⁸. A possibility of an indirect process characterization by means of reflected laser light is explained in¹⁶. The cooling of a droplet after its detachment and examples of blind joints are discussed in¹⁷ and an application for joining the parts of different materials and geometrical properties are elaborated in¹⁹. Later a sequential formation of droplets was presented and the chaotic regimes of sequential-droplet formations were elaborated and discussed in²⁰. Lately, some promising studies were done on the application of droplet welding of coated steel sheets.²¹

Determining the process parameters, especially the time course of the laser power, proves to be of the central importance for the repeatable formation of droplets with

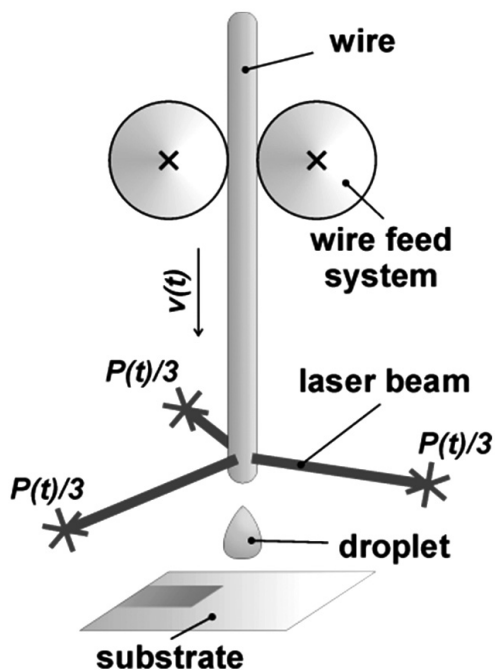


Figure 1: In the laser droplet-formation process (LDFP) a thin metal wire is fed to the focus of laser beams. A hot molten droplet is formed at the tip of the wire, detached by a sudden increase in the laser power and deposited on the substrate.

Slika 1: Pri laserskem tvorjenju kapljice (LTK) dodajamo tanko kovinsko žico v gorišče laserskih žarkov. Vročo staljeno kapljico, ki nastane na koncu žice, ločimo s kratkotrajnim povečanjem laserske moči. Kapljica pade na podlago, kjer tvori spoj.

desired properties. The first experimental investigations showed that it is difficult to achieve a repeatability of the process and to avoid undesired radial scatter and splashing of the melt by the heuristically determined laser pulses. At the beginning, a laser pulse of a constant power was used with a steel wire, however, the time course of the laser power and velocity of the wire movement were later identified to be the most important process parameters. A simple theoretical analysis of the process²² as well as the experimental results showed that it is convenient to divide LDFP into two phases: the pendant droplet formation and the detachment phase. With this approach the process was significantly improved. However, in order to further improve the control of droplet properties, like the size, temperature homogeneity and heat content, and to avoid undesired splashes, a numerical model of the process was built.

The numerical model enables the simulation of the process at different sets of process parameters. With the use of the numerical model and genetic-algorithm optimization method, the process parameters can be optimized in accordance with the selected optimization objectives. These optimization objectives incorporate the desired droplet properties corresponding to the purpose of an application. The theoretical approach showed to be very useful not only to get a better insight into the process, but especially as a general tool to significantly decrease the number of the experiments needed to find new process parameters when some of the parameters are changed (i.e., wire material or diameter, laser optics, wire velocity, etc.).

The article starts with a description of the physical and numerical model of the process. An application of genetic algorithms for determining the pendant-droplet-formation pulse is described together with the applied objective functions. At the end of the theoretical part of the paper the procedure for determining the droplet-detachment pulse is explained on the basis of a simplified model of the keyhole phenomenon. In the second part of the paper we focus on the experimental verification of theoretical results. The laser droplet-formation process is explained for a specific case of a nickel wire. The results of the theoretical treatment with determined laser pulses and the corresponding simulations are presented in parallel with the experimental results for both pendant-droplet formation and detachment of a droplet. In the last section we discuss the results and underline the significance of this research for a further development of the process.

2 THEORETICAL MODEL AND NUMERICAL MODEL

With the aim of theoretically determining the laser pulse, a numerical model of the process was built. The basic equation of this model is the heat equation in cylindrical coordinates $(r; \vartheta, z)$:

$$\frac{\partial T(r, \vartheta, z, t)}{\partial t} = D(T) \left[\frac{1}{r} \frac{\partial}{\partial r} \left(r \frac{\partial T(r, \vartheta, z, t)}{\partial r} \right) + \frac{1}{r^2} \frac{\partial^2 T(r, \vartheta, z, t)}{\partial \vartheta^2} + \frac{\partial^2 T(r, \vartheta, z, t)}{\partial z^2} \right] \quad (1)$$

where T is the temperature and $D(T) = k(T)/\rho(T)c_p(T)$ is the temperature-dependant heat-diffusion coefficient. In this equation the temperature-dependent gradient of the heat-conduction coefficient k was neglected.

Phase transitions were treated as jumps in specific heat:

$$c_{pt}(T) = c_p(T) + L\delta(T - T_p) \quad (2)$$

where c_{pt} is the total specific heat, including the latent heat L , c_p is the specific heat at the instant temperature, δ is the Dirac delta function and T_p is the temperature of the phase transition. For the numerical approximation of δ , a Gaussian function was used:

$$\delta(T - T_p) \approx \frac{1}{\sqrt{2\pi}\Delta T} \exp\left(-\frac{(T - T_p)^2}{2\Delta T^2}\right) \quad (3)$$

Here ΔT is the adaptable width of the Gaussian function.

The temperature of the wire at the beginning of the process is the same as the environmental temperature T_0 , therefore we formulate the initial condition as:

$$T(\vec{r}, 0) = T_0 \quad (4)$$

With respect to the boundary conditions we consider the thermal radiation from the hot surface as:

$$j_r(\vec{r}_{sur}, t) = -\sigma T^4 \quad (5)$$

Since the radiation flux from the wire is much larger than the radiation flux from the environment to the wire, the latter is neglected in this formulation.

The energy flux of the laser beams to the wire is a function of the spatial part $j_l(\vec{r})$, the temporal part $g(t)$ and it depends on the material absorptivity A :

$$j_f(\vec{r}_{sur}, t) = A j_l(\vec{r}) g(t) \quad (6)$$

The boundary condition on the surface of the wire is finally formulated as:

$$k(T) \frac{\partial T}{\partial n} = j_f - j_r \quad (7)$$

where k is the thermal conductivity and $\partial T/\partial n$ is the temperature gradient in the direction perpendicular to the surface. The sum of thermal fluxes is on the right-hand side of the equation.

The heat equation including the described initial and boundary conditions can be solved numerically using an explicit finite-difference scheme in cylindrical coordinates.²³ With the described numerical model the time development of the temperature field of the wire at various sets of process parameters can be simulated. Based on the simulations a proper set of process parameters can be determined and optimized. This work is focused on determining the laser pulse.

3 LASER-PULSE DETERMINATION

The laser pulse for pendant-droplet formation and the pulse for droplet detachment were determined separately. In the first part of the process the heat input is essential and in the second part a sufficient force is needed to detach the droplet. Although both parts of the process are coupled, we treated them separately for the sake of simplicity. The pendant-droplet-formation pulse was parameterized with seven parameters (**Figure 2**) and these were subject to optimization. The droplet-detachment pulse was determined on the basis of a simplified keyhole-effect model. We need to stress that only the parameterized laser pulse was optimized in this investigation, while the other parameters were pre-selected by selecting the wire, limiting our experimental setup and the desired size of the droplet and were not subject to optimization. However, the described optimization procedure can also be used to optimize other parameters.

3.1 Laser pulse for pendant-droplet formation

In the pendant-droplet-formation phase of the process, a well-melted pendant droplet has to be produced at the tip of the wire. Besides, the splashing of the melt and the radial scatter of deposited droplets have to be reduced. Since the droplet properties (i.e., heat content and temperature homogeneity) are importantly influenced in this part of the process, the laser pulse should be determined in accordance with the desired droplet properties.

The selection of a proper method for laser-pulse determination depends on the time necessary for one

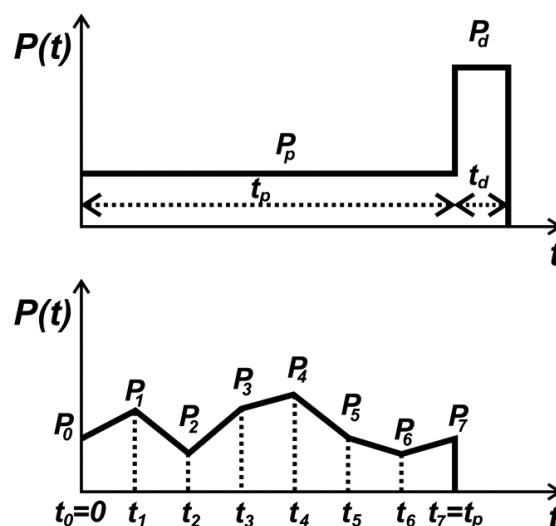


Figure 2: Simple laser pulse for LDFP consists of two parts: pendant-droplet-formation part and detachment part (top). In the present work we parameterized the first part of the pulse with seven parameters in order to further optimize the heat input (bottom).

Slika 2: Enostaven laserski blisk za LTK je sestavljen iz dveh delov: del za tvorjenje viseče pretaljene kapljice in del za ločitev kapljice (zgoraj). V predstavljenem delu smo prvi del bliska parametrizirali s sedmimi parametri za nadaljno optimizacijo vnosa toplote (spodaj).

process simulation. The numerical model was implemented in the C++ language. It is basically 3D and can be used either for a 2D or 3D simulation of the process. An increased spatial dimensionality of the model drastically increases the simulation time, therefore, the dimensionality of the problem is reduced. Since three laser beams are positioned equidistantly around the circumference of the wire, and the diameter of the laser beam is similar to the wire radius, the process can be considered as quasi-symmetrical. In this ax-symmetrical case the angular dependence can be abandoned and a 2D model is sufficient to describe the process.

A short simulation time allows an implementation of the optimization method that requires many process simulations. We choose the genetic-algorithm method²⁴⁻²⁶ for the process optimization.

To perform the optimization, we need to determine the fitness function that includes the objectives of the optimization encoded in a single mathematical expression. We determined two different fitness functions. The first fitness function was assigned as:

$$J_1 = 1 - \frac{m_t}{m} + \frac{m_i}{m} \quad (8)$$

where m_t/m is the portion of the melted material, and m_i/m is the portion of the vaporized material. The objective of this function is to get the highest possible amount of the melted material at the lowest possible vaporization. By finding the minimum of this function, we achieve the best trade-off between the amounts of the melted and vaporized material at the end of a laser pulse.

The second fitness function is more complex and composed of two parts:

$$J_2 = \frac{1}{2} \sqrt{\frac{\sum_{j=1}^N (T_j(t_v) - T_z)^2 \cdot \frac{m_j}{m_D}}{T_z}} + \frac{1}{2} \cdot \frac{1}{M} \sum_{k=1}^M \frac{m_{ik}(t_k)}{m_D} \quad (9)$$

where $T_j(t_v)$ is the temperature of the j -th volume part of the wire at the time t_v and m_j is its mass; m_D is the mass of the observed part of the wire and T_z is the desired final temperature of the wire; m_{ik} is the mass of the vaporized material at the time t_k .

The first part of the fitness function is calculated at the end of the laser pulse t_v and should bring the final temperature of the wire as close to the desired temperature T_z as possible. The role of the second part of the fitness function is to prevent vaporization during the pulse. It is calculated as the sum of the portions of the vaporized material at the $M = 100$ intervals from the beginning, $t = 0$, to the end of the laser pulse, $t = t_v$.

With these two fitness functions and the selection of desired temperatures T_z , different laser pulses for pendant-droplet formation were determined. In addition, the arbitrary-fitness function can be constructed in order to meet the demand of a specific application. The optimization was performed by combining the executable

C++ file, the returning value of the fitness function at the selected set of parameters and MATLAB Genetic Algorithm Toolbox, creating a new set of parameters. The time for the optimization of one laser pulse was around 20 h including several hundred process simulations.

3.2 Laser pulse for droplet detachment

After a successful formation of a pendant droplet at the tip of the wire an additional force is needed to overcome the surface tension force²⁰ and detach the droplet from the wire. This additional force is provided by an onset of the keyhole. The keyhole is a highly nonlinear phenomenon and therefore difficult to model, particularly in the first transient phase when the keyhole is being formed. Since the numerical model of the transient phase of the keyhole effect was not found in the literature, we built a simplified numerical model of this part of the process. We treated the keyhole as a fast vaporization of the material and we neglected the self-focusing dynamics of the keyhole due to the surface tension. In this way we could approximately simulate the growth of the keyhole.

It was shown in²² that a droplet can be detached from the wire when the depth of the keyhole approximately reaches the axes of the wire. Therefore, the droplet-detachment pulse was determined in the following way: First, a constant laser power was selected for the laser pulse. Second, the time development of the temperature field was calculated for the selected laser power and the temperature on the axis of the wire was checked on each time step. Third, the calculation was stopped when the temperature on the axis of the wire reached the boiling temperature, that is when the keyhole reached the axis of the wire.

With this procedure the necessary time to form a keyhole and detach the droplet from the wire, or better, its upper limit, was determined since the keyhole growth, considering the self-focusing, was even faster. It is important to minimize the detachment-pulse time in order to reduce the unnecessary heating of the wire with the high-power laser beam, resulting in undesired effects like vaporization and splashes of the melt.

4 EXPERIMENTS AND RESULTS

The theoretical model, pulse determination and optimization procedure described above are general and independent of the wire, laser and wire-feed unit. However, in order to evaluate the adequacy of theoretical work, we determined the laser pulses and performed experiments for a specific case of a nickel wire of a diameter 0.7 mm using the experimental setup described below. The results of numerical calculations and experimental outcomes are described in the following section.

4.1 Experimental system

The main parts of the experimental system are: a laser, a wire-feed unit, an opto-mechanical positioning system and a measuring computer.

The heart of this system is a Nd:YAG pulse laser which operates at the wavelength of $\lambda = 1064$ nm. The maximum frequency of the laser-pulse generation is $\nu = 300$ Hz and the average power is $\bar{P} = 0.25$ kW. The minimum power of the laser pulse is $P_{\min} = 0.48$ kW and the maximum laser power is $P_{\max} = 8$ kW. The minimum and maximum durations of the laser pulse are $t_{\min} = 0.3$ ms and $t_{\max} = 20$ ms. The time course of the laser power of a pulse can be set with a time step of 0.1 ms and a power step of 40 W.

The wire-feed unit enables the maximum acceleration of the wire, $a_{\max} = 20$ m/s², and the maximum velocity is $v_{\max} = 0.3$ m/s. The step size of the wire move is $z_{\min} = 3.1$ μ m.

For the investigation of LDFP the primary laser beam is split into three laser beams of equal power. These laser beams are led by means of optic fibres to exit the optics of the laser. This optics is equidistantly positioned

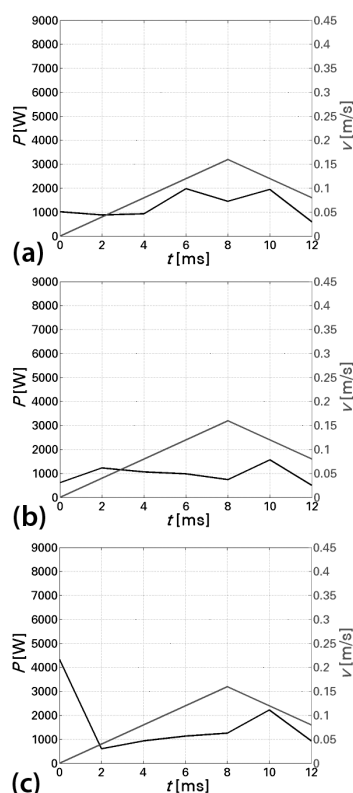


Figure 3: Examples of laser pulses (black line): a) laser pulse determined with the fitness function J_1 and laser pulses determined with the fitness function J_2 with the selected final temperatures: b) $T_{z1} = 2000$ K and c) $T_{z2} = 3000$ K. Grey line denotes the velocity profile of the wire movement.

Slika 3: Primeri laserskih bliskov (črna črta): a) laserski blisk, določen s kriterijsko funkcijo J_1 in laserska bliska, določena s kriterijsko funkcijo J_2 in različnimi ciljnimi končnimi temperaturami: b) $T_{z1} = 2000$ K in c) $T_{z2} = 3000$ K. Siva črta prikazuje hitrostni profil podajanja žice.

around the wire in the plane perpendicular to the wire. The focal length of the exit lens is $f = 100$ mm and the diameter of the laser beam in focus is $d_f = 0.4$ mm. For an easier positioning of the wire and monitoring of the process, the laser optics is equipped with the CCD cameras connected to the screens. Laser optics can be precisely positioned in accordance with the wire using a system of micrometer positioning stages.

4.2 Pendant-droplet formation

The laser droplet-formation process was separated into two phases. The first phase is the formation of a pendant droplet at the tip of the wire and the second phase is the detachment of the droplet from the wire. Therefore, we divided the total laser-pulse duration of 20 ms into a 12 ms part for the formation of the pendant droplet and the remaining 8 ms of the laser pulse for the droplet detachment.

First, the laser pulses for pendant-droplet formation were theoretically determined as described in section 3.1. Examples of the laser pulses are shown in **Figure 3**.

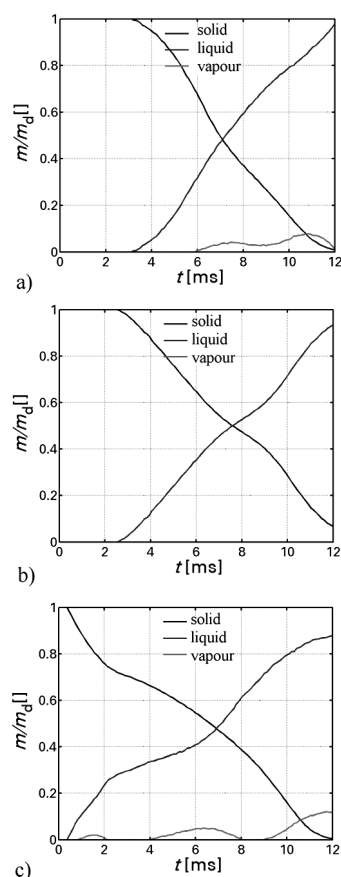


Figure 4: Time courses of the shares of the material in solid, liquid and vapour phases during the laser pulses. Graphs correspond to the laser pulses shown in **Figure 3**.

Slika 4: Časovni potek deleža materiala v trdnem, tekočem in plinastem stanju med trajanjem laserskega bliska. Slike po vrsti ustrezajo laserskim bliskom s **slike 3**.

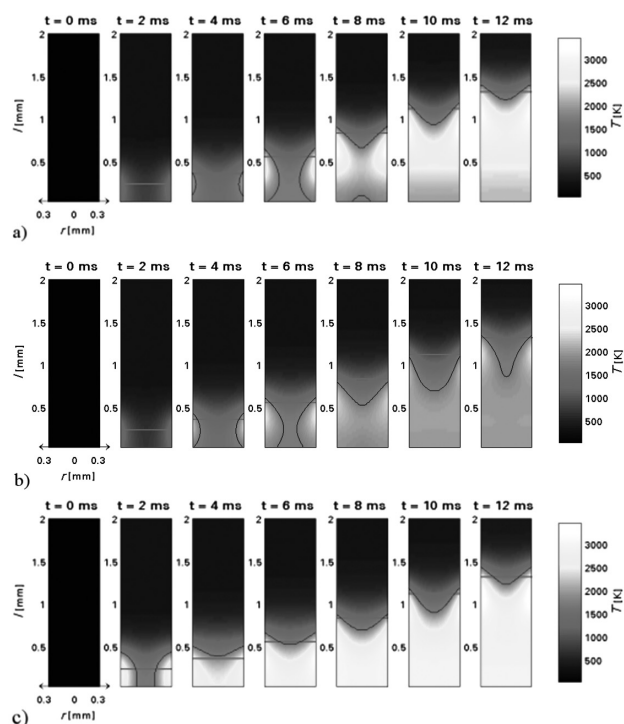


Figure 5: Evolution of the temperature field of the wire. Images correspond to the laser pulses shown in **Figure 3**.

Slika 5: Razvoj temperaturnega polja žice. Slike ustrezajo laserskim bliskom s **slike 3**.

The first pulse is determined with the fitness function J_1 that was used to assure the best trade-off between the shares of the melted and vaporized material. With the second J_2 fitness function we aimed at bringing the uniform temperature of the droplet as near to the desired temperature as possible. Besides, we wanted to decrease the vaporization of the material during the pendant-droplet formation, which was achieved with the second term in the fitness function. The first selected temperature is just above the melting temperature of nickel and the second is near the boiling temperature of nickel. The above-mentioned figure shows how the pulses differ, not just in the energy, but also in the time course of the laser power. At the beginning they differ a lot, but at the end they all have similar shapes. The laser power increases in the interval from 8 ms to 10 ms because the wire is moving with the largest velocity. At the end, when the velocity is decreased, the laser power is correspondingly reduced.

From the theoretical model we can also predict the share of the material in each phase during the laser-pulse duration, as shown in **Figure 4**.

As can be seen from the above figure, at the beginning, all material is in the solid phase. After a certain period the melting sets in. By the end of the pulse most of the material is melted and some of the material is vaporized. In the model vaporization is treated as the overheated liquid material that turns into a liquid if it cools down.

The evolution of the temperature field of a cross-section of the wire is shown in **Figure 5**.

The horizontal line denotes the position of laser beams and the black curves divide the material in different phases. The temperature fields can be compared to the experimental results. Three typical final states of the pendant droplet after solidification are shown in **Figure 6**.

The dashed cross in the image denotes the final position of the laser beam and the non-dashed cross was used for an easier positioning of the wire.

The first temperature field of the wire predicts the melted wire, but, as we can see in the photo, the tip of the wire is not completely melted. There is a knob on the wire tip that corresponds to the area of the lowest temperature predicted by our model. The core of the wire was probably not completely melted and the consequence is an irregular shape of the droplets.

As shown in the second figure of the temperature field, the predicted temperature of the wire tip is just above the melting temperature of nickel (1727 K). In the image of the experimental outcome we can see that no droplet was formed at the tip of the wire. The only noticeable effect of laser heating is a deformation of the wire at the position where the highest wire temperature is predicted by the model. This deformation is denoted with a white arrow in the image of the experimental outcome. The reason for a disagreement of the model prediction with the experimental results is the presumption on the uniform heating of the wire circumference, due to the simplification of the model.

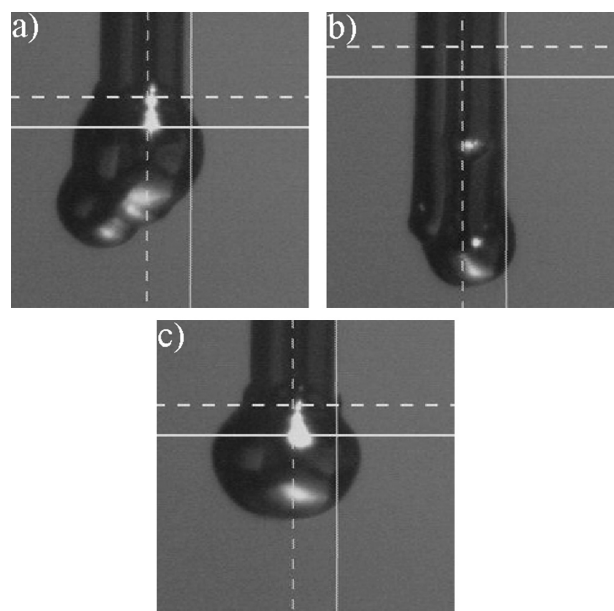


Figure 6: Typical examples of experimental outcomes of pendant-droplet formation. Droplets correspond to the laser pulses shown in **Figure 3** denoted with the same letters.

Slika 6: Tipični primeri eksperimentalnih tvorjenj viseče kapljice. Kapljice ustrezajo laserskim bliskom s **slike 3** in so označene z ustreznimi črkami.

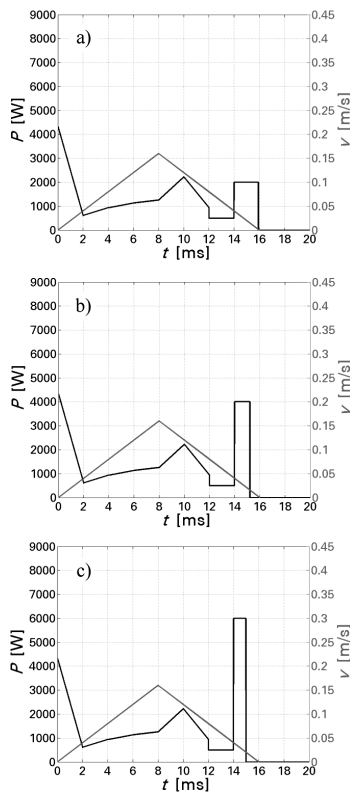


Figure 7: Three examples of laser pulses with the same pendant-droplet-formation parts and different detachment parts. Droplet-detachment pulses are of: a) 2000 W, b) 4000 W and c) 6000 W.

Slika 7: Trije primeri laserskih bliskov z enakim začetnim delom za tvorjenje viseče kapljice in različnimi bliski za ločitev kapljice. Bliski za ločitev kapljice imajo moči: a) 2000 W, b) 4000 W in c) 6000 W.

In the third case the model predicts a very hot tip of the wire near the boiling temperature. The experimental outcomes yield a repeatable formation of the melted droplets at the tip of the wire.

4.3 Droplet detachment

After the formation of a pendant droplet, we have to detach it from the wire. An additional high-intensity laser pulse is needed to assure a droplet detachment. This additional laser pulse is determined as described in section 3.2. The laser power is selected in advance and the duration of a laser pulse is determined in line with the requirement that the boiling temperature reaches the axis of the wire.

The best laser pulse for pendant-droplet formation was selected and a short time of 2 ms for the minimum laser power of $P_{min} = 480$ W was added to that pulse. This pause was heuristically introduced to allow a droplet relaxation, since the droplet oscillates after it is formed at the tip of the wire. Three examples of the calculated laser pulses are shown in **Figure 7**.

The required time for droplet detachment decreases with an increased laser power as expected. The dependence of the necessary pulse duration on the applied laser power is shown in **Figure 8**.

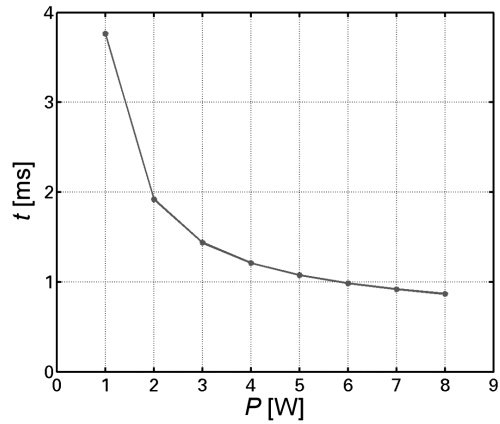


Figure 8: Dependence of detachment-pulse duration on the selected laser power

Slika 8: Odvisnost trajanja bliska za ločitev kapljice od izbrane moči laserja

The time development of the temperature field of the wire during a droplet-detachment pulse is shown in **Figure 9**.

The detachment pulse is stopped when the boiling temperature reaches the axis of the wire. The horizontal line denotes the position of the laser beams. The results of the model show that more material is melted when a higher laser power is used in spite of a shorter pulse time.

After the theoretical determination of detachment pulses, the experiments were performed for the evaluation of theoretical results. A laser pulse for a droplet detachment cannot be tested alone. Therefore, different detachment pulses were added after a relaxation period 2 ms that followed the same pendant-droplet-formation pulse.

With each laser pulse 10 droplets were produced and deposited on the substrate placed horizontally 3.5 mm below the focus of the laser beams. Examples of droplets are shown in **Figure 10**.

Radial scatter and a number of splashes on the substrate depend on the applied laser pulse. Droplets are systematically shifted to the left. The images of typical droplets in **Figure 10** show that the droplets differ also in the roughness of the contact region and the shape of a droplet on the substrate.

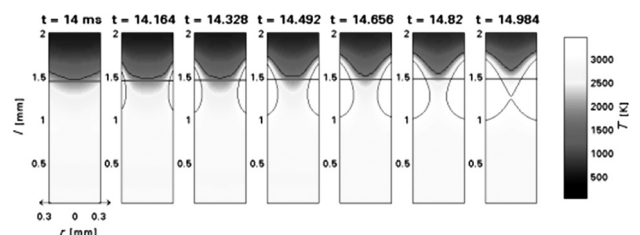


Figure 9: Time development of the temperature field during a droplet-detachment pulse

Slika 9: Časovni razvoj temperaturnega polja kapljice med bliskom za ločitev kapljice

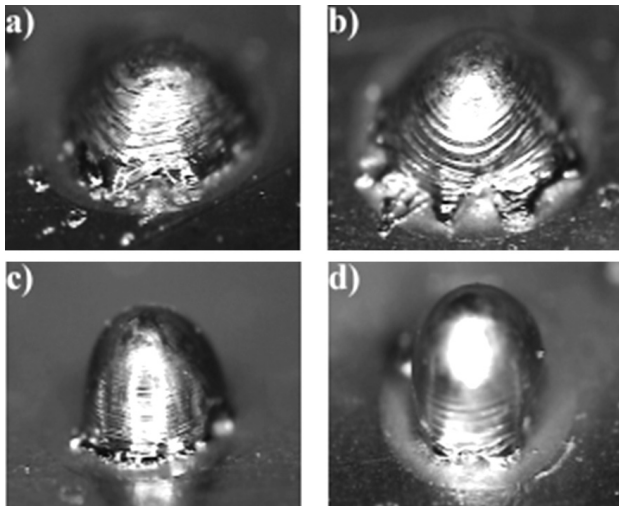


Figure 10: Magnifications of typical droplets from the sets produced with different detachment pulses

Slika 10: Povečava tipičnih kapljic iz zaporedij, tvorjenih z različnimi bliski za ločitev kapljice

For the purpose of evaluation and comparison a more detailed quantitative analysis of the experimental results was performed. The basic criterion for the successfulness of the process is the detachment of a droplet. Undesired splashes on the substrate were also counted. The repeatability of droplet deposition and droplet size was characterized with the size and standard deviation of these parameters. The results of the analysis are presented in **Table 1**.

We introduced variability of the process, V :

$$V = \frac{\sigma_d}{\bar{d}} + \frac{\sigma_r}{\bar{d}} \quad (10)$$

where the standard deviation of the droplet diameter is $\sigma_d = \sqrt{\sigma_{dx}^2 + \sigma_{dy}^2}$, the standard deviation of the droplet position from the expected position is $\sigma_r = \sqrt{\sigma_{rx}^2 + \sigma_{ry}^2}$ and \bar{d} is the average droplet diameter for a set. The ratio between the number of splashes on the substrate N_{izb} and the number of detached droplets in a set N_{kap} was calculated.

At the highest power of a detachment pulse, a droplet was always detached, but accompanied by numerous splashes. At a smaller laser power, droplets sometimes stay undetached. At a laser power of 2 kW droplets always stayed attached to the wire. At a laser power of 4 kW two droplets stayed undetached and at 5 kW one

droplet stayed undetached. At a laser power of 6 kW all the droplets detached from the wire. Also, the variability of the process decreases with the laser power. The process variabilities at the laser powers of 4 kW, 5 kW and 6 kW are very similar.

5 DISCUSSION AND CONCLUSION

A laser droplet-formation process is discussed in the article. For the first time a more detailed physical and numerical model of the process is presented. After building an experimental system and conducting quite an extensive experimental work we find out that the process is very complex in a sense of a high number of influencing parameters and instable in a sense of the sensitivity to small parameter change. To get a deeper insight into the process we decided to build a more detailed theoretical and numerical model of the process. Instead of using the model just for the analysis of the process we decided to determine certain selected process parameters on the basis of a numerical optimization of the process. In order to model the keyhole growth we proposed a very simple model that adequately serves our purpose.

The results of experimental work show that some theoretically determined laser pulses yield very good results. In some cases we notice a weaker agreement between the theoretical and experimental results, which is the consequence of a relatively simplified theoretical model. However, based on the numerical simulation of the process the experimental results can still be easily understood and interpreted. The theoretical model and optimization procedure are not meant to replace the experimental work completely, but can significantly decrease the extent of the required work. In this manner we should understand the importance of the presented work as being complementary to the experimental work. It allows a faster search for proper parameters and an easier interpretation of experimental results, especially when an important part of the process is changed like the wire material, laser optics, wire-feed system, etc. Though we give a quantitative statistical description of experimental results for the purpose of comparing experimental outcomes, the suitability of the process for a certain application should be determined by the final user in accordance with the specific demands of the application.

Table 1: Quantitative analysis of the experimental outcome for different detachment pulses

Tabela 1: Kvantitativna analiza eksperimentalnih rezultatov za različne ločitvene bliske

P	\bar{d}/mm	σ_d/\bar{d}	\bar{r}_x/mm	\bar{r}_y/mm	\bar{r}/mm	σ_r/\bar{d}	ν	N_{izb}/N_{kap}
8 kW	1.237	0.155	1.024	1.585	1.895	0.355	0.510	100/10 = 10
6 kW	1.223	0.169	-0.008	1.199	1.213	0.155	0.324	48/10 = 4.8
4 kW	1.149	0.098	0.679	1.276	1.458	0.255	0.323	29/8 = 3.6
5 kW	1.111	0.163	0.332	0.843	0.946	0.181	0.344	45/9 = 5

6 REFERENCES

- ¹ D. Attinger, D. Poulidakos, Melting and resolidification of a substrate caused by molten microdroplet impact, *Journal of Heat transfer*, 123 (2001) 12, 1110–1122
- ² A. M. Ahmed, R. H. Rangel, Metal droplet deposition on non-flat surfaces: effect of surface morphology, *International Journal of Heat and Mass Transfer*, 45 (2002), 1077–1091
- ³ S. Cheng, S. Chandra, A pneumatic droplet-on-demand generator, *Experiments in fluids*, 34 (2003), 755–762
- ⁴ J. Brünahl, A. M. Grishin, Piezoelectric shear mode drop-on-demand inkjet actuator, *Sensors and Actuators A*, 101 (2002), 371–382
- ⁵ H. Sohn, D. Y. Yang, Drop on demand deposition of superheated metal droplets for selective infiltration manufacturing, *Materials Science and Engineering A*, 392 (2005) 1–2, 415–421
- ⁶ S. X. Cheng, T. Li, S. Chandra, Producing metal droplets with a pneumatic droplet-on-demand generator, *Journal of Materials Processing Technology*, 195 (2005), 295–302
- ⁷ J. Haidar, An analysis of the formation of metal droplets in arc welding, *Journal of Physics D: Applied physics*, 31 (1998), 1233–1244
- ⁸ E. L. Dreizin, Droplet welding: A new technology for welding electrical contacts, *Welding Journal*, 76 (1997), 67–73
- ⁹ J. J. C. Buelens, Metal droplet deposition: review of innovative joining technique, *Science and Technology of Welding and Joining*, 6 (1997) 2, 239–243
- ¹⁰ F. Wang, W. K. Hou, S. J. Hu, E. Kannatey-Asibu, W. W. Schultz, P. C. Wang, Modelling and analysis of metal transfer in gas metal arc welding, *Journal of Physics D: Applied physics*, 36 (2003), 1143–1152
- ¹¹ W. W. Appelman, Miniaturisation of droplet deposition, Technical report, Philips Centre for Manufacturing Technology, Eindhoven 1995
- ¹² Y. Wu, R. Kovacevic, Mechanically assisted droplet transfer process in gas metal arc welding, *Proceedings of the Institution of Mechanical Engineers, Part B, Journal of engineering manufacture*, 216 (2002), 555–564
- ¹³ P. P. Conway, E. K. Y. Fu, K. Williams, Precision high temperature lead-free solder interconnections by means of high-energy droplet deposition techniques, *CIRP Annals*, 51 (2002) 1, 177
- ¹⁴ E. Govekar, B. Jahrsdoerfer, J. Klemenčič, P. Mužič, I. Grabec, Characterization of laser droplet formation process by IR camera images and AE signals, *Dynamic Days*, Dresden, 2001
- ¹⁵ W. Hovig, B. Jahrsdorfer, Laser droplet weld - ein innovatives fügeverfahren, *Laser in Elektronikproduktion & Feinwerktechnik*, LEF 2001, 2001
- ¹⁶ J. Klemenčič, Investigation of laser droplet formation from thin wire, Master thesis, FS, UL, Ljubljana, 2003
- ¹⁷ B. Jahrsdorfer, G. Eßer, M. Geiger, E. Govekar, Laser droplet weld – an innovative joining technology opens new application possibilities, *Photon Processing in Microelectronics and Photonics II*, Proceedings of SPIE, 2003, 4977
- ¹⁸ E. Govekar, J. Klemenčič, T. Kokalj, B. Jahrsdorfer, P. Mužič, I. Grabec, Characterization of laser droplet formation process by acoustic emission, *Ultrasonics*, 42 (2004), 99–103
- ¹⁹ B. Jahrsdorfer, M. Schmidt, M. Geiger, Laser droplet welding and its potential for joining dissimilar materials, *Laser Assisted Net Shape Engineering 4*, Proceedings of LANE 2004, 2004
- ²⁰ B. Krese, M. Perc, E. Govekar, The dynamics of laser droplet generation, *Chaos*, 20 (2010), 013129
- ²¹ A. Jerič, I. Grabec, E. Govekar, Laser droplet welding of zinc coated steel sheets, *Science and Technology of Welding and Joining*, 14 (2009) 4, 362–368
- ²² T. Kokalj, J. Klemenčič, P. Mužič, I. Grabec, E. Govekar, Analysis of the laser droplet formation process, *Journal of Manufacturing Science and Engineering*, 128 (2006) 1, 307–314
- ²³ J. W. Thomas, *Numerical Partial Differential Equations: Finite Difference Methods*, Springer-Verlag, New York 1995
- ²⁴ D. Whitley, A genetic algorithm tutorial, *Statistics and Computing*, 4 (1994), 65–85
- ²⁵ K. F. Man, K. S. Tang, S. Kwong, Genetic algorithms: Concepts and applications, *IEEE Transactions on Industrial Electronics*, 5 (1996) 43, 519–534
- ²⁶ A. E. Eiben, J. E. Smith, *Introduction to Evolutionary Computing*, Springer, Berlin 2003

COMPARISON OF THE TEMPERATURE FIELDS OF CONTINUOUSLY CAST STEEL SLABS WITH DIFFERENT CHEMICAL COMPOSITIONS

PRIMERJAVA TEMPERATURNEGA POLJA KONTINUIRNO ULITIH JEKLENIH SLABOV RAZLIČNIH KEMIJSKIH SESTAV

**Frantisek Kavicka¹, Karel Stransky¹, Bohumil Sekanina¹, Josef Stetina¹,
Milos Masarik², Tomas Mauder¹, Vasilij Gontarev³**

¹Brno University of Technology, Technicka 2, 616 69 Brno, Czech Republic

²Evráz Vitkovice Steel, a.s. Ostrava, Czech Republic

³University of Ljubljana, Aškerčeva 12, 1000 Ljubljana, Slovenia
kavicka@fme.vutbr.cz

Prejem rokopisa – received: 2012-08-21; sprejem za objavo – accepted for publication: 2012-12-19

The numerical model made by the authors was used for simulating the transient temperature fields of the continuously cast steel slabs with two different chemical compositions. The model solves the Fourier-Kirchhoff equation of the temperature fields of the slab-crystallizer system and the slab-ambient system with the following main thermophysical parameters: thermal conductivity, specific-heat capacity, density and enthalpy. When both melts follow each other closely, the critical state of the so-called breakout occurs at a certain point in the secondary cooling zone of a caster. It is probably a combination of surface defects. However, different chemical compositions of the two steels and their mixture are apparently decisive. Therefore, the temperature model simulated the temperature history of every point of a cross-section of a slab during its movement through the caster from the level of the melt in the crystallizer to the cutting torch for both melts and their mixture. The calculation of the temperature field of a slab is mainly focused on the part of the slab before the breakout and its surroundings. The results for the temperature field are used to set up a model of chemical heterogeneity of the steel supported by the material investigation of the samples taken from the breakout.

Keywords: continuously cast slab, temperature field, chemical composition, heterogeneity, numerical model, breakout

Uporabljen je bil originalen numerični model za simulacijo prehodnega temperaturnega polja kontinuirno ulitih jeklenih slabov dveh različnih kemijskih sestav. Model rešuje Fourier-Kirchhoffovo enačbo za sistema slab-kristalizator oz. slab-okolje z naslednjimi glavnimi termo-fizikalnimi parametri: toplotna prevodnost, specifična toplotna kapaciteta, gostota in entalpija. Ko se talina v formi zmeša s prejšnjo, pride do kritičnega stanja, t. i. prodora v določeni točki livne sekundarne hladilne cone. To nastane verjetno zaradi kombinacije površinskih napak. Tako je različna kemijska sestava dveh jekel in njihovo mešanje očitno odločilno pri tem pojavu. Temperaturni model je simuliral temperaturni potek v vsaki točki prečnega prereza slaba med njegovim gibanjem skozi celotni livni stroj od nivoja taline v kristalizatorju do rezalnega plamena za obe talini in njune mešanice. Izračun temperaturnega polja slaba je bil osredinjen predvsem na del slaba pred prodorom in njegovo okolico. Model kemijske heterogenosti jekla se lahko uveljavi z rezultati temperaturnega polja in z raziskavami vzorcev, ki so bili odvzeti iz območja prodora.

Ključne besede: kontinuirno ulit slab, temperaturno polje, kemijska sestava, heterogenost, numerični model, prodor

1 INTRODUCTION

The authors continue the study of the causes for the breakouts of continuously cast steel slabs of 250 mm × 1530 mm covered in the previous publications.¹⁻³ This is a defect that cannot be repaired. The break was detected in the unbending point of a slab, at a distance of 14.15 m away from the level of the melt inside the mould, where a breakout occurred between the 7th and 8th cooling segments of the secondary cooling zone. The difference in the heights between the level inside the mould and the breakout point was 8605 m. This tear in the shell occurred on the small radius of the caster. Here, the slab is beginning to straighten out and the breakout of the steel can occur in the points of the increased local chemical and temperature heterogeneities of the steel. The changes in the chemical composition of the steel during the actual continuous casting are especially dangerous. This change in the chemical composition of

the steel of two qualities, A and B, was carried out very quickly, by changing the tundish. Inside the mould, steel B mixed with steel A of the previous melt. Therefore, the results of the calculation of the temperature fields of the slabs with the chemical compositions A, B and of the mixed composition A + B will be presented. The mixed content of each element is considered as the average value of the composition A and B.

2 3D NUMERICAL MODEL OF THE TEMPERATURE FIELD OF A STEEL SLAB AND PREPARATION FOR THE SIMULATION

The optimisation of the production on casters, with the aim of achieving the maximum savings and maximum quality of the product is unthinkable without the knowledge of the course of the solidification and cooling of the concasting. The solidification and cooling of a

concast slab is a global problem of the 3D transient heat and mass transfer. If the heat conduction within the heat transfer in this system is decisive, the process is described with the Fourier-Kirchhoff equation. It describes the temperature field of the solidifying slab in all three of its states: at the temperatures above the liquidus (i.e., the melt), within the interval between the liquidus and solidus (i.e., in the mushy zone) and at the temperatures below the solidus (i.e., the solid state). In order to obtain these results, it is convenient to use the explicit numerical method of finite differences. A numerical simulation of the release of latent heats of the phase or structural changes is carried out by introducing the enthalpy function dependent on temperature T . The latent heats are expressed after an automated generation of the network (pre-processing) ties on the entry of the thermophysical material properties of the investigated system. They are the heat conductivity k , the specific heat capacity c and the density ρ of the cast metal.

The temperature distribution in the slabs described with the enthalpy balance equation is as follows:

$$\begin{aligned} \frac{\partial(\rho H)}{\partial t} + \frac{\partial}{\partial x}(\rho u H) + \frac{\partial}{\partial y}(\rho v H) + \frac{\partial}{\partial z}(\rho w H) = \\ = \frac{\partial}{\partial x} \left(k \frac{\partial T}{\partial x} \right) + \frac{\partial}{\partial y} \left(k \frac{\partial T}{\partial y} \right) + \frac{\partial}{\partial z} \left(k \frac{\partial T}{\partial z} \right) \end{aligned} \quad (1)$$

The simplified equation (1), suitable for an application on the radial casters with a great radius, where only the speed (of the movement of the slab) component w in the z -direction is considered, is:

$$\begin{aligned} \frac{\partial(\rho H)}{\partial t} + \frac{\partial}{\partial z}(\rho w H) = \\ = \frac{\partial}{\partial x} \left(k \frac{\partial T}{\partial x} \right) + \frac{\partial}{\partial y} \left(k \frac{\partial T}{\partial y} \right) + \frac{\partial}{\partial z} \left(k \frac{\partial T}{\partial z} \right) \end{aligned} \quad (2)$$

The unknown enthalpy of the general nodal point of a slab in the next time step ($t + \Delta t$): $H_{i,j,k}^{(t+\Delta t)}$ is expressed with the explicit formula and it is a function of the enthalpies of the same node and six adjacent nodes in the Cartesian coordinate system from the previous time step t .

The thermophysical properties of the cast materials, k , c and ρ , contained in the equation and dependent on the chemical compositions are also functions of the temperature.⁴ The function of enthalpy H is not known as an analytical function, but as a set of tabular values, which means that a reverse determination of the temperature is numerically a highly demanding task. It is also dependent on the composition of the steel and on the rate of cooling.

Figure 1 shows that the task is symmetrical along the x -axis; it is, therefore, sufficient to investigate only one half of the cross-section. The 3D model was first designed as an off-line version and later as an on-line version so that it could work in real time. After the correction and testing, it will be possible to implement it on any caster thanks to the universal nature of the code. The numerical model takes into account the temperature field of the entire slab (from the meniscus of the level of the melt in the mould to the cutting torch) with the number of the nodes exceeding 10^6 on the half of the cross-section of the rectangular profile. The solution is performed under these boundary conditions:

$$T = T_{\text{cast}} \text{ at the meniscus} \quad (3a)$$

$$-k \frac{\partial T}{\partial n} = 0 \text{ at the plane of symmetry} \quad (3b)$$

$$-k \frac{\partial T}{\partial n} = h(T_{\text{surf}} - T_{\text{mould}}) \text{ in the mould} \quad (3c)$$

$$-k \frac{\partial T}{\partial n} = h(T_{\text{surf}} - T_{\text{amb}}) + se(T_{\text{surf}}^4 - T_{\text{amb}}^4) \quad (3d)$$

in the secondary and tertiary cooling zones

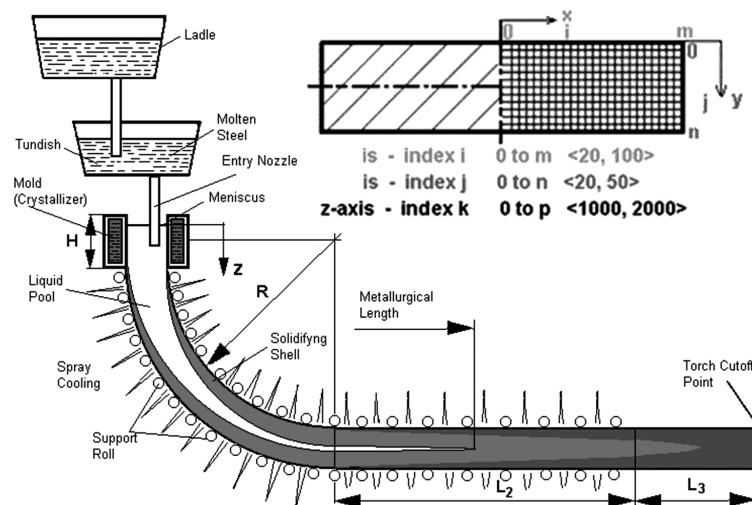


Figure 1: Caster and definition of the coordinate system
Slika 1: Livni stroj in definicija koordinatnega sistema

$$-k \frac{\partial T}{\partial n} = q \text{ beneath the support rollers} \quad (3e)$$

The initial condition for obtaining a solution is the setting of the initial temperature in individual points of the network. The suitable value is the highest possible temperature, i.e., the casting temperature T_{cast} .

It is, therefore, a solution of a distinctly non-linear task, since even for the boundary conditions their dependence on the surface temperature of a continuously cast slab is respected. All the boundary conditions were derived and were then divided to the areas of the mold (the primary cooling) and of the secondary and tertiary cooling. The zero heat flow perpendicular to the symmetry plane is the boundary condition that is common to all the zones of the caster.⁵

In equations (1–3) T is the temperature in K, t is the time in s, k is the heat conductivity in $\text{W m}^{-1} \text{K}^{-1}$, ρ is the density in kg m^{-3} , x, y, z are the axes in the given directions in m, u, v, w are the velocities in the given directions (the shift rate) in m s^{-1} , H is the specific enthalpy in J kg^{-1} , T_{surf} , T_{amb} are the surface and ambient temperatures in K, T_{cast} , T_{mould} are the casting and the mould temperatures in K, σ is the Stefan-Boltzmann constant ($5.76 \times 10^{-6} \text{ W m}^{-2} \text{K}^{-4}$), ε is the emissivity (0.8), n is normal to the surface in m, h in $\text{W m}^{-2} \text{K}^{-1}$ is the heat-transfer coefficient (HTC), q in W m^{-2} is the specific heat flow.

The heat-transfer coefficient h is a function of the local cooling rate and the surface temperature, the temperature T_{amb} is the cooling-water temperature in the secondary-cooling zone and the air temperature, where only radiation occurs. Based on the results of the previous investigations, the boundary conditions are set identically within each zone individually. The definition of the boundary conditions under the cooling jet is especially difficult. In order for the model to function correctly, it is necessary to determine the correct value of the heat-transfer coefficient h underneath the jet. Therefore, extensive experiments were conducted on a laboratory device simulating the process of solidification within the secondary-cooling zone. These measurements were conducted for various operation conditions, i.e., the pressure of the water and the shift rate. The numerical model contains a function that calculates the current on the basis of the entered water pressure, the shift rate, the positions of the jet and the surface temperature.

The casting speed was 0.0130 m s^{-1} (steel A) and 0.0126 m s^{-1} (steel B), the superheat was $23 \text{ }^\circ\text{C}$ (steel A) and $18 \text{ }^\circ\text{C}$ (steel B), the solidus temperature was $1427.0 \text{ }^\circ\text{C}$ (steel A) and $1480.6 \text{ }^\circ\text{C}$ (steel B), the liquidus temperature was $1493.9 \text{ }^\circ\text{C}$ (steel A) and $1512.3 \text{ }^\circ\text{C}$ (steel B).

The chemical composition of steel A in mass fractions (%) was: $w(\text{C}) = 0.416$, $w(\text{Cr}) = 0.95$, $w(\text{Ni}) = 0.03$, $w(\text{Mn}) = 0.7$, $w(\text{Mo}) = 0.206$, $w(\text{Si}) = 0.28$.

The chemical composition of steel B in mass fractions (%) was: $w(\text{C}) = 0.174$, $w(\text{Cr}) = 0.07$, $w(\text{Ni}) = 0.02$, $w(\text{Mn}) = 1.46$, $w(\text{Mo}) = 0.005$, $w(\text{Si}) = 0.23$.

The thermophysical properties of the steels were calculated using the IDS solidification analysis package of a prestigious laboratory (the Laboratory of Metallurgy, Helsinki University of Technology). The IDS package calculates enthalpy, specific heat, density, thermal conductivity, thermal contraction, etc., from the liquid state down to the room temperature using graphic or numeric outputs of the results. The dependences of the main

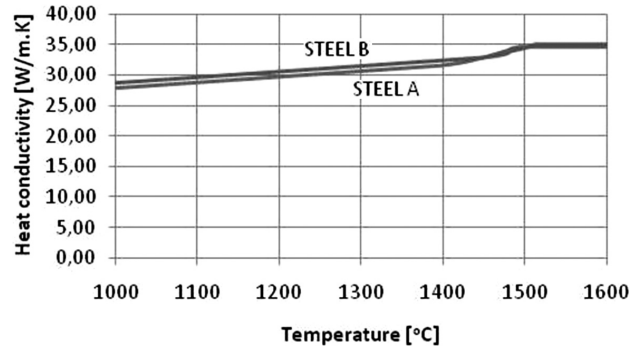


Figure 2: Heat conductivity of steels A and B and its dependence on temperature

Slika 2: Toplotna prevodnost jekel A in B v odvisnosti od temperature

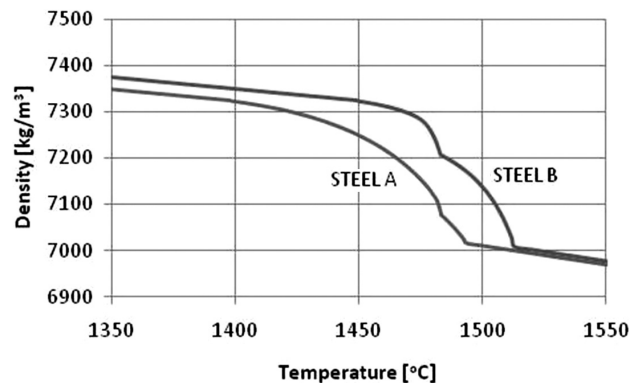


Figure 3: Density of steels A and B and its dependence on temperature

Slika 3: Gostota jekel A in B v odvisnosti od temperature

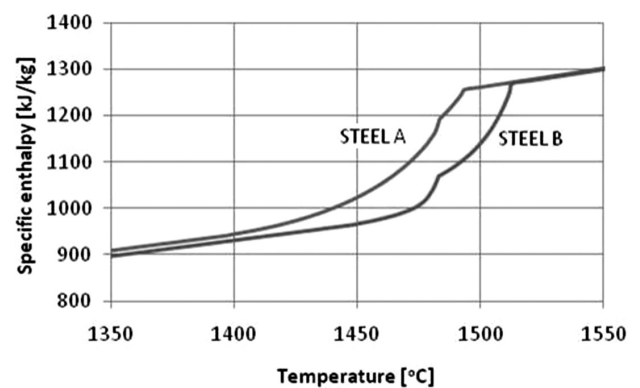


Figure 4: Enthalpy of steels A and B and its dependence on temperature

Slika 4: Entalpija jekel A in B v odvisnosti od temperature

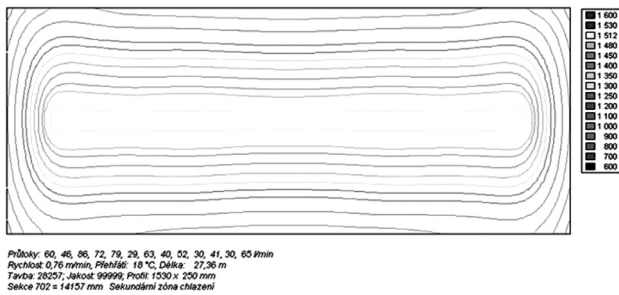


Figure 5: Isotherms in the cross-section of the breakout for the steel slab of B quality

Slika 5: Izoterme v prečnem prerezu prodora jeklenega slaba B

thermophysical properties on the temperature – the heat conductivity, the density and the enthalpy of both steels are shown in Figures 2 to 4. The definitions of the boundary conditions for all three variants of the calculation were identical for all the cooling zones.

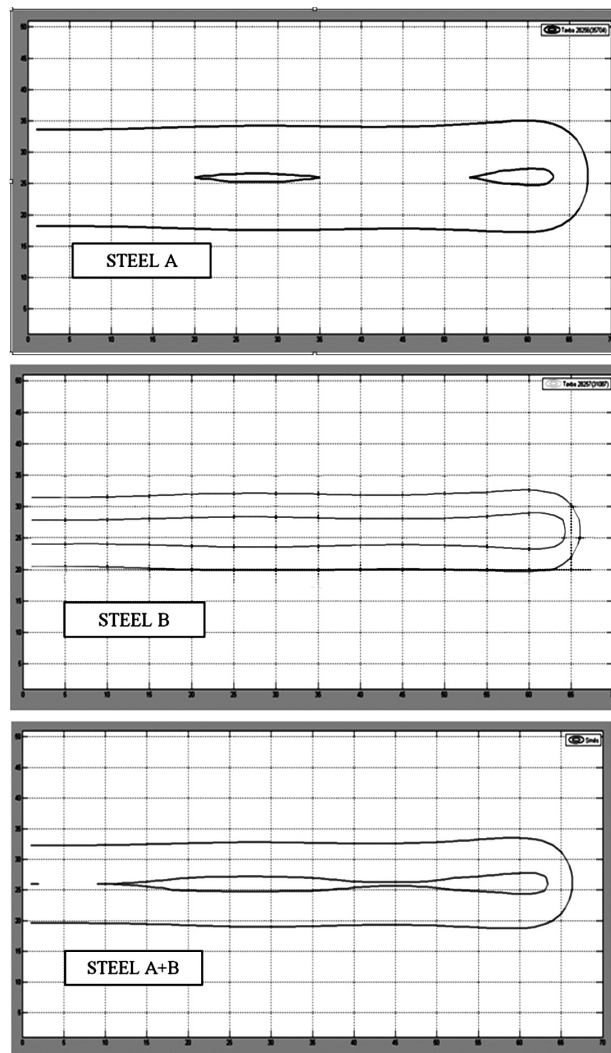


Figure 6: Isoliquidi and isosolidi in the cross-section of the breakout for the steel slabs of A, B and A + B qualities

Slika 6: Izolikvidusne in izosolidusne črte v prečnem prerezu prodora za jekli A in B ter za A + B

3 NUMERICAL RESULTS

The off-line version of the original temperature model was now used to simulate the temperature fields of the steel slab of A quality, the steel slab of B quality and the steel slab of A + B quality (with the average chemical compositions). After the computation, it is possible to obtain the temperatures for each node of the network and for any time during the process. The course of the calculated isotherms in the cross-section of the breakout, for example, for a slab of B quality at a distance of 14.15 m from the level of the melt in the mold is in Figure 5.

The courses of the calculated isoliquidi and isosolidi as the characteristic isotherms in one half of the cross-section of the breakout for the steel slabs of A, B and A + B qualities are in Figure 6. The isoliquidi and isosolidi in both longitudinal axial sections of the steel slabs of A, B and A + B qualities are plotted in Figures 7 and 8.

4 CONCLUSIONS

In the secondary-cooling zone, where the slab is beginning to straighten out, the breakout of the steel can occur in the points of increased local chemical and temperature heterogeneities of the steel, from the increased

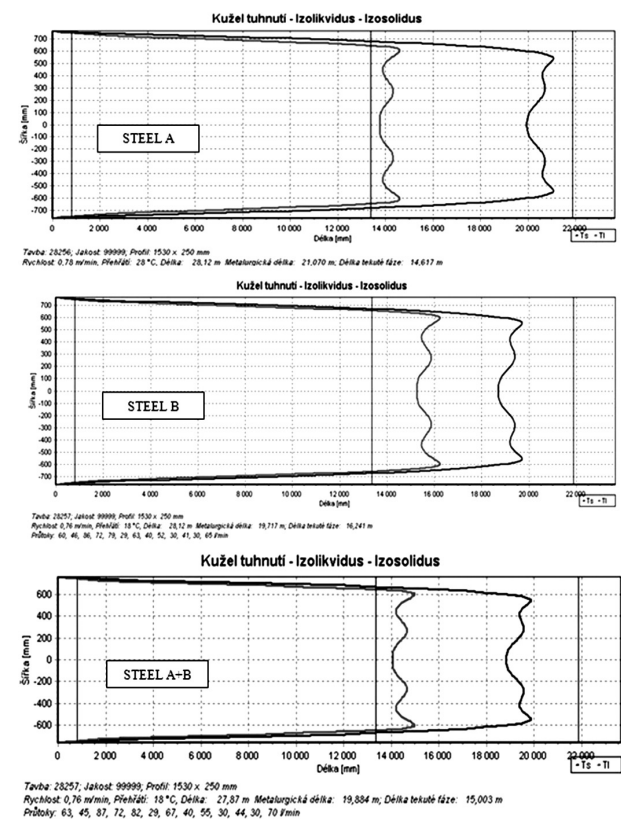


Figure 7: Isoliquidi and isosolidi in the horizontal section for the steel slabs of A, B and A + B qualities

Slika 7: Izolikvidusne in izosolidusne črte v horizontalnem prerezu za jekli A in B ter za A + B

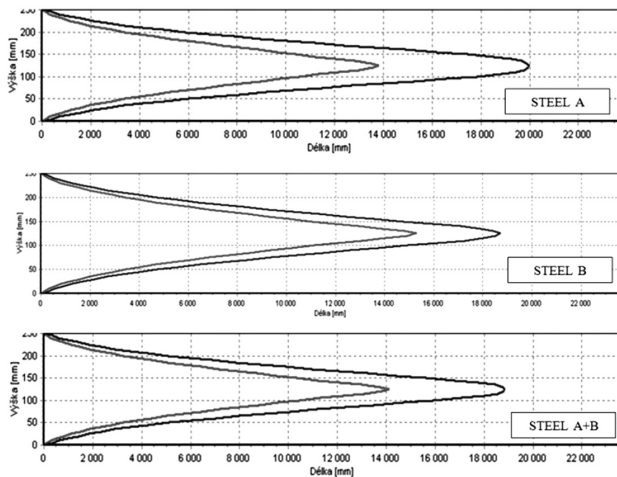


Figure 8: Isoliquidi and isosolidi in the vertical-axis section for the steel slabs of A, B and A + B qualities

Slika 8: Izolikvidusne in izosolidusne črte v vertikalnem osnem prerezu za jekli A in B ter za A + B

tension as a result of the bending of the slab and also a high local concentration of non-metal, slag inclusions. The changes in the chemical composition of the steel during the fill-up of the tundish with continuous casting are especially dangerous. The consequence of this operation, an immediate change in the chemical composition of the steel, which is not prevented by a breakout system directly inside the mould, can lead to an immediate interruption of the concasting and a breakout at a greater distance from the mould than usual, thus leading to a significant material loss and downtime.

During the continuous casting of the slab of 250 mm × 1530 mm and after a quick change of the tundish, a change in the chemical composition of steel A and B occurred. Inside the mould, steel B thus mixed with steel A of the previous melt. After 20 min of casting steel B with a different chemical composition, the caster stopped as a result of a breakout at a distance of 14.15 m from the level of the melt in the mold. Therefore, this critical state of continuous casting was analyzed via the temperature model that may be followed by an analysis of the chemical heterogeneity in the plain of the breakout. The results of the formation of the temperature fields of the steel slabs of quality A, B, and A + B (with the average chemical compositions) were obtained. The objective of the paper is to analyse the temperature fields in the plain of the breakout, which may be followed by

an analysis of chemical heterogeneities in this plain. In the case of a breakout we do not have more detailed information about the internal relationship between the dimensional quantities and the essence of the breakout, and we do not even have a partial mathematical and physical description of this phenomenon. That is why it is necessary to use the theory of similarity for a dimensional analysis determining the dimensionless criteria.⁶ Based on the π -theorem, 5 similarity criteria were derived containing 12 technological, geometrical and thermo-physical dimensional quantities that characterise both steel grades A and B and also the process of their continuous casting. This analysis also provides the calculations of the temperature fields of the slabs to be cast, in order to determine the quantities needed for the fulfilment of some of these criteria. The analysis performed by using the similarity criteria clearly demonstrates a significantly increased tendency for steel B to breakout, in comparison with steel A.

Acknowledgment

This analysis was conducted using a program devised within the framework of the GA CR project No. P107/11/1566.

5 REFERENCES

- ¹ F. Kavicka, K. Stransky, B. Sekanina, J. Stetina, T. Mauder, The calculation of the temperature field of a concast steel slab tightly before the breakout, Metal 2011 Conference Proceedings Papers Symp. A, Metal. Ostrava, Tanger, (2011), 93–98
- ² F. Kavicka, K. Stransky, J. Dobrovska, B. Sekanina, A breakout of a slab after quick changing the tundish and steel quality, Metal 2011 Conference Proceedings Papers Symp. A, Metal. Ostrava, Tanger, (2011), 99–104
- ³ C. Ojeda et al., Mathematical Modeling of Thermal-Fluid Flow in the Meniscus Region During an Oscillation Cycle, AISTech 2006 Proceedings, 1 (2006), 1017–1028
- ⁴ S. Louhenkilpi, E. Laitinen, R. Nieminen, Real-Time Simulation of Heat Transfer in Continuous Casting, Metallurgical Transactions B, 24B (1993) 4, 685–693
- ⁵ J. Stetina, A dynamic model of temperature field of concast steel slab, PhD Thesis, VSB-TU Ostrava, Faculty of Metallurgy and Materials Engineering, Ostrava, 2007
- ⁶ K. Stransky, J. Dobrovska, F. Kavicka, J. Stetina, B. Sekanina, M. Masarik, Heterogeneity of continuously cast steel slab shortly before breakout, Metal 2012, Proceedings of Abstracts and CD ROM of the 20th International Metallurgical & Materials Conference Brno, Czech Republic, (2012)

INVESTIGATION OF THE THERMOMECHANICAL PROPERTIES AND MICROSTRUCTURE OF SPECIAL MAGNESIUM ALLOYS

PREISKAVA TERMOMEHANSKIH LASTNOSTI IN MIKROSTRUKTURE POSEBNIH MAGNEZIJEVIH ZLITIN

Petr Lichý, Michal Cagala, Jaroslav Beňo

VŠB-Technical University of Ostrava, Faculty of Metallurgy and Materials Engineering, Department of Metallurgy and Foundry Engineering, 17. listopadu 15/2172, 708 33 Ostrava, Czech Republic
petr.lichy@vsb.cz

prejem rokopisa – received: 2012-08-31; sprejem za objavo – accepted for publication: 2013-01-03

Thanks to their high specific strength together with a low density, magnesium-based alloys have an extensive potential for the use of their castings in automotive industry. The castings based on these materials show relatively good mechanical properties that decrease significantly with an increasing temperature of their thermal exposure. The aim of this work is to study the properties of two alloys commonly used (Mg-Al-Zn, Mn type). From the studied materials the test castings were made and these were formed into the test bars used for a tensile test. This test was carried out within the temperature range of 20–300 °C. Further on, the tests of the thermomechanical properties were complemented with a microstructure analysis with the aim of checking metallurgical interventions (the effect of inoculation).

Keywords: castings, magnesium alloys, thermomechanical properties, microstructure

Zaradi velike specifične trdnosti in majhne gostote imajo magnezijeve zlitine velik potencial za uporabo v obliki ulitkov v avtomobilski industriji. Ulitki iz teh materialov kažejo relativno dobre mehanske lastnosti, ki pa se močno zmanjšajo, če so izpostavljeni povišanim temperaturam. Namen tega dela je študij teh lastnosti pri dveh pogosto uporabljenih vrstah zlitine (Mg-Al-Zn, Mn). Iz preiskovanih materialov so bili izdelani preizkusni ulitki, iz katerih so bile pripravljene palice za natezne preizkuse. Ti so se izvajali v temperaturnem območju 20–300 °C. Ugotovitve termomehanskih lastnosti so bile dopolnjene z analizo mikrostrukture, namenjene za preverjanje metalurških ukrepov (učinek inokulacije).

Ključne besede: ulitki, magnezijeve zlitine, termomehanske lastnosti, mikrostruktura

1 INTRODUCTION

Magnesium alloys have always been very prospective materials, in particular for automobile and aircraft industries where the most important requirement is for a low weight or sufficiently high specific strength, i.e., the strength-characteristics-to-low-specific-weight ratio. In spite of the above mentioned reasons, a more extensive use of these alloys in the above industrial branches is limited by their low resistance to corrosion and a decrease in their mechanical properties under higher temperatures. Standard alloys are not stable under high temperatures and therefore not suitable for the applications, in which they would be stressed by such temperatures. In addition, a more advanced casting technology must be taken into account as magnesium and its alloys are highly reactive metals. But these difficulties can already be partly eliminated by choosing a suitable preparation in a liquid metal, moulding mixture or a protective atmosphere in a melting device.

The use of magnesium alloys in a car structure can considerably help in reducing the car weight without deteriorating its safety.¹

2 DIVISION OF MAGNESIUM ALLOYS ACCORDING THEIR USES

The basis for the foundry magnesium alloys are binary alloys enhanced with additional alloying elements in order to improve technological properties, mechanical properties or to increase the corrosion resistance. There are the basic systems – Mg-Al, Mg-Zn and Mg-Mn. The most widespread magnesium alloys for manufacturing castings are the Mg-Al-(Zn, Mn)-type alloys. The advantages of these materials are as follows:

- They are well castable and have a low thaw point, which improves some other foundry characteristics;
- A proper alloying-element selection can eliminate the occurrence of casting defects – microshrinks and thermal cracks.

The AZ91 alloy is perhaps the most frequently used from this group.² A rather fast decrease in the strength when stressing them with a growing temperature is a disadvantage of these alloys. The alloys of the Mg-Al-Sr and Mg-Al-RE types could compensate for the low resistance to high temperatures with better microstructural stabilities and also fairly good strength properties³ under these conditions. These parameters are decisive when using these materials for the parts that are exposed to a considerable thermal stress, e.g., engine blocks. In

Table 1: Chemical compositions of the used magnesium alloys in mass fractions, w/%**Tabela 1:** Kemijska sestava uporabljenih magnezijevih zlitin v masnih deležih, w/%

Alloy	Element									
	Zn	Al	Si	Cu	Mn	Fe	Ni	Ca	Be	residue
AZ91D	0.56	8.80	0.06	0.004	0.20	0.004	0.001	0.000	0.000 7	<0.01
AZ91Be	0.62	8.22	0.03	0.001	0.15	0.006	0.000	0.000	0.009 0	<0.01
AMZ40	0.14	3.76	0.02	0.001	0.34	0.003	0.000	0.000	0.001 1	<0.01
AM60	0.07	5.78	0.03	0.001	0.33	0.003	0.001	0.000	0.000 9	<0.01

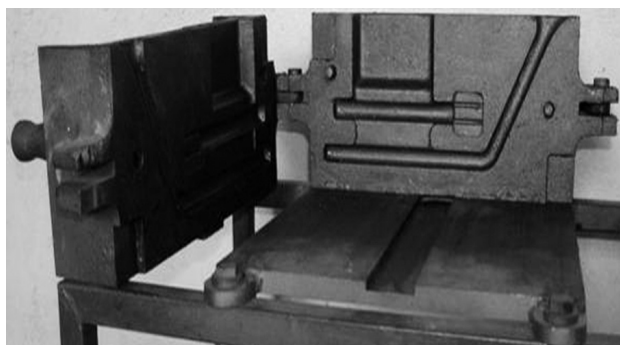
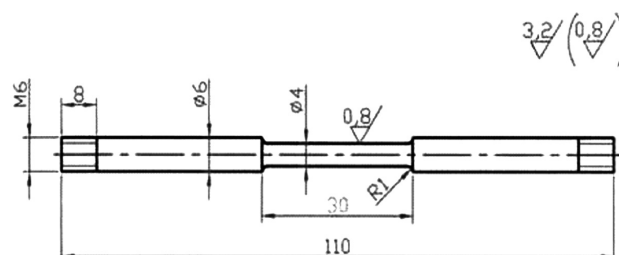
addition, another important requirement is the corrosion resistance (internal and external) because the majority of drive units are cooled with a liquid and the used materials have to be able to resist the corrosive effects of the cooling medium for a long time. The alloys retaining a sufficient strength under the temperatures of up to 250 °C are of the Mg-Y-RE, Mg-Sc and Mg-Gd types without an aluminium addition. These materials meet all the above mentioned requirements for industrial use, but a problematic issue is their economical availability. The requirement for a high resistance to creep is met by the magnesium alloys with thorium (up to the temperatures of 370 °C). Then, the Mg-Li type alloys belong to the lightest structural materials; however, it is difficult to manufacture and treat them.

3 DESCRIPTION OF THE USED ALLOYS

The main alloying element of magnesium alloys is aluminium. For the experimental evaluation both commonly used alloys (AZ91, AZ91Be, AM60) and the AMZ40 alloy were chosen as they had not yet been industrially processed in the Czech Republic. All the compared materials were supplied by a Czech manufacturer and **Table 1** shows their chemical compositions taken from the supplier's certificates.

4 PREPARATION OF THE TEST SAMPLES

Castings were gravity cast in an iron mould (**Figure 1**) that was preheated before the casting to achieve a sufficient running property of the metal. The

**Figure 1:** Metal mould for casting the test bars according to the ČSN 42 0334 standard**Slika 1:** Kovinska kokila za ulivanje preizkusnih palic, skladna s standardom ČSN 42 0334**Figure 2:** Scheme of a test bar destined for the general tensile test (dimensions are in millimeters)**Slika 2:** Shematski prikaz preizkusne palice za natezni preskus (dimenzije so v milimetrih)

samples for the tensile test (**Figure 2**), the metallographic analysis and the measurements of the other mechanical properties were subsequently made from these castings. The material was melted in a steel crucible in an electric resistance furnace. To ensure the metal's protection during the melting, a covering preparation with a commercial product named EMGESAL was used to prevent excessive oxidation or burning on the melt surface.

During the measurement the temperatures of the metal mould and the cast alloy were observed for process checking and description.

To ensure the improved mechanical properties of the large-sized castings poured in the sand moulds, the melt was treated in foundries with a preparation based on hexachloroethane supplied under the commercial name of MIKROSAL MG T 200. After introducing the nuclei, the casting structure became finer and a fine-grained structure of the material with improved mechanical properties was formed. In our case this preparation was also used for the melt.

5 MICROSTRUCTURES OF THE CAST SAMPLES

The microstructures of the used alloys were evaluated in different parts of the casting from which the test bars were prepared. The differences between the structures of the observed materials could only be found in the central parts of the castings where the heat removal during the solidification and cooling was not so intensive. **Figures 3** and **4** show the microstructures of the AZ91 alloy cast in a preheated metal mould. In the AZ91 alloy without an inoculant addition (**Figure 3**) high shares of the Mg₁₇Al₁₂

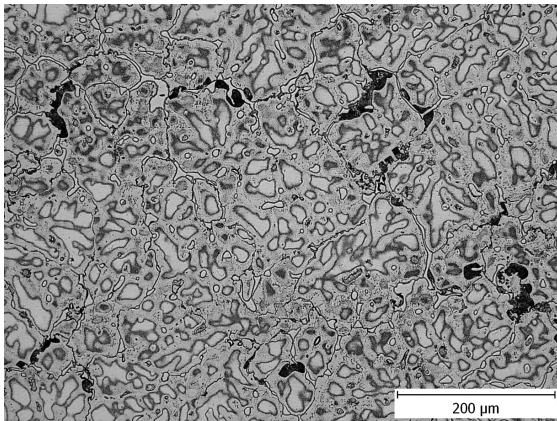


Figure 3: Non-inoculated material AZ91
Slika 3: Material AZ91 brez inokulacije

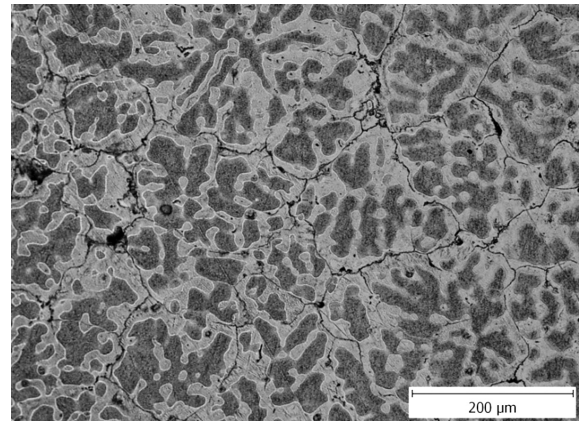


Figure 6: Inoculated material AM60
Slika 6: Inokuliran material AM60

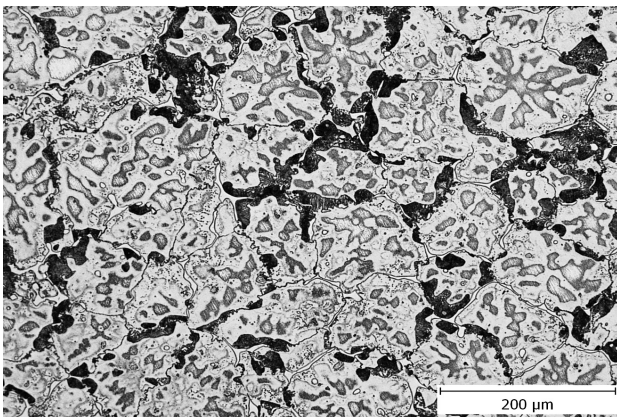


Figure 4: Inoculated material AZ91
Slika 4: Inokuliran material AZ91

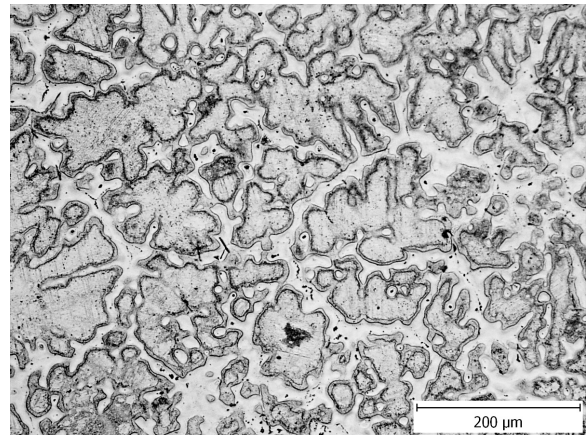


Figure 7: Non-inoculated material AMZ40
Slika 7: Material AMZ40 brez inokulacije

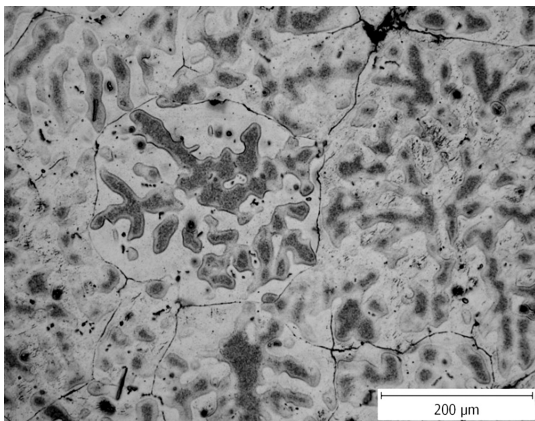


Figure 5: Non-inoculated material AM60
Slika 5: Material AM60 brez inokulacije

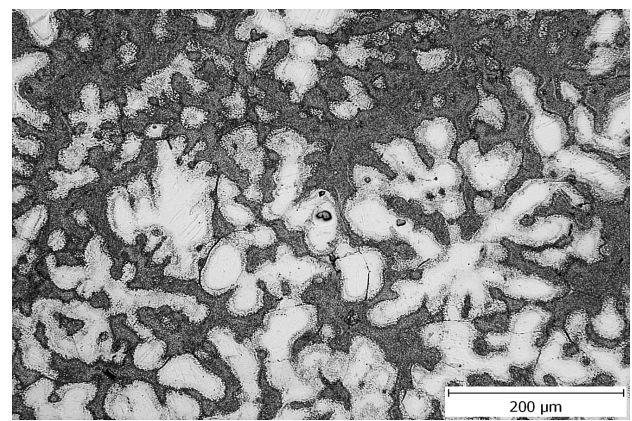


Figure 8: Inoculated material AMZ40
Slika 8: Inokuliran material AMZ40

tabular precipitate and $\alpha+\beta$ eutectic can be observed. In the alloy with an inoculant addition (**Figure 4**) the precipitate share was considerably higher. The situation was similar in the case of AZ91Be, an alloy with a beryllium addition.

The figures of the AM60 alloy microstructure evidently show lower proportions of the $Mg_{17}Al_{12}$ precipi-

tate and the eutectic phase in the non-inoculated material structure (**Figure 5**) as well as in the inoculated one compared to the AZ91 alloys, due to a lower aluminium content in the alloy. There are apparent material grain boundaries in the microstructure figures and the inoculant-addition effect is clearly evident here (**Figure 6**). In the case of the AMZ40 alloy the difference between the

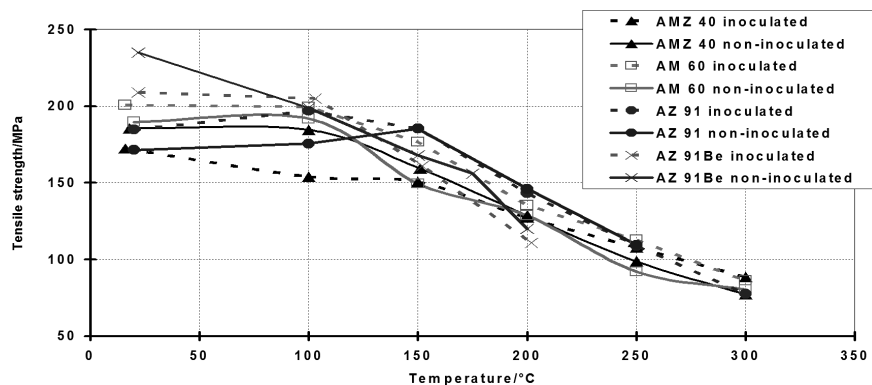


Figure 9: Thermal dependence of the tensile strength

Slika 9: Temperaturna odvisnost natezne trdnosti

non-inoculated material (Figure 7) and the inoculated one (Figure 8) is the least significant of all the studied alloys. This material structure with the minimum proportion of the $Mg_{17}Al_{12}$ precipitate is very close to the AM60 alloy due to their similar chemical compositions.

6 MEASUREMENT OF THE MECHANICAL PROPERTIES AT ELEVATED TEMPERATURES

The tensile test was carried out on a TSM 20 tension-testing machine. The elevated-temperature test was performed as a general one. When measuring mechanical properties, we carried out the above mentioned general test at room temperature and at elevated temperatures, beginning at 100 °C, at a gradient of 50 °C, up to 300 °C. The final temperature for the observed alloys varied and it was selected according to the possibilities, with respect to a limited amount of specimens. When testing at elevated temperatures, the holding time at the temperature for each specimen was 5 min for the temperature equalization on the surface and inside the specimen.

7 ACHIEVED RESULTS

The influence of the test temperature on the resulting values of the tensile strength of the materials was evaluated with the tensile test. The graph in Figure 9 shows the results for the metallurgically untreated alloys and for the alloys influenced by the inoculating agent. The objectives of the tensile test were to compare the particular alloy types, observe the inoculation effect and the influence of the elevated temperature on mechanical properties (the tensile strength). The highest tensile strength values under room temperature were achieved for the AZ91Be alloy (above 200 MPa). As a matter of fact, the AZ91, AM60 and AMZ40 alloys showed the same tensile strengths. A considerable decrease in the tensile strengths of the AZ91, AZ91Be and AMZ40 alloys was observed with the growing test temperature.

Below the temperature of 300 °C the lowest strengths of about 80 MPa were observed. The inoculation effect was more significant only for the AZ91 and AM60 alloys, where it was also reflected in the microstructures of these alloys. During the tests under room temperature a growth by 8 % or 10 %, respectively, was observed. With the growing test temperature (above 150 °C) the tensile strengths considerably decreased. The steepest drop was observed for the AZ91Be alloy where the tensile strength below the temperature of 200 °C was only about 120 MPa. In the case of the AMZ40 alloy there was no inoculation effect, which was also confirmed with the analysis of the given-alloy microstructure.

8 CONCLUSION

The presented work aimed at studying the thermo-mechanical properties of magnesium alloys. The highest tensile strength was achieved for the AZ91Be alloy at room temperature. The inoculation effect was more significant only at low temperatures and for the AZ91 and AM60 alloys, where a grain refinement was evident in the microstructures of the observed samples. In the other materials no structure refinement was observed, perhaps due to the extensive heat removal from the castings.

Acknowledgement

This work was performed within the frame of the research project TA02011333 (Technology Agency of the CR).

9 REFERENCES

- M. J. F. Gándara, Mater. Tehnol., 45 (2011) 6, 633–637
- B. L. Mordike, T. Ebert, Materials Science A, 302 (2001), 37–45
- S. Roskosz, J. Adamiec, M. Blotnicki, Archives of Foundry Engineering, 7 (2007) 1, 143–146

IMPACT OF CASTING SPEED ON THE TEMPERATURE FIELD OF CONTINUOUSLY CAST STEEL BILLETS

VPLIV LIVNE HITROSTI NA TEMPERATURNO POLJE KONTINUIRNO ULITIH GREDEC IZ JEKLA

Lubomir Klimes¹, Josef Stetina¹, Pavol Bucek²

¹Brno University of Technology, Faculty of Mechanical Engineering, Technická 2896/2, 616 69 Brno, Czech Republic

²Zelezniarne Podbrezova, Research and Development Center, Kolkaren 35, 976 81 Podbrezova, Slovakia
klimes@fme.vutbr.cz

Prejem rokopisa – received: 2012-08-31; sprejem za objavo – accepted for publication: 2013-01-04

In continuous casting, the casting speed is one of the most important parameters that influence the entire process of steel production and its productivity. From the physical point of view, the casting speed affects the temperature field formation along the cast steel blank, e.g., the surface and corner temperatures as well as the solidification of the steel, e.g., the shell thickness, the isosolidus and isoliquidus curves, the metallurgical length and the width of the mushy zone. In order to achieve a particular steel structure, the temperature ranges in particular positions (e.g., due to the straightening), and to minimize the occurrence of defects, it is very important to pay attention to a proper determination of the casting speed. The aim of this paper is to investigate the impact of the casting speed on the temperature field formation of continuously cast steel billets, and on the aforementioned parameters. Three steel grades with various chemical compositions and the originally implemented numerical model of the transient temperature field of continuously cast billets in Zelezniarne Podbrezova in Slovakia were utilized for the analysis. The results proved the significant influence of the casting speed on the temperature field formation and on related parameters. The conclusions may be utilized, e.g., for the determination of the casting speed and for the setup of the caster.

Keywords: continuous casting, casting speed, dynamic solidification model, temperature field

Pri kontinuirnem ulivanju je hitrost ulivanja eden od odločilnih parametrov, ki vplivajo na celoten proces proizvodnje jekla in na storilnost. Iz fizikalnega vidika hitrost ulivanja vpliva na nastanek temperaturnega polja vzdolž jeklene gredice, kot na primer na temperaturo robov in površine ulitega bloka, kot tudi na strjevanje jekla, kot na primer debelina strjene skorje, krivulje izosolidusa in izoliquidusa, metalurška dolžina in širina kašastega področja. Da bi dosegli želeno strukturo jekla, temperaturno področje v določenih položajih (npr. zaradi ravnanja) in da bi zmanjšali nastanek poškodb, je zelo pomembno, da smo pozorni na pravilno določitev hitrosti ulivanja. Namen prispevka je raziskati vpliv hitrosti ulivanja na oblikovanje temperaturnega polja pri kontinuirno ulitih gredicah in na že navedene parametre. Za analize so bila uporabljena tri različna jekla z različnimi kemijskimi sestavami in originalen numerični model prehodnega temperaturnega polja gredic v Zelezarni Podbrezova na Slovaškem. Rezultati potrjujejo pomemben vpliv hitrosti ulivanja na nastanek temperaturnega polja in s tem povezanih parametrov. Ugotovitve se lahko uporabijo na primer za določitev hitrosti ulivanja in za postavitev livne naprave.

Ključne besede: kontinuirno ulivanje, hitrost ulivanja, dinamični model strjevanja, temperaturno polje

1 INTRODUCTION

The quality and productivity of continuously cast steel blanks depend on many technological parameters and caster options.¹ The casting speed, which is directly related to the productivity, is one of the most important parameters for continuous steel casting. Its appropriate setting according to the operating conditions, the steel grade being cast and the caster parameters is crucial in order to produce steel blanks with the desired quality and structure, and also to minimize the occurrence of defects. In addition, the produced steel and its properties can be further optimized.² The importance of the proper setting of the casting speed is obvious when taking into account the parameters on which the casting speed may have an influence: mainly the entire temperature distribution (e.g., the surface and corner temperatures that are very often required to fit a certain range of temperatures, e.g., due to the straightening) along the cast blank, the isosolidus and isoliquidus curves that characterize the solidification process, the metallurgical length, or, e.g., the shell thickness along the blank.³

Nowadays, dynamic solidification models are commonly used in steelworks for the control and monitoring of casting.^{4,5} The on-line models for the casting control are fast and rather simple, whereas the off-line models enable an analysis of multiple and detailed factors, but require a long time to run.⁶ Numerical models of the temperature field of continuous casting often utilize the finite-difference method,⁷ the finite-volume method⁸, or the finite-element method.⁹ Recently, new computational approaches are also used, due to their specific advantages, e.g., the meshless finite-point method,¹⁰ the front-tracking boundary-element method,¹¹ or the very fast moving-slice-based models.¹²

The numerical solidification models allow a precise determination of the entire temperature distribution along the cast blank, the prediction of surface defects and the improvement of steel quality.¹³ The numerical model in the off-line mode working as a simulator also makes it possible to perform a case study and an analysis of the operating parameters without any affect on the real caster and the steel production in a steelworks.⁶ Hence, it

is a good idea to utilize the dynamic solidification models in order to determine a suitable casting speed for continuously cast blanks.

The purpose of this paper is to investigate the influence of the casting speed on the temperature field formation and the related parameters of continuously cast billets. For the analysis, three steel grades and the 200 mm × 200 mm billets, which are cast in Zeleziarne Podbrezova in Slovakia, are considered. The analysis was carried out by means of the originally implemented dynamic solidification model of continuously cast billets.

2 DYNAMIC SOLIDIFICATION MODEL

The study of the influence of the casting speed on the thermal behavior of continuously cast steel billets was performed with the use of the originally developed numerical model of the transient temperature field.^{14,15} The model, which is fully 3D, allows a calculation of the transient temperature distribution along the entire, continuously cast billets from the pouring level inside the mould, through the secondary and tertiary cooling zones, to the torch where the semi-infinite billets are cut to desired lengths suitable for the next processing step (**Figure 1**). Since the temperature field is symmetric with respect to the longitudinal vertical plane (**Figure 1**), only one half of the billet is considered.

The transient heat transfer and the solidification of the billet is governed by the Fourier-Kirchhoff equation:

$$\frac{\partial H}{\partial t} = \nabla \cdot (k \nabla T) + v_z \frac{\partial H}{\partial z} \quad (1)$$

where H is the volume enthalpy (J m^{-3}), T is the temperature (K), t is time (s), k is the thermal conductivity ($\text{W m}^{-1} \text{K}^{-1}$), v_z is the casting speed (m s^{-1}) and z is the spatial coordinate along the cast billet (m). The mass transfer and the fluid flow of the melt inside the billet are neglected. The thermodynamic function of the volume enthalpy¹⁶ in Eq. (1), which is defined as follows:

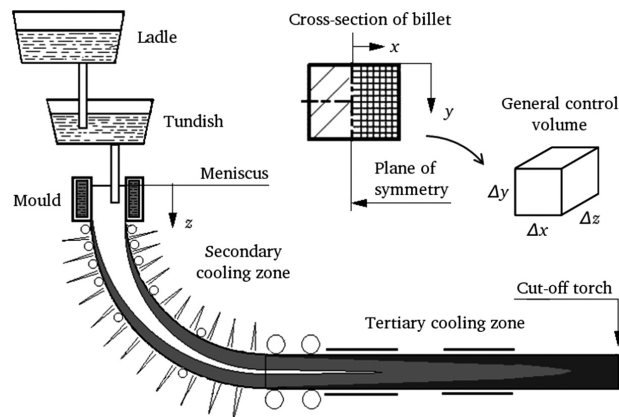


Figure 1: The billet caster and the mesh definition
Slika 1: Naprava za ulivanje gredic in opredelitev mreže

$$H(T) = \int_0^T \left(\rho c - \rho L_f \frac{\partial f_s}{\partial \theta} \right) d\theta \quad (2)$$

where ρ is the density (kg m^{-3}), c is the specific heat ($\text{J kg}^{-1} \text{K}^{-1}$), L_f is the latent heat (J kg^{-1}) and f_s is the solid fraction (1), is used due to the release of the latent heat of structural and mainly phase changes, which the steel undergoes during its solidification.¹⁷

The model is completed with the initial (3) and boundary conditions (4a)–(4d):

$$T_{i,j,k}^0 = T_0 \quad (3)$$

$$T_{i,j,0}^t = T_{\text{cast}} \text{ in the meniscus plane} \quad (4a)$$

$$-k \frac{\partial T}{\partial n} = 0 \text{ in the plane of symmetry} \quad (4b)$$

$$-k \frac{\partial T}{\partial n} = \dot{q} \text{ in the mould and beneath the rollers} \quad (4c)$$

$$-k \frac{\partial T}{\partial n} = h(T - T_\infty) + \sigma \varepsilon (T^4 - T_\infty^4) \text{ in the secondary and tertiary cooling zones} \quad (4d)$$

where T_0 is the initial temperature (K), T_{cast} is the casting temperature (K), \dot{q} is the heat flux (W m^{-2}), h is the heat transfer coefficient ($\text{W m}^{-2} \text{K}^{-1}$), T_∞ is the ambient temperature (K), $\sigma = 5.67 \cdot 10^{-8} \text{ W m}^{-2} \text{K}^{-4}$ is the Stefan-Boltzmann constant and ε is the emissivity (1).

In order to accurately and reliably predict the temperature field of cast blanks by means of solidification models, it is also worth pointing out the variability of the thermophysical properties (H , k , ρ , c : see Eq. (1) and Eq. (2)) according to the chemical composition of the steel being cast and their dependency on the temperature. Due to the mentioned reasons, the developed solidification model utilizes the results of the solidification analysis package IDS.¹⁸ It enables the calculation of the temperature dependency of the aforementioned thermophysical properties according to the chemical composition of the steel. The precise chemical composition can be obtained, e.g., from the chemical analysis of a sample from the tundish.

The dynamic solidification model of continuously cast billets was created with the use of the control-volume method.¹⁹ This approach is based on meshing the entire 3D billet into control volumes, and then the energy balance is established for each control volume of the billet. With the use of the explicit discretization in time,¹⁹ the energy balance of the general control volume (i, j, k) (**Figures 1** and **2**) in the Cartesian coordinates reads:

$$\sum_{i=1}^6 \dot{Q}_i + v_z \Delta x \Delta y (H_{i,j,k-1}^t - H_{i,j,k}^t) = \frac{\Delta x \Delta y \Delta z}{\Delta t} (H_{i,j,k}^{t+\Delta t} - H_{i,j,k}^t) \quad (5)$$

where \dot{Q} denotes the heat transfer rate (W), Δx , Δy , Δz are the spatial dimensions (m) of the control volume and

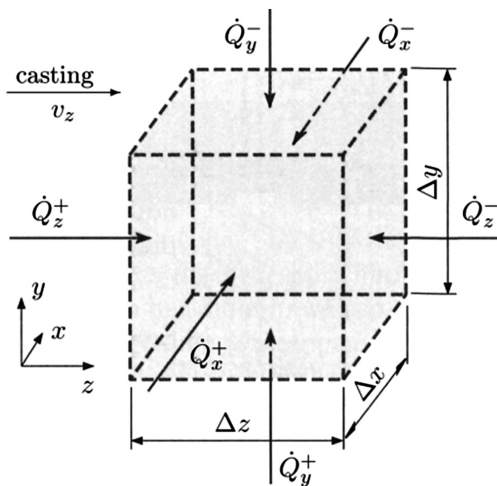


Figure 2: The energy balance of the general control volume in Cartesian coordinates

Slika 2: Energijska bilanca splošnega kontrolnega volumna v kartezičnih koordinatah

Δt is the time step (s). The first term on the left-hand side in Eq. (5) represents the sum of the conduction heat transfer rates given by Fourier's law¹⁹ to the control volume from the neighboring six control volumes (**Figure 2**). For instance, the heat transfer rate to the control volume in the positive direction of the x -axis is then:

$$\dot{Q}_x^+ = -k\Delta y\Delta z \frac{T_{i,j,k}^t - T_{i-1,j,k}^t}{\Delta x} \quad (6)$$

The second term on the left-hand side in Eq. (5) takes into account the energy incoming to the control volume due to the movement of the billet through the caster with the casting speed v_z . The term on the right-hand side in Eq. (5) represents the change of the internal energy of the control volume during the time step Δt , including the release of the latent heat (comprised in the enthalpy) due to the solidification.^{16,17}

In the case of the explicit time discretization,¹⁹ the unknown enthalpy of the general control volume (i, j, k) in time $t + \Delta t$ can be then directly calculated from Eq. (5) with the use of known values of the temperature and enthalpy in time t :

$$H_{i,j,k}^{t+\Delta t} = H_{i,j,k}^t + \frac{\Delta t}{\Delta x\Delta y\Delta z} \sum_{i=1}^6 \dot{Q}_i + v_z \frac{\Delta t}{\Delta z} (H_{i,j,k-1}^t - H_{i,j,k}^t) \quad (7)$$

In the case of the boundary-control volume, the particular heat transfer rates in Eq. (7) are replaced by the corresponding heat transfer rates determined from the boundary conditions (4a)–(4d). The desired temperature in time $t + \Delta t$ is then recalculated from the enthalpy given by Eq. (7) with the use of the temperature-enthalpy relationship provided by the solidification package IDS according to the particular chemical composition of the cast steel.

In the curved region (the radial part) of the caster, the Cartesian coordinate system is transformed to the cylindrical system (the Cartesian coordinates y and z are transformed to the radius coordinate and to the angle coordinate, respectively) and the equations (5)–(7) are appropriately modified.

The model used in the presented analysis utilizes 1136520 control volumes (21 in axis x , 41 in axis y , and 1320 in axis z) with the size of the general control volume of 5 mm × 5 mm × 15 mm. Due to the unconditional stability¹⁹ of the explicit time discretization and the numerical stability also for higher casting speeds, the time step was set to 0.35 s. With the described configuration of the mesh and the time step, the numerical model is still able to run faster than real time. For example, on the HP Z800 workstation the computing time reaches 90 % of the real time.²⁰

The heat transfer coefficients in the boundary condition (4d) for the cooling nozzles in the secondary cooling were determined experimentally in the laboratory on the hot models.²¹ **Figure 3** presents the experimentally measured heat-transfer coefficient for the cooling nozzle TG1 used in the secondary cooling. In order to quantify the heat withdrawal in the mould and the secondary cooling zone,²⁰ the heat flux in the mould given by Eq. (4c) was equivalently expressed to the heat transfer coefficient and plotted in **Figure 4**.

As can be seen from Eq. (1), Eq. (5), and Eq. (7), the casting speed v_z straightforwardly influences the entire transient temperature distribution of cast billets, and therefore the appropriate setting of the casting speed is a crucial issue in continuous casting.

The developed dynamic solidification model was experimentally verified on the billet caster with the use

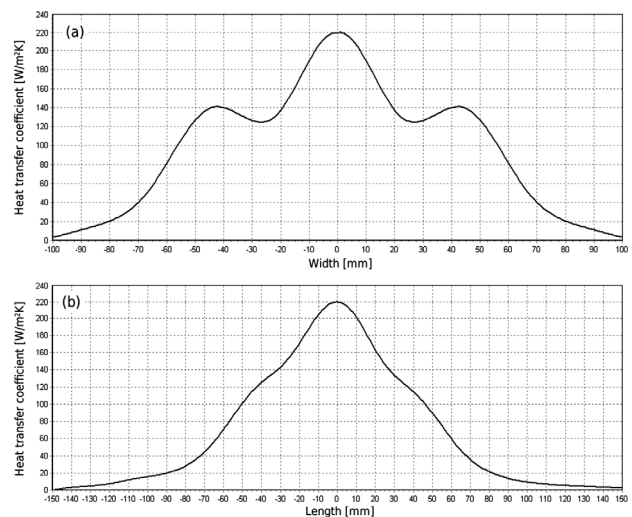


Figure 3: The heat transfer coefficient for the cooling nozzle TG1 and the water flow 0.64 l/min in the centerline of the nozzle: a) perpendicular to the casting direction, b) along the casting direction

Slika 3: Koeficient prenosa toplote za hladilno šobo TG1 in pretok vode 0,64 l/min v simetrali šob: a) pravokotno na smer ulivanja, b) vzdolž smeri ulivanja

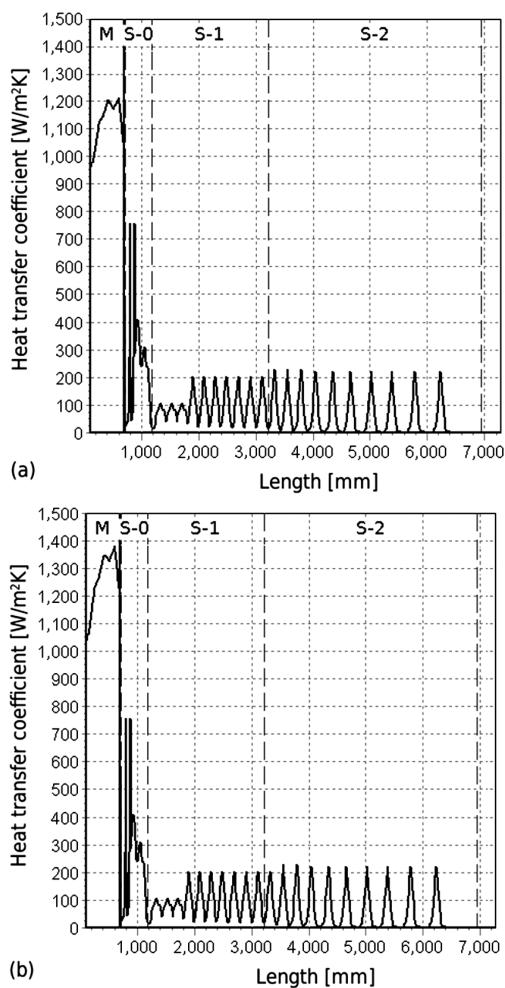


Figure 4: The heat transfer coefficient in the mould and in the secondary cooling zone: a) small radius surface, b) large radius surface of cast billet

Slika 4: Koeficient prenosa toplote v kokili in v sekundarni coni hlajenja: a) površina z majhno ukrivljenostjo, b) površina z veliko ukrivljenostjo lite gredice

of two pyrometers placed behind the mould in the secondary cooling zone (1500 mm from the pour level) and in the tertiary cooling zone (15420 mm from the pour level). Both the pyrometers were positioned in the centerline of the small radius surface of the cast billets. The maximum temperature difference between the measured temperatures by the pyrometers and the calculated temperatures by the solidification model was 40 °C.²⁰

3 ANALYSIS SETUP AND PARAMETERS

The study was carried out for the 200 mm × 200 mm steel billets that are continuously cast in Zeleziarne Podbrezova in Slovakia. The radial billet caster has the tubal mould, it comprises the secondary cooling with three independent cooling zones (denoted by S-0, S-1, and S-2 in figures) including 96 water cooling nozzles of three

types and two straightening mills (denoted by SM-1, SM-2 in figures).

The following three steel grades are considered (only the main elements are listed in mass fractions *w*): unalloyed fine-grained steel for constructions and welding S355J2G3 (0.187 % C, 1.17 % Mn, 0.22 % Si, 0.016 % P, and 0.012 % S), carbon steel for refining C60 (0.617 % C, 0.73 % Mn, 0.29 % Si, 0.014 % P, 0.013 % S, 0.03 % Cr, 0.05 % Ni, and 0.18 % Cu), and heat-resistant Cr-Mo steel for use at higher temperatures 13CrMo4-5 (0.144 % C, 0.53 % Mn, 0.24 % Si, 0.007 % P, 0.006 % S, 0.98 % Cr, 0.46 % Mo, 0.12 % Cu, and 0.019 % Al). The range of the casting speed was considered to be between 0.7 m/min and 1.1 m/min; all three mentioned steel grades are commonly cast with a casting speed of 0.9-1.0 m/min. In figures, only the casting speeds 0.7 m/min, 0.9 m/min, and 1.1 m/min are pictured for reasons of clarity.

For the analysis the casting temperature was set identically to the real casting process: 1553 °C for the grade S355J2G3, 1515 °C for the grade C60, and 1547 °C for the grade 13CrMo4-5. The analysis was carried out for the identical setting of the caster, mainly the water flow rates through the cooling nozzles in the secondary cooling and through the mould for all the considered steel grades.

4 RESULTS AND DISCUSSION

4.1 Surface and corner temperatures

The analysis confirmed a significant dependency of the temperature field of the cast billets on the casting speed. For all steel grades, a very similar thermal behavior was observed (**Figure 5** for the steel grade S355J2G3): the higher casting speed, the higher both the corner temperature and the surface temperature beneath the nozzles. Moreover, with an increasing casting speed the rise of both the surface and corner temperatures decreases (**Figure 5**). As already mentioned, although all three investigated steel grades have various chemical

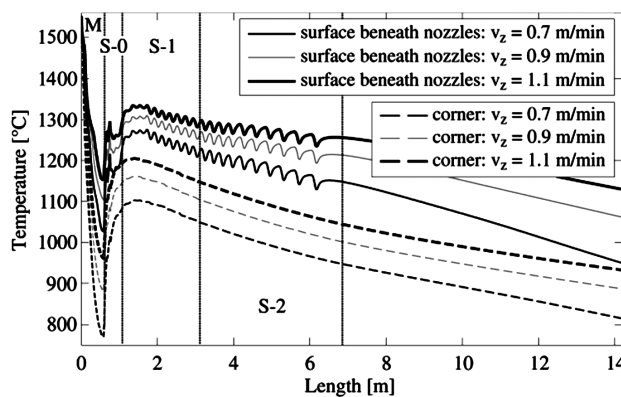


Figure 5: The impact of the casting speed on the surface and corner temperatures for the steel grade S355J2G3

Slika 5: Vpliv hitrosti ulivanja na temperaturo površine in robov pri jeklu S355J2G3

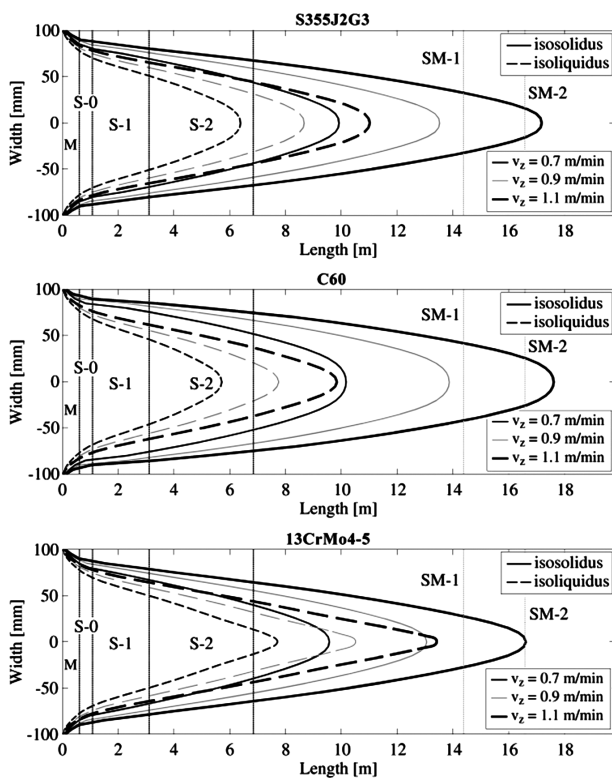


Figure 6: The influence of the casting speed on the isosolidus and isoliquidus curves, and the mushy zone

Slika 6: Vpliv hitrosti ulivanja na izosolidusne, izoliquidusne krivulje in na kašasto področje

compositions and each of them is intended for a different usage, their relative courses of the surface and the corner temperatures along the caster with a casting speed in the range between 0.7 m/min and 1.1 m/min are almost identical. The only significant difference is the temperature shift of both the surface and the corner temperature curves due to the various casting temperatures.

4.2 Isosolidus and isoliquidus curves, metallurgical length, mushy zone

The thermal behavior inside the cast billets, the solidification process, and the influence of the casting

speed on them can be investigated in the longitudinal axial cross-section of the billet with the use of the isosolidus and isoliquidus curves. Moreover, the isosolidus curve is directly related to the metallurgical length, which is an important parameter of continuous casting.

Figure 6 shows the influence of the casting speed on the solidification process of steel in the core of the billets: the isosolidus and isoliquidus curves, and the mushy zone where both the liquid and solid phases coexist.

As can be observed from **Figure 6**, the profile of the isosolidus and isoliquidus curves, the metallurgical length as well as the width of the mushy zone differs for each of the three investigated steel grades. In general, the higher casting speed makes both the isosolidus and isoliquidus longer (a positive shift in the length) and lengthens the metallurgical length as well (**Figure 6**). Moreover, the higher casting speed also enlarges the mushy zone. It implies that the positive shift of the isosolidus curve due to the increasing casting speed is larger than the shift of the isoliquidus curve.

For instance, consider the steel grade C60 (see the middle graph in **Figure 6**): for the casting speed of 0.7 m/min the metallurgical length is 10.1 m and the width of the mushy zone (in the axis of the billet) is 4.5 m. For the casting speed of 0.9 m/min, the metallurgical length increases to 13.9 m and the width of the mushy zone to 6.1 m. However, in the case of the casting speed of 1.1 m/min, the metallurgical length reaches 17.6 m (e.g., in the positions of both the straightening mills SM-1 and SM-2 the billet still contains the liquid phase) and the mushy zones distends to 7.7 m.

4.3 Shell thickness

The casting speed also has an impact on the rate of the shell thickness growth along the caster. A similar shell thickness behavior was observed for all three investigated steel grades. In general, the higher casting speed, the slower rate of the shell thickness growth (**Figure 7**). The shell inside the mould grows almost linearly, and behind the mould the rate of the shell thickness growth declines due to the abrupt reduction of the heat withdrawal. In the secondary cooling the rate of the shell thickness growth slowly increases owing to the

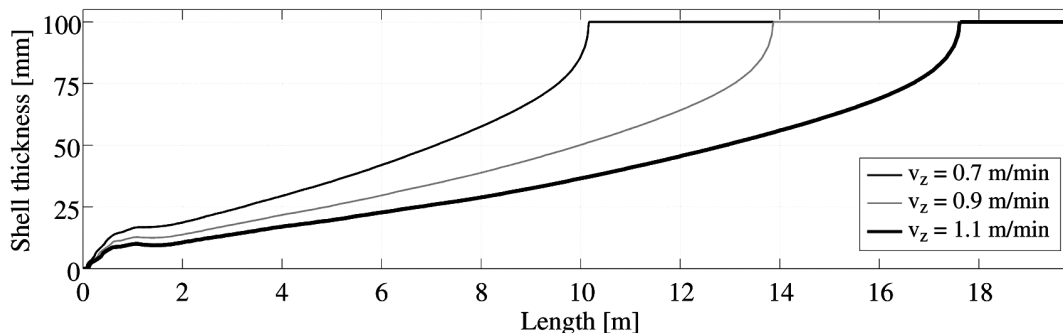


Figure 7: The influence of the casting speed on the shell thickness for the steel grade C60

Slika 7: Vpliv hitrosti ulivanja na debelino skorje pri jeklu C60

heat withdrawal of the cooling nozzles and also of the free convection and radiation heat transfer mechanisms.

For instance, **Figure 7** for the steel grade C60. In the length of 10.1 m where the billet cast with the casting speed of 0.7 m/min is completely solidified (i.e., the shell thickness is 100 mm), the shell thickness of the billet cast with the casting speed of 0.9 m/min is only 50 mm and the shell thickness of the billet cast with the casting speed of 1.1 m/min is even only 35 mm. The billet cast with the casting speed of 0.9 m/min is completely solidified in the length of 13.8 m, where the shell thickness of the billet cast with the casting speed of 1.1 m/min is only 55 mm.

4.4 Local period of solidification

The solidification process of the steel billets can also be investigated by the local period of solidification, which represents the local width of the mushy zone expressed in time related to the casting speed. Thus, for the given point (x, y) in the cross-section of the billet (**Figure 1**), the local period of solidification $lps(x, y)$ expresses the time (s) needed for the solidification (**Figure 6**), i.e., for cooling down from the liquidus temperature (where the first grains of solid phase appear) to the solidus temperature (where the last melt is solidified) along the billet assuming its movement through the caster with the casting velocity:

$$lps(x, y) = \frac{L_{solidus}(x, y) - L_{liquidus}(x, y)}{v_z} \quad (8)$$

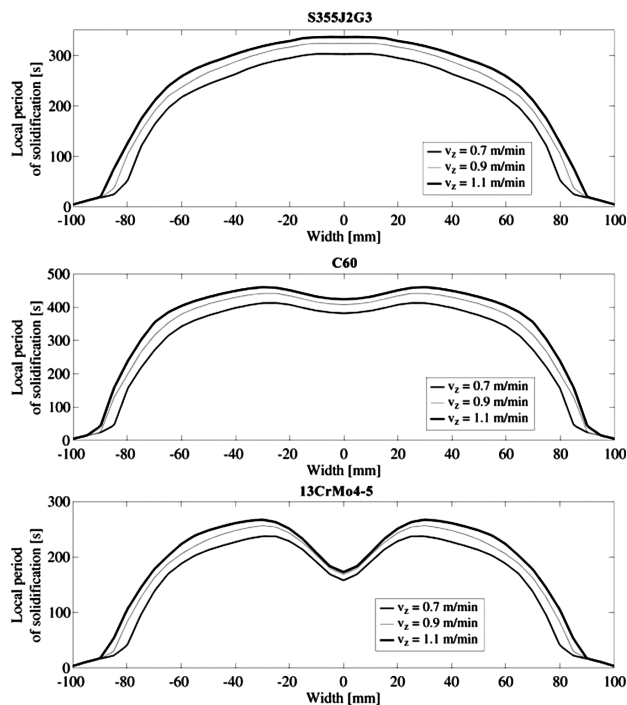


Figure 8: The influence of the casting speed on the local period of solidification in the axial cross-section

Slika 8: Vpliv hitrosti ulivanja na lokalni čas strjevanja v osnem prerezu

where $L_{solidus}(x, y)$ (m) and $L_{liquidus}(x, y)$ (m) are the lengths of the isosolidus and isoliquidus curves in the cross-section point (x, y) (**Figure 6** plotted for $y = 100$ mm), and v_z is the casting velocity ($m\ s^{-1}$). The local periods of solidification in the horizontal centerline of the cross section (i.e., for the cross section points (x, y) for which $y = 100$ mm) of cast billets are shown in **Figure 8**.

In general, a higher casting speed makes the local period of solidification longer (**Figure 8**). However, the profiles of the local periods of solidification are different for particular steel grades. This behavior is mainly caused by the different steel structure attained during the solidification of the particular steel grade directly related to the chemical composition and by the setup of cooling.²⁰ It was shown that a modification of the chemical composition in the range of the chemical composition given by norms and standards can change the profile of the local period of solidification.²²

In the case of the grade S355J2G3, the slowest solidification is in the core of the billet. However, the slowest solidification of the grade C60 is not in the core, but about 30 mm out of the core (width = ± 30 mm in **Figure 8**). The described behavior is even more evident in the case of the grade 13CrMo4-5, where the slowest solidification is in approximately the same position (width = ± 30 mm) as in the case of C60, but it needs an extra 80 s to be solidified than the core of the billet (width = 0 mm).

5 CONCLUSION

The paper presents the results of an analysis aimed at the impact of the casting speed on the temperature field of continuously cast steel billets and related parameters. The analysis was carried out with the use of the originally implemented dynamic solidification and three various steel grades were taken into account: common unalloyed steel for constructions, carbon steel for refining, and anticorrosive Cr-Mo steel for use at higher temperatures. The casting speed in the range between 0.7 m/min and 1.1 m/min was considered.

The performed analysis proved that the casting speed can significantly influence the temperature field and the solidification during the continuous steel casting. In general, the higher casting speed increases the temperature of the cast billets due to a reduced heat withdrawal. Consequently, the isosolidus and isoliquidus curves become longer and it also causes an increase of the metallurgical length. The higher casting speed also causes a drop in the shell growth as well as making the mushy zone wider, which implies a longer local period of solidification.

The study confirmed that the dynamic solidification models make it possible to perform an analysis of the caster and billets responses to various operating conditions and situations. The results can then be used by operators to set-up the caster.

Acknowledgement

The presented research was supported by the project GACR P107/11/1566 of the Czech Science Foundation and by the BUT project FSI-J-12-22. The main author, the holder of Brno PhD Talent Financial Aid sponsored by Brno City Municipality, also gratefully acknowledges that financial support.

6 REFERENCES

- ¹ A. Cramb Ed., Making, shaping and treating of steel: casting, 11th edition, Assn of Iron & Steel Engineers, 2003
- ² P. Popela, Optimizing mechanical properties of iron during melting process, *ZAAM: Zeitschrift für Angewandte Mathematik und Mechanik*, 77 (1997) 2, S649–S650
- ³ M. Sadat, A. H. Gheysari, S. Sadat, The effects of casting speed on steel continuous casting process, *Heat and Mass Transfer*, 47 (2011) 12, 1601–1609
- ⁴ Y. Meng, B. G. Thomas, Heat-Transfer and Solidification Model of Continuous Slab Casting: CON1D, *Metallurgical and materials transactions B*, 34 (2003) 5, 685–705
- ⁵ J. Stetina, L. Klimes, T. Mauder, F. Kavicka, Final-structure prediction of continuously cast billets, *Mater. Tehnol.*, 46 (2012) 2, 155–160
- ⁶ B. G. Thomas, Modeling of the continuous casting of steel-past, present, and future, *Metallurgical and materials transactions B*, 33 (2002) 6, 795–812
- ⁷ B. Petrus, K. Zheng, X. Zhou, B. G. Thomas, J. Bentsman, Real-time, model-based spray-cooling control system for steel continuous casting, *Metallurgical and materials transactions B*, 42 (2011) 1, 87–103
- ⁸ J. C. Ma, Z. Xie, Y. Ci, G. L. Jia, Simulation and application of dynamic heat transfer model for improvement of continuous casting process, *Materials science and technology*, 25 (2009) 5, 636–639
- ⁹ M. Gonzalez, M. B. Goldschmit, A. P. Assanelli, E. F. Berdaguer, E. N. Dvorkin, Modeling of the solidification process in a continuous casting installation for steel slabs, *Metallurgical and materials transactions B*, 34 (2003) 4, 455–473
- ¹⁰ L. Zhang, Y. M. Rong, H. F. Shen, T. Y. Huang, Solidification modeling in continuous casting by finite point method, *Journal of materials processing technology*, 192–193 (2007), 511–517
- ¹¹ A. Fic, A. J. Nowak, R. Bialecki, Heat transfer analysis of the continuous casting process by the front tracking BEM, *Engineering analysis with boundary elements*, 24 (2000) 3, 215–223
- ¹² B. Sarler, R. Vertnik, A. Z. Lorbiecka, I. Vusanovic, B. Sencic, A multiscale slice model for continuous casting of steel, *International conference on modeling of casting, welding and advanced solidification processes*, IOP Conference series – Materials science and engineering, 33 (2012), 012021
- ¹³ C. A. Santos, J. A. Spim, A. Garcia, Mathematical modeling and optimization strategies (genetic algorithm and knowledge base) applied to the continuous casting of steel, *Engineering applications of artificial intelligence*, 16 (2003) 5–6, 511–527
- ¹⁴ J. Stetina, F. Kavicka, T. Mauder, L. Klimes, Transient simulation temperature field for continuous casting steel billet and slab, *Proceedings of METEC InSteelCon 2011*, 13–23
- ¹⁵ J. Stetina, F. Kavicka, The influence of the chemical composition of steels on the numerical simulation of a continuously cast slab, *Mater. Tehnol.*, 45 (2011) 4, 363–368
- ¹⁶ C. R. Swaminathan, V. R. Voller, A general enthalpy method for modeling solidification processes, *Metallurgical transactions B*, 23 (1992) 5, 651–664
- ¹⁷ D. M. Stefanescu, *Science and Engineering of Casting Solidification*, Second edition, Springer, 2009
- ¹⁸ J. Miettinen, S. Louhenkilpi, H. Kytönen, J. Laine, IDS: Thermodynamic-kinetic-empirical tool for modelling of solidification, microstructure and material properties, *Mathematics and computers in simulation*, 80 (2010) 7, 1536–1150
- ¹⁹ F. P. Incropera, D. P. DeWitt, T. L. Bergman, A. S. Lavine, *Principles of heat and mass transfer*, Seventh edition, Wiley, 2012
- ²⁰ J. Stetina, L. Klimes, Analysis of continuous casting of steel billets with the use of the transient 3D numerical model of temperature field, *Technical report for Zeleziarne Podbrezova*, Slovakia, Brno University of Technology, 2011
- ²¹ M. Raudensky, J. Horsky, Secondary cooling in continuous casting and Leidenfrost temperature effects, *Ironmaking and steelmaking*, 32 (2005) 2, 159–164
- ²² L. Klimes, J. Stetina, L. Parilak, P. Bucek, Influence of Chemical Composition of Cast Steel on the Temperature Field of Continuously Cast Billets, *Proceedings of Metal 2012*, Ostrava: Tanger, 2012, 34–39

DEVELOPMENT OF THE PRODUCTION OF ULTRAFINE-GRAINED TITANIUM WITH THE CONFORM EQUIPMENT

RAZVOJ PROIZVODNJE ULTRADROBNOZRNATEGA TITANA Z OPREMO CONFORM

Michal Duchek, Tomas Kubina, Josef Hodek, Jaromir Dlouhy

COMTES FHT a.s., Průmyslová 995, 334 41 Dobruška, Czech Republic
michal.duchek@comtesfht.cz

Prejem rokopisa – received: 2012-09-10; sprejem za objavo – accepted for publication: 2012-12-18

Ultrafine-grained titanium belongs to the materials that possess a high potential for medical applications and, thanks to its mechanical properties, it is already frequently employed in this field. The know-how for manufacturing ultrafine-grained titanium represents one of the most complex issues in the titanium processing. The CONFORM process is one of the techniques available for this purpose. The principle of the CONFORM technique is the continuous ECAP (Equal Channel Angular Pressing) process. At present, it is primarily used for processing the materials with a low flow stress and a good formability. This paper gives a description of this forming technique and its applications in the production of titanium semi-products. Grade-4 titanium was used for the experimental programme. The factors explored in the process trials included the impacts of the shape of the exit chamber and of the temperatures at the key locations within the CONFORM process on the resulting microstructure of the titanium product. Numerical simulations of the process were performed in the DEFORM 3D software using various friction conditions. The actual flow of the material was compared with the results of the simulation.

Keywords: titanium, CONFORM, ECAP, ultrafine grain

Ultradrobnozrnat titan spada k materialom, ki imajo velike možnosti za uporabo v medicini in se že uporablja na tem področju po zaslugi svojih mehanskih lastnosti. Tehnologija izdelave ultradrobnozrnatega titana je najbolj kompleksen izziv pri njegovi proizvodnji. Postopek CONFORM je ena od razpoložljivih tehnik za ta namen. Osnova tehnike CONFORM je kontinuiran postopek ECAP (stiskanje skozi pravokoten kanal). Sedaj se uporablja za predelavo materialov z nizko napetostjo tečenja in dobro preoblikovalnostjo. Članek opisuje to tehniko preoblikovanja in njeno uporabo pri proizvodnji titanovih polproizvodov. Titan čistosti grade-4 je bil uporabljen za preizkuse. V preizkusnih procesih so bili uporabljeni nekateri dejavniki na ključnih mestih pri CONFORM-u, vključno z učinkom oblike izhodnega kanala in temperature, na mikrostrukturo proizvoda iz titana. Numerične simulacije procesa so bile izvršene s programsko opremo DEFORM 3D z uporabo različnih razmer pri trenju. Resnični tok materiala je bil primerjan z rezultati simulacije.

Ključne besede: titan, CONFORM, ECAP, ultradrobna zrna

1 INTRODUCTION

Numerous SPD processes (Severe Plastic Deformation) were developed in the recent 15 years. These processes are used for achieving a grain refinement in materials, typically to a grain size between 100 nm and 400 nm. Their efficiency in processing a large volume of a material is, however, still insufficient for industrial-scale applications. This drawback was eliminated with the CONFORM method. The method has been known for a long time. Today, it is used for the continuous industrial-scale production of sections, mostly from aluminium. Essentially, it is an upgraded ECAP (Equal Channel Angular Pressing) method, where the feedstock is forced through a die by a friction force exerted by a roll that turns ECAP into a continuous process.

This ECAP–CONFORM process was reported for the first time in¹. In this study, a commercial-grade aluminium wire was extruded using one to four passes. The preparation of ultrafine-grained titanium using this method was reported in². In this study, a 7.2 mm × 7.2 mm square wire with an accumulated strain of $e = 6$

was subsequently redrawn into a diameter wire 3 mm (resulting in the total strain of 7.9).

In the present paper, the production of commercial-grade-titanium round bars using a single pass through the ECAP–CONFORM equipment is described.

2 EXPERIMENTAL WORK

The feedstock consisted of the CP Ti grade 2 bar with a diameter of 10 mm. Their chemical composition is listed in **Table 1**. It was measured using a Bruker Q4 Tasman optical emission spectrometer and a Bruker G8 Galileo gas analyzer.

Table 1: Chemical composition of the feedstock in mass fractions (w/%)
Tabela 1: Kemijska sestava surovca v masnih deležih (w/%)

Fe	O	C	H	N	Ti
0.046	0.12	0.023	0.0026	0.0076	99.822

Titanium bars were converted into the bars of the same diameter as that of the feedstock using a CONFORM 315i machine.

The resulting microstructure was examined using a Nikon Eclipse MA 200 optical microscope. The specimens for the observation in the optical microscope were prepared by metallographic grinding and polishing and then etched using a Kroll agent. The specimens for an EBSD analysis were prepared using a JEOL SM-09010 ion polisher. The EBSD analysis was conducted using a JEOL 7400 electron microscope with a HKL-NORD-LYSS EBSD camera. The data were processed using the Channel5 software.

The mechanical properties at room temperature were measured using the cylindrical tension-test specimens with a gauge length of 25 mm and a diameter of 5 mm. In addition, impact-toughness tests were conducted using 3 mm × 4 mm section specimens.

The coefficient of the friction between CP-Ti and Inconel (the material of the die chamber) was measured by means of a tribological pin-on-disc test.

The process of continuous extrusion of titanium was modelled using the DEFORM 3D software based on the FEM method. The strain and temperature fields that varied with time were analysed with mathematical tools. The heat-transfer coefficient between the titanium feedstock and the wheel was measured to be 1000 W/(m² K). The input material data were obtained from the material-data calculation in the JMatPRO software.

3 RESULTS AND DISCUSSION

In the trials of extruding a Ti wire with the CONFORM equipment, the key parameters varied: the speed of the wheel, die-chamber temperatures, the cooling downstream of the die chamber and others. The temperature vs. the time record from the experiment is shown in **Figure 1**. The decisive parameter for the entire process is the die-chamber temperature that varied between the initial 500 °C and the final value of 350 °C. Numbers 1–4 in the figure denote the time instants, at which the samples were taken for an EBSD analysis. The point, at

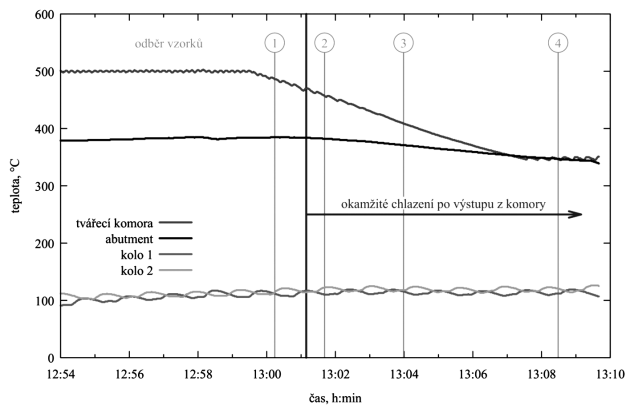


Figure 1: Temperatures at the key locations during the ECAP-CONFORM processing of a titanium bar

Slika 1: Temperature na ključnih mestih med ECAP-CONFORM stiskanjem titana

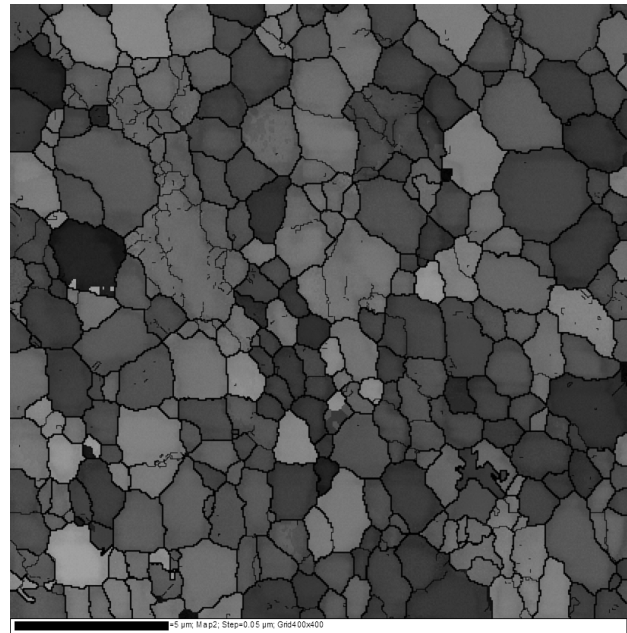


Figure 2: EBSD micrograph of specimen no. 4

Slika 2: EBSD-posnetek vzorca št. 4

which the Ti wire was cooled right after exiting the die chamber, is identified as well.

The microstructure of specimen 1 consists of undeformed equiaxed grains. The grain-size pattern is bimodal and the average grain size is 1.9 μm. Neither the small nor the large grains show signs of deformation.

The microstructure of specimen 2 is identical to that of specimen 1. The chamber temperature of 450 °C is sufficient for the microstructure to recover/recrystallize. No effects of cooling were observed. The recovery/recrystallization and potential grain growth were finished before the specimen was cooled.

Specimen 3 (the die-chamber temperature of 400 °C) contains a small amount (10–15 %) of distorted unrecrystallized grains. The specimen was cooled with water upon exiting the chamber. The deformed grains with a size of no more than 5 μm × 10 μm are divided by low-angle boundaries into subgrains. Their average size is 1.9 μm.

Specimen 4 was formed at the die-chamber temperature of 350 °C and then cooled with water upon exiting the chamber. Its microstructure consists of slightly elongated, deformed grains that, however, lack the above-mentioned substructure (**Figure 2**). The EBSD analysis focused on the centre of the circular cross-section of the extruded product. The analysed surface is on the plane that is parallel to the bending plane/flow plane in the CONFORM chamber. On the EBSD maps shown, the axis of the extruded section is vertical. The grain size in this specimen was 1.4 μm.

The textures in all the specimens are aligned on the basal plane. The texture of specimen 4 is documented in **Figure 3**.

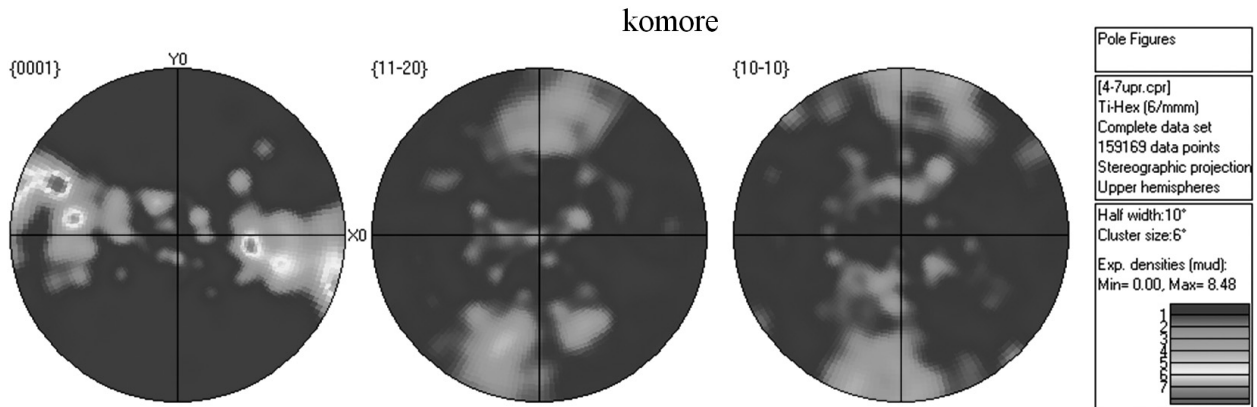


Figure 3: Areal densities of the points
Slika 3: Področja gostote točk

Table 2: Mechanical properties and the average grain size in various states of CP-Ti
Tabela 2: Mehanske lastnosti in povprečna velikost zrn pri različnih stopnjah CP-Ti

Condition	$R_{p0.2}$	R_m	A_g	A_5	Z	KCV	d
	MPa	MPa	%	%	%	J cm ⁻²	μm
Feedstock	354.3	470.4	9.3	32.3	64.2	64.2	23.5
Upon pass 1	620.1	693.5	12.0	26.3	55.7	27.5	1.4

The mechanical properties of the feedstock and of the Ti wire upon a single pass at the die-chamber temperature of 350 °C are listed in **Table 2**. As expected, the yield stress and ultimate strength of the product are higher than those of the feedstock. On the other hand, its contraction and elongation as well as the impact toughness upon the first pass are lower than those of the feedstock.

Figure 4 shows the macrostructure of the product in the die chamber after the processing was interrupted. The dead zones in the transitional region are clearly visible. The traces of deformation can be seen at some points.

Figure 5a shows a micrograph of the undeformed material. The average grain size in this case is 25 μm. The microstructure above the abutment is shown in **Fig-**

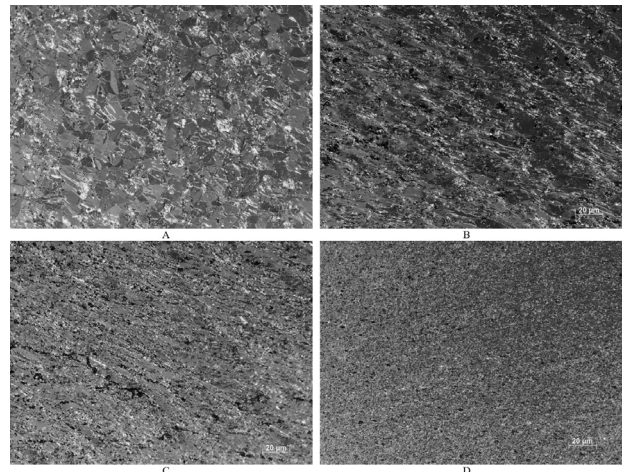


Figure 5: Microstructures in the selected locations within the die chamber. The notation corresponds to that in **Figure 4**.

Slika 5: Mikrostrukture na izbranih lokacijah v komori. Oznake ustrezajo tistim na **sliki 4**.

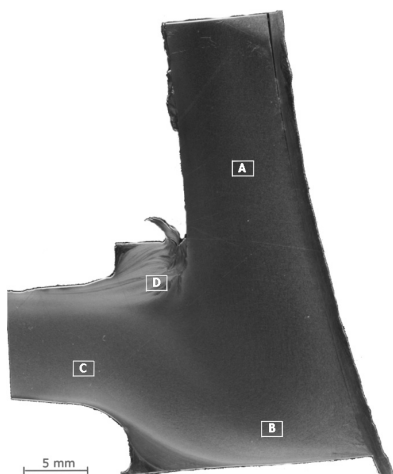


Figure 4: Macrostructure of CP-Ti inside the die chamber
Slika 4: Makrostruktura v notranjosti CP-Ti komore

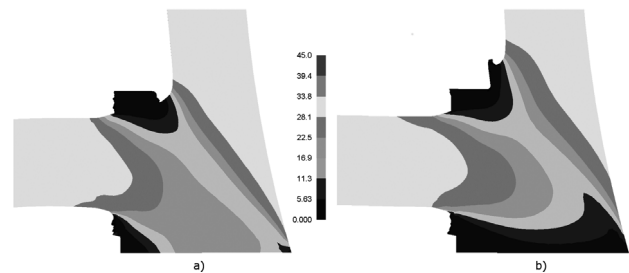


Figure 6: Distribution of the absolute material-flow velocity in mm s⁻¹. Variant: a) with the friction coefficient of 0.2; b) friction coefficient of 0.7.

Slika 6: Razporeditev absolutne hitrosti toka materiala v mm s⁻¹. Varianta: a) koeficient trenja 0,2, b) koeficient trenja 0,7.

ure 5b. In this location, the grains are elongated in the direction at an angle of 45°. The elongation is not uniform; instead, it shows a wave-like pattern. A better alignment of the grains can be seen in **Figure 5c**, which shows a micrograph of the bottom part of the die-exit area. The dead zones exhibit the finest grains without any traces of the flow lines (**Figure 5d**).

3.1 Comparison between mathematical simulation and physical experiment

The coefficient of friction between CP-Ti and the tool material was measured using a non-standard, tribological test arrangement: $\mu = 0.62$. The result is not conclusive, as the conditions of the test cannot perfectly match those of the real-world titanium-forming process.

Two FEM simulations were performed with two different friction-coefficient values (0.2 and 0.7), while keeping the other initial and boundary conditions identical.

A sample result of the calculation of the absolute flow velocity is shown in **Figure 6** for both values of the friction coefficient. Upon comparing the results with an actual specimen (**Figure 4**), it becomes apparent that the value of $\mu = 0.7$ is closer to the actual value. A comparison between the distribution of the zones with the minimum movement of the material calculated by the numerical simulations and that found in the specimen upon interrupting the forming process suggests the same result: the value of $\mu = 0.7$ is more appropriate. The obtained value is very far from the values of the coefficient of friction during the wire drawing with lubrication.³

4 CONCLUSIONS

The process trials were performed, whereby the impact of the settings of the CONFORM equipment on the microstructure of the resulting Ti wire was explored. The strongest influence is that of the die-chamber tempe-

rate. The smallest average grain size found with the EBSD analysis is 1.4 μm . The limit temperature for achieving this value in an uninterrupted process was 350 °C. The Ti wire produced under these conditions showed a strength of 693 MPa and an impact toughness of 27.5 J cm⁻².

The main goal of this study was to describe the continuous extrusion of titanium by means of a mathematical model. The model was constructed in the FEM software DEFORM-3D. The outcome of the simulations is in good agreement with the experimental results. The die chamber of the Conform™ machine was adapted for titanium forming.

The coefficient of friction between titanium and the die-chamber temperature was 0.7. In the further optimisation efforts, the die chamber will be adjusted in order to suppress the dead zones where no movement of the material occurs. This will be first verified with a mathematical simulation and then with additional process trials including multiple passes in order to obtain a nanostructured titanium bar.

Acknowledgments

This study was undertaken as part of the TIP FR-TII/415 Research and development of nanostructured materials for medical applications project funded by the Ministry of Industry and Trade of the Czech Republic.

5 REFERENCES

- ¹ G. J. Raab, R. Z. Valiev, T. C. Lowe, Y. T. Zhu, Continuous processing of ultrafine grained Al by ECAP-Conform, *Materials Science and Engineering: A*, 382 (2004) 1–2, 30–34
- ² G. Raab et al., Long-Length Ultrafine-Grained Titanium Rods Produced by ECAP-Conform, *Materials Science Forum*, 584–586 (2008), 80–85
- ³ B. Plášek, V. Tittel, Lime-based lubricants improve wire drawing, *Wireworld International*, 29 (1987) 2, 33–34

CONVERSION OF THE Ms70 ALPHA-BRASS TORSION-TEST DATA INTO HOT-FORMING PROCESSING MAPS

PRETVORBA PODATKOV TORZIJSKEGA PREIZKUSA ALFA MEDI Ms70 V PROCESNE ZEMLJEVIDE VROČE PREDELAVE

Tomáš Kubina¹, Josef Bořuta², Rudolf Pernis³

¹COMTES FHT, Prumyslova 995, 334 41 Dobruška, Czech Republic

²Material & Metallurgical Research Ltd., Pohraniční 693/31, 706 02 Ostrava-Vitkovice, Czech Republic

³Faculty of Special Technology, Alexander Dubček University in Trenčín, Trenčín, Slovak Republic
tomas.kubina@comtesfht.cz

Prejem rokopisa – received: 2012-09-16; sprejem za objavo – accepted for publication: 2012-12-03

The present paper gives a summary of the plastic behaviour of the Ms70 deep-drawing cartridge brass under the hot-forming conditions explored by using a SETARAM-Vitkovice torsion plastometer. The specimens were cut from the hot-extruded and, subsequently, cold-drawn brass bars.

Formability tests were performed on the diameter 6 mm specimens at (650, 700, 750, 800 and 850) °C and at the speeds of (16, 80, 400 and 800) r/min. These testing conditions are equivalent to the conditions of the ordinary industrial hot extrusion of brass: the single most problematic operation in the manufacturing process in terms of an occurrence of serious defects.

The results of the torsion tests were converted into the conventional format: the maximum flow-stress levels vs. the peak-strain intensity. The points thus obtained can be used for finding the activation energy for forming Q , which is useful for determining the thermally compensated strain rate with the aid of the Zener-Hollomon Z parameter.

The power-dissipation maps with the axes showing the deformation temperature and logarithmic strain rate were computed using a dynamic material model. The calculation of the dissipation efficiency was verified by comparing it with the known data on the 30 % zinc brass. The maps constructed in this manner allow the data from the torsion and compression plastometers to be compared. The paper also includes a discussion of the changes in the processing maps at higher strains showing the optimum regions for the hot extrusion of brass.

Keywords: flow stress, brass, hot formability, strain rate, torsion test, power-dissipation maps

V članku je povzetek plastičnega vedenja globokovlečne medí Ms70 pri vroči predelavi z uporabo torzijskega plastometra SETARAM-Vitkovice. Vzorci so bili izrezani iz vroče iztiskane in nato hladno vlečene palice iz medí.

Preizkusi preoblikovalnosti so bili izvršeni na vzorcih premera 6 mm pri temperaturah (650, 700, 750, 800 in 850) °C in hitrostih (16, 80, 400 in 800) r/min. Te razmere pri preizkusih so enakovredne tistim pri navadnem industrijskem iztiskanju medí; najbolj problematični operaciji pri procesu izdelave zaradi pojava hujših poškodb.

Rezultati torzijskih preizkusov so bili pretvorjeni v navadno obliko: maksimalne natezne napetosti proti največjemu raztezku. Tako dobljene točke se lahko uporabí za izračun aktivacijske energije preoblikovanja Q , ki je uporabna za določanje toplotno kompenzirane hitrosti trganja z uporabo Zener-Hollomon Z -parametra.

Zemljevidi spreminjanja moči z osmi, ki prikazujejo temperaturo deformacije in logaritem hitrosti preoblikovanja, so bili izračunani z dinamičnim modelom materiala. Izračun spreminjanja učinkovitosti je bil preverjen s primerjavo poznanih podatkov za med s 30 % cinka. Tako konstruirani zemljevidi omogočajo primerjavo podatkov iz torzije in plastometra. Članek vključuje tudi razpravo sprememb v zemljevidih procesiranja pri višjih napetostih in prikazuje optimalna področja za vročo ekstruzijo medí.

Ključne besede: napetost tečenja, med, vroča preoblikovalnost, hitrost preoblikovanja, torzijski preizkus, mape spreminjanja moči

1 INTRODUCTION

The Ms70 brass belongs to the group of alpha brasses with deep-drawing properties that are used for making cartridge shells in a cold process. The conventional method of the production of brass cartridge shells uses rolled feedstock. The punching of the blanks from a strip leads to large amounts of waste material that requires reprocessing in metallurgical plants. Munitions plants have launched the projects introducing a zero-waste production of brass cartridge shells from Ms70 bars. This change from the rolled strip feedstock to hot-extruded bars required a technology upgrade in the metallurgical plants.

The hot-extrusion process proved to be the critical stage in the production of brass bars. As the Ms70 brass exhibits excellent cold formability, it is difficult to form it at high temperatures. The flow stress of the Ms70 brass in the extrusion process is governed primarily by the forming temperature, the strain rate and the strain. The most common technique for exploring the flow stress at elevated temperatures is the tension testing.^{1,2} However, its results are not adequate for mapping the forming processes at high temperatures and high strain rates. As measuring the flow stress in a production is not cost-effective, the forming process was simulated using a torsion plastometer.³

A conversion of the results of the compression plastometer testing into the processing maps for the

30 % zinc brass was reported in^{4,5}. The evaluation was based on the dynamic material model reported by Prasad⁶. The total energy absorbed by the deformed body P is converted into two forms: G – causing a rise in the temperature; and J – leading to microstructural changes. The factor that partitions the energy between G and J is the strain-rate coefficient m . There is an effect of the stress as well. The J content can be calculated using the following equation:

$$J = \frac{\sigma \dot{\epsilon} m}{m+1} \quad (1)$$

where σ is the flow stress and $\dot{\epsilon}$ denotes the strain rate. An ideal linear dissipator term is given by $m = 1$ and $J = J_{\max} = \sigma \dot{\epsilon} / 2$. The dissipation efficiency for a non-linear dissipator may be expressed as a dimensionless parameter:

$$\eta = \frac{J}{J_{\max}} = \frac{2m}{(m+1)} \quad (2)$$

The variation of η with the temperature and strain rate represents a dissipation of the power through the microstructural changes in the workpiece material. The purpose of this study was to compare and contrast the energy-dissipation maps constructed using the data from the compression and torsion plastometers.

2 MATERIALS AND METHODS

The computer that controls the plastometer records the following quantities: time, torque M_k , axial force F , temperature T and the number of twists N . The test specimen for a torsion plastometer is a bar with the diameter of D (radius R) and a gauge length of L . The key output of the torsion test for a formability assessment is the number of twists to fracture N_f . As twisting causes the test bar to shrink in length, the grips are fixed from the beginning of the twisting cycle. Consequently, the axial force F begins to act on the bar. The flow stress is given by the following equation:

$$\sigma = \sqrt{\left(\frac{3\sqrt{3}M_k}{2\pi R^3}\right)^2 + \left(\frac{F}{\pi R^2}\right)^2} \quad (3)$$

The strain intensity e in the torsion testing was found from:

$$e = \frac{2}{\sqrt{3}} \arg \sinh\left(\frac{2\pi RN}{3L}\right) \quad (4)$$

Table 1: Chemical composition of the Ms70 brass for torsion testing
Tabela 1: Kemijska sestava medi Ms70 za torzijske preizkuse

Element	Cu	Pb	Sn	Fe	Ni	Mn	Al	Si
Content, w/%	70.39	0.0004	0.0042	0.0232	0.0022	0.0003	0.0012	0.0002
Element	As	Sb	Bi	Cr	Cd	Ag	P	Zn
Content, w/%	0.0001	0.0031	0.0001	0.0001	0.0001	0.0001	0.0002	balance

In a hot-torsion test, the stress-strain dependence is monitored under the prescribed conditions (specimen geometry, temperature, strain rate).⁷

The experimental hot-torsion testing was performed using the Ms70 deep-drawing brass with a chemical composition given in **Table 1**. The test specimens were 10 mm diameter bars. Ms70 brass bars were produced in the following sequence: melting in an electric induction furnace, semi-continuous casting of round ingots, hot extrusion and final sizing in a cold-drawing process.

The hot-torsion testing of Ms70 brass bars was performed according to a 4 × 5 schedule. This means that four strain-rate values of (0.2, 1, 5 and 10) s⁻¹ corresponding to the twisting speeds of (16, 80, 400 and 800) min⁻¹ were combined with five temperature levels of T is (650, 700, 750, 800 and 850) °C.

3 DISCUSSION OF RESULTS

The results of the torsion testing at 650 °C are shown in **Figure 1**. The tests at the other temperatures were evaluated in an identical manner.⁸

The peak stress values σ_p and the corresponding strain levels e_p were derived from these plots. The peak stress (the maximum stress) σ_p is governed by two variables: the temperature and the shear-strain rate. This dependency can be expressed as the function $\sigma_p = f(t, e)$,

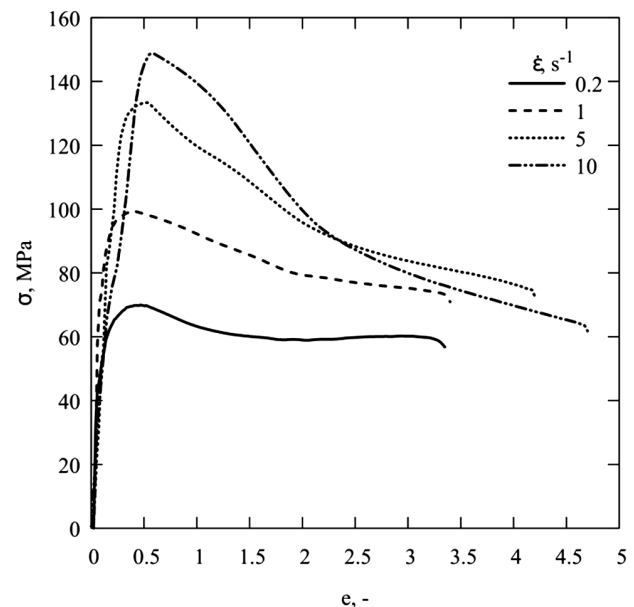


Figure 1: Flow stress of the Ms70 brass at 650 °C
Slika 1: Krivulje tečenja medi Ms70 pri 650 °C

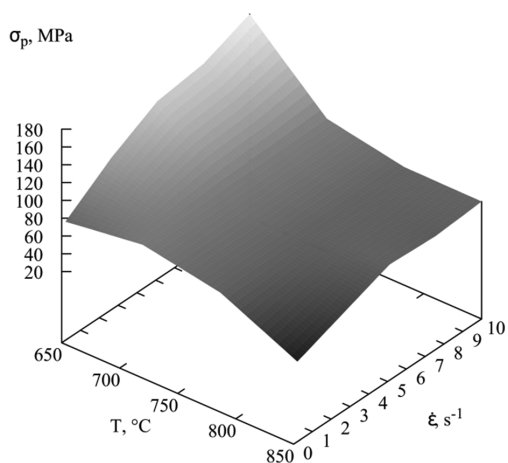


Figure 2: Representation of the $\sigma_p = f(t, e)$ function in a 3D plot
Slika 2: Prikaz funkcije $\sigma_p = f(t, e)$ v 3D-diagramu

which is shown as a 3D-plot in **Figure 2**. This dependence is in line with the expected deformation behaviour of the single-phase materials. The peak flow-stress values decline with the increasing temperature and decreasing strain rate. The $\sigma_p - e$ plots reveal that the Ms70 brass undergoes a recovery during the deformation. The shapes of these curves suggest that a dynamic recrystallization is the primary mechanism. Values σ_p and e_p were used to calculate the activation energy of the deformation and were published in an article.⁹

The ultimate strain e_f (strain to fracture) is another characteristic of a material's formability. The values of the strain to fracture for a torsion testing of the Ms70 brass are summarised in **Figure 3**. The effects of the differences between the strain rates are indistinct but certain trends can be found. Despite the scatter in the measured values resulting from the sensitivity of the torsion test to the inhomogeneity of the test bar surface,

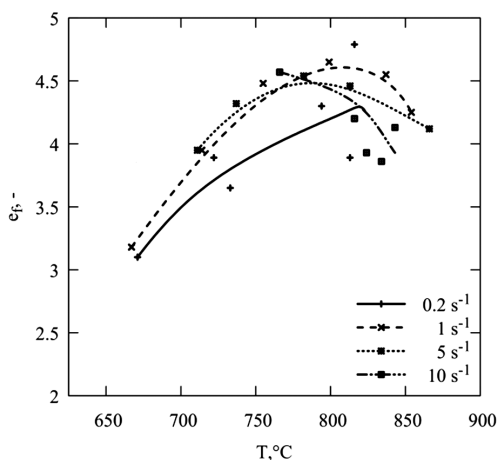


Figure 3: Relationship between the strain intensity to fracture and temperature
Slika 3: Odvisnost med intenziteto napetosti do preloma in temperaturo

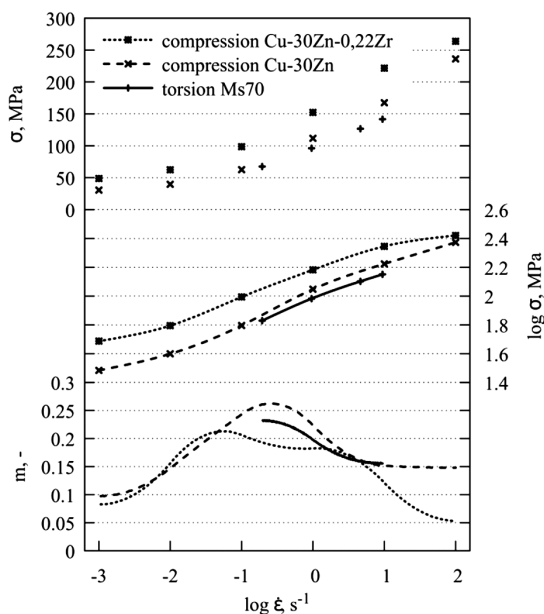


Figure 4: Conversion of the results of the plastometer testing at 650 °C from the recorded stress values at the strain of $e = 0.5$ into the strain-rate coefficient m

Slika 4: Pretvorba rezultatov preizkusov na plastometru pri 650 °C iz zabeleženih vrednosti napetosti pri hitrosti trganja $e = 0,5$ v koeficient hitrosti natezanja m

it is clear that the optimum forming temperature is between 800 °C and 850 °C.

Power-dissipation maps were constructed using the dynamic material model. The power-dissipation coefficient η was found using the following procedure: The stress-strain rate function was transformed into the log-stress vs. log-strain rate relationship (**Figure 4**).

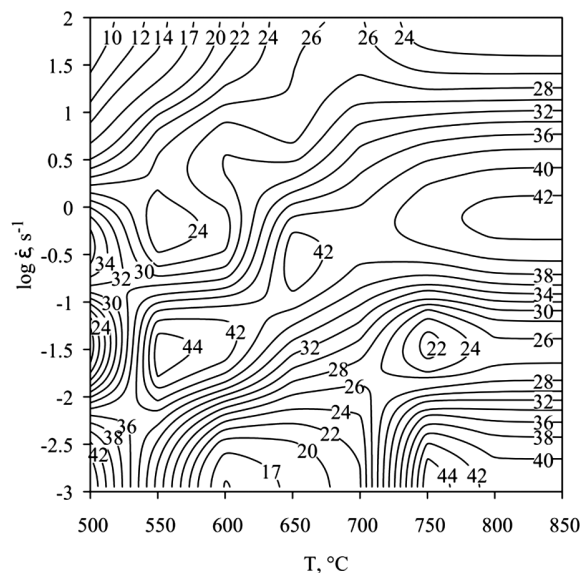


Figure 5: Power-dissipation map for the alpha brass with 30 % Zn constructed from the data from¹⁰ for the strain of 0.5. The numbers represent dissipation efficiency in fractions (%).

Slika 5: Zemljevid raztrosa moči za alfa med s 30 % Zn, konstruiran iz podatkov iz¹⁰ za hitrost trganja 0,5. Številke pomenijo učinkovitost raztrosa v deležih (%).

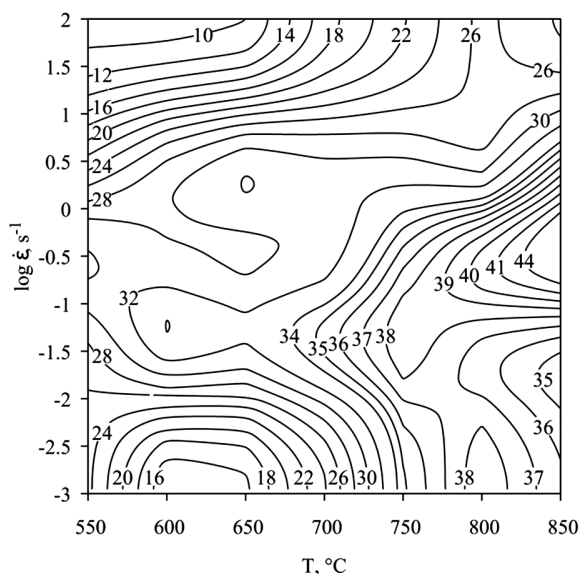


Figure 6: Power-dissipation map for the alpha brass with 30 % Zn and 0.20 % Zr constructed from the data from⁵ for the strain of 0.5. The numbers represent dissipation efficiency in fractions (%).

Slika 6: Zemljevid raztrosa moči za alfa med s 30 % Zn in 0,20 % Zr, konstruiran iz podatkov iz⁵ za hitrost trganja 0,5. Številke pomenijo učinkovitost raztrosa v deležih (%).

Cubic splines were used to find the log-stress values between the experimentally measured points, from which the strain-rate coefficient was calculated. **Figure 4** illustrates three different dependences at the temperature of 650 °C. The stress curve from the torsion plastometer

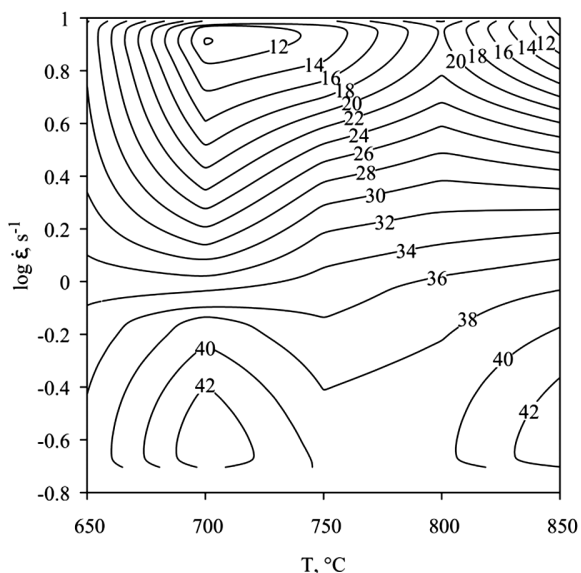


Figure 7: Power-dissipation map for the alpha brass with a chemical composition according to **Table 1** constructed from the data measured with the SETARAM-VÍTKOVICE torsion plastometer for the strain rate of 0.5. The numbers represent dissipation efficiency in fractions (%).

Slika 7: Zemljevid raztrosa moči za alfa med s kemično sestavo iz **table 1**, konstruiran iz podatkov, izmerjenih s torzijskim plastometrom SETARAM- VÍTKOVICE , za hitrost trganja 0,5. Številke pomenijo učinkovitost raztrosa v deležih (%).

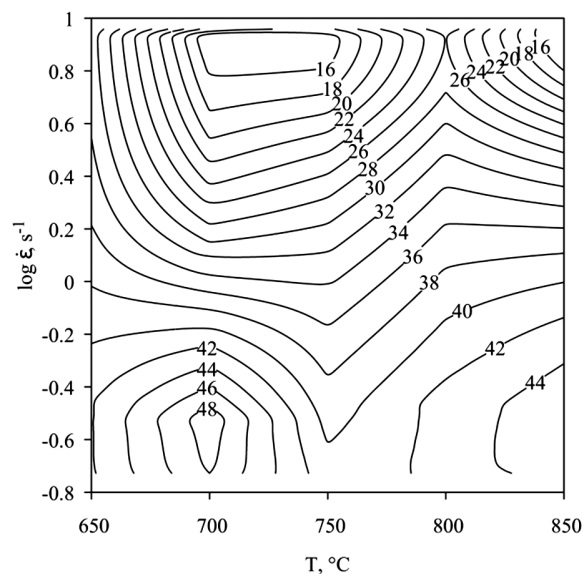


Figure 8: Power-dissipation map for the alpha brass with a chemical composition according to **Table 1** constructed from the data measured with the SETARAM-VÍTKOVICE torsion plastometer for the strain rate of 0.9. The numbers represent dissipation efficiency in fractions (%).

Slika 8: Zemljevid raztrosa moči za alfa med s kemično sestavo iz **table 1**, konstruiran iz podatkov izmerjenih s torzijskim plastometrom SETARAM- VÍTKOVICE, za hitrost trganja 0,9. Številke pomenijo učinkovitost raztrosa v deležih (%).

has a narrow range of strain rates. The other curves are based on the values for the 30 % Zn brass published in¹⁰ and the values for the brass with the mass fraction of Zn 30 % and 0.22 % Zr reported in⁵. The strain-rate coefficient *m* vs. the log-strain-rate relationship is very similar in all the CuZn30 brasses, regardless of the testing-machine type. The peak value of the *m* coefficient is lower in the brass with a 0.22 % Zr addition.

Figure 5 shows the power-dissipation map for the 0.5 strain in the brass with 30 % zinc. This map was developed using the values published in¹⁰. Upon the comparison with the map shown in¹⁰, certain differences become apparent, such as that between the high temperature and low-strain rate areas. In the original map, dissipation increases in this area. In the map constructed upon a re-calculation, a region with a decrease followed by an increase is found. The maps re-calculated for the brass with 30 % zinc and 0.22 % Zr do not exhibit any substantial differences (**Figure 6**). Their characters are very similar but the absolute values are shifted. This may be attributed to the algorithm used for constructing the 3D map. The new procedure obviates excessive smoothing of dissipation-coefficient curves at the individual temperature levels. The older maps were constructed to verify the entire procedure: to allow a comparison with the power-dissipation map for the 0.5 strain obtained from the torsion test.

As evidenced by **Figure 7**, the ranges of the strain rates and temperatures are narrower than in the studies reported in^{5,10}. The SETARAM torsion plastometer

cannot cover the range of high strain rates due to the physical limitations of the torsion testing. The lower strain rates are achievable with the use of an additional gearbox. However, they were not explored as the original experiment was aimed at the dynamic recrystallization as the governing recovery process. A comparison with the re-calculated power-dissipation maps in **Figures 5** and **6** shows a good agreement with the shape for the brass with 30 % zinc (**Figure 5**). However, substantial deviations can be found at the points representing the limit strain rates, as the procedure for finding the m values is very sensitive to the algorithm for calculating cubic splines and to the accuracy of the flow-stress values. The strength of the torsion test lies in the use of the large strains, which are not achievable in the compression plastometers. Consequently, the power-dissipation maps were available for the high strains as well, such as that in **Figure 8** for the 0.9 strain. The map documents a high efficiency of the dissipation through the microstructural changes at the lower strain rates for all the deformation temperatures.

4 CONCLUSION

The torsion test allows the temperature and strain-rate dependences of the flow stress to be studied under various deformation conditions. Using the peak stress values found, i.e., the values representing the flow stress, the extrusion force can be calculated and the examples for Ms70 are published in¹¹. The torsion simulation over a wide range of deformation temperatures suggested that the capacity of the Ms70 brass for deformation may become depleted. A technological testing of hot extrusion^{12,13} showed that the formability of brass is poor, which leads to transverse surface cracking. The results of the torsion plastometer testing were converted into the power-dissipation maps for selected strain levels. The dissipation-efficiency η values are comparable with the identically processed literature data. However, there are variances resulting from the difference between the algorithms for computing 3D maps and from the sensitivity to the correct data processing of the boundary strain rates.

Acknowledgment

The results presented in this paper were obtained within the project West-Bohemian Centre of Materials and Metallurgy CZ.1.05/2.1.00/03.0077, co-funded by the European Regional Development Fund.

5 REFERENCES

- ¹ M. Buršák, J. Bacsó, Skúšanie, kontrola a hodnotenie kvality materiálov, Emilena, Košice 2008
- ² R. Pernis, O. Híreš, J. Kasala, Rozdelenie mechanických vlastností ťahanej mosadznej tyče po priereze. In: Metal 2009, 18th international material and metallurgical conferences, Hradec nad Moravicí, ČR [CD-ROM], Ostrava, Tanger, 2009, 8
- ³ I. Schindler, J. Bořuta, Utilization Potentialities of the Torsion Plastometer, Silesian Technical University, Katowice, 1998, 104
- ⁴ D. Padmavardhani, Y. Prasad, Effect of zinc content on the processing map for hot-working of alpha-brass, Materials science and engineering A, 157 (1992) 1, 43–51
- ⁵ D. Padmavardhani, Y. Prasad, Effect Of Zirconium On The Processing Maps For Hot-working Of Alpha And Alpha-beta Brass, Zeitschrift Fur Metallkunde, 84 (1993) 1, 57–62
- ⁶ Y. Prasad et al., Modeling of dynamic material behavior in hot deformation: Forging of Ti-6242, Metallurgical and Materials Transactions A, 15 (1984), 1883–1892
- ⁷ J. Bořuta et al., Plastometrický výzkum deformačního chování řízeně tvářených materiálů, Hutnické listy, 61 (2008) 1, 80–87
- ⁸ J. Bořuta, T. Kubina, A. Bořuta, Deformační napětí mosazi Ms70 při zkoušce krutem za tepla, Kovářství, (2009) 39, 13–16
- ⁹ R. Pernis, J. Kasala, J. Bořuta, High temperature plastic deformation of CuZn30 brass – calculation of the activation energy, Kovove Materialy, 48 (2010) 1, 41–46
- ¹⁰ D. Padmavardhani, Y. Prasad, Characterization of hot deformation-behavior of brasses using processing maps. 1. alpha-brass, Metallurgical Transactions A, 22 (1991) 12, 2985–2992
- ¹¹ R. Pernis, J. Bidulská, Nový přístup při výpočte lisovacej sily z výsledkov krutovej skúšky, Výrobné inžinierstvo, 7 (2008) 4, 17–19
- ¹² J. Kasala, O. Híreš, R. Pernis, Start-up phase modeling of semi continuous casting process of brass billets, In: Metal 2009, 18th international material and metallurgical conferences, Hradec nad Moravicí, ČR [CD-ROM], Ostrava, Tanger, 2009, 6
- ¹³ R. Pernis, O. Híreš, J. Jurenová, Povrchové trhliny pri lisovaní mosadze CuZn30 za tepla, In: Metal 2007, 16th international material and metallurgical conferences, Hradec nad Moravicí, ČR [CD-ROM], Ostrava, Tanger, 2007, 9

RECYCLED POLYMER/CLAY COMPOSITES FOR HEAVY-METALS ADSORPTION

RECIKLIRAN KOMPOZIT POLIMER-GLINA ZA ADSORPCIJO TEŽKIH KOVIN

Fares D. Alsewailem¹, Saad A. Aljilil²

¹Petrochemicals Research Institute, King Abdulaziz City for Science and Technology (Kacst), P.O. Box 6086, 11442 Riyadh, Saudi Arabia
²The National Center for Water Technology, King Abdulaziz City for Science and Technology (Kacst), P.O. Box 6086, 11442 Riyadh, Saudi Arabia
fsewailem@kacst.edu.sa

Prejem rokopisa – received: 2012-09-26; sprejem za objavo – accepted for publication: 2012-11-27

Post-consumer plastics in the form of disposable cutlery, plates, cups, and containers for dairy products that are made of polystyrene (PS) were used to formulate polymer/clay composite materials for the purpose of using them as an adsorbent for the removal of heavy metals from waste water. The clay used in this study was a natural clay obtained from the Tabuk region in the north of Saudi Arabia. The composites were formulated by mixing 5–10 % mass fractions of clay with PS in the molten state using conventional polymer-processing equipment. Composites of virgin PS and clay were also formulated in order to compare their ability to adsorb heavy metals with that of the recycled composites. The results showed that composites based on recycled PS have a good adsorption capability in comparison with those of the virgin composites. For example, the amount of lead adsorbed per gram of adsorbent was tripled when using composites containing only 5 % of clay and 95 % of recycled PS in comparison with those with virgin PS.

Keywords: clay, polystyrene, recycled PS, heavy metals

Iz odpadne potrošniške plastike v obliki jedilnega pribora za enkratno uporabo: krožnikov, skodelic in embalaže za mlečne proizvode, iz polistirena (PS), je bil pripravljen kompozitni material polimer-glina kot adsorbent za odstranitev težkih kovin iz odpadne vode. Glina, uporabljena v tej študiji, je naravna glina, pridobljena iz območja Tabuk na severu Savdske Arabije. Kompoziti so bili izdelani z mešanjem masnih deležev 5–10 % gline s PS v staljenem stanju s konvencionalno opremo za predelavo polimerov. Za primerjavo zmožnosti adsorpcije težkih kovin so bili izdelani kompoziti z deviškim PS in glino ter reciklirani kompoziti. Rezultati so pokazali, da imajo kompoziti na osnovi recikliranega PS večjo vpojno zmogljivost v primerjavi z deviškim kompozitom. Na primer, količina adsorbiranega svinca na gram adsorbenta se je v primerjavi z deviškim PS pri uporabi kompozita s 5 % gline in 95 % recikliranega PS potrojila.

Ključne besede: glina, polistiren, reciklirani PS, težke kovine

1 INTRODUCTION

Waste water including heavy metals is an inimitable class of waste water, with all heavy metals being toxic pollutants. Lead ions in waste water, for example, is a pollutant and dangerous to human and water environments. As a result, it is necessary to eliminate heavy metals from the waste water before discharging it into the environment. The removal of heavy metals from aqueous solutions may be achieved by applying several physical and chemical methods, such as ion exchange, extraction, flotation, coagulation, electro-deposition and precipitation. However, most of these methods are considered non-viable due to the cost factor. Various materials have been utilized for heavy-metals removal from waste water include activated carbon, lime and bio-sorbents.¹ For the large-scale treatment of waste water for heavy-metals removal we need to look for a low-cost material as an alternative, cost-effective adsorbent for the removal of heavy metals such as lead ions from waste water.

Polymeric adsorbents may be used in the adsorption of heavy metals because of their easy regeneration and strong mechanical properties in comparison with other adsorbents such as activated carbon, cellulose and silica

gel.² For example, CHA-111 AND MCH-111 polymeric adsorbents were used as perfect adsorbents for adsorption pollutants such as phenols from waste water.^{3–5} Despite the fact that polymers are preferably utilized to adsorb heavy-metal ions, the higher costs of these materials may hinder their employment as cost-effective adsorbents for the large-scale production of heavy-metal free water.

In this work we tried to look for low-cost adsorbents for the removal of lead from waste water by choosing two discarded materials that can be obtained with no cost. These two materials were natural clay and discarded post-consumer polystyrene. In our previous publication⁶ we proved that natural clay taken from the north of Saudi Arabia may be used as a cost-effective adsorbent for lead ions. In the current work, we report on the formulation of clay with post-consumer polystyrene articles that are eventually discarded in landfills as waste materials. Recycled polystyrene/clay composite material for the purpose of using it as an adsorbent for heavy-metals removal from waste water was formulated by the current research. The clay used in this study was a natural clay obtained from the Tabuk region in the north of Saudi Arabia. The composites were formulated by mixing the mass fractions 5–10 % of clay with poly-

styrene (PS) in the molten state using conventional polymer-processing equipment. Composites of virgin PS and clay were also formulated in order to compare their ability to adsorb heavy metals with that of the recycled composites. The adsorption isotherms of the two polymer composites are also discussed here and the equilibrium parameters required to design a batch absorber are also estimated.

2 EXPERIMENTAL

2.1 Materials

The polymers used in this study were virgin polystyrene and recycled polystyrene. The virgin polystyrene was supplied by the SABIC Company in Saudi Arabia, while the recycled polystyrene was post-consumer plastics in the form of disposable cutlery, plates, cups, and containers for dairy products that are made of polystyrene. A lead-ion solution was prepared from lead nitrate purified LR [Pb(NO₃)₂] and was supplied by S.define- Limited (Laboratory Rasayan).

2.2 Preparation of the polymer composites

The thermoplastic polymer is polystyrene (PS). Polystyrene has a suitable affinity for clay particles and is readily melt processed using conventional techniques such as internal mixing and extrusion. The polymer can be a so-called "virgin" polymer, i.e., a newly formed polymer, or it can be derived from polymer scrap, such as recycled polymer, as it permits the reuse of polymer materials which might otherwise be discarded, necessitating disposal in a landfill or similar.

The clay material was milled to a size below about 100 mesh and then washed with distilled water several times to remove the impurities. The clay was then dried in a vacuum oven overnight. The dried clay was then dry mixed with polymer particles, and an emulsifier, alkyl-trimethyl-ammonium, was incorporated to ease the dispersion of the clay in the polymer matrix. The composites were formulated by mixing 5–10 % of clay with PS in the molten state using a dynisco mini extruder (LME) at a temperature above the melting or softening point of the polystyrene, above about 180 °C. The extrudate was collected in a water bath, dried and subsequently ground to granules of different sieve sizes, ranging from 0.5 mm to about 3 mm.

2.3 Scanning Probe Microscopy

The morphology of the neat PS and the prepared PS/clay composites was visualized using a scanning probe microscope (SPM); solver next (NT-MDT).

2.4 Adsorption Isotherm

Stock lead solutions with a concentration of 1000 µg/g were diluted to the required concentrations

(50–1300 µg/g), and then used in the equilibrium experiments. After that, the initial concentration of the lead ion samples and the final concentration for these samples were diluted and analyzed by atomic absorption spectroscopy (model AAnalyst 700, PerkinElmer). The adsorption isotherm experiments were performed by placing a constant mass of polymer composite (1 g) in 50 ml of lead-ion solution in glass bottles in a constant agitation shaker. In each isotherm run, the temperature used was 20 °C and the particle size was 0.5 mm. The adsorption process reached equilibrium after 30 min; however, the equilibrium experiments were conducted for 3 hours to insure that the equilibrium state was attained. The samples were then filtered using filter papers, diluted, and the concentrations were measured. The adsorbed concentration was calculated from the mass-balance equation on the batch absorber as follows:

$$q_e = V(C_o - C_e)/M \quad (1)$$

where M indicates the adsorbent mass, V is the solution volume, q_e is the adsorbed lead-ions concentration in mg/g, C_o is the initial concentration of lead ions and C_e is the lead ions concentration in the bulk solution at equilibrium. The amount of lead ions adsorbed on the adsorbent versus the lead ions equilibrium concentration in the solution can be plotted to obtain the equilibrium adsorption isotherm curve and the maximum capacity of the adsorption of lead ions by the polymer composites. The spent adsorbents, polymer/clay composites, may be regenerated by treating with strong acids such as hydrochloric acid (HCl).

3 RESULTS AND DISCUSSION

The amount of lead adsorbed on polystyrene/clay composites, virgin and recycled, versus the lead concentration in the solution was plotted to obtain the equilibrium adsorption isotherm curves for the two composite systems. This is shown in **Figures 1** and **2**. As a first observation we can see from **Figures 1** and **2** that the adsorption capacities for such composite systems are low. Here we have polystyrene as the major phase that is a non-polar polymer with no functional groups on the surface and hence its activity towards lead ions adsorption may be attributed to other factors other than its surface functionality. Surface morphologies in the form of the rough topology of the polystyrene granules used in the adsorption isotherm experiments may be responsible for such performance. Another explanation for the adsorption of lead ions on the polystyrene is that, the lead ions may be adsorbed by the polystyrene with van der Waals forces because of the adsorption of the lead ions on the polymer is of the Langmuir monolayer type. The same trend was observed by Zhang,⁷ where he attributed the adsorption to the monolayer adsorption in addition to the capillary condensation and micropore filling.

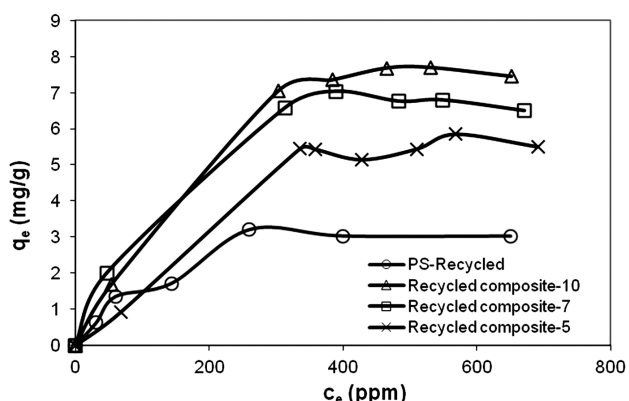


Figure 1: Equilibrium isotherm experiments for the adsorption of lead ions on the recycled polymer/clay composites with different amounts of clay in mass fractions: 5 %, 7 % and 10 %

Slika 1: Ravnotežne izoterme za adsorpcijo ionov svinca na recikliranem kompozitu polimer-glina z različno vsebnostjo glin v masnih deležih: 5 %, 7 % in 10 %

It is clear from **Figures 1** and **2** that composites based on recycled PS have a good adsorption ability in comparison with those of the virgin composites. For example, the amount of lead adsorbed per gram of adsorbent was tripled when using composites containing only 5 % of clay and 95 % of recycled PS in comparison with those containing virgin PS. The adsorption behavior of the neat recycled and virgin PS is also shown in **Figures 1** and **2** in order to compare their adsorption ability with those reinforced with clay particles. Needless to say that the adsorption capacity of neat clay, that is Tabuk clay in this study, is much higher than that of the composite system.⁶

The maximum capacity for the adsorption of lead ions on the recycled polymer composite was on recycled polymer-10, as shown in **Figure 1**. It is clear that recycled polymer-10 was more efficient in terms of lead adsorption when compared with that of the other types of recycled polymers (recycled polymer-5 and recycled

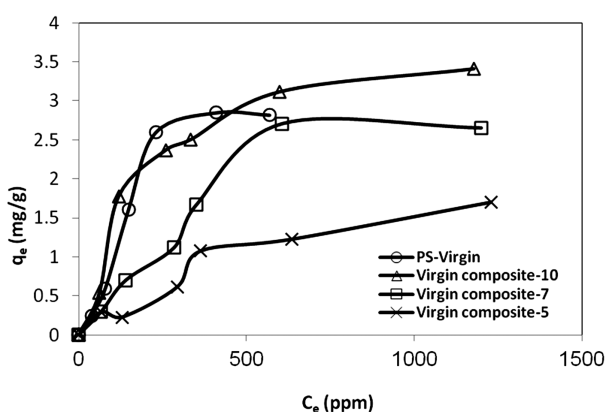


Figure 2: Equilibrium isotherm experiments for the adsorption of lead ions on the virgin polymer/clay composites with different amounts of clay in mass fractions: 5 %, 7 % and 10 %

Slika 2: Ravnotežne izoterme za adsorpcijo ionov svinca v deviškem kompozitu polimer-glina z različno vsebnostjo glin v masnih deležih: 5 %, 7 % in 10 %

polymer-7). The polar groups (such as carbonyl and hydroxyl) that may exist on the surfaces of a recycled polymer from exposure to the sun may enhance the adsorption of metals ions. The surface of a recycled polymer material may play an important role in adsorption of the adsorbate, where it has many different polar groups, such as carbonyl and hydroxyl.⁸ **Figure 3** shows that the recycled composites have a distinct peak of IR at a wave number of between 1700 and 1800, which is an indication of the presence of a carbonyl group. In addition, the mixed clay plays another role in enhancing the adsorption of the lead ions on the recycled polymer composite.

In contrast to what is seen with the recycled composites, the neat virgin PS behaves better in terms of adsorption capacity in comparison with that of the virgin composites, especially at a low clay content, from 5–7 %. This may be attributed to diminishing the role of the clay particles in the absence of a functional group on the PS surface. It should also be noted that, as shown in **Figure 2**, the maximum capacity of the adsorption of lead ions on the virgin polymer composite, was less than that of the recycled composites. **Figure 4** shows the appearance of the neat PS and the composite surfaces taken by the SPM. It is clear that while the neat PS surface appears relatively smooth, the clay particles were not dispersed well within the virgin PS matrix, as shown in **Figure 4b**. In contrast, the clay particles were dispersed evenly in the recycled PS matrix, as shown in **Figure 4c**. This may be due to the help of the carbonyl group on the recycled PS surface.

Two isotherm models – Langmuir and Freundlich – were applied to describe the experimental data for the polymer composites used in this study.

The Langmuir model suggests that the adsorption of heavy-metal ions on the adsorbent surface is a monolayer and this is applied to evaluate the maximum capacity of the adsorption.⁷ The Langmuir isotherm model is written as follows:

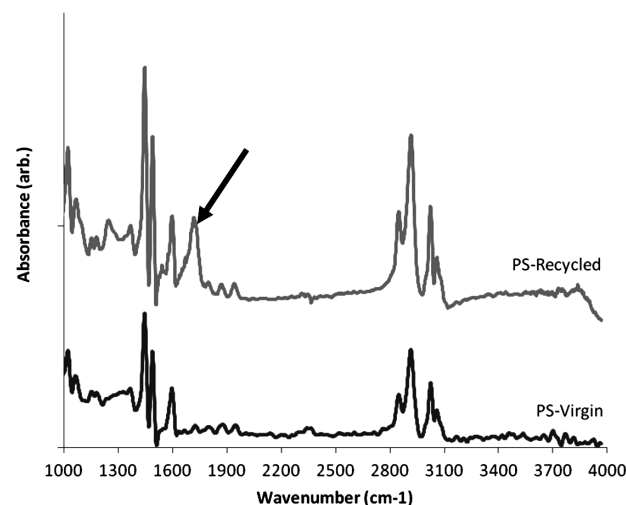


Figure 3: FTIR comparison of virgin and recycled PS
Slika 3: FTIR-primerjava deviškega in recikliranega PS

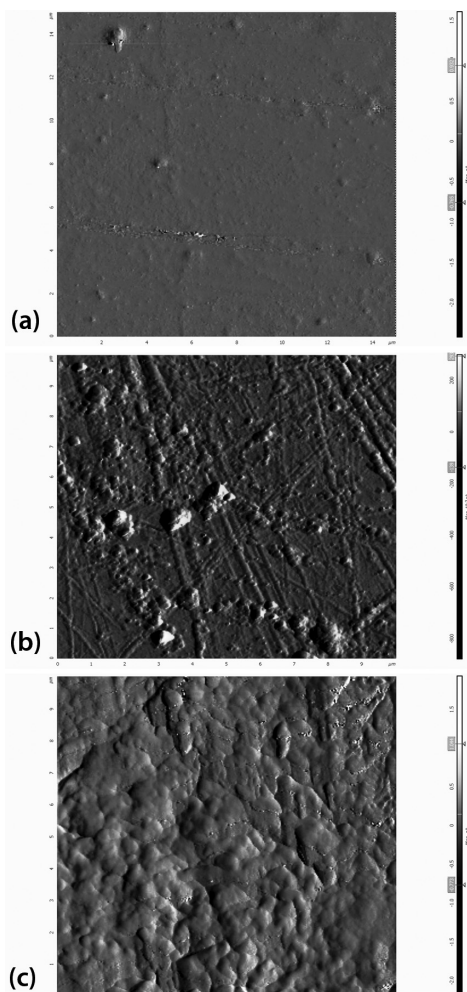


Figure 4: SPM graphs of PS/clay composites: a) neat PS; b) virgin composites; c) recycled composites

Slika 4: SPM-posnetki kompozita polimer-glina: a) gladek PS; b) deviški kompozit; c) recikliran kompozit

Table 1: Langmuir constants for the lead-ions adsorption on the recycled polymer/clay composites

Tabela 1: Langmuirova konstanta za adsorpcijo ionov svinca na recikliranem kompozitu polimer-glina

Material	$K/(l/g)$	$b/(l/mg)$	R^2
Recycled composite-5	0.1845	0.0316	0.9788
Recycled composite-7	7.880	1.1844	0.9833
Recycled composite-10	0.1629	0.0198	0.9862

$$q_e = \frac{KC_e}{1+bC_e} \quad (2)$$

where k and b are constants. The mathematical forms of the Langmuir model in the linear form is given below:

$$C_e/q_e = 1/K + (b/K)C_e \quad (3)$$

The Langmuir parameters K and b may be obtained by using the linear regression technique with equation 3. Figures 5 and 6 show the linear relationship between C_e/q_e and C_e for the polymer composites, recycled and

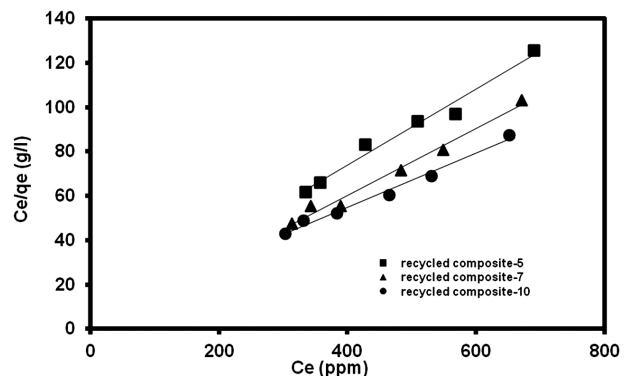


Figure 5: Langmuir isotherm fit for the experimental data of recycled polymer composites

Slika 5: Ujemanje Langmuirove izoterme z eksperimentalnimi podatki za kompozite iz recikliranega polimera

Table 2: Langmuir constants for the lead-ions adsorption on the virgin polymer/clay composites

Tabela 2: Langmuirova konstanta za adsorpcijo ionov svinca na deviškem kompozitu polimer-glina

Material	$K/(l/g)$	$b/(l/mg)$	R^2
Virgin composite-5	0.005	0.0020	0.9838
Virgin composite-7	0.008	0.0019	0.8828
Virgin composite-10	0.023	0.0060	0.9988

virgin. The equilibrium parameters K and b are listed in Tables 1 and 2.

The Freundlich isotherm model may be used to describe the adsorption isotherm of heterogeneous adsorption surfaces. The model is given by the following relation:

$$q_e = K_f C_e^{(1/n)} \quad (4)$$

The model, given by eq. 4, may be written in linear form as follows:

$$\lg q_e = \lg K_f + (1/n) \lg C_e \quad (5)$$

The equilibrium constants K_f and n may be calculated using the linear regression technique with equation 5.

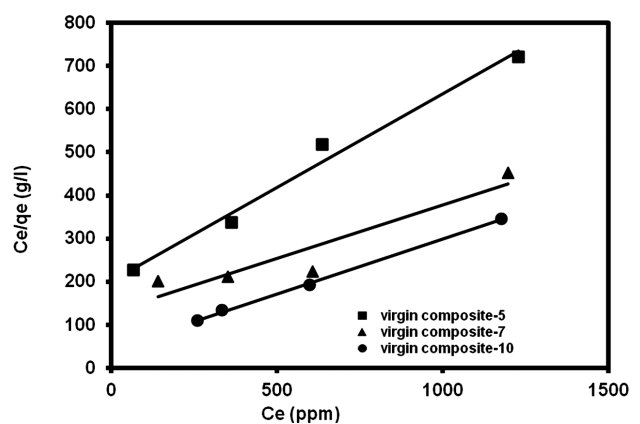


Figure 6: Langmuir isotherm fit for the experimental data of the virgin polymer composites

Slika 6: Ujemanje Langmuirove izoterme z eksperimentalnimi podatki za kompozite iz deviškega polimera

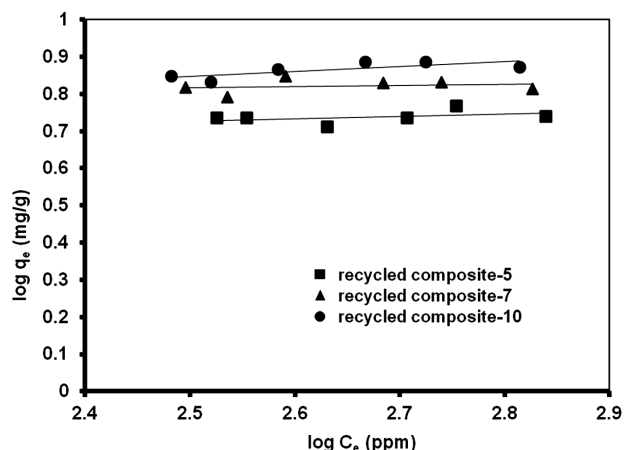


Figure 7: Freundlich isotherm fit for the experimental data of the recycled polymer composites

Slika 7: Ujemanje Freundlichove izoterme z eksperimentalnimi podatki za kompozite iz recikliranega polimera

When the value of n is greater than one, this may indicate that the adsorption of lead ions by the polymer is favorable.⁹ **Figures 7 and 8** demonstrate the linear relationship between $\lg q_e$ and $\lg C_e$ for the polymer composite systems employed in this study. The equilibrium constants, K_f and n , are presented in **Tables 3 and 4**.

Table 3: Freundlich constants for the lead-ions adsorption on the recycled polymer/clay composites

Tabela 3: Freundlichova konstanta za adsorpcijo ionov svinca na recikliranem kompozitu polimer-glina

Material	$K_f/(l/g)$	n	R^2
Recycled composite-5	3.77	16.584	0.1679
Recycled composite-7	5.59	35.587	0.0341
Recycled composite-10	3.39	7.855	0.5564

Table 4: Freundlich constants for the lead-ions adsorption on the virgin polymer/clay composites

Tabela 4: Freundlichova konstanta za adsorpcijo ionov svinca na deviškem kompozitu polimer-glina

Material	$K_f/(l/g)$	n	R^2
Virgin composite-5	0.0245	1.641	0.9712
Virgin composite-7	0.0319	1.528	0.8787
Virgin composite-10	0.5869	3.959	0.9558

The data represented by **Figures 5 to 8** and **Tables 1 to 4** show that both models describe the experimental data well, except in the case of the recycled composites data fitted to Freundlich model, as seen from **Table 3**, where the values of R^2 are extremely low.

4 CONCLUSIONS

The results from the adsorption isotherm showed that the recycled polymer composites were more efficient than the virgin polymer composites. This may be attributed to the functional groups, such as the carbonyl that may exist on the surfaces of a recycled polymer, i.e., the PS, from a prolonged exposure to sunlight. In

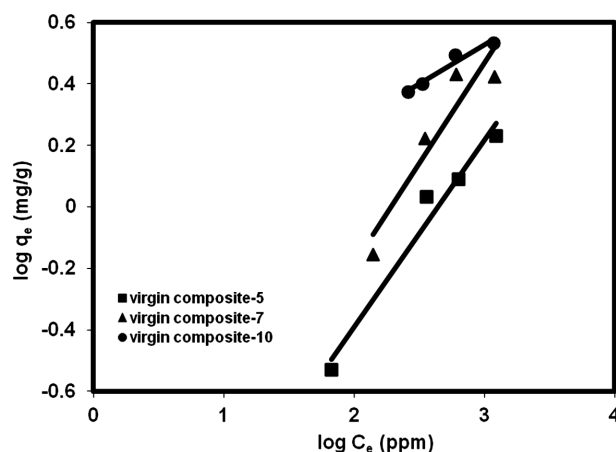


Figure 8: Freundlich isotherm is used to fit the experimental data of the virgin polymer composites

Slika 8: Ujemanje Freundlichove izoterme z eksperimentalnimi podatki za kompozite iz deviškega polimera

addition, the clay mixed with the recycled polymer plays another role in enhancing the adsorption of the lead ions on the recycled polymer composites. The presence of the carbonyl group on PS surface may contribute to a better dispersion of the clay particles in the PS matrix. The results also showed the recycled polymer composites have an acceptable adsorption capacity for the lead ions compared to the virgin composites. This finding could be an advantage when it comes to utilizing plastic waste for waste water treatment.

The experimental data were fitted using Langmuir and Freundlich models. Both models used were effective in describing the experimental data, except for the data for the recycled composites that was fitted to the Freundlich model.

Acknowledgments

The authors thank the King Abdulaziz City for Science and Technology for providing the support for this study.

5 REFERENCES

- V. M. Nurchi, I. Villaescusa, *Coordination Chemistry Reviews*, 256 (2012), 212
- A. Li, Q. Zhang, G. Zhang, J. Chen, Z. Fei, F. Liu, *Chemosphere*, 47 (2002), 981
- Z. Y. Xu, Q. X. Zhang, C. L. Wu, L. S. Wang, *Chemosphere*, 35 (1997), 2269
- Z. Y. Xu, Q. X. Zhang, J. L. Chen, L. S. Wang, G. K. Anderson, *Chemosphere*, 38 (1999), 2003
- B. C. Pan, Y. Xiong, Q. Su, A. M. Li, J. L. Chen, Q. Z. Zhang, *Chemosphere*, 51 (2003), 953
- S. A. Aljlil, F. D. Alsewailem, *Applied Clay Science*, 42 (2009), 671
- Y. H. Zhang, *Adsorption*, Shanghai Scientific & Technological Literature Publishing House, Shanghai 1989, 125
- W. Ruixia, C. Jinlong, C. Lianlong, F. Zheng-hao, L. Ai-min, Z. Quanxing, *Adsorp. Sci. Technol.*, 22 (2004), 523
- M. S. El-Geundi, *Adsorption Science and Technology*, 7 (1990), 114

INFLUENTIAL FACTORS IN THE SURFACE-HARDNESS TESTING OF A NITRIDED LAYER

VPLIVNI FAKTORJI PRI PREIZKUŠANJU TRDOTE POVRŠINE NITRIRANE PLASTI

Franjo Cajner, Darko Landek, Ivan Kumić, Amalija Vugrinčić

Faculty of Mechanical Engineering and Naval Architecture (FMENA), University of Zagreb, Ivana Lucica Street No. 1, 10000 Zagreb, Croatia
darko.landek@fsb.hr

Prejem rokopisa – received: 2012-09-27; sprejem za objavo – accepted for publication: 2012-12-04

Nitrocarburizing is one of the frequently applied processes that significantly improve the service life of steel parts in the complex activities of mechanical loads, wear and corrosion damages. Characterization and confirmation of the quality of a nitrided/nitrocarburized layer is a prescribed norm including a determination of the surface hardness, nitriding hardening depth, compound-zone thickness and its porosity. In the testing of the surface hardness, in spite of determined conditions, there are additional factors that can affect the obtained result and can lead to a misunderstanding between a customer and a provider of the service of nitriding. In this paper, possible influential factors related to the surface hardness are considered and statistically analyzed by the ANOVA two-factor test. The considered influential factors are: the surface-preparation method and the loading force. The tests carried out during the research indicated a significant influence of the loading force and of the surface preparation on the results of the nitrided/nitrocarburized-steel surface hardness. Also, the indentation size effect is confirmed in the hardness tests with a small loading force.

Keywords: nitriding/nitrocarburizing, surface hardness

Nitrocementacija je pogosto uporabljen postopek, ki občutno izboljša zdržljivost jeklenih komponent pri kompleksnem delovanju mehanskih obremenitev, obrabe in korozijskih poškodb. Karakterizacija in potrditve kvalitete nitrirane/nitrocementirane plasti je predpisana in vključuje določanje trdote površine, globino utrjevanja z nitridi, debelino spojinske cone in njeno poroznost. Pri preizkušanju trdote površine so kljub točno določenim pogojem prisotni še dodatni faktorji, ki lahko vplivajo na rezultate in lahko povzročijo nesoglasje med uporabnikom in izvajalcem nitriranja. V tem članku so mogoči vplivni faktorji obravnavani in statistično analizirani z ANOVA-preizkusom dveh faktorjev. Obravnavana faktorja sta: metoda priprave površine in sila obremenjevanja. Preizkusi so pokazali močan vpliv sile obremenjevanja in priprave površine na rezultate trdote nitrirane/nitrocementirane površine. Pri merjenju trdote z majhnimi obremenitvami pa je bil ugotovljen tudi vpliv velikosti odtisa.

Ključne besede: nitriranje/nitrocementiranje, trdota površine

1 INTRODUCTION

Nitrocarburizing is a thermochemical process for modifying the work-piece surface where carbon and nitrogen are diffused into the surface to form a surface layer consisting of a compound layer and a diffusion layer.¹ The ISO 15787:2001(E) standard prescribes drawings and characterization of the nitrocarburized layer. The characterization of the layer includes the surface-hardness testing, determination of the effective depth of nitriding, thickness of the compound layer and its porosity.² The above mentioned standard is supplemented with the ISO 6507-1:2005 standard, according to which the hardness should be tested with the Vickers hardness test method.³ However, even in the case when all the requirements of these standards are fully satisfied, the results of a nitrocarburized-layer characterization may differ due to a number of influential factors. These differences in the results may lead to a misunderstanding between a customer and a provider of the service of nitriding. Here, the inaccuracies and imprecision of a surface-hardness testing are of special importance. The results of a nitrocarburized-layer surface hardness testing are significantly affected by the following factors:

indentation load of the indenter, accuracy and precision of the hardness tester, preparation of the test-sample surface, porosity of the compound layer, and the measurer's experience.⁴

2 EXPERIMENTS

In order to determine the effect of surface preparation and of the applied load on the results, hardness tests were carried out on the surface of the normalized annealed 21CrMo5-7 steel after it had been nitrocarburized in a TENIFER salt bath (580 °C/2 h oil cooling). Before the hardness tests, the surfaces of the nitrocarburized samples were prepared by grinding and polishing according to **Table 1** (the treatments marked as: A, B, C). The aim of the polishing was to reduce or remove the porous part of the compound layer in order to reduce the adverse effect of the porosity on the hardness test results. The hardness of the nitrocarburized layer was tested with the Vickers hardness test method under three different loads: 4.9 N, 9.81 N, and 49.03 N (HV0.5, HV1, and HV5). The nitriding hardness depth (NHD) was determined on a cross-section of a metallographic test sample

with the Vickers test under the load of 4.9 N (HV0.5) according to the ISO 15787:2001(E) standard. Optical microscopy was applied to the same sample to determine the thickness of the compound layer and its porosity.

Table 1: Preparation of the test sample surface for hardness testing
Tabela 1: Priprava preizkusne površine vzorca za merjenje trdote

Sample	Sandpaper grain size/duration (min)
A	P1000/10
B	P1000/10 + P2000/5
C	P600/5 + P1000/5 + P2000/5

3 RESULTS

The surface-hardness test results for the nitrocarburized samples prepared with three different surface treatments and with three different loads applied are presented in **Figure 1**. The nitriding hardness depth (**Figure 2**) is 0.22 mm. From the same figure one can see that the hardness decreases sharply with an increased distance from a sample edge. An analysis of variance (ANOVA) was carried out to determine the significance of the surface preparation and scale loading on the results of the hardness tests conducted on a sample surface. The ANOVA results (**Figure 3**) confirmed the significant influence of the surface pre-treatment and the selection of the indentation load of the indenter on the results of hardness tests.

Generally, lower hardness values were measured when a larger amount of the material was removed from the surface of a nitrocarburized sample, i.e., when sand paper with larger grains was used before the testing. The nitrocarburized layer is thin and the hardness decreases sharply with an increased distance from a sample edge.

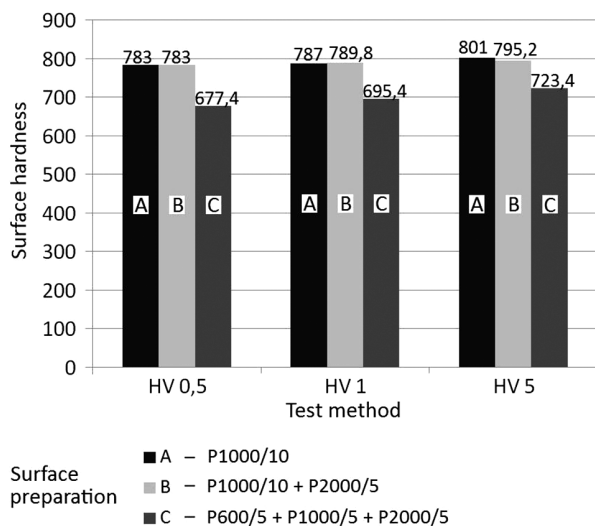


Figure 1: Surface hardness of nitrocarburized 21CrMo5-7 steel samples after different surface preparations (**Table 1**) and applied loads

Slika 1: Trdota površine nitrocementiranega vzorca iz jekla 21CrMo5-7 pri različnih pripravah površine (**Tabela 1**) in uporabljernih obremenitvah

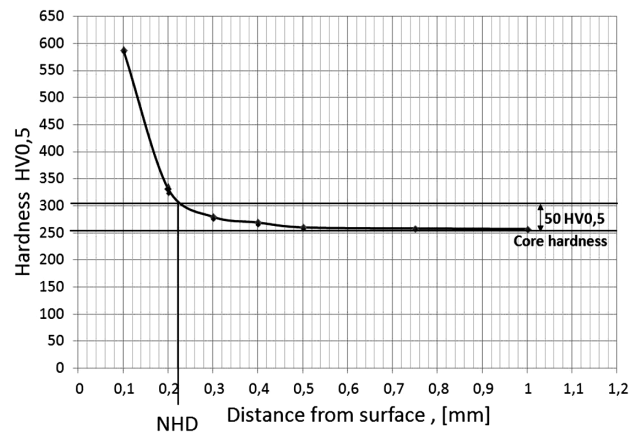


Figure 2: Hardness distribution on the cross-section of a nitrocarburized EN 21CrMo5-7 steel sample

Slika 2: Potek trdote preko prečnega prereza nitrocementiranega vzorca jekla EN 21CrMo5-7

Therefore, if the hardest part of the layer is removed by grinding, the hardness of the surface is thus reduced. Although samples A and B have been treated in a similar way, sample B, which has been additionally treated with

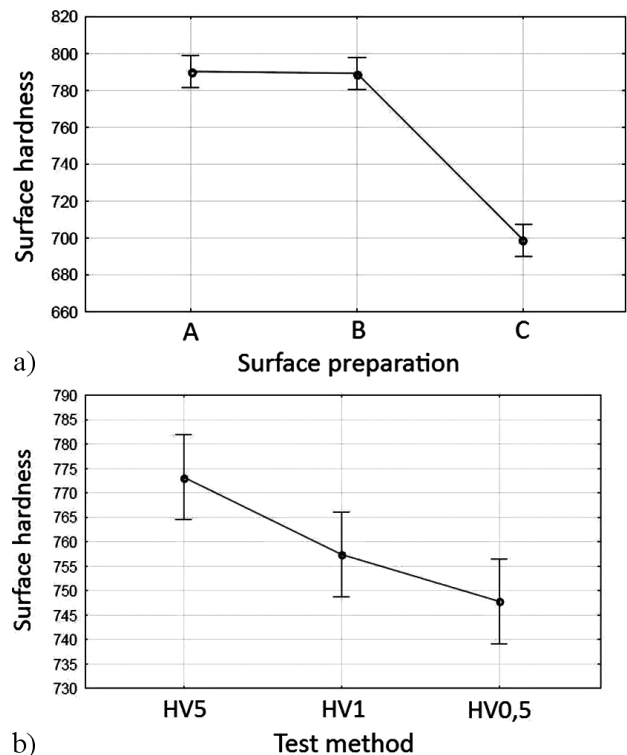


Figure 3: Influence of the surface preparation and test load on the measured values of the surface hardness on the same nitrocarburized EN 21CrMo5-7 steel sample: a) effect of the surface condition on the measured values of surface hardness, b) effect of the indentation load of the indenter on the measured values of surface hardness

Slika 3: Vpliv priprave površine in obremenitve pri preizkusu na izmerjeno vrednost trdote površine na enakem nitrocementiranem vzorcu jekla EN 21CrMo5-7: a) vpliv priprave površine na izmerjeno vrednost trdote površine, b) vpliv obremenitve pri vtiskovanju vtisnega telesa na izmerjeno vrednost trdote površine

finer grade sandpaper, exhibited a better reflection of the light, which made the measurement of diagonals easier, while the hardness of the surface remained almost the same. Accordingly, the surface preparation of sample B could be considered optimal (as it shows a good reflection of the light along with the preserved good properties of the nitrocarburized layer).

If we consider the change in the surface hardness in dependence on the indentation load of the indenter, we can notice that higher values of hardness are obtained when higher loads are applied. This is in line with the expectations that the hardness measured under low loads will depend greatly on the applied force due to the short diagonals of indentations, which can hardly be measured accurately. This phenomenon, known as the *Indentation Size Effect* (ISE), is of significance at low loads.⁴ The compound-layer thickness (CLT) of sample A was approximately 16 μm , with a porous part of approximately 8 μm . The mean CST of sample B was approximately 15 μm and it was reduced to only 5 μm on the damaged spots produced by rough grinding. If the ground surfaces of samples A, B, and C are compared using a light microscope, one can notice that a part of a compound layer has been removed in the process of surface preparation. The rougher surface of sample C after the surface preparation (the surface is damaged, more material has been removed) is the most probable cause for the values of the surface hardness that are lower than those of sample B.

4 CONCLUSION

The following conclusions can be drawn from the investigation into the effect of a surface treatment and indentation load of the indenter on the test results for the nitrocarburized EN 21CrMo5-7 steel surface hardness:

- A nitrided layer with the compound-layer thickness (CLT) of 16 μm and with the porosity of 8 μm was obtained. The nitrided hardness depth (NHD) was 0.22 mm.

- The values of the surface hardness (according to the Vickers test) greatly depend on the quality of the surface and the applied load. By using sandpaper with larger grains to grind the spot to be measured, the porous part of the compound layer is removed, the layer becomes thinner and the measured values of the surface hardness are lower. When the loads of 0.981 N and 4.89 N were applied, higher values of the surface hardness were obtained for the same measurement spot with the load of 0.981 N than those obtained in the test with the load of 0.489 N.
- During the preparation of the hardness testing of the compound-layer porous part, a compromise between grinding and polishing has to be made in order to obtain a good light reflection and to preserve a sufficient thickness of the surface layer.

Acknowledgements

This investigation was carried out within the research projects "Surface engineering in manufacturing of engineering components and tools" and "Modelling of material properties and process parameters" funded by the Ministry of Science, Education and Sports of the Republic of Croatia, within the Faculty of Mechanical Engineering and Naval Architecture, University of Zagreb.

5 REFERENCES

- ¹ D. Pye, Practical Nitriding and Ferritic Nitrocarburizing, ASM International, Metals Park, OH, USA 2003
- ² ISO 15787:2001(E) – Technical product documentation – Heat-treated ferrous parts – Presentation and indication ISO Committee, Geneva 2001
- ³ ISO 6507-1:2005 – Metallic materials – Vickers hardness test – Part 1: Test method, ISO Committee, Geneva 2005
- ⁴ ASM Handbook, Mechanical Testing and Evaluation, Vol. 8, ASM International, Metals Park, OH 2000

MECHANICAL AND MICROSTRUCTURAL PROPERTIES OF THE FLY-ASH-BASED GEOPOLYMER PASTE AND MORTAR

MEHANSKE IN MIKROSTRUKTURNE LASTNOSTI GEOPOLIMERNIH VEZIV IN MALT IZ LETEČEGA PEPELA

Radomir Zejak¹, Irena Nikolic², Dragoljub Blečić², Vuk Radmilović³, Velimir Radmilović³

¹University of Montenegro, Faculty of Civil Engineering, Džordža Vašingtona bb, 81000 Podgorica, Montenegro

²University of Montenegro, Faculty of Metallurgy and Technology, Džordža Vašingtona bb, 81000 Podgorica, Montenegro

³Faculty of Technology and Metallurgy, University of Belgrade, Karnegijeva 4, 11120 Belgrade, Serbia
irena@ac.me

Prejem rokopisa – received: 2012-12-03; sprejem za objavo – accepted for publication: 2012-12-14

In this paper we have investigated the influence of synthesis parameters on the mechanical properties of the fly-ash-based geopolymer paste and mortars. Moreover, the influence of an addition of limestone sand on the microstructure of fly-ash-based geopolymers was investigated as well. An addition of limestone sand increased the compressive strength of the fly-ash-based geopolymer mortar, in comparison to the strength of the geopolymer paste, by changing the composition of the gel phase in the geopolymer structure and with the physical strengthening due to the presence of well connected grains of the sand. The results have shown that the compressive strength and Young's modulus of elasticity of the fly-ash-based geopolymer mortar are correlated. The values of these parameters increase as the alkali and silicate dosages increase. At one point, they reach the maximum values and then start to decrease. On the other hand, the parameters that considerably increase the compressive strength slightly decrease the flexural strength of the geopolymer mortar.

Keywords: geopolymerization, fly ash, mortar, flexural strength, compressive strength, Young's modulus

Članek obravnava raziskavo vplivov parametrov sinteze na mehanske lastnosti geopolimernih veziv in malt iz letečega pepela. Preiskovan je bil tudi vpliv dodatka peska iz apnenca na mikrostrukturo geopolimera iz letečega pepela. Dodatek peska iz apnenca je povečal tlačno trdnost geopolimerne malte iz letečega pepela v primerjavi s trdnostjo geopolimernega veziva s spreminjanjem sestave želirne faze v strukturi geopolimera in s fizikalnim utrjevanjem zaradi prisotnosti dobro povezanih zrn peska. Rezultati so pokazali pri geopolimeru iz letečega pepela povezavo med tlačno trdnostjo in Youngovim modulom elastičnosti. Vrednosti teh parametrov naraščajo z naraščanjem dodatkov silikatov in alkalij. V določeni točki dosežejo največjo vrednost in se potem začnejo zmanjševati. Po drugi strani pa parametri, ki občutno povečajo tlačno trdnost, rahlo zmanjšajo upogibno trdnost geopolimerne malte.

Ključne besede: geopolimerizacija, leteči pepel, malta, upogibna trdnost, tlačna trdnost, Youngov modul

1 INTRODUCTION

Geopolymerization is an innovative technology that can transform a variety of aluminosilicate materials with alkali activation into useful, environmentally friendly materials known as geopolymers (inorganic polymers). These materials may be successfully applied in civil engineering as a replacement for cement binders. Geopolymerization is also known as a waste-minimization technology because it may utilize waste material (coal fly ash and metallurgical slag) as raw material.

The mechanism of geopolymerisation may be summarized in a few steps:

(1) Dissolution process, in which a breaking of Al-O-Si and Si-O-Si bonds in the source material and a liberation of Al³⁺ and Si⁴⁺ in an alkali silicate solution occur. Together with the dissolution, a hydrolysis of dissolved Al and Si occurs, leading to the formation of aluminate and silicate monomeric species;

(2) Polycondensation of the Al and Si species in an amorphous three-dimensional aluminosilicate network (gel), in which the Si⁴⁺ and Al³⁺ cations are tetrahedrally

coordinated as [SiO₄]⁴⁻ and [AlO₄]⁵⁻ and linked by oxygen bridges.¹ The negative charge of the AlO₄⁻ group is charge-balanced by alkali cations (Na⁺ and/or K⁺)²;

(3) Hardening of aluminosilicate gel.

The empirical formula of a geopolymer is: Mn [(-SiO₂)_z·AlO₂]_n·wH₂O, where Mn is a cation, usually an alkali (Na⁺ or K⁺), *n* is a degree of polycondensation, *w* ∈ 3 and *z* is 1, 2 or 3.³

Geopolymers may be characterized with a variety of properties like a good thermal resistance⁴⁻⁶ and resistance to aggressive environment,^{7,8} but the basic engineering request is a high compressive strength. Depending on the processing conditions, geopolymers may show different values of compressive strength. Engineering demands for an improvement in the mechanical properties of geopolymers have resulted in considering possible geopolymer applications in the form of mortars or concrete.⁹⁻¹³

Fly ash, the by-product from coal-fired power stations, is mainly used for a geopolymer synthesis. Although fly ash is not considered to be a hazardous waste, the high quantity of ash produced all over the

world imposes the necessity of finding a solution for this environmental problem. In this sense, a utilization of fly ash through the geopolymerization process may be considered as a promising solution.

The goal of this study was to investigate the influence of the synthesis parameters, the alkali and silicate dosages, on the mechanical properties of the fly-ash-based geopolymer paste and mortar and to investigate the influence of a sand addition on the microstructural properties of the fly-ash-based geopolymers.

2 EXPERIMENT

The fly ash sourced for this investigation was supplied from the coal-fired power station Pljevlja in Montenegro. Its chemical composition is given in **Table 1**.

Table 1: Chemical composition of fly ash
Tabela 1: Kemijska sestava letečega pepela

Compound	Content, w/%
SiO ₂	49.45
Fe ₂ O ₃	5.23
Al ₂ O ₃	21.77
TiO ₂	0.66
CaO	13.34
Na ₂ O	0.46
ZnO	4.5·10 ⁻³
MgO	1.29
MnO	0.02
P ₂ O ₅	0.24
K ₂ O	1.4
LOI*	4.35

*Loss on ignition

The geopolymer paste was prepared by mixing fly ash with an alkali silicate solution, in a solid-to-liquid ratio of 1. An alkali silicate activator was prepared by mixing the NaOH and Na₂SiO₃ solutions at the mass ratios of 1, 1.5 and 2. The concentrations of the NaOH solution were (7, 10 and 13) M and a commercial sodium silicate solution ($w(\text{Na}_2\text{O}) = 8.5\%$, $w(\text{SiO}_2) = 28.5\%$, a density of 1.4 g/cm³) was used. The geopolymer paste was cast in a cylindrical plastic mould, sealed with lead and left to rest in an oven for 48 h at the temperature of 65 °C.

Geopolymer mortar was prepared by mixing the geopolymer paste with crushed limestone sand. The granulometry distribution obtained with the sieve method is given in **Table 2**. The prepared mixtures were cast into the standard 40 mm × 40 mm × 160 mm prism moulds covered with polyethylene film sheets and left in an oven for 48 h at 65 °C. After this time, the samples were allowed to cool down, then removed from the moulds and left to rest for additional 14 d at ambient temperature before any testing was performed. The samples were tested for the compressive and flexural strengths as well

as the modulus of elasticity. All the tests were performed using a minimum of three samples per mortar mix.

Table 2: Analytical sieving analysis of limestone sand
Tabela 2: Analitična sejalna analiza peska iz apnenca

Sieve size opening mm	Cumulative mass fraction of a sample pass through each sieve %
0.063	3.45
0.09	7.2
0.125	10.24
0.25	15.88
0.5	28.41
1.0	54.47
2.0	74.78
4.0	97.90
8.0	100.00

The samples of the geopolymer paste were tested only for the compressive strength, while the samples of the geopolymer mortar were subjected to testing for all the mechanical properties (compressive strength, flexural strength and Young's modulus of elasticity).

The flexural strength was determined from the modulus of the rupture test, while the Young's modulus of elasticity was calculated from the linear stress/strain response prior to failure. The samples remaining from the flexural-strength tests were used for testing the compressive strength of the geopolymer mortar.

Microstructural investigations of the geopolymer mortar were carried out using the FEI 235DB focused-ion-beam system at the National Center for Electron Microscopy at Berkeley, equipped with an EDAX Genesis energy dispersive spectrometer (EDS). The SEM images were recorded with a secondary electron detector (SED). A cross-sectioning of the geopolymer paste (without a sand addition) was carried out using 1000 pA gallium ion beam and a microstructural characterization was performed using an electron beam at the 5 kV operating voltage. In order to minimize electron charging effects, a through-lens back-scattered electron detector (TLD-B) was used for image recording.

3 RESULTS AND DISCUSSION

3.1 Mechanical properties of fly-ash-based geopolymers

Mechanical properties of fly-ash-based geopolymers are of primary importance regardless of possible applications in civil engineering. One of the basic conditions for a possible use of geopolymers in construction is a satisfactory strength, which can be significantly enhanced with an addition of sand. Two of the most important factors that greatly influence mechanical properties are alkali and silicate dosages. The influence of an alkali dosage on the mechanical properties of the geopolymer paste and mortar was evaluated through the

change in the NaOH concentration, while the influence of a silicate dosage was investigated through the change in the $w(\text{Na}_2\text{SiO}_3)/w(\text{NaOH})$ ratio.

The results have shown that the mechanical properties of the fly-ash-based geopolymer paste and mortar greatly depend on the reaction parameters of the geopolymerization process. Depending on the reaction parameters, the compressive strength of fly-ash-based geopolymers may be considerably increased with an addition of sand. The change in the compressive strength of the fly-ash-based geopolymer paste and mortar as a function of the reaction parameters is given in **Figures 1** and **2**. It is evident that the compressive strength of the geopolymer mortar is considerably higher than the compressive strength of the geopolymer paste. One of the reasons for that is the fact that well connected grains of sand physically strengthen the fly-ash-based geopolymers. The compressive strengths of both the geopolymer paste and mortar increase with the increase in the NaOH concentration (**Figure 1**) and the $w(\text{Na}_2\text{SiO}_3)/w(\text{NaOH})$ mass ratio (**Figure 2**). At one point, they reach the maximum values and then decrease. The maximum values of the compressive strength were obtained using the 10 M NaOH at the $w(\text{Na}_2\text{SiO}_3)/w(\text{NaOH})$ mass ratio of 1.5. Moreover, the compressive strength of the geopolymer mortar is higher than the strength of the geopolymer paste by 58.7 %.

The results of the investigation of geopolymer mortars have shown that the Young's modulus of elasticity is related to the compressive strength. The increase in the NaOH concentration from 7 M to 10 M leads to an increase in the Young's modulus. The maximum value of the Young's modulus of elasticity (9.1 GPa) was reached using 10 M NaOH. A further increase in the alkaline (NaOH) dosage to 13 M slightly reduced the modulus of elasticity of the geopolymer mortar (**Figure 3**). The same behaviour of the fly-ash-based geopolymer mortar was

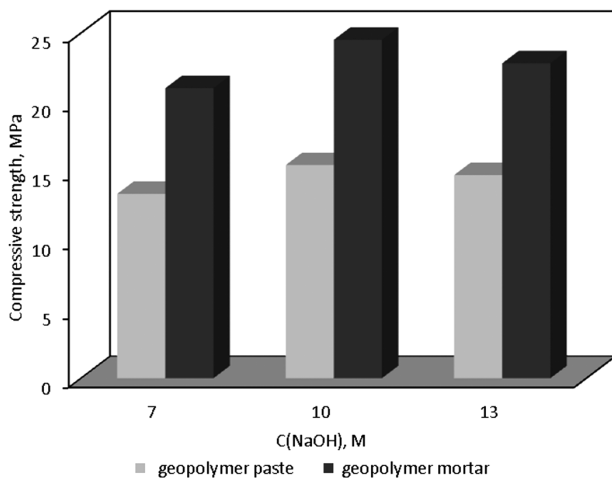


Figure 1: Change in the compressive strength of geopolymer paste and mortar as a function of the NaOH concentration

Slika 1: Spreminjanje tlačne trdnosti geopolimernega veziva in malte v odvisnosti od koncentracije NaOH

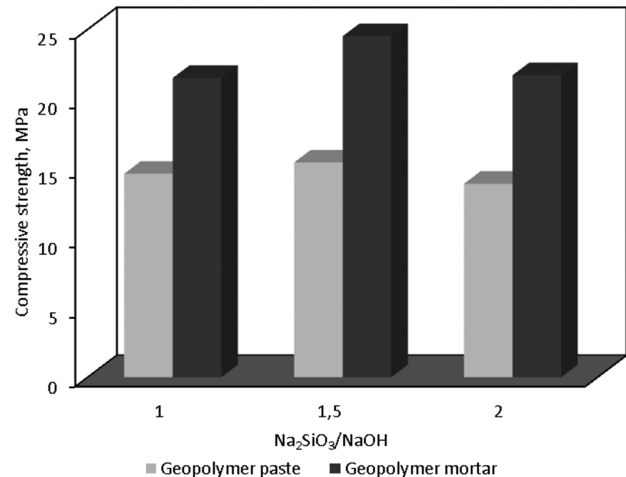


Figure 2: Change in the compressive strength of geopolymer paste and mortar as a function of the $w(\text{Na}_2\text{SiO}_3)/w(\text{NaOH})$ mass ratio

Slika 2: Spreminjanje tlačne trdnosti geopolimernega veziva in malte v odvisnosti od masnega razmerja $w(\text{Na}_2\text{SiO}_3)/w(\text{NaOH})$

observed with the change in the silicate dosage (**Figure 4**). The fly-ash-based geopolymer mortar reached the maximum value of the Young's modulus at the $w(\text{Na}_2\text{SiO}_3)/w(\text{NaOH})$ ratio of 1.5. A further increase in the silicate dosage, i.e., a change in the $w(\text{Na}_2\text{SiO}_3)/w(\text{NaOH})$ ratio, led to a reduction in the Young's modulus of elasticity. A similar observation of the influence of the silicate dosage on the Young's modulus of elasticity was observed by Duxon et al.¹⁴

On the other hand, the flexural strength of the fly-ash-based geopolymer composites is inversely related to the compressive strength and Young's modulus of elasticity. The parameters that considerably increase the compressive strength and Young's modulus of elasticity slightly reduce the flexural strength of the fly-ash-based geopolymer composites. The minimum values of the flexural strength correspond to the maximum values of the compressive strength and Young's modulus of

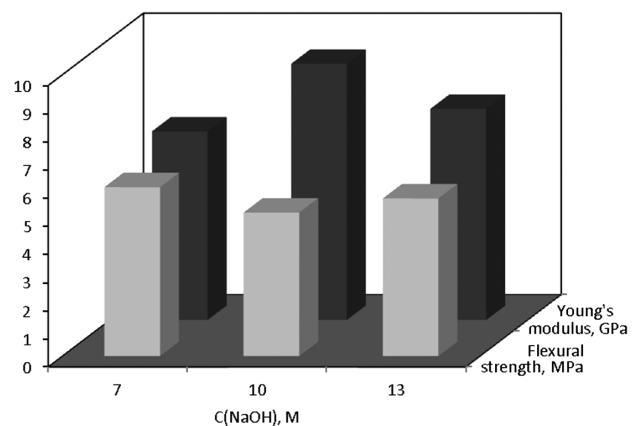


Figure 3: Change in the flexural strength and Young's modulus of elasticity of geopolymer mortar as a function of the NaOH concentration

Slika 3: Spreminjanje upogibne trdnosti in Youngovega modula elastičnosti geopolimernega malte v odvisnosti od koncentracije NaOH

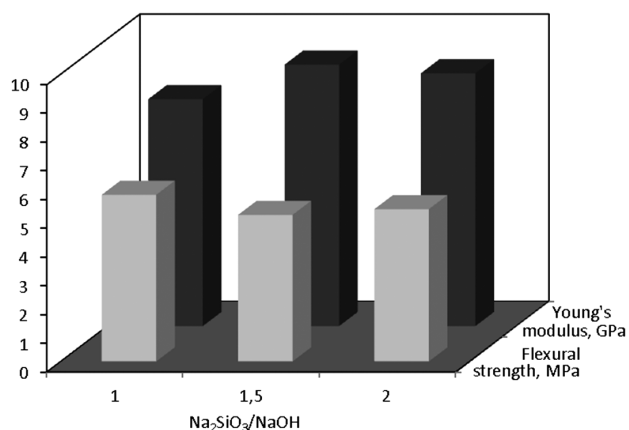


Figure 4: Change in the flexural strength and Young's modulus of elasticity of geopolymer mortar as a function of the $w(\text{Na}_2\text{SiO}_3)/w(\text{NaOH})$ mass ratio

Slika 4: Spreminjanje upogibne trdnosti in Youngovega modula elastičnosti geopolimerne malte v odvisnosti od masnega razmerja $w(\text{Na}_2\text{SiO}_3)/w(\text{NaOH})$

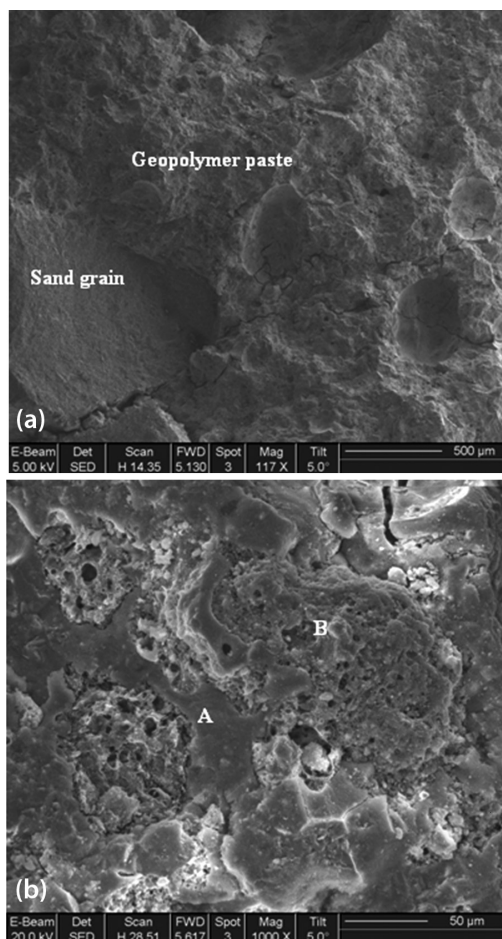


Figure 5: a) Microstructure of geopolymer mortar prepared using 10 M NaOH at the $w(\text{Na}_2\text{SiO}_3)/w(\text{NaOH})$ mass ratio of 1.5; b) geopolymer paste (as a part of geopolymer mortar); A – gel; B – unreacted fly ash particles

Slika 5: a) Mikrostruktura geopolimerne malte, pripravljene z 10 M NaOH, pri masnem razmerju $w(\text{Na}_2\text{SiO}_3)/w(\text{NaOH})$ 1,5; b) geopolimerno vezivo (kot del geopolimerne malte); A- vezivo; B- nereagirani delci letočega pepela

elasticity that were reached using 10 M NaOH (Figure 3), at the $w(\text{Na}_2\text{SiO}_3)/w(\text{NaOH})$ ratio of 1.5 (Figure 4). The highest value of the flexural strength was obtained using 7 M NaOH at the $w(\text{Na}_2\text{SiO}_3)/w(\text{NaOH})$ mass ratio of 1.

3.2 SEM –EDS microanalysis

The microstructure of the geopolymer mortar is characterized by the presence of sand grains and geopolymer paste (Figure 5a). The geopolymer paste consists of a gel phase (A) and unreacted fly-ash particles (B), (Figure 5b). The strength of the geopolymer mortar primarily depends on the structure of the gel, while the presence of the well connected grains of sand additionally strengthen the structure of the mortar. Besides, the unreacted fly-ash particles play the role of microaggregates contributing to the overall strength of the geopolymer mortar. The results of an EDS analysis of the gel phase in the mortar (Figure 6a) have shown a quantity of Ca that is considerably higher than the Si, Al, and Na contents. On the other hand, the results of an EDS analysis of the gel phase of the geopolymer paste prepared without an addition of sand, but with the same reaction parameters, have shown the quantities of Si, Al, and Na that are considerably higher than the Ca content.

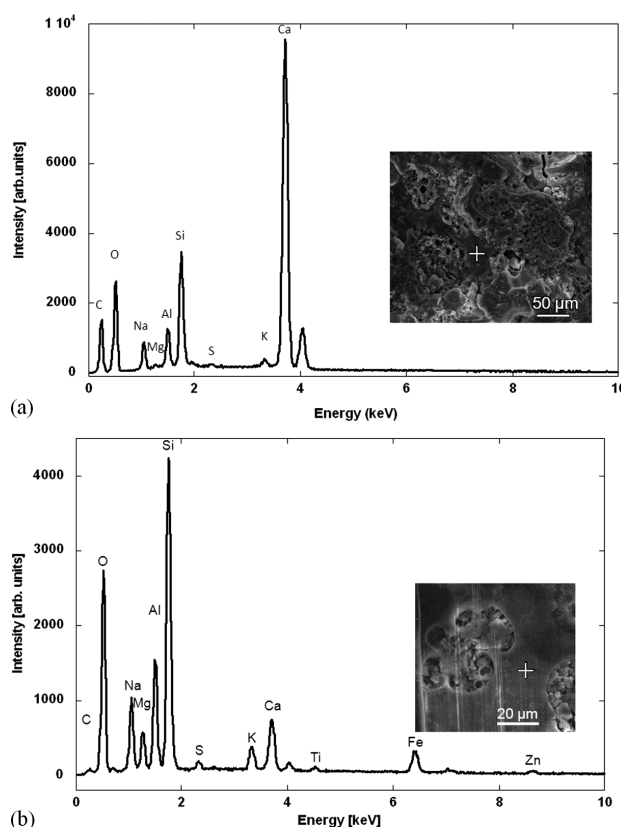


Figure 6: EDS of the: a) gel phase of fly-ash-based geopolymer mortar and b) paste (in the absence of sand)

Slika 6: EDS veziva: a) geopolimerne malte iz letočega pepela in b) veziva (brez peska)

In this case, Ca in the gel phase only originates from the fly ash (**Figure 6b**).

The previous research showed that the main gel forming elements are Si, Al and Na and that the structure of the geopolymer gel is determined by the $w(\text{Si})/w(\text{Al})$ ratio.¹⁵ But, in the geopolymer mixture with a high Ca content, the influence of Ca must be taken into account because the properties of the gel also greatly depend on the Ca content.^{16,17}

Table 3: Content of elements ($w/\%$) and their ratios in the gel phases of geopolymer mortar and paste

Tabela 3: Vsebnost elementov ($w/\%$) in njihov delež v vezivu geopolimerne malte in lepila

Ratio	Geopolymer mortar	Geopolymer paste
$w(\text{Na})/w(\text{Si})$	0.48	0.42
$w(\text{Na})/w(\text{Al})$	1.23	1.17
$w(\text{Si})/w(\text{Al})$	2.65	2.8
$w(\text{Ca})/w(\text{Si})$	3.04	0.17
Si	6.31	17.14
Al	2.38	6.11
Ca	19.17	2.85

There is no considerable difference between the $w(\text{Na})/w(\text{Si})$, $w(\text{Na})/w(\text{Al})$ and $w(\text{Si})/w(\text{Al})$ ratios in the gel phase of the geopolymer paste and mortar (**Table 3**). But, in the case of $w(\text{Ca})/w(\text{Si})$, the ratio is considerably higher in the gel phase of the geopolymer mortar than in the geopolymer paste, which indicates a strong influence of Ca on the structure of the geopolymer mortar. On the other hand, in the gel phase of the geopolymer mortar the observed quantities of Al and Si are considerably lower than their contents in the gel phase of the geopolymer paste without an addition of limestone sand (**Table 3**). It could be that the presence of Ca in some way depletes the Al and Si dissolution, but this assumption needs to be further studied.

As the limestone sand was used for the geopolymer-mortar synthesis, it is necessary to take into account the presence of Ca in the gel phase as a result of the limestone dissolution in a strongly alkaline medium. Besides, a certain amount of Ca in the gel originates from fly ash. The reaction mechanism of the geopolymerisation varies significantly, depending on the presence of Ca in the geopolymer mixture. In the absence of Ca, the main product of the geopolymerisation process is an aluminosilicate inorganic polymer (the gel), while in the presence of Ca, additional Ca-bearing phases are formed.¹⁸ The reaction pathway during the geopolymerization is strongly influenced by the Ca presence, because it strongly reacts with the soluble silicate and aluminate species provided during the dissolution step. This leads to the formation of a calcium silica hydrate and calcium aluminate hydrate gel phases.¹⁹ It is considered that these Ca phases additionally strengthen the geopolymer structure, but a clear understanding of how Ca influences the reaction mechanism of the geopolymerization has not yet been established. It is assumed that the calcium silica hydrate gel fills the voids

and pores within the geopolymer paste leading to an increase in the compressive strength.¹⁸ Moreover, it is also considered that Ca is capable of acting as a charge-balancing cation within the geopolymer structure participating, in this way, in the geopolymerization process.²⁰

4 CONCLUSIONS

In this paper, the influence of the synthesis parameters and a limestone-sand addition on the mechanical and microstructural properties of the fly-ash-based geopolymer paste and mortar was investigated. The results have shown that the compressive strength of the geopolymer paste may be increased by adding limestone sand. Moreover, the compressive strength correlates with the Young's modulus of elasticity of the fly-ash-based geopolymer mortars. Both the compressive strength and Young's modulus of elasticity increase with an increase in the NaOH concentration and the $w(\text{Na}_2\text{SiO}_3)/w(\text{NaOH})$ mass ratio, reaching their maximum values at one point and then decreasing. On the other hand, the parameters that increase the compressive strength slightly decrease the flexural strength of the fly-ash-based geopolymer mortar. The maximum value of the compressive strength corresponds to the minimum value of the flexural strength of the fly-ash-based geopolymer mortar, indicating that the fly-ash-based geopolymers may be considered to be brittle materials. An addition of limestone sand increases the compressive strength of the fly-ash-based geopolymers by changing the structure of the geopolymeric gel phase. The gel phase of the geopolymer mortar is characterized by a content of Ca that is considerably higher than in the geopolymer paste, resulting in a higher compressive strength of the geopolymer mortar. In addition, the physical presence of the well connected grains of sand also contributes to the strengthening of the geopolymer mortar.

Acknowledgements

The authors would like to acknowledge the financial support of the Montenegrin Ministry of Science in the framework of the project No.01-460. The FIB-SEM analysis was performed at the National Center for Electron Microscopy at Lawrence Berkeley National Laboratory, funded by the U.S. Department of Energy under the Contract DE-AC02-05CH11231.

5 REFERENCES

- P. Duxson, A. Fernández-Jiménez, J. L. Provis, G. C. Lukey, A. Palomo, J. S. J. van Deventer, Geopolymer technology: the current state of the art, *Journal of Materials Science*, 42 (2007) 9, 2917–2933
- F. Pacheco-Torgal, J. Castro-Gomes, S. Jalali, Alkali-activated binders: A review: Part 1. Historical background, terminology, reaction mechanisms and hydration products, *Construction and Building Materials*, 22 (2008), 1305–1314

- ³ J. Davidovits, Geopolymers, inorganic polymeric new materials, *Journal of Thermal Analysis*, 37 (1991), 1633–1656
- ⁴ D. L. Y. Kong, J. G. Sanjayan, Effect of elevated temperatures on geopolymer paste, mortar and concrete, *Cement and Concrete Research*, 40 (2010), 334–339
- ⁵ D. L. Y. Kong, J. G. Sanjayan, K. Sagoe-Crentsil, Comparative performance of geopolymers made with metakaolin and fly ash after exposure to elevated temperatures, *Cement and Concrete Research*, 37 (2007), 1583–1589
- ⁶ D. L. Y. Kong, J. G. Sanjayan, Damage behavior of geopolymer composites exposed to elevated temperatures, *Cement and Concrete Composites*, 30 (2008), 986–991
- ⁷ V. Sata, A. Sathonsaowaphak, P. Chindaprasirt, Resistance of lignite bottom ash geopolymer mortar to sulfate and sulfuric acid attack, *Cement and Concrete Composites*, 34 (2012), 700–708
- ⁸ R. R. Lloyd, J. L. Provis, J. S. J. van Deventer, Acid resistance of inorganic polymer binders. 1. Corrosion rate, *Materials and Structures*, 45 (2012), 1–14
- ⁹ M. Steinerova, Mechanical properties of geopolymer mortars in relation to their porous structure, *Ceramics –Silikaty*, 55 (2011) 4, 362–372
- ¹⁰ S. Jumrat, B. Chatveera, P. Rattanadecho, Dielectric properties and temperature profile of fly ash-based geopolymer mortar, *International communications in Heat and Mass Transfer*, 38 (2011), 242–248
- ¹¹ J. Temuujin, A. van Riessen, K. J. D. MacKenzie, Preparation and characterization of fly ash based geopolymer mortars, *Construction and Building Materials*, 24 (2010), 1906–1910
- ¹² P. K. Sarker, R. Haque, K. V. Ramgolam, Fracture behaviour of heat cured fly ash based geopolymer concrete, *Materials and Design*, 44 (2013), 580–586
- ¹³ X. S. Shia, F. G. Collins, X. L. Zhaob, Q. Y. Wanga, Mechanical properties and microstructure analysis of fly ash geopolymeric recycled concrete, *Journal of Hazardous Materials*, 237–238 (2012), 20–29
- ¹⁴ P. Duxson, J. L. Provis, G. C. Lukey, S. W. Mallicoat, W. M. Kriven, J. S. J. van Deventer, Understanding the relationship between geopolymer composition, microstructure and mechanical properties, *Colloids and Surfaces A: Physicochemical and Engineering Aspects*, 269 (2005), 47–58
- ¹⁵ H. Xu, J. S. J. van Deventer, Effect of Source Materials on Geopolymerization, *Industrial and Engineering Chemistry Research*, 42 (2003), 1698–1706
- ¹⁶ J. Temuujin, A. van Riessen, R. Williams, Influence of calcium compounds on the mechanical properties of fly ash geopolymer pastes, *Journal of Hazardous Materials*, 167 (2009), 82–88
- ¹⁷ K. Dombrowski, A. Buchwald, M. Weil, The influence of calcium content on the structure and thermal performance of fly ash based geopolymers, *Journal of Materials Science*, 42 (2007), 3033–3043
- ¹⁸ D. Khale, R. Chaudhary, Mechanism of geopolymerization and factors influencing its development: a review, *Journal of Materials Science*, 42 (2007), 729–746
- ¹⁹ P. Duxson A. Fernández-Jiménez, J. L. Provis, G. C. Lukey, A. Palomo, J. S. J. van Deventer, Geopolymer technology: the current state of the art, *Journal of Materials Science*, 42 (2007), 2917–2933
- ²⁰ L. Chao, S. Henghu, L. Longtu, A review: The comparison between alkali-activated slag (Si+Ca) and metakaolin (Si+Al) cements, *Cement and Concrete Research*, 40 (2010), 1341–1349